A Thesis Submitted for the Degree of PhD at the University of Warwick

Numerical Simulations of Unsteady Complex Geometry Flows

by

Yan Liu

A thesis submitted in partial fulfilment
of the requirements for the degree of
Doctor of Philosophy in Engineering

Supervisor: Dr Paul G. Tucker

University of Warwick, School of Engineering

February, 2004

Contents

List of Figures

List of Tables

Acknowledgments

There are really just so many people I would like to thank for helping me over these past years.

First and foremost, my special thanks to Paul Tucker, my supervisor, for his unstinting encouragement, support and help at all times, rough and smooth alike. And for his patience, too, and for so generously sharing his knowledge with me. And again for all his financial support, particularly in the latter stage of my studies. I count myself fortunate to have had such a supervisor.

My thanks go, too, to Professor Carpenter, who made so many helpful suggestions as I set up and followed through my heat transfer experiments - and for his financial support as well for me to attend a conference.

Drs Y. M. Chung and B. W. Zhong made so many helpful suggestions for my project - my questions were answered always with patient explanation. My programming skills benefited greatly from much generous help from Alex, as did my heat transfer experiments from the kind help of Geoff, Roger, Zacharie and Mr Wallace (technician).

I have not always found the English language easy to cope with! All around me I have found people helping me in many ways. But I will single out for particular thanks to Mr Anthony Divett for devoting to me so much of his time and thought to help me so generously, and to guide and teach me so much.

Colleagues, too, are so important. I have been blessed to have Giovanni, Karen, Reza and Rich, whom I thank for help with software, for their constant good humour and for teaching me the English that one can never find in books...! And Adam, Fatta, James, Mark, Patrick and Rich - I wish them all well in their PhD study.

Lastly, there are those whose names I will have overlooked in my haste. May they forgive me, for their contribution too has been just as invaluable.

This research has been funded by a University of Warwick Special Scholarship, for which I am most grateful.

Declaration

This thesis, and the material in it, is my own work. It has not been submitted for a degree at any other university.

As part of the work carried out, the following papers were published.

- Liu, Y., Tucker, P. G., Jouvray, A. and Carpenter, P. W., 2003, "Computation of a non-isothermal complex geometry flow using non-linear URANS and zonal LES", *Proc. 3rd Int. Symp. on Turbulence and Shear Flow Phenomena*, Kasagi, K. *et al.* (Eds.), Sendai, Japan, pp. 87-91.
- Tucker, P. G., Liu, Y., Chung, Y. M. and Jouvray, A., 2003, "Computation of an unsteady complex geometry flow using novel non-linear turbulence models", *Int. J. Numer. Meth. Fluids*, Vol. 43, pp. 979-1001.
- Tucker, G. P., Davidson, L. and Liu, Y., 2003, "Hybrid $k-l$ based large eddy simulation modelling", *Proc. 4th Int. Symp. on Turbulence, Heat and Mass Transfer*, Hanjalić, K., Nagano, Y. and Tummers, M. J. (Eds.), Antalya, Turkey, pp. 681-688.
- Zhong, B., Tucker, P. G. and Liu, Y., 2003, "On a hybrid LES/RANS approach and its application to flow over a matrix of surface mounted cubes", *Proc. 4th Int. Symp. on Turbulence, Heat and Mass Transfer*, Hanjalić, K., Nagano, Y. and Tummers, M. J. (Eds.), Antalya, Turkey, pp. 705-712.

Abstract

Numerical simulations have been here carried out for turbulent flows in geometries relevant to electronic systems. These include plane and ribbed channels and a central processor unit (CPU). Turbulent flows are random, three-dimensional and time-dependent. Their physics covers a wide range of time and space scales. When separation and reattachment occur, together with streamline curvature, modelling of these complex flows is further complicated.

It is well known that, when simulating unsteady flows, the traditional, steady, linear Reynolds-averaged Navier-Stokes (RANS) models often do not give satisfactory predictions. By contrast, unsteady, non-linear RANS models may perform better. Hence the application of these models is considered here. The non-linear models studied involve explicit algebraic stress and cubic models. The Reynolds Stress Model (RSM) has been also evaluated.

Modelling strategies more advanced than RANS, i.e. Large Eddy Simulation (LES) and zonal LES (ZLES), have also been tested.

Validation results from URANS, LES and ZLES indicate that the level of agreement of predictions with benchmark data is generally consistent with that gained by the work of others. For the CPU case, flow field and heat transfer predictions from URANS, LES and ZLES are compared with measurements. Overall, for the flow field, ZLES and LES are more accurate than URANS. Zonal low Reynolds number URANS models (using a near wall $k - l$ model) perform better than high Reynolds number models. However, for heat transfer prediction, none of the low Reynolds number models investigated performed well.

Nomenclature

Latin Symbols	**Definition**
$A_\epsilon, A_\mu, C_{\epsilon 0}, C_{\mu 0}$	Model constants in the $k - l$ model
c_p	Specific heat capacity at constant pressure
$c_1 \sim c_7$, $C_1 \sim C_5$	Model constants
C_{b1}, C_{b2}, C_{w1}	Model constants in the S-A model in Eq. (3.17)
C_k, C_ϵ	SGS model constants in Eq. (3.74)
C_μ	Model constant
C_s	The Smagorinsky constant in Eq. (3.69)
d	Wall distance
$D()/Dt$	Material derivative
$E, \tilde{E}$	Turbulence model constants in Eq. (3.50) and Eq. (3.53) respectively
i, j	Tensor indices (streamwise: 1; wall normal: 2; spanwise: 3.)
k	Turbulent kinetic energy, $\overline{u_i' u_j'}/2$, or thermal conductivity
l	Integral length scale or length scale
Nu	Nusselt number
p	Instantaneous static pressure
P	Mean static pressure
p'	Fluctuating component of static pressure
Pr	Prandtl number
Pr_t	Turbulent Prandtl number
q''	Heat flux
Re	Reynolds number
Re_t	Turbulent Reynolds number, $k^2/\nu\epsilon$
S_{ij}	Strain rate tensor, $\frac{1}{2}\left(\frac{\partial u_i}{\partial x_j} + \frac{\partial u_j}{\partial x_i}\right)$
t	Time or instantaneous temperature
T	Mean temperature

t'	Fluctuating component of temperature
u, v, w	Instantaneous velocities in the x, y and z directions respectively
U, V, W	Mean velocities in the x, y and z directions respectively
U_b	Bulk velocity
V_t	Turbulent velocity scale
u_i'	Fluctuating component of velocity in direction x_i
$\overline{u_i'u_j'}$ or $\rho\overline{u_i'u_j'}$	Reynolds stress tensor
u_τ	Friction velocity, $\sqrt{\tau_w/\rho}$
x_i	Cartesian space coordinate, i=1,2, 3 correponding to x, y, z - streamwise, wall normal and spanwise directions respectively
y^+	Dimensionless wall distance, $\rho y u_\tau/\mu$
y^*	Dimensionless wall distance, $\rho y c_\mu^{1/4} k^{1/2}/\mu$

Greek Symbols

α	Under-relaxation factor
β	Constant pressure gradient
δ_{ij}	Kronecker delta ($\delta = 1$ if $i = j$ and $\delta = 0$ if $i \neq j$)
ϵ	Dissipation rate of turbulence energy
$\tilde{\epsilon}$	Modified dissipation rate of turbulence energy
Δ	Filter width
κ	van Karman constant
ν	Molecular kinematic viscosity
ν_t	Kinematic turbulent viscosity
μ	Molecular dynamic viscosity
μ_t	Dynamic turbulent viscosity
ρ	Fluid density
τ	Kolmogorov time scale, $\sqrt{\nu/\epsilon}$
ϕ	Free variable
Ω_{ij}	Vorticity tensor, $\frac{1}{2}\left(\frac{\partial u_i}{\partial x_j} - \frac{\partial u_j}{\partial x_i}\right)$
ω	Specific dissipation rate
σ_k	Diffusion Prandtl number for k

σ_ϵ	Diffusion Prandtl number for ϵ
τ_{ij}, τ_w	Reynolds stress tensor and wall shear stress respectively

Subscripts

ave	Average value
b	Bulk value
int	Interface value
p	Nodal point value
s	Surface value
w	Wall value

Superscripts

$'$	Correction or fluctuation value
$\overline{(\ \ )}$	Time averaged or filtered value

Chapter 1

Introduction

1.1 Background

1.1.1 Electronics cooling systems

In 1965, Gordon Moore postulated what has come to be known as Moore's law, shown in Fig. 1.1. This states that the transistor density on integrated circuits doubles with every two years. This exponential growth with ever-shrinking transistor sizes has resulted in increased performance at a decreased cost. In 26 years the number of transistors on one chip has increased more than 3200 times, from 2300 on the 4004 in 1971 to 7.5 million on the Pentium II computer processor by 1997. By 2002, the number had further increased to 55 million. By the year 2012, a computer such as Intel should have the ability to integrate 1 billion transistors onto a production die, operating at 10GHz (www.digitalplays.com). Fig. 1.2 shows a typical history of car engine control modules (Myers, 2003). As can be seen, over time the size and cost of the typical module has decreased, while the required functionality has significantly increased. A similar trend can be observed in other electronics applications.

This trend has led to an increase in both the raw power on silicon, as well as in the power density. Fig. 1.3 shows the evolution of CPU power in the performance desktop market over the past decade (Viswanath *et al.*, 2000). It can be seen from this graph that as the frequency scales rise over time, the power dissipation of the microprocessors

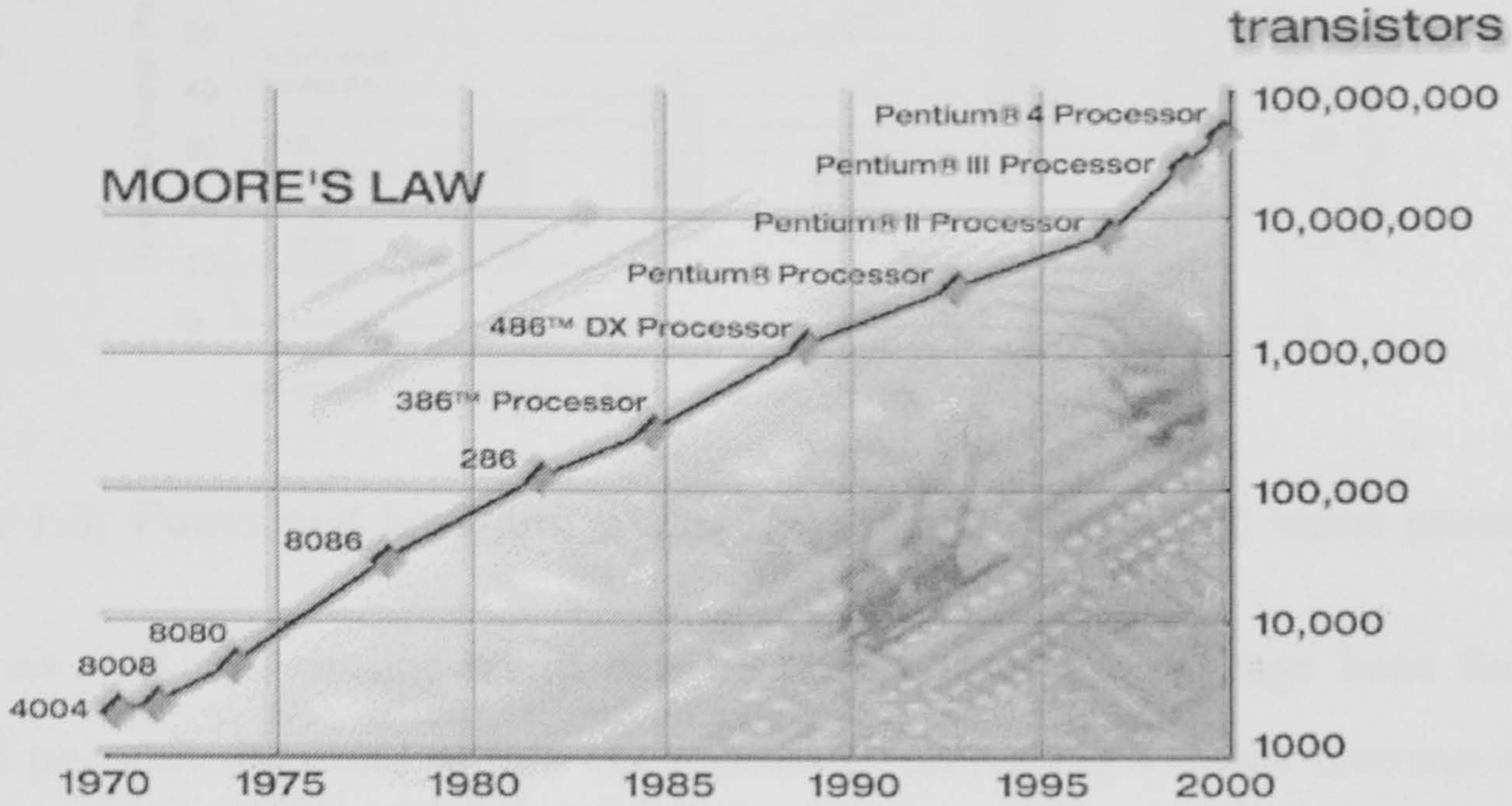

Figure 1.1: Moore's law.

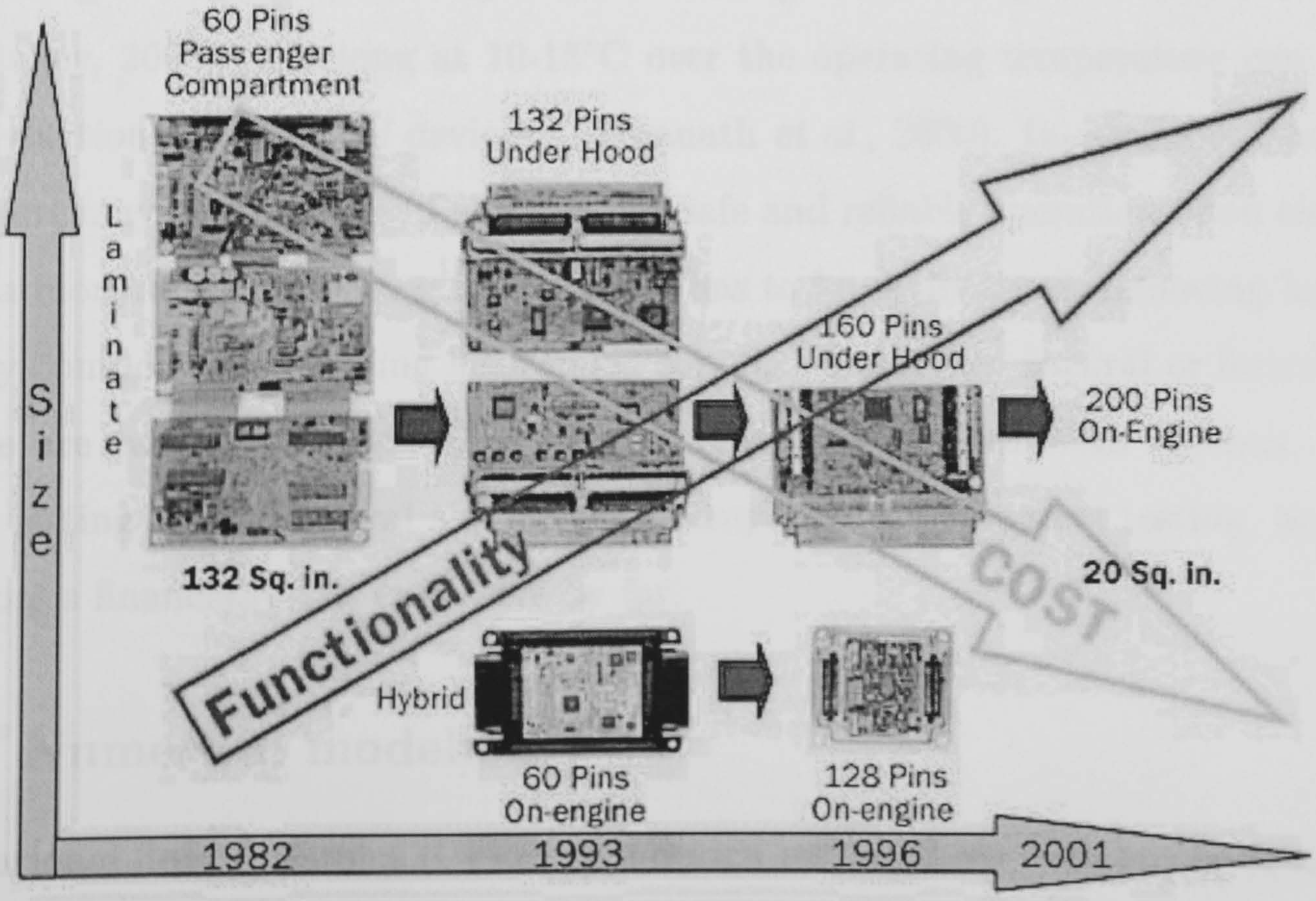

Figure 1.2: History of typical car engine control modules.

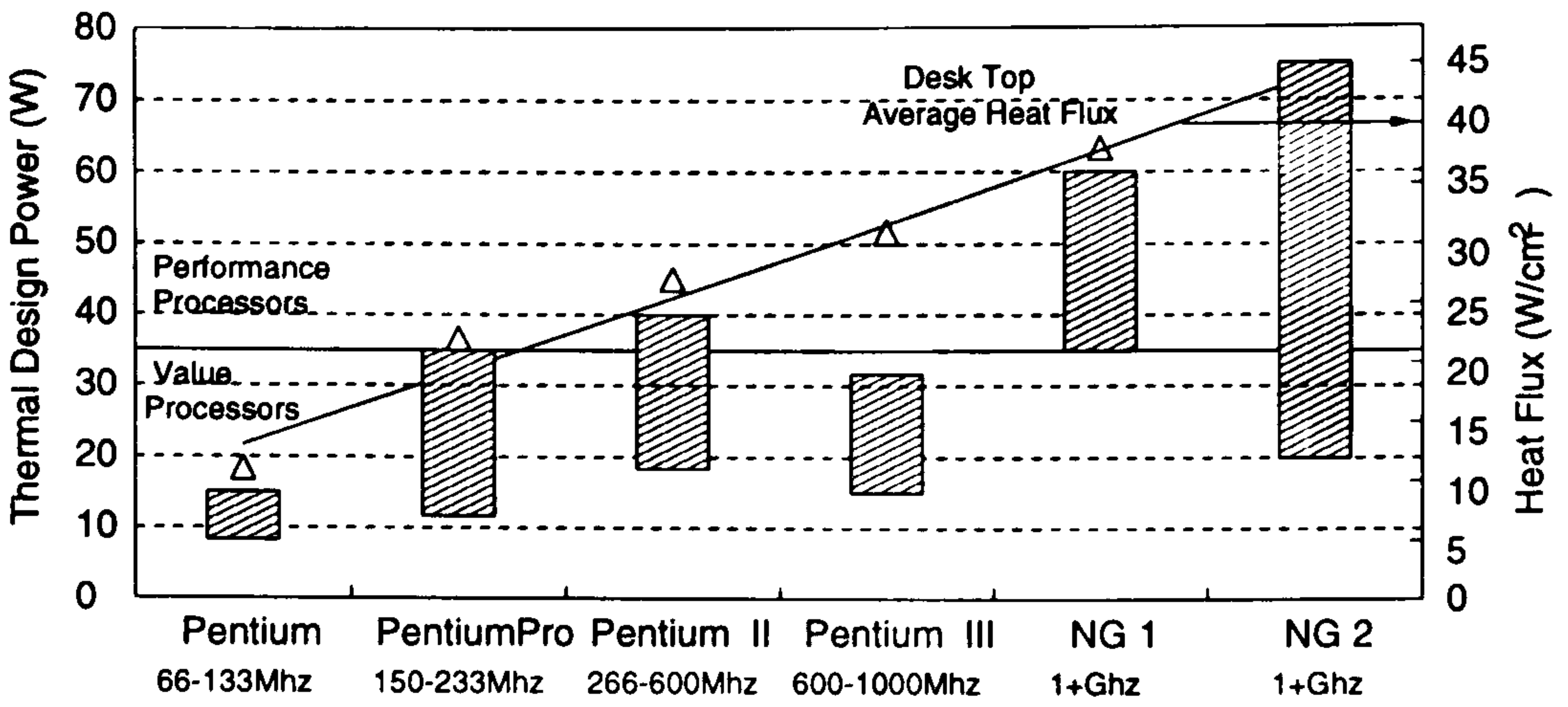

Figure 1.3: Power and heat-flux trends in the performance and value processors.

increases as well. A similar trend can be observed in the average heat flux (power dissipated per unit die area) within the processor, indicating a linear increase over time.

The above examples illustrate that on the one hand, with rapid development of microchip and packaging technology, electronic system size and cost decrease, as system functionality increases. On the other hand, high power dissipation makes thermal control or management even more important.

According to statistics, the major factor causing electronic system failure is temperature (Bailey, 2003). Working at 10-15°C over the operating temperature can lead to a 50% reduction in the life of devices (Viswanath *et al.*, 2000). In addition, overheated components may malfunction. Therefore, for safe and reliable operation of an electronic system, a more stable operating temperature has to be maintained, removing heat generated by components, by using heat sinks, convection whether natural or forced.

There are two ways of assessing thermal reliability of electronics systems, namely physical testing and numerical simulation. Compared with physical testing, numerical simulation is financially less expensive by far.

1.1.2 Numerical modelling

Computational fluid dynamics (CFD), as a design and analysis tool, has been extended to electronics systems for a number of years, being transfered from such traditional areas as aircraft, car, turbomachinery and so on. CFD allows design engineers to build and optimize a virtual prototype of a system, and further to simulate flow conditions and heat transfer within the enclosure by solving the equations governing fluid flow and heat transfer.

With increasing power densities and diminishing physical sizes, reliable prediction of fluid flow and heat transfer in electronic systems is becoming ever more essential. Flow inside an electronic enclosure is usually at a low Reynolds number, typically Re in a range of $100 < Re < 5000$. Protruding electronic components cause flow separation, re-attachment and recirculation. Thermal boundary conditions are generally non-uniform as a result of irregular power dissipation. Flow therefore becomes very complex and can be unsteady (time-dependent) because of upstream or Rayleigh-Bénard instability etc.. Such complex geometry flow is difficult to simulate accurately.

Garimella *et al.* (2002) summarize the requirements, the present status and the future of CFD for electronics cooling systems according to studies carried out by a number of panels. In reality, CFD is currently more suitable for the initial or early design phase, but not for the final stage, where more detail is necessary. This is because of the lack of computational techniques that can simulate electronics cooling systems with high predictive accuracy. In addition, there is a matter of problem definition, and also solution uniqueness issues (for example, treatment of surface roughness of components, boundary conditions and so on). Most of the simulations presented in the literature deal with steady flows. However, flows inside electronics systems are generally unsteady or oscillatory (in the sense that they have large-scale coherent structures). Therefore, as Baelmans (2002) points out, to obtain reliable predictions for complex flows in electronics systems, highly accurate modelling approaches are needed to capture flow phenomena detail, such as unsteadiness and vortex shedding. Such methods include advanced Unsteady Reynolds Averaged Navier-Stokes (URANS) models, Large Eddy Simulation (LES) and hybrid RANS/LES and so on.

Because of relatively low computational costs compared with LES, URANS (in which all eddies are modelled by means of statistical methods) prediction is still commonly preferred for engineering applications. It is widely recognized that linear models based on the isotropic Boussinesq hypothesis (this relates mean flow velocity gradients to turbulence-induced stresses via a coefficient called the eddy viscosity) cannot predict flows having either rotation or curvature effects. For complex turbulent flows (where turbulence stresses are different in different directions), advanced turbulence models such as non-linear models or Reynolds Stress Model (RSM) may give an improved performance. However, in general, URANS does not accurately capture unsteady flow features.

In LES, only large, unsteady, geometry-dependent eddies (called the Lagrangian scales) are fully resolved in space and time, while the effects of small eddies are modelled. Hence, LES is capable of capturing the dynamics of turbulence, but its application to complex industrial flows is still costly and thus limited to relatively low Reynolds number and simple geometry flows.

More recently, the intermediate approach between RANS and LES, termed zonal LES (ZLES) or hybrid RANS/LES, has received much attention from researchers. In ZLES, URANS or RANS modelling is used in the near-wall regions and LES in the remaining part of the flow. Hence the advantage of ZLES is that it can capture the unsteady behaviour of turbulent flow and reduce costs of LES for wall-bounded flows.

This present work focuses on an idealized electronic system which is representative of an electronic central processor unit (CPU) as shown in Fig. 1.4. Within the system, printed circuit boards have been removed. However, a heater is mounted on a baffle plate (see Chapter 5). For this fan-cooled system, Gr/Re^2 (<0.01, where Gr and Re are respectively Grashof and Reynolds numbers based on the height of Region 1) is small. Therefore, buoyancy effects are negligible and cooling is due to forced convection.

This study is a continuation of the work of Tucker and Pan (2000). In previous studies, Tucker *et al.* (2000, 2001, 2003a) made URANS computations without heat transfer, using linear models (e.g. mixing length, Wolfshtein (1969) $k - l$, Launder and Spalding (1974) $k - \epsilon$ models; Chen and Patel (1998) $k - l/k - \epsilon$ zonal model, and Speziale's (1987) non-linear k-l model. Their results show that, although some linear and Speziale's non-linear models gave reasonable predictions for velocities and turbulent intensities, average errors were still large. It was also found that the Speziale's non-linear model was extremely expensive to converge and did not give a better predictive accuracy than a linear zonal k-l / k-ϵ model, while the standard two-equation k-ϵ model gave the worst predictions.

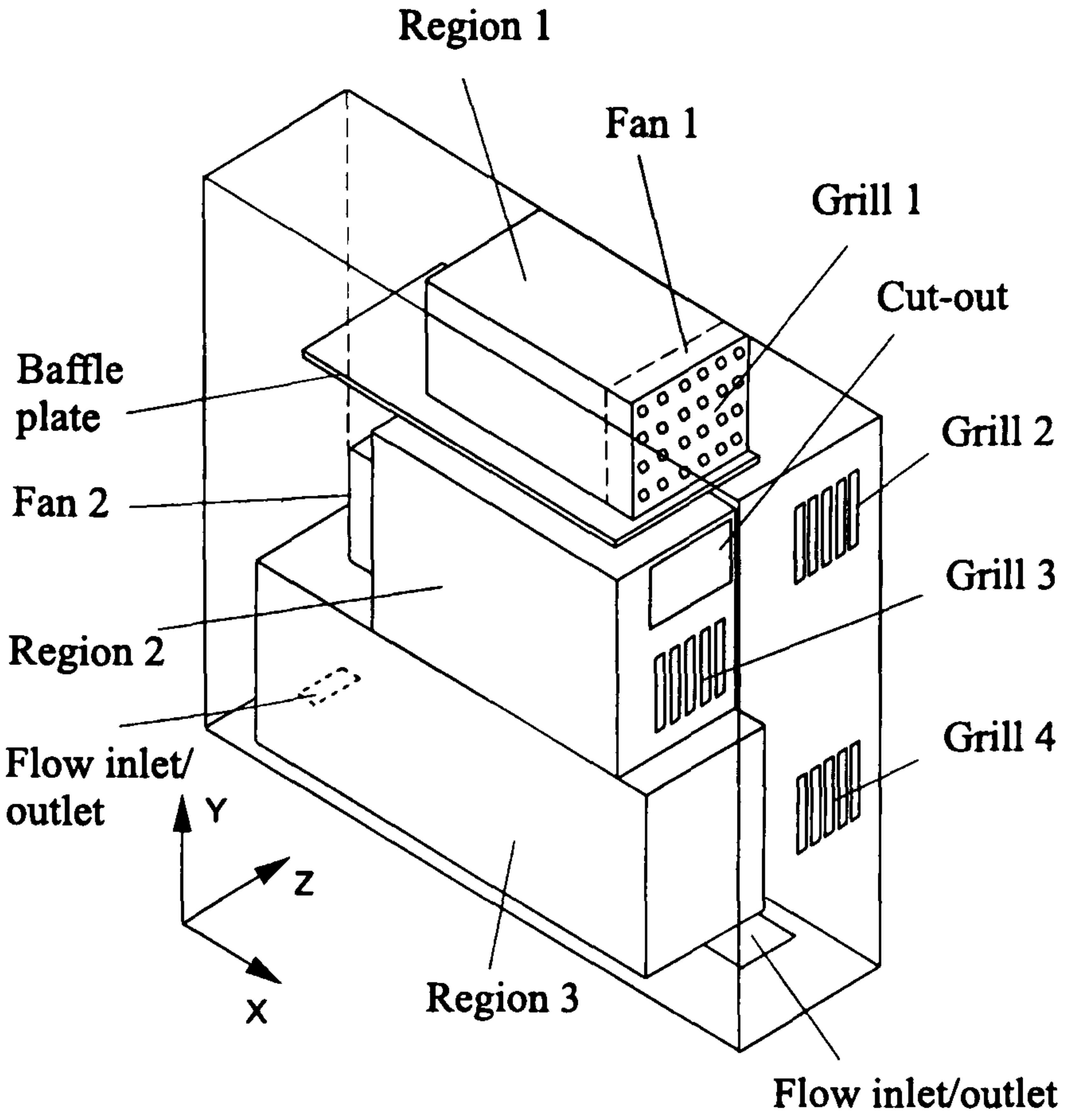

Figure 1.4: Schematic of an idealized system studied

1.2 Objectives of the study

In order to improve fluid flow and heat transfer predictions (with both accuracy and computational economy in mind) in electronic systems, and in particular for the CPU case, the following objectives have been pursued:

(1) **To assess the performance of some RANS models and other approaches involving**:

- the Spalart-Allmaras (1994) one-equation model (S-A);
- low Reynolds number versions of the standard $k-\epsilon$ model, namely Launder-Sharma (1974) (LS) and Chien (1982) (CH) models;
- the Gatski and Speziale (1993) explicit algebraic stress model (EASM):
  - (a) a high Reynolds number version, i.e. the original form, EASM;
  - (b) two low Reynolds number versions with damping functions of Abid *et al.* (1995) and Abe *et al.* (1994);
- the Craft *et al.* (1993) cubic model;
- two zonal non-linear models, namely $k-l$/EASM and $k-l$/HCubic (within

zonal models, the $k-l$ model is used for the near-wall regions, while away from the walls, either the EASM or the high Reynolds number form of the cubic model (HCubic) is employed);

- the full Reynolds Stress Model (RSM) or second moment closure;
- zonal LES (ZLES) including Spalart *et al.*'s (1997) S-A based DES and $k-l$ based zonal LES;
- pure LES;
- use of the eddy diffusivity model for heat flux.

(2) **To carry out heat transfer experiments to obtain temperature and Nusselt number.**

To validate the turbulence models incorporated into the in-house NEAT code (Tucker, 2000), the following flow test cases have been selected:

- a two-dimensional (2D) plain channel flow for RANS, and a three-dimensional (3D) channel flow for ZLES and pure LES;
- a 2D backward-facing-step flow;
- a 2D ribbed-duct flow;
- a 3D square-duct flow.

1.3 Thesis outline

Chapter 2 reviews numerical simulations for some flow geometries related to electronic systems. Properties of turbulence and its modelling using DNS, RANS, ZLES and LES are described in Chapter 3. The numerical procedures employed in this study are introduced in Chapter 4. Chapter 5 describes the heat transfer experimental setup and procedure for the CPU case. Chapter 6 presents validation cases, followed by presenation of the computed flow field and heat transfer obtained from URANS, ZLES and pure LES for the CPU case.

Final conclusions are drawn in Chapter 8. Further suggestions for future work are given in the same chapter.

Chapter 2

Literature Review

2.1 Introduction

By avoiding time-consuming and expensive experiments, electronics cooling simulation can reduce both product design cycle times and development costs. Fig. 2.1 depicts the bridging role of CFD between product development and markets (Bailey, 2003), where virtual prototyping is based on CFD. Using CFD, it is possible to select components that are well suited for the application from a thermal standpoint. It could take months and much greater expense to achieve the same goal using physical testing.

Numerical simulation of electronic equipment is often conducted at the following three levels: chip/component, package/board and system (Maudgal and Joshi, 1995). In general, at the chip or component level, the details of the system are neglected; while at the system level, the details of the component and board are modelled in some robust economical and idealized way.

A typical electronic system is the computer shown on the left of Fig. 2.2. Chips and boards are assembled in a cabinet. The right-hand figure shows an idealized physical model, used for a system level simulation. Chips are treated as flat blocks with no roughnesses (this can be accounted for by altering the wall modelling of the turbulence model). As for heat-producing components, these are treated as flat plates with uniform heat-generation rates. A fan mounted on the edge of the cabinet is treated as a planar

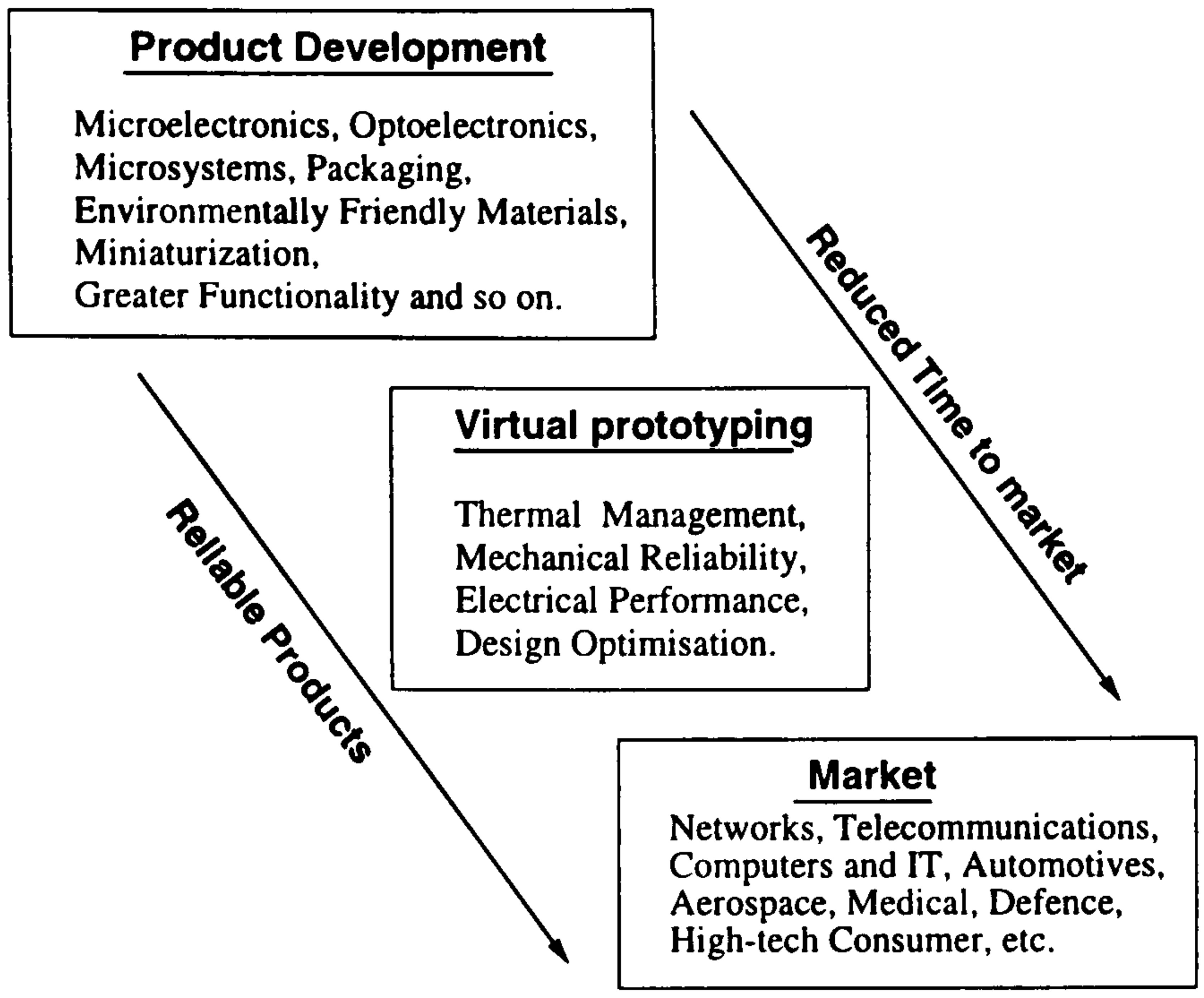

Figure 2.1: Impact of CFD on product development and market.

momentum source.

Flow inside an enclosure is either laminar or turbulent. However, the vast majority of electronic system flows are, as with other engineering flows, turbulent. To shed light on electronic system flows, researchers have studied a number of idealized fundamental models to mimic elements of real-life systems. These include square cavities, ribbed ducts and grooved channel flows and so on. Both experimental and numerical studies have been made. As observed by Tucker (1997), numerical studies mostly use Reynolds-averaged Navier-Stokes Equation modelling (RANS). To a much lesser extent, Large-eddy Simulation (LES) (see Chapter 3 for detail) is employed. The following sections will review some of this work.

2.2 Cavity flows

Heindel *et al.* (1995) numerically and experimentally investigate 3D steady laminar natural convection in a cavity with a 3×3 array of discrete heat sources flush-mounted to one vertical wall. The results show that with increasing Rayleigh number, the flow and heat transfer becomes more uniform across each heater face. Good agreement is found between prediction and measurement.

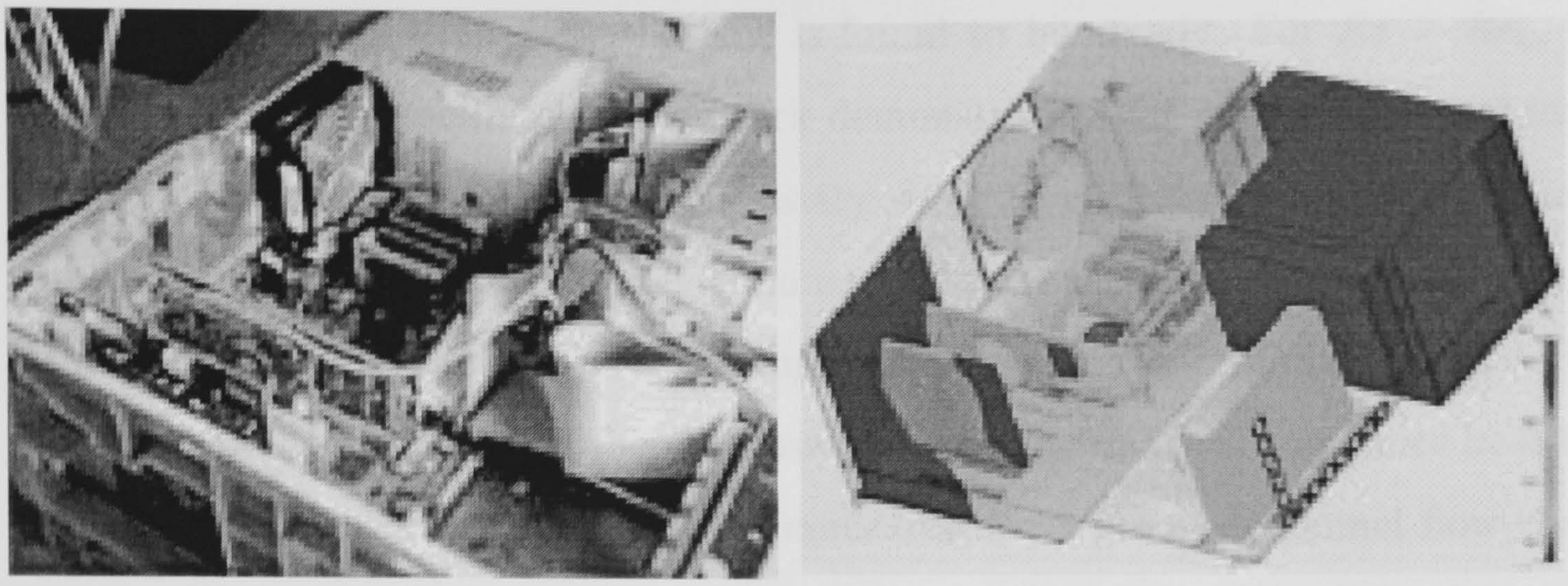

Figure 2.2: Computer system and its physical modelled configuration

Maudgal and Joshi (1995) perform a numerical study for 3D steady laminar natural convection in an enclosure idealising a desktop computer. The enclosure contains three boards with uniform heat-generation rates. The results reveal that the heat dissipation rate of the boards significantly influences the temperature rise in the system. Also the enclosure wall material properties affect temperature distribution in the enclosure.

Heindel *et al.* (1996) also perform a 2D steady conjugate natural convection study for protruding heat sources mounted on the vertical wall of a rectangular cavity. The heat sources simulate an array of computer chips mounted on a substrate, showing also the relative importance of substrate conduction and natural convection in a fluid is shown.

Hanjalić (1994) makes steady turbulent predictions in 2D cavities with various heating configurations. Hanjalić demonstrates some deficiencies in the two-equation $k-\epsilon$ model compared with an algebraic model. He concludes that Reynolds stress models should be used in industry for high accuracy. However, as noted by Spalart (2000), even this model has limitations.

2.3 Ribbed-channel flows

Ghaddar *et al.* (1986a) numerically investigate the isothermal flow in a two-dimensional periodically grooved channel. It is found that a critical Reynolds number, Re_c, for the onset of unsteadiness is a strong function of geometric parameters. When Reynolds number, Re, is less than Re_c, the flow is found to be steady. For $Re \geq Re_c$, the flow becomes cyclic and oscillatory. The work demonstrates that grooved-channel instability is a complex interaction between the cavity shear layer and the channel interior. Heat transfer is found to be considerably enhanced by the unsteady oscillatory flow behaviour (Ghaddar *et al.*, 1986b). The pumping loss increase was minimal. Hence the work illustrates the value of using coherent unsteadiness to dramatically enhance heat transfer.

Amon (1992) performs numerical simulations for a grooved-channel flow comparing three techniques of heat transfer enhancement by destabilization. The three methods involve: active flow modulation by imposing an external oscillatory flow (Ghaddar *et al.*, 1986b); passive flow modulation by tripping (Ratts *et al.*, 1988) and supercritical flow pattern ($Re > Re_c$). Overall, passive heat transfer enhancement is found to be most effective when pumping losses are considered. Nigen and Amon (1993) demonstrate heat transfer enhancement due to self-sustained oscillations in 2D grooved-channel flows. The geometries investigated include a real electronic package.

All the above works are concerned with laminar flows. In practice, as noted earlier, most engineering flows are turbulent. Next, attention will be paid to turbulent flows. Such flows are the focus of the present study.

Tropea and Gackstatter (1985) experimentally investigate the effect of varying Reynolds number, block ratio (i.e. the ratio of block height to channel height, e/H, see Fig. 2.3) and length-to-height ratio (l/e, see Fig. 2.3) on the flow over a 2D fence and a 2D block using LDA (Laser Doppler Anemometer) (in general, when the height of the block $e \gg l$ – the length of the block, the block is called a fence). The results indicate that the reattachment length is a function of Re, e/H and l/e. In a certain range of e/H, the secondary recirculation zone appears on the wall opposite the block in addition to the main recirculation region.

Durst *et al.* (1988) experimentally and numerically study the fully developed flow over two fences in tandem in a channel. The standard $k - \epsilon$ model with a wall function is employed. The numerical results from a third-order accurate scheme are in better agreement with experimental data than those obtained from a first-order accurate scheme

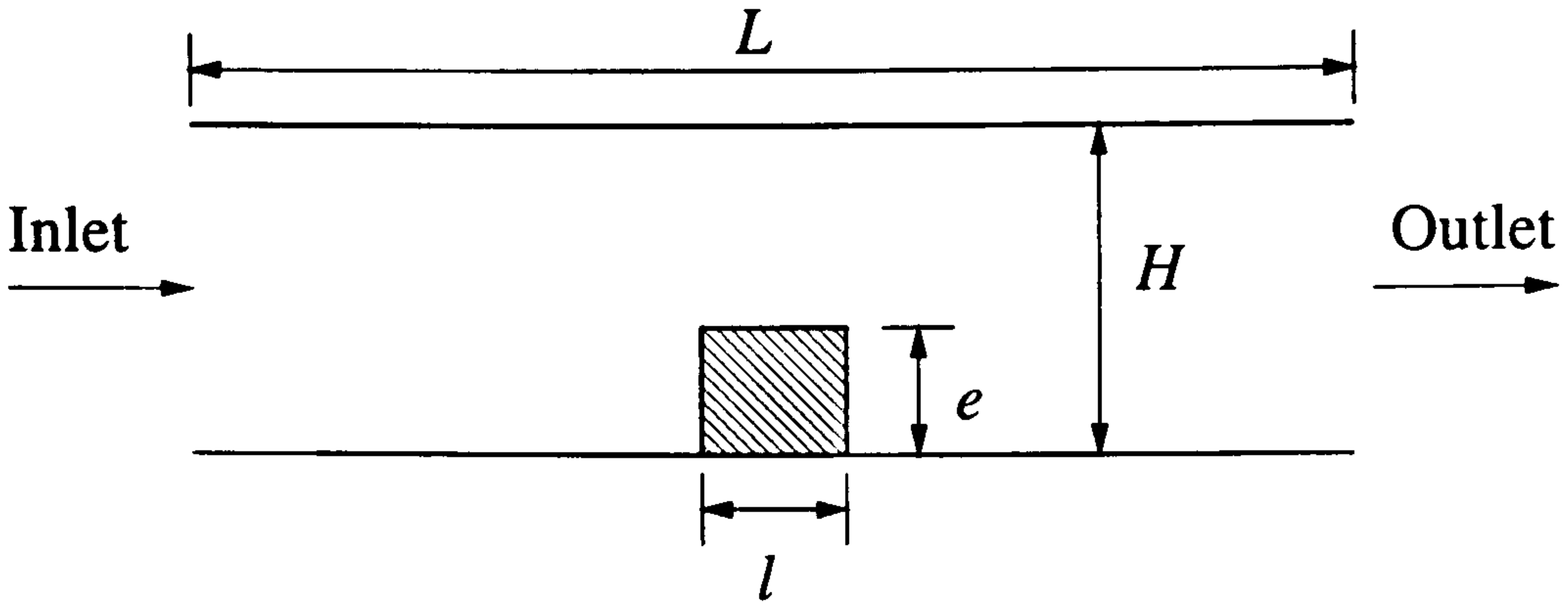

Figure 2.3: Schematic of a channel with a block.

in terms of the reattachment length and separation location. The earlier work of Durst and Rastogi (1980) compares the results obtained from the $k-\epsilon$ model, with and without currvature correction (i.e. incorporating streamline-curvature effects in the linear $k-\epsilon$ model), and with measurements for flow past a single fence . It is found that the model with curvature correction improves the predicted reattachment length.

Wietrzak and Polikakos (1990) make flow and heat transfer predictions for a 2D block-roughened channel flow. The block mounted on one channel wall models a sensor chip. The effects of various configurations, compositions and locations of the chip on flow and heat transfer are investigated. The Jones and Launder (1972) low Reynolds number $k-\epsilon$ model is used. Numerical results show that, as would be expected, varying the block height, location and Reynolds number influences flow and heat transfer. In addition, solid materials properties and heater physical size also affect heat transfer.

Acharya *et al.* (1994) compare the standard $k-\epsilon$ and Speziale's (1987) nonlinear $k-\epsilon$ model predictions for three 2D-ribbed-channel cases with measurements. Measured inlet boundary conditions are used. Comparisons are made in terms of mean velocities, cross-stream velocities, turbulence intensities and shear stresses. The results show that the nonlinear model generally improves the streamwise turbulence intensities. Apart from this, the two models perform similarly, both predicting quite well the core flow region and the region close to reattachment. Both models perform poorly in the separation regions. Later, Acharya *et al.* (1998) make heat transfer predictions for the same geometry as also in Acharya *et al.* (1994). For the flow field, they examine the performances of the standard $k-\epsilon$ model with three different wall functions (involving Launder and

Spalding (1974), Chieng and Launder (1980) and Johnson and Launder (1982)) and Speziale's nonlinear model with the wall functions of Launder and Spalding (1974). For the thermal field, the wall functions of Launder and Spalding (1974) are employed. Both linear and nonlinear models underpredict the local Nusselt number. No benefit is found from the nonlinear model for heat transfer prediction. As discussed in the paper, this is because the nonlinear model does not show any significant improvement in turbulence intensities close to the heated wall (it is well known that there is close connection between heat transfer and turbulence level). In addition, Acharya *et al.* (1993) assess the flow and heat transfer predictions made from the linear and nonlinear $k-\epsilon$ models for a periodically fully developed ribbed duct flow. The findings are similar to those reported in Acharya *et al.* (1998).

Iacovides and Raisee (1999) present the flow and heat transfer results obtained from three low-*Re* models and make comparisons between the predictions and measurements for both 2D and 3D ribbed-square flows. Models used range from linear to nonlinear, involving the Launder-Sharma (1974) with both old Yap (1987) (LSY) and new Yap corrections (LSNY), Chen and Patel (1988) zonal or two-layer $k-l/k-\epsilon$ model, Reynolds stress models (RSMs) (Iacovides and Toumpanakis, 1993) with old and new Yap corrections, and the zonal RSM model. The modified or new Yap correction avoids the use of the wall distance. Overall, for both 2D and 3D flows, the performances of the models are consistent. The zonal models underpredict wall heat transfer, but the zonal RSMs improve the linear zonal model predictions. The LSNY performs better than the LSY. The low-Re RSMs with the old Yap term produce a *Nu* distribution for the most part closer to the measurements than the RSMs with the new Yap term. Therefore, they conclude that the use of low-Reynolds-number turbulence models appears to be essential when heat transfer is concerned, and that the low-Re RSMs yield heat transfer predictions are superior to those of the linear models. Similar results can be found in Iacovides and Raisee (2000) for air flow in a 2D ribbed channel.

Bredberg and Davidson (1999) also make flow and heat transfer predictions for two ribbed 2D ducts using three linear, and one nonlinear, low-Reynolds-number models. The linear models include the Abid *et al.* (1995) and Peng *et al.* (1997) $k-\omega$ models, and the Chen and Patel zonal model. The nonlinear model is the Gatski and Speziale (1993) explicit algebraic stress model (EASM) coupled with Abid *et al.* (1995) damping functions. The heat transfer is predicted by an effective diffusivity approximation with constant Prandtl number. Overall, the predicted flow fields for all the models tested agree well with experimental data. However, for thermal fields, the predicted local Nusselt numbers do not show a good match with measurements. The zonal model greatly underpredicts Nu for the two cases. Notably, the complex EASM overpredicts reattachment length and also does not improve the heat transfer predictions compared with the two $k-\omega$ models.

Bredberg *et al* (2000) further investigate near-wall behaviour and its effect on heat transfer using several low-Reynolds-number models for two ribbed-2D-channel flows. The models studied involve LSY, Abid *et al.* (1995) $k-\omega$ and Chen and Patel zonal models. In their study, they illustrate that the turbulence models evaluated have a strong Reynolds-number dependency on the flow and thus on Nusselt number. On the whole, the $k-\omega$ and $k-\epsilon$ with Yap correction models predict reasonable heat transfer results, while the zonal model largely underpredicts these values. They argue that this is caused by the different near-wall behaviour of the models, and especially by turbulence level.

Ooi *et al.* (2002) employ Spalart-Allmaras (1994) one-equation (S-A), two-layer $k-l/k-\epsilon$ (Chen and Patel, 1988) and Durbin and Pettersson-Reif (2001) v^2-f models to simulate the flow and heat transfer in 3D ribbed ducts. The computations are carried out using the commercial software, Fluent 5.5. Several configurations with different rib spacing are investigated. Ribs are mounted either on one wall or on two opposite walls. For the case with ribs on one wall, it is found that the predicted Nusselt number distribution on the wall with ribs obtained from the v^2-f model agrees well with the measurements of Rau *et al.* (1998). The S-A model performs better than the zonal one, but still underpredicts Nu. However, for the case with ribs on two opposite walls, the Nu predictions from all the models used on a smooth side-wall do not agree well with the measurements of Liou *et al* (1993). This is because all the models cannot correctly capture the secondary flow.

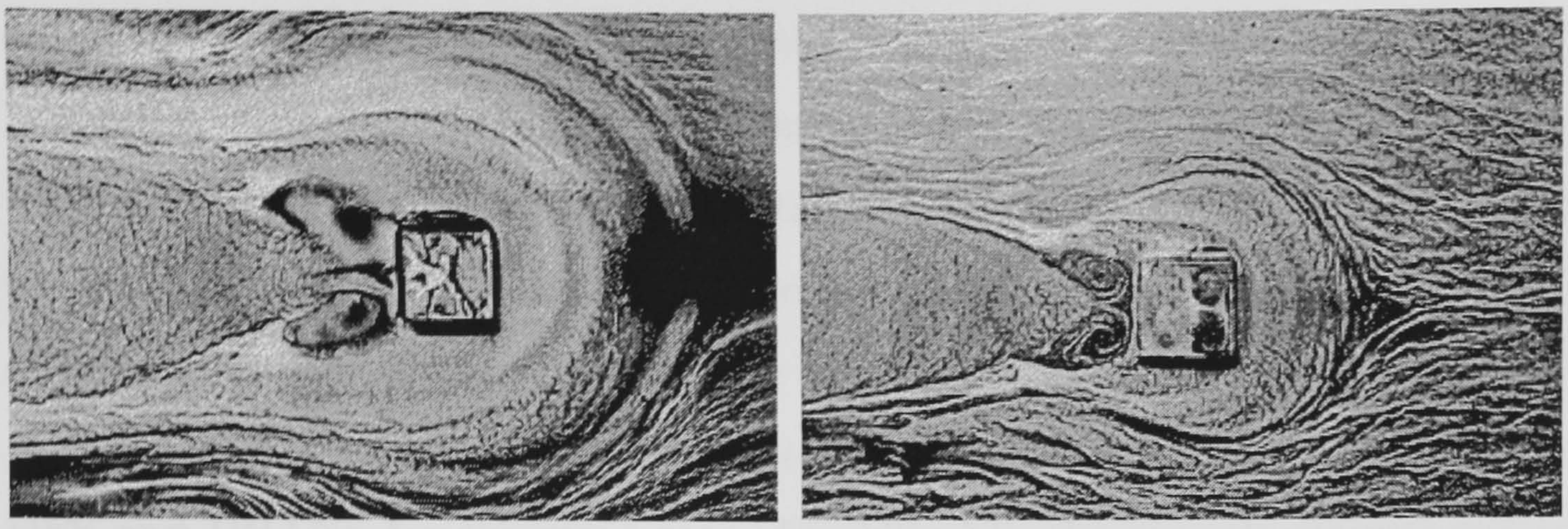

Figure 2.4: Oil-film visualizations of a single cube in a developing laminar (left) and turbulent (right) channel flow ($Re_H = 5000$) from Meinders and Hanjalić (1998).

2.4 Flows over wall-mounted cubes

Over the past years, flows over isolated, wall-mounted cubes have been the subject of many investigations. Larousse *et al.* (1991), Martinuzzi and Tropea (1993) experimentally study the flow around a single wall-mounted cube in a fully developed turbulent channel flow. Meinders *et al.* (1999) present the convective heat transfer characteristics of a single wall-mounted cube in a developing turbulent channel flow. Fig. 2.4 illustrates the top-view of flow patterns from oil-film visulization experiments in laminar and turbulent developing channel flows (Meinders and Hanjalić, 1998). As can be seen, this flow is more complex than a 2D ribbed-channel flow: a horseshoe vortex appears in front of the cube, an arc-shaped vortex in the wake of the cube and flow recirculations at the top and side faces of the cube. Comparing these two figures, it is found that in the turbulent case, the recirculation regions are generally smaller.

Meinders and Hanjalić (1999) report experimental flow and heat transfer results for a wall-mounted matrix of cubes in a channel. The measurements provide reliable validation information for numerical simulations. Mathey *et al.* (1999) perform LES for this case using Smagorinsky and dynamic subgrid models (in the dynamic subgrid model, a model coefficient is computed dynamically instead of being a constant as in the Smagorinsky model). The flow field predictions show good agreement with measurements. The heat transfer simulations generally match experimental data. Similarly computed results are obtained by Ničeno *et al.* (2002) using the Smagorinsky model on unstructured meshes. Moreover, Ničeno *et al.* (2002) point out that LES on unstructured meshes, combined with simultaneous computation of conduction in solids, offers a practical approach to predict flow and heat transfer details in real electronic cooling systems. However, unstructured meshes are not LES suitable due to the quality of grids (Malan, 1999).

Schmidt and Thiele (2002) compare the flow-field predictions obtained from LES, DES and URANS for the same case. For URANS, the high-Reynolds-number version of EASM is used. Both the DES and URANS use the same relatively coarse grid. The mean velocity predictions from the EASM and DES are in reasonable agreement with measurements, while the LES gives better predictions than the former two methods particularly in the recirculation regions. However, for Reynolds stresses like the EASM, DES does not perform well. As argued by Schmidt and Thiele, the coarse RANS mesh leads to poor DES performance for Reynolds stresses.

Zhong *et al.* (2003) also visit the same cube case, but using the $k - l$ based zonal LES (ZLES) and the Smagorinsky LES. For the LES computation, a much finer grid is used compared with the ZLES. The ZLES flow and heat transfer results are encouraging, being comparable in accuracy to those from the LES.

2.5 Other geometry flows

Chung *et al.* (2003) study unsteady laminar flow and heat transfer around a sharp 180° bend. This geometry flow is a simplification of flow round the baffle plate (which can be regarded as an idealized circuit board) positioned in the CPU geometry shown in Fig. 1.4. Results show when $Re < 600$, the flow remains steady, and when $Re > 600$, the flow becomes unsteady. As the flow becomes oscillatory, heat transfer is increased dramatically and the reattachment length decreases compared with steady flow. Chung and Tucker (2004) further extend this work exploring active and passive flow contrast. Both approaches are found to give significant heat transfer increase.

Djilali and Bouhadji (2001) simulate the two-dimensional unsteady separated-reattaching flow over a bluff rectangular plate (for electronic systems, numerous circuit boards can be idealized by this configuration). An oscillatory flow is imposed at the inlet. The flow is laminar. The results demonstrate that small-amplitude oscillations at the inlet have a dramatic influence on the mean and unsteady character of the flow. Heat transfer is significantly enhanced due to vortex shedding and advection along the surface.

Eveloy *et al.* (2000) investigate both natural and forced convection heat transfer in enclosures with single and multicomponent printed-circuit boards (PCB). Computations obtained from a commercial code, Flotherm, are compared with measurements in terms of component junction temperature and flow patterns. Laminar and turbulent flows are studied. For turbulent flows, the standard $k - \epsilon$ model is employed. Results demonstrate that an overall good level of predictive accuracy is obtained for a single-component PCB. However, for a multicomponent PCB, the computed temperature results are not in a good agreement with measurements.

2.6 Summary

Numerical simulation procedures for flow and heat transfer in electronics systems have been outlined. Experimental and numerical investigation of the idealized geometries related to electronics cooling systems have also been reviewed, including cavity flows, 2D- and 3D-ribbed-channel flows, flows around wall-mounted cubes, a sharp 180° bend, and flows over rectangular plates and PCBs. The numerical approaches involved range from (U)RANS, ZLES to LES. The review shows there has been little application of non-linear models, LES- and ZES-related approaches to realistic electronics systems. From the simulation results reviewed, it has been found that RANS model performances tend to be problem dependent. Due to the strong relationship between heat transfer and near-wall turbulence level, it is clearly important to accurately predict near-wall flow behaviour. When a flow becomes unsteady or oscillatory, heat transfer is usefully increased.

The literature suggests that to accurately predict separated flows over complex geometries, numerical methods of high accuracy (i.e. three-dimensional and time-dependent) such as LES, ZES and advanced unsteady RANS modelling, at a proper cost, are superior for capturing physical flow details.

Chapter 3

Turbulence and its modelling

3.1 Introduction

3.1.1 Turbulence

The two basic states of Newtonian fluid flow, laminar and turbulent, are generally distinguished by means of the Reynolds number (Re), or by other similar numbers, measuring the ratio of the destabilizing and stabilizing forces such as inertia and viscous friction. In most cases, there is a critical Reynolds number Re_c. When Re is less than Re_c, the flow is said to be laminar. Laminar flows are smooth and steady, or periodic, or at least easily repeatable. When Re is greater than Re_c, the flow becomes turbulent. Turbulence is an unsteady (or time-dependent) three-dimensional phenomenon. Most flows of interest in practical engineering are turbulent. Typical examples are flows over car and aeroplane surfaces. Flows in most electronic systems are also turbulent. The main properties of turbulence (Tennekes and Lumley, 1972) are as follows:

- **Irregularity**. Turbulent fluid motion is irregular, random and chaotic. Therefore, turbulent flows are unsteady or unstable.

- **Diffusivity**. Owing to the randomness of turbulent flows, turbulence is diffusive. This feature greatly enhances the transfer of momentum, of heat and also mass transfer.

- **Dissipation**. Turbulent flows are dissipative, typically with an energy cascade. Kinetic energy is continuously being transferred from the main flow to the largest eddies. The energy from large eddies is dissipated successively by smaller eddies (note that reverse energy cascades, i.e. transfer energy from smaller to larger scales, can also occur in complex turbulent flows). Eventually, the smallest eddies convert kinetic energy into heat or internal energy by viscous dissipation. The whole process is known as the "energy cascade".

3.1.2 Turbulent scales

Turbulent flow is composed of a wide range of scales (eddy sizes). Small eddies have short time scales, which tend to make them statistically independent of mean flow. The smallest eddies present in flows are determined by the viscosity of the fluid. The largest (or integral length scale) are limited by the dimensions of the flow geometry. A complete spectrum of sizes lies in between. The range of scales is a strong function of Re. The ratio of the largest length scale to smallest is proportional to $Re^{3/4}$ (see Tennekes and Lumley, 1972) (where Re is the Reynolds number based on an integral scale of the flow). It is plausibly assumed that the rate of energy supply is equal to the rate of dissipation (ϵ) for small eddies. Therefore, small eddies tend to be universal, isotropic and in equilibrium. For the smallest scales, the Kolmogorov length scales are determined by (see Davidson, 2001)

$$\underbrace{\eta}_{[L]} = \underbrace{\nu^a}_{[L]^2/[T]} \quad \underbrace{\epsilon^b}_{[L]^2/[T]^3} \tag{3.1}$$

where ν is the kinematic viscosity, L and T represent the dimensions of length and time, respectively. Using dimensional analysis, the following two equations are obtained:

$$\begin{cases} 2a + 2b = 1 \\ -a - 3b = 0 \end{cases} \tag{3.2}$$

Solving these equations, we can find that a = 3/4, b = -1/4, thus:

$$\eta = \left[\frac{\nu^3}{\epsilon}\right]^{1/4} \tag{3.3}$$

In the same way, we can obtain the Kolmogorov time and velocity scales, which are expressed respectively as:

$$\tau = \left[\frac{\nu}{\epsilon}\right]^{1/2}, \quad V_t = (\nu\epsilon)^{1/4} \tag{3.4}$$

3.1.3 Turbulent flow prediction methods

A number of approaches for dealing with turbulence are available. They are:

- **Direct Numerical Simulation (DNS)**

DNS is the most straightforward method for the solution of turbulent flows. In DNS, to get approximate solutions, the governing equations are discretized directly, and solved numerically together with suitable initial and boundary conditions. A detailed representation of a turbulent flow field can be obtained. Accurate solutions depend on the numerical scheme used, and on the quality of grid generated. This method is completely free of modelling assumptions. The only error source is numerical approximation. Although DNS has been a very useful tool for the study of physics of transition and turbulence over the past years, it has two shortcomings (Piomelli, 1999). Firstly, numerical schemes with high accuracy applied have little flexibility in dealing with complex geometry flows. Secondly, DNS is still too expensive, especially for high-Reynolds-number flows, owing to the need for a very fine grid to resolve all scales of motion present in turbulent flow. To resolve the smallest eddies, the smallest size of grid cell should be of the order of the Komogorov length scales mentioned above. In one dimension, the grid points required are proportional to $Re^{3/4}$. For three-dimensional flows, the total number of grid points is proportional to $Re^{9/4}$. Obviously, if Re is large, the mesh demanded is very fine. For these reasons, the application of DNS is limited to simple geometry flows at low-Reynolds-numbers.

For current computing power, Baelmans (2002) estimates the computational time required to resolve typical component, PCB and system level problems at electronics systems using DNS to be as shown in Table 3.1. This table illustrates that the application of DNS for routine design in electronic industry is many years away.

Table 3.1: Estimated computational time for DNS based simulations.

		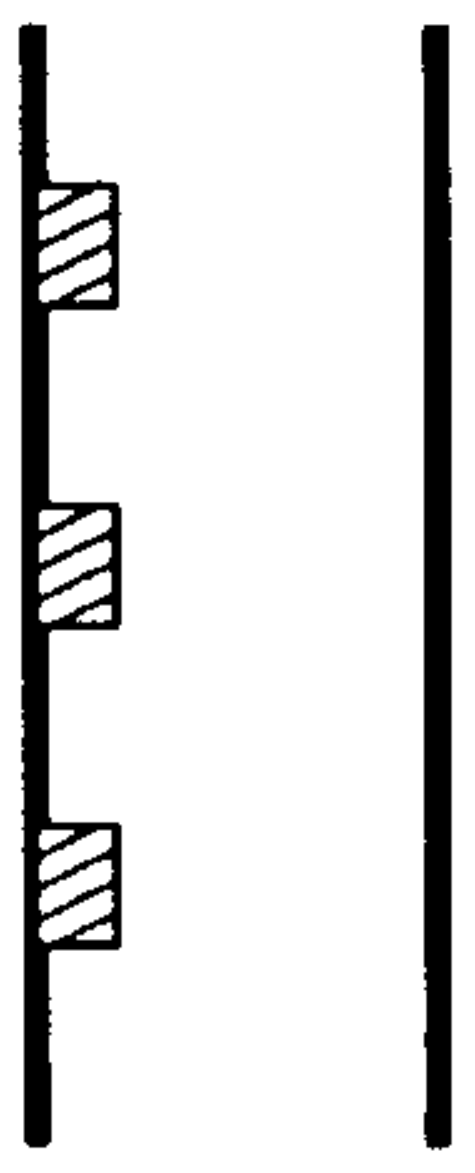	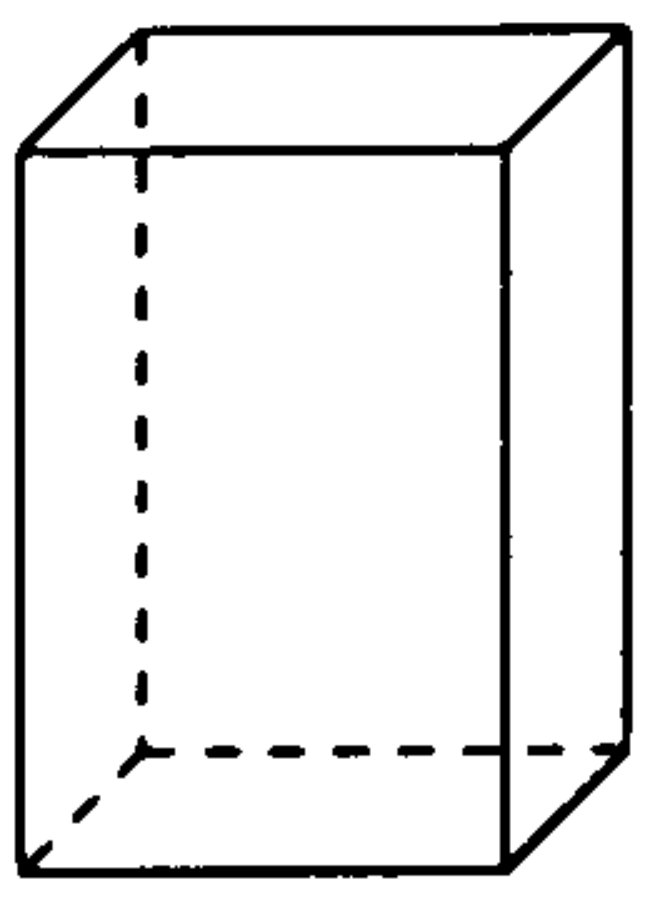
Dimensions	30x30x70 mm ^{3}	30x500x500 mm ^{3}	2x2x2 m ^{3}
Number of cells	$2\text{x}10^6$	$2.3\text{x}10^8$	$2.5\text{x}10^{11}$
Workstation	7 days	4 years	5000 years
Top 10 computer	2 mins	6 h	8 months

- **Reynolds-averaged Navier-Stokes Equations (RANS) modelling**

When time- or ensemble-averaging the Navier-Stokes equations, one obtains the well-known Reynolds-averaged Navier-Stokes equations. As a consequence of time-averaging, the mean quantities present a fairly smooth function of time and space, while for the original Navier-Stokes equations, the solutions depend randomly on space and time. It should be mentioned that the averaging time must be much longer than all the time scales of the turbulent flow, but much smaller than any coherent unsteadiness component. The effect of turbulent fluctuations on the flow appears in an unknown term called the "Reynolds stress". This term needs to be modelled to close the system.

Half a century of research into turbulence modelling has developed numerous models for Reynolds stresses, ranging from simple models, such as the mixing length, to two-equation models, algebraic and full Reynolds stress models. To date, RANS modelling has been widely used in engineering applications. When RANS modelling is applied to an unsteady turbulent flow, it is usually termed URANS (Unsteady Reynolds-Averaged Navier-Stokes) prediction or sometimes VLES (Very Large Eddy Simulation).

However, RANS modelling suffers from several drawbacks. First of all, no universal model is available. Any model is calibrated for limited cases or for limited boundary conditions. Therefore, empirical constants and correlations between variables are not universal. The reason for this is that large eddies are affected strongly by boundary

Table 3.2: Comparison of RANS and LES.

	RANS	LES
Methodology	Modelling the effect of all eddies	Resolving large eddies and modelling small eddies (SGS)
Empiricism	Strong	Weak
Grid requirement	Not fine For wall-bounded flows: $y^+ < 1$ (low Re), or $y^+ > 30$ (high Re)	Very fine For wall-bounded flows: $y^+ < 1$, $\Delta x^+ \approx 50 \sim 150$ $\Delta z^+ \approx 15 \sim 40$
Accuracy for complex flows	Low	High
Computational cost	Economic	Expensive

conditions. This means that various geometries or boundary conditions can generate different turbulence structures. Thus, it is impossible to model the effect of all large eddies in different flows in the same way. Secondly the RANS cannot, in general, accurately capture unsteady phenomena.

- **Large Eddy Simulation (LES)**

LES is a technique intermediate between the DNS and RANS approaches. In LES, only large energy-carrying scales are numerically resolved, and the effects of the small scales or unresolved scales on the resolved fields are modelled. Since the small scales tend to be more isotropic and universal in nature, and less affected by boundary conditions than the large ones, it is reasonably assumed that simple models for small scales or so-called sub-grid scale (SGS) models can perform well.

Compared with DNS, LES is computationally economical since there is no need to resolve all scales of motion. It can be used at much higher Reynolds numbers than DNS. The differences between LES and RANS approach are summarised in Table 3.2. LES has undisputed advantages over RANS. Firstly, LES is able to capture the dynamics of turbulence, associated with the large-scale turbulent eddies and their mutual interaction involving the mixing of momentum, heat and scalar transport (Leschziner, 2002). Secondly, owing to its methodology, LES has the capacity to predict complex flows with separation more accurately than RANS. However, LES also has drawbacks such as high cost and grid quality demand, especially for wall-bounded flows. Near a wall, the flow structure is very anisotropic. The important coherent structures are the streaks. These structures are relatively finely spaced in the spanwise direction. They are approximately 1000 viscous units long, 100 viscous units wide and 30$\sim$50 viscous units high in the streamwise, spanwise and normal directions respectively (Ferziger, 1996). Therefore, to resolve the fine structure, a very fine grid is required, not only in the wall-normal (y) direction, but also in the spanwise (z) and streamwise (x) directions (see Table 3.2). Hence, the number of grid points required in the viscous sublayer increases with $Re^{1.8}$ (Chapman, 1979) in comparison with $Re^{0.4}$ away from the wall. This high demand for grid restricts the applications of LES to low and moderate *Re* flows. Pure LES of high *Re* flows is beyond the capability of current computers.

- **Zonal LES (ZLES)**

Owing to the limits of current computer power and to computational expense, pure LES is unlikely to see use in industries such as aerospace for several decades (Spalart, 2000). Therefore, Spalart *et al* (1997) proposes a hybrid RANS/LES strategy termed Detached Eddy Simulation (DES). The motivation for DES is to combine advantages from RANS and LES, i.e. to reduce the costs of pure LES for wall-bounded flows, and to improve the accuracy of pure RANS predictions for separate flows. In this sense, DES is an intermediate approach between RANS and LES. In DES, RANS modelling is used in the boundary layers, and LES in the remaining part of the flow. The rationale for this method is that full LES behaviour at the near-wall resembles quasi-steady RANS and hence the use of RANS in this region will not damage accuracy, i.e. the turbulence time scale is much less than that resolved in the near-wall regions. In DES, the Spalart-Allmaras (S-A) (1994) one-equation model is applied to the whole domain. The only difference between RANS model and sub-grid scale model for LES regions is the choice of length scale in the S-A destruction term. The interface location is decided by this length scale, which relates the grid parameters.

Following Spalart *et al.*'s strategy, a number of variations have been developed. Different RANS models and sub-grid scale models have been tested (see Section 3.4 for detail). In general, this strategy is called zonal LES (ZLES) or hybrid RANS/LES including DES and subsequently developed variations.

3.2 Turbulence models (RANS)

3.2.1 Reynolds stress and turbulent heat flux tensors

For a turbulent flow as illustrated on the left in Fig. 3.1, in general, the instantaneous variables, such as velocity components, pressure and temperature, decompose into mean and fluctuating elements as follows:

$$\begin{cases} u_i = U_i + u'_i \\ p = P + p' \\ t = T + t' \end{cases} \tag{3.5}$$

By first substituting Eq. (3.5) into the continuity, Navier-Stokes and energy equations for incompressible flows, and then taking an ensemble or time (only for statistically steady turbulent flows) mean, the mean continuity, Reynolds-averaged Navier-Stokes and energy equations can be obtained in the following tensor forms:

$$\frac{\partial U_j}{\partial x_j} = 0 \tag{3.6}$$

$$\rho\frac{\partial U_i}{\partial t} + \rho\frac{\partial\left(U_i U_j\right)}{\partial x_j} = -\frac{\partial P}{\partial x_i} + \frac{\partial}{\partial x_j}\left[\mu\frac{\partial U_i}{\partial x_j}\right] + \frac{\partial \tau_{ij}}{\partial x_j} \tag{3.7}$$

$$\rho\frac{\partial T}{\partial t} + \rho\frac{\partial\left(U_j T\right)}{\partial x_j} = \frac{\partial}{\partial x_j}\left[\frac{\mu}{Pr}\frac{\partial T}{\partial x_j}\right] + \frac{\partial(-\rho\overline{u'_j t'})}{\partial x_j} \tag{3.8}$$

where $\tau_{ij} = -\rho\overline{u'_i u'_j}$ is the Reynolds stress tensor and $-\rho\overline{u'_j t'}$ is the turbulent heat flux tensor.

For periodic flows, such as a vortex-shedding flow behind a cylinder shown on the right in Fig. 3.1 (where T_p and T_t represent the cyclic unsteadiness period and turbulence fluctuating time, respectively), an instantaneous variable following Johansson *et al.* (1993) and Bosch and Rodi (1998) can be broken down into three parts given by

$$u = U + \tilde{u} + u' = \langle u \rangle + u' \tag{3.9}$$

where $\langle u \rangle$ is the phase or ensemble-averaged part, resolved in the numerical calculation corresponding to the mean values in Eqs. (3.6-8) , U being the time mean, $\tilde{u}$ the periodic component (amplitude) and u' the turbulent fluctuating component. A turbulence model is a mathematical model which is used to approximate the Reynolds stresses and heat fluxes to close the system of Eqs. (3.6-8). The available turbulence models can be roughly divided into the following two main categories:

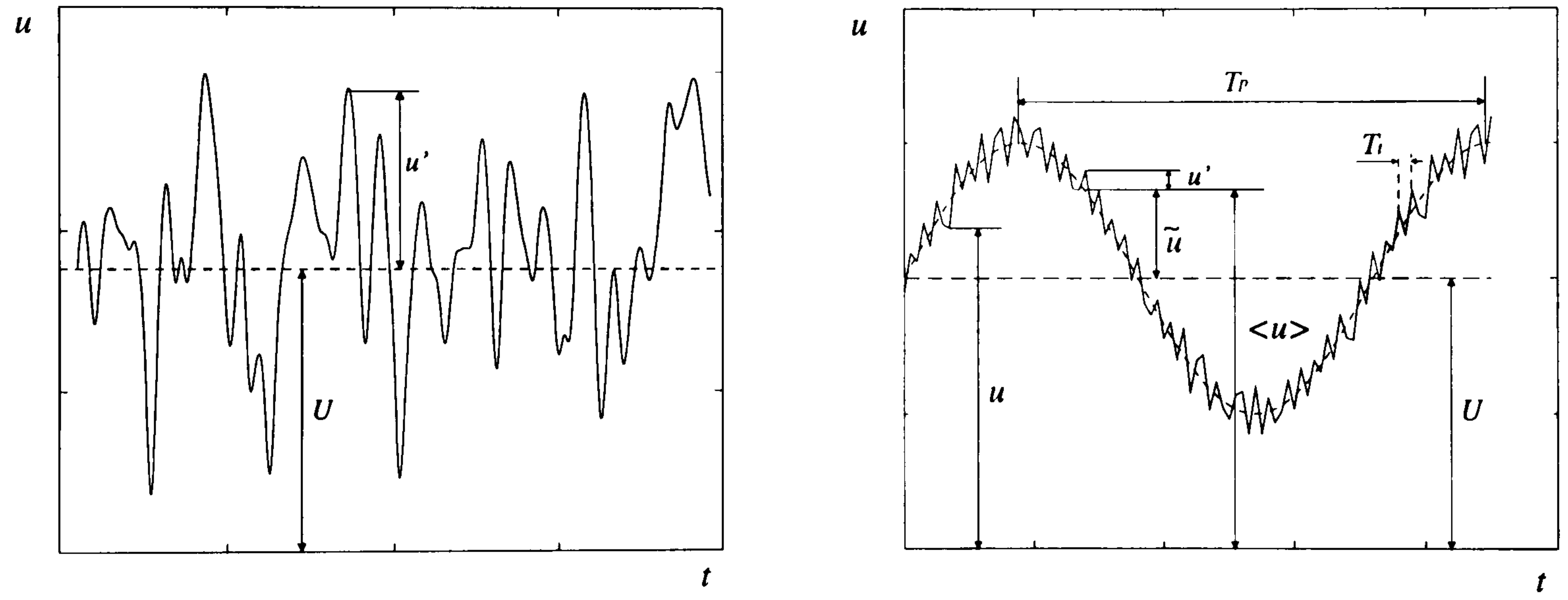

Figure 3.1: Typical velocity time trace at a point in turbulent flows. Left: a typical turbulent flow; right: a periodic turbulent flow.

- **Eddy Viscosity Models (EVMs)**
  - Linear Eddy Viscosity Models (LEVMs)
    - Zero-equation or algebraic models
    - One-equation models

        - ∗ Two-equation models
    - Non-linear Eddy Viscosity Models (NLEVMs)

- **Reynolds stress or second moment closure model**
    - Full Reynolds Stress Model (FRSM)
    - Algebraic Reynolds Stress Model (ARSM)
    - Explicit Algebraic Stress Model (EASM)

In the following sections, a brief discussion of turbulence models is given ranging from the simplest to the most advanced (i.e. state of the art).

3.2.2 Linear Eddy Viscosity Models (LEVMs)

In LEVMs, Reynolds stresses are related to the averaged velocity gradients (i.e. the mean strain rate) through the turbulent viscosity μ_t. This relation is the Boussinesq (1877) hypothesis. It is expressed as

$$-\rho\overline{u_i'u_j'} = 2\mu_t S_{ij} = \mu_t\left(\frac{\partial U_i}{\partial x_j} + \frac{\partial U_j}{\partial x_i}\right) \tag{3.10}$$

Boussinesq postulated this isotropic assumption on analogy with the classical interpretation of viscous stresses in laminar flow using the fluid viscosity μ, i.e. replacing μ by μ_t to obtain the Reynolds stresses. If μ_t is known, the Reynolds stresses can then be calculated. In this sense, the task of the turbulence model is to determine μ_t.

In order to make Eq. (3.10) valid upon contraction (i.e. setting indices $i = j$), $2/3\rho\delta_{ij}k$ should be added to the right hand side of Eq. (3.10) to ensure $-\rho(\overline{u'^2} + \overline{v'^2} + \overline{w'^2}) = -2k$. Hence, Eq. (3.10) becomes

$$-\rho\overline{u_i'u_j'} = \mu_t\left(\frac{\partial U_i}{\partial x_j} + \frac{\partial U_j}{\partial x_i}\right) - \frac{2}{3}\rho k\delta_{ij} \tag{3.11}$$

where δ is the Kronecker delta ($\delta = 1$, if $i = j$ and $\delta = 0$, if $i \neq j$). It should be pointed out that Eq. (3.11) produces isotropic turbulence fields, because turbulence energy is assumed to distribute equally in all directions (i.e. $\overline{u'^2} = \overline{v'^2} = \overline{w'^2} = \frac{2}{3}k$). Like the molecular dynamic viscosity ($\mu = \rho\nu$), μ_t can be expressed as $\mu_t = \rho\nu_t$. The dimension of ν_t is the same as ν, i.e. $[L]^2/[T]$. By dimension analysis, ν_t can be given by

$$\nu_t \quad \propto \quad V_t \;\; l \tag{3.12}$$

where V_t is a turbulent velocity scale and l is a turbulent length scale. Unlike their viscous counterparts, the turbulent viscosity is not a fluid property, but is a function of the state of turbulence. Therefore, both the turbulent velocity and length scales are determined by the state of turbulence. Over the years, numerous prescriptions for V_t and l have been proposed.

(1) Zero-equation or algebraic models

For a boundary-layer type of flow, the Prandtl (1925) mixing-length hypothesis gives

$$\mu_t = \rho l_{\text{mix}}^2 |\frac{\partial U}{\partial y}| \tag{3.13}$$

where l_{mix} is the mixing length ($l_{\text{mix}} = \kappa y$, where y is the wall-normal distance and κ is von Karman's constant). l_{mix} must be modified near walls and in the outer part of the boundary layer. Modifications have been made since Prandtl's mixing-length model was first proposed. The most important developments for this type of model involve van Driest's (1956) damping function, the Cebeci-Smith (1974) and Baldwin-Lomax (1978) models. The latter two models have been used frequently in the aerospace field.

Algebraic models have the advantage of simplicity and are widely used with considerable success for flows for which they have been fine tuned, such as attached boundary layers, jets and wakes. However, because the turbulence viscosity is determined locally in this model, it cannot be expected that this type of model can work well for flows where the state of turbulence is not locally determined, but is instead related to the upstream history of the flow such as separated flows. Wilcox (1998) gives a thorough discussion of algebraic models.

(2) One-equation models

One-equation models attempt to improve on the zero-equation models by accounting at least in part for non-local effects on the turbulent eddy viscosity. In this type of model, only one transport equation is solved. Among the existing one-equation models, the Wolfshtein (1969) $k - l$ and Spalart-Allmaras (1994) (S-A) models are widely used. The two models are outlined below.

For the $k - l$ model (Wolfshtein, 1969), a transport equation for the turbulent kinetic energy (k) is solved to obtain the turbulent velocity scale ($V_t = k^{\frac{1}{2}}$). A turbulent length scale which depends on geometrical conditions is prescribed by an algebraic expression. The equation for k reads

$$\rho\frac{\partial k}{\partial t} + \rho\frac{\partial (U_j k)}{\partial x_j} = \underbrace{\frac{\partial}{\partial x_j}\left[\left(\mu + \frac{\mu_t}{\sigma_k}\right)\frac{\partial k}{\partial x_j}\right]}_{\text{Diffusion term}} + \underbrace{\tau_{ij}\frac{\partial U_i}{\partial x_j}}_{\text{Production term}} - \underbrace{\rho\epsilon}_{\text{Dissipation term}} \tag{3.14}$$

where the dissipation rate is defined by

$$\epsilon = \frac{k^{\frac{3}{2}}}{l_\epsilon} \tag{3.15}$$

and the length scale of dissipation is decided by $l_\epsilon = c_{\epsilon 0}\, y\left(1 - e^{-A_\epsilon y^*/c_\mu^{1/4}}\right)$, where $y^* = y\rho k^{1/2}c_\mu^{1/4}/\mu$. The turbulent viscosity is calculated from

$$\mu_t = \rho c_\mu l_\mu k^{1/2} \tag{3.16}$$

where $l_\mu = c_{\mu 0}\, y\left(1 - e^{-A_\mu y^*/c_\mu^{1/4}}\right)$ is the viscosity length scale. The values of the constants present in the above expressions are: $\sigma_k = 1$, $A_\epsilon = 0.263$, $A_\mu = 0.016$, $c_{\epsilon 0} = c_{\mu 0} = 2.4$, $c_\mu = 0.09$.

The Wolfshtein $k - l$ model is a low-Reynolds-number model. As can be seen in the expressions of l_ϵ and l_μ, near-wall damping functions are used for both length scales. As for near-wall treatments, discussion will be provided later. The empirical constants existing in this model cause it to lack general application.

The S-A model determines a modified kinematic turbulent viscosity directly from a transport equation, which takes the following form:

$$\rho\frac{D\tilde{\nu}}{Dt} = \underbrace{G_\nu}_{\text{Production term}} + \underbrace{\frac{1}{\sigma_{\tilde{\nu}}}\left[\frac{\partial}{\partial x_j}\left\{(\mu+\rho\tilde{\nu})\frac{\partial\tilde{\nu}}{\partial x_j}\right\} + C_{b2}\rho\left(\frac{\partial\tilde{\nu}}{\partial x_j}\right)^2\right]}_{\text{Diffusion term}} - \underbrace{Y_\nu}_{\text{Destruction term}} \tag{3.17}$$

where

$$G_\nu = C_{b1}\rho\tilde{S}\tilde{\nu}, \quad Y_\nu = C_{w1}\rho f_w\left(\frac{\tilde{\nu}}{d}\right)^2 \tag{3.18}$$

and

$$\begin{cases} \tilde{S} = S + \frac{\tilde{\nu}}{k^2d^2}f_{v2}, \quad f_{v2} = 1 - \frac{\chi}{1+\chi f_{v1}} \\ S = \sqrt{2\Omega_{ij}\Omega_{ij}}, \quad \Omega_{ij} = \frac{1}{2}\left(\frac{\partial U_i}{\partial x_j} - \frac{\partial U_j}{\partial x_i}\right) \\ f_w = g\left[\frac{1+C_{w3}^6}{g^6+C_{w3}^6}\right]^{1/6}, \quad g = r + C_{w2}\left(r^6 - r\right), \quad r = \frac{\tilde{\nu}}{\tilde{S}k^2d^2} \end{cases} \tag{3.19}$$

The ν_t is then given by

$$\nu_t = \tilde{\nu}f_{v1} \tag{3.20}$$

where

$$f_{v1} = \frac{\chi^3}{\chi^3 + c_{v1}^3}, \quad \chi = \frac{\tilde{\nu}}{\nu} \tag{3.21}$$

It should be mentioned that the transition terms are omitted from the original form in Eq. (3.17) for simplicity. The constants can be found in Spalart and Allmaras (1994).

This model was designed specifically for aerospace applications. It is now gaining popularity for external flows. However, for internal flows, this model has not seen extensive use. Both the $k - l$ and S-A models will be tested in this project.

(3) Two-equation models

To address the deficiency of prescribing empirically the length scale for the k-based one-equation models, an additional transport equation for a second turbulent quantity is used to achieve a turbulent length scale. This gives rise to the name: two-equation model. Over the years, a number of two-equation models have been proposed, such as those of Rotta (1951) or Spalding's (1967) $k - l$ model, Rodi and Spalding's (1970) $k - kl$

($l = C_D k^{3/2}/\epsilon$), Spalding's (1969) $k - W$ ($W = (\epsilon)^2/(C_D k)^2$), Speziale *et al*'s (1992) $k - \tau$ ($\tau = k/\epsilon$) and Wilcox's (1998) $k - \omega$ ($\omega = \epsilon/k$) model. It can be easily found that any turbulent quantity introduced above, i.e. l, W, τ or ω, is a function of k and ϵ. However, the direct use of the turbulent energy dissipation rate ϵ as the second variable has had the widest application for obtaining the length scale. Therefore, in this study, the emphasis is placed on the $k - \epsilon$ model group. For the $k - \epsilon$ models, the length scale is obtained from

$$l = \frac{k^{3/2}}{\epsilon} \tag{3.22}$$

the turbulent viscosity then being computed from

$$\nu_t = c_\mu k^{1/2} l = c_\mu \frac{k^2}{\epsilon} \tag{3.23}$$

- **The standard $k - \epsilon$ model**

Perhaps the most significant $k - \epsilon$ model version is proposed by Jones and Launder (1972). Later, Launder and Spalding (1974) address wall functions. This version is called the standard $k - \epsilon$ model or high-Reynolds-number model (HR). It can only be applied to fully turbulent regions free of viscous effects on the turbulence. The modelled ϵ equation is given by

$$\rho\frac{\partial \epsilon}{\partial t} + \rho\frac{\partial (U_j \epsilon)}{\partial x_j} = \underbrace{\frac{\partial}{\partial x_j}\left[\frac{\mu_t}{\sigma_\epsilon}\frac{\partial \epsilon}{\partial x_j}\right]}_{\text{Diffusion term}} + \underbrace{c_{\epsilon 1}\frac{\epsilon}{k}\tau_{ij}\frac{\partial U_i}{\partial x_j}}_{\text{Production term}} - \underbrace{\rho c_{\epsilon 2}\frac{\epsilon^2}{k}}_{\text{Destruction term}} \tag{3.24}$$

where the coefficients $c_{\epsilon 1}$, $c_{\epsilon 2}$, σ_ϵ are given in Table 3.3.

When a wall is present, the turbulent quantities (k, ϵ and μ_t) are calculated explicitly in the near-wall region using wall functions (see Section 3.2.6), instead of solving the differential equations (3.14) and (3.24).

The standard $k - \epsilon$ model is the one most widely used in industrial applications because of its robustness and computational economy. It is included in almost every commercial and in-house code. However, this high-Reynolds-number model still suffers from weaknesses. One of them is that wall functions do not work well for non-equilibrium flows such as those with separation owing to the assumption made of local equilibrium.

In such cases, integrating transport equations for k and ϵ all the way to the wall might be a good choice. These models involved are known as low-Reynolds-number models.

- **Low-Reynolds-number $k - \epsilon$ models**

Following the original work of Jones and Launder (1972) introducing viscous diffusion terms and damping functions modifying the constants appearing in Eq. (3.24), a variety of modifications have been proposed. Patel *et al.* (1985) gives a review of seven variants of low-Reynolds-number $k - \epsilon$ models and compares their performances for different boundary-layer flows. Although none of them gives overwhelmingly satisfactory performance for all the cases tested, to some extent the Launder-Sharma (1974) model (LS), Chien (1982) model (CH) and Lam-Bremhorst (1981) model (LB) perform better than others.

Owing to the difficult convergence of the LB model, it is abandoned in the present study. Both CH and LS models are considered. The k equation is the same as Eq. (3.14). The equation for ϵ can be written in the general form (Patel *et al*, 1985) below:

$$\rho\frac{\partial\tilde{\epsilon}}{\partial t}+\rho\frac{\partial\left(U_j\tilde{\epsilon}\right)}{\partial x_j}=\frac{\partial}{\partial x_j}\left[\left(\mu+\frac{\mu_t}{\sigma_\epsilon}\right)\frac{\partial\tilde{\epsilon}}{\partial x_j}\right]+c_{\epsilon1}f_1\frac{\tilde{\epsilon}}{k}\tau_{ij}\frac{\partial U_i}{\partial x_j}-\rho c_{\epsilon2}f_2\frac{\tilde{\epsilon}^2}{k}+E \qquad (3.25)$$

where

$$\tilde{\epsilon}=\epsilon-D \qquad (3.26)$$

$$\mu_t=c_\mu f_\mu\frac{k^2}{\tilde{\epsilon}} \qquad (3.27)$$

The constants and damping functions appearing in the above equations are summarised in Table 3.3. Table 3.3 also shows boundary conditions for k and ϵ. It is well known that the LS model over-predicts the turbulent kinetic energy, and thus the length scale in regions of flow impingement or separation (Yap, 1987). To address this problem, Yap (1987) proposes an *ad hoc* modification term, called the Yap correction. This increases the dissipation rate ϵ and thus reduce the kinetic energy k. The term is incorporated into the ϵ equation as a source term. It takes the following form:

$$Yap=0.83\frac{\epsilon^2}{k}\max\left[\left(\frac{k^{1.5}/\epsilon}{2.55y}-1\right)\left(\frac{k^{1.5}/\epsilon}{2.55y}\right)^2,0\right] \qquad (3.28)$$

Table 3.3: Constants and damping functions for the $k-\epsilon$ group of models.

Model	D	$\tilde{\epsilon}_w$-B.C.	c_μ	$c_{\epsilon 1}$	$c_{\epsilon 2}$	σ_k	σ_ϵ
Standard (HR)	0	Wall functions	0.09	1.44	1.92	1.0	1.3
LS	$2\nu\left(\frac{\partial\sqrt{k}}{\partial y}\right)^2$	0	0.09	1.44	1.92	1.0	1.3
CH	$2\nu\frac{k}{y^2}$	0	0.09	1.35	1.8	1.0	1.3
AKN	0	$\frac{2\mu k}{y^2}$	0.09	1.5	1.9	1.4	1.4

	f_μ	f_1	f_2	E
LS	$e^{\frac{-3.4}{(1+R_t/50)^2}}$	1.0	$1-0.3e^{-R_t^2}$	$2\mu\frac{\mu_t}{\rho}\left(\frac{\partial^2 U}{\partial y^2}\right)^2$
CH	$1-e^{-0.0115y^+}$	1.0	$1-0.22e^{-(R_t/6)^2}$	$-2\mu\frac{\tilde{\epsilon}}{y^2}e^{-0.5y^+}$
AKN	$\left(1-e^{-\frac{y^*}{14}}\right)$ $\times[1+\frac{5}{R_t^{3/4}}e^{-(\frac{R_t}{200})^2}]$	1.0	$(1-e^{-\frac{y^*}{3.1}})$	0

The Yap term is usually most active just beyond the viscous sub-layer. In a high-Reynolds-number computation this is covered with wall functions. As shown in Eq. (3.28), the Yap correction contains the wall-normal distance and is known to perform poorly on surfaces of complex shape. Accordingly, a new version of the Yap term taking the differential form has been proposed by Iacovides and Raisee (1997). Here, the original Yap correction is used for the sake of simplicity.

In order to reproduce the correct near-wall asymptotic behaviours of turbulence (i.e. $k \propto y^2$, $\epsilon \propto y^0$, $\nu_t \propto y^3$ and $-\overline{u'v'} \propto y^3$ for $y \to 0$) and further to improve the near-wall predictions in the context of the $k-\epsilon$ model, various attempts have been made. One of them is that proposed by Abe *et al.* (1994) (AKN), who modify the damping functions f_μ and f_2 given in Table 3.3. The results shown for a backward-facing-step flow are in very good agreement with experiments. Rokni and Sunden (1999) apply the Speziale's (1987) non-linear model coupled with the AKN model to duct flows with success.

It should be mentioned that the above noted low-Reynolds-number extensions of the standard $k-\epsilon$ model demand that y^+ at first off-wall nodes should be much less than unity. Moreover the empirical damping functions are not universal.

3.2.3 Non-linear Eddy Viscosity Models (NLEVMs)

The above described zero-, one- and two-equation models are based on the linear isotropic Boussinesq (1877) hypothesis (in reality, turbulence is non-isotropic). Obviously, this postulation cannot produce any difference between normal stresses such as those that drive secondary flows in non-circular ducts. Also, it cannot be expected to predict accurately flows with separation, streamline curvature and swirl. For such complex flows, more advanced turbulence models should be used. The non-linear eddy viscosity models are among this group.

Over the years, a number of extended Boussinesq constitutive relations have been proposed. Essentially these are achieved by adding new empirical terms into the linear Boussinesq constitution to account for either compressibility, or streamline curvature, or anisotropy of the Reynolds stresses (see Spalart, 2000). The additional terms consist either of quadratic, or of cubic combinations of strain and vorticity. Yoshizawa (1984), Nisizima and Yoshizawa (1987), Speziale (1987) and Shih *et al.* (1993) have all developed similar quadratic extensions of the linear Reynolds stress expression adopting different strategies. The coefficients present in these non-linear terms are very different from each other. This is because each model is calibrated to suit particular cases. Although the inclusion of quadratic products of strain and vorticity can improve predictions of anisotropy of turbulence, the quadratic level is not able adequately to account for the various effects of streamline curvature or swirl on the turbulent stresses. Craft *et al.* (1993, 1996) demonstrate that a cubic stress-strain relation is essential for capturing characteristics of flows with streamline curvature and swirl. Therefore, Craft *et al.* (1993, 1996) propose a cubic stress-strain construction. The important feature for the cubic relation is the inclusion of the strain-dependent eddy viscosity coefficent, which makes the model sensitive to curvature. Suga (1995) discusses the development and calibration of the model in detail. The cubic expression of the Reynolds stress tensor is given by

$$-\rho\overline{u_i'u_j'} = \underbrace{\tau_{ijl}}_{\text{Linear part}} + \underbrace{\tau_{ijnl}}_{\text{Non-linear part}} \tag{3.29}$$

where

$$\tau_{ijl} = -\frac{2}{3}\rho k\delta_{ij} + 2\mu_t S_{ij} \tag{3.30}$$

$$\begin{aligned}\tau_{ijnl} = & -4c_1\mu_t\frac{k}{\tilde{\epsilon}}(S_{ik}S_{kj} - \frac{1}{3}S_{kl}S_{kl}\delta_{ij}) - 4c_2\mu_t\frac{k}{\tilde{\epsilon}}(\Omega_{ik}S_{kj} + \Omega_{jk}S_{ki}) \\ & -4c_3\mu_t\frac{k}{\tilde{\epsilon}}(\Omega_{ik}\Omega_{jk} - \frac{1}{3}\Omega_{lk}\Omega_{lk}\delta_{ij}) - 8c_4\mu_t\frac{k^2}{\tilde{\epsilon}^2}(S_{ki}\Omega_{lj} + S_{kj}\Omega_{li})S_{kl} \\ & -8c_5\mu_t\frac{k^2}{\tilde{\epsilon}^2}(\Omega_{il}\Omega_{lm}S_{mj} + S_{il}\Omega_{lm}\Omega_{mj} - \frac{2}{3}S_{lm}\Omega_{mn}\Omega_{nl}\delta_{ij}) \\ & -8c_6\mu_t\frac{k^2}{\tilde{\epsilon}^2}S_{ij}S_{kl}S_{kl} - 8c_7\mu_t\frac{k^2}{\tilde{\epsilon}^2}S_{ij}\Omega_{kl}\Omega_{kl}\end{aligned} \tag{3.31}$$

The turbulent viscosity is calculated by

$$\mu_t = c_\mu \rho f_\mu \frac{k^2}{\tilde{\epsilon}} \tag{3.32}$$

where

$$\begin{aligned}& c_\mu = \tfrac{0.3}{1+0.35\eta^{1.5}}\left(1 - e^{-0.36e^{0.75\eta}}\right) \\ & f_\mu = 1 - e^{-(\frac{R_t}{90})^{1/2}-(\frac{R_t}{400})^2} \\ & \eta = \max(\tilde{S}, \tilde{\Omega}) \\ & \tilde{S} = \tfrac{k}{\tilde{\epsilon}}\sqrt{2S_{ij}S_{ij}}, \quad \tilde{\Omega} = \tfrac{k}{\tilde{\epsilon}}\sqrt{2\Omega_{ij}\Omega_{ij}}\end{aligned}$$

The transport equations for k and ϵ used in this cubic model are the LS model with Yap correction and the modified source term E. The near-wall E term is modelled as follows:

$$E = \begin{cases} 0.0022\frac{\mu_t\tilde{S}k^2}{\tilde{\epsilon}}\left(\frac{\partial^2 U_i}{\partial x_j \partial x_k}\right)^2, & R_t \leq 250 \\ 0, & R_t > 250 \end{cases} \tag{3.33}$$

The empirical coefficients $c_1 \sim c_7$ are -0.1, 0.1, 0.26, $-10c_\mu^2$, 0, $-5c_\mu^2$ and $5c_\mu^2$ respectively. This version is usually called a two-equation low-Reynolds-number cubic model as distinct from the three-equation one (see Craft *et al.* (1996) or Suga (1995)). The three-equation version ($k - \epsilon - A_2$) is more complex than the two-equation. This is due to the inclusion of an extra transport equation for the stress-anisotropy invariant (A_2). However, use of the three-equation version broadens the range of applicability of the model, especially for flows far from equilibrium including transition. Chen *et al.* (1998a,

b) apply the two- and three-equation cubic models to transitional boundary layers pertinent to turbomachinery aerodynamics, and the flow around a highly loaded compressor cascade. Apsley and Leschziner (1998) also investigate a separated diffuser flow using these models. Barakos and Drikakis (2000) employ the same models for transonic flows. The studies for all of these applications show that, compared with linear models, the cubic models improve predictions. However, in relation to electronic systems, the geometries considered above are relatively simple.

It has been recognized that the Speziale's (1987) quadratic model is not strongly realizable (i.e. negative normal stresses can arise). Mompean *et al.* (1996) demonstrate that near walls $\overline{u'^2}$ becomes excessively high. Consequently $\overline{v'^2}$ and $\overline{w'^2}$ become negative (ensuring the sum of the three components is equal to k).

This study will focus on the application of the Craft *et al.* two-equation cubic model rather than the Speziale model (in view of the fact that Tucker and Pan (2000) have investigated the latter model for the CPU case, and Tucker *et al.* (2003a) find it very unstable needing to resort to strong Reynolds stress clipping to secure convergence).

3.2.4 Reynolds Stress or Second Moment Closure Model (RSM)

- **Full Reynolds Stress Model (FRSM)**

In FRSM, the Boussinesq assumption is abandoned. Instead the exact transport equations for the Reynolds stresses are used. They are derived from the Navier-Stokes equations and written as follows:

$$\frac{\partial}{\partial t}(\rho\overline{u_i'u_j'}) + \frac{\partial}{\partial x_k}(\rho U_k\overline{u_i'u_j'}) = \underbrace{D_{ij}}_{\text{Diffusion}} + \underbrace{P_{ij}}_{\text{Stress production}} + \underbrace{\Phi_{ij}}_{\text{Pressure−strain}} - \underbrace{\epsilon_{ij}}_{\text{Dissipation}} \tag{3.34}$$

where $P_{ij} = -\rho\left(\overline{u_i'u_j'}\frac{\partial U_j}{\partial x_k} + \overline{u_j'u_k'}\frac{\partial U_i}{\partial x_k}\right)$ (which transfers energy from the mean flow) is exact and does not require any modelling. The other terms, D_{ij}, Φ_{ij} (which redistributes energy amongst the Reynolds stress components) and ϵ_{ij} (which converts mechanical energy into heat in the small-scale turbulence) on the right hand side of Eq. (3.34), need to be modelled. To save coding effort, the FLUENT commercial package is used here for the FRSM. Therefore, only the modelled terms required to close the equations employed in FLUENT (see Fluent 5 User's Guide) are described below.

For the diffusion term D_{ij}, the generalised gradient-diffusion model of Lien and Leschziner (1994) is used, given by

$$D_{ij} = \frac{\partial}{\partial x_k}\left(\mu + \frac{\mu_t}{\sigma_k}\frac{\partial \overline{u_i'u_j'}}{\partial x_k}\right) \tag{3.35}$$

where $\sigma_k = 0.82$ (for the standard $k - \epsilon$ model, σ_k=1.0).

The pressure-strain correlation term Φ_{ij} and ϵ are two terms of importance and are also the most problematic. Various models for these have been proposed in the literature. FLUENT provides several models for Φ_{ij} involving Gibson and Launder (1978) linear and Speziale *et al.* (1991) (SSG) quadratic high-Reynolds-number forms. The latter is chosen for the present study, in which Φ_{ij} takes the following form

$$\Phi_{ij} = \Phi_{ij,1} + \Phi_{ij,2} + \Phi_{ij}^{w} \tag{3.36}$$

where $\Phi_{ij,1}$, $\Phi_{ij,2}$ and Φ_{ij}^{w} are the slow, rapid and wall-reflection parts respectively. They are modelled respectively as

$$\Phi_{ij,1} = -(C_1\rho\epsilon + C_1^* P)b_{ij} + C_2\rho\epsilon\left(b_{ik}b_{kj} - \frac{1}{3}b_{mn}b_{mn}\delta_{ij}\right) \tag{3.37}$$

$$\begin{aligned}\Phi_{ij,2} = {} & (C_3 - C_3^*\sqrt{b_{ij}b_{ij}})\rho k S_{ij} + C_4\rho k(b_{ik}S_{jk} + b_{jk}S_{ik} - \tfrac{2}{3}b_{mn}S_{mn}\delta_{ij}) \\ & + C_5\rho k(b_{ik}\Omega_{jk} + b_{jk}\Omega_{ik})\end{aligned} \tag{3.38}$$

$$\Phi_{ij}^{w} = 0 \tag{3.39}$$

where the Reynolds stress anisotropy tensor b_{ij} is defined as

$$b_{ij} = \frac{\overline{u_i'u_j'}}{2k} - \frac{1}{3}\delta_{ij} \tag{3.40}$$

$P = \frac{1}{2}P_{kk}$, and the constants are $C_1 = 3.4$, $C_1^* = 1.8$, $C_2 = 4.2$, $C_3 = 0.8$, $C_3^* = 1.3$, $C_4 = 1.25$, $C_5 = 0.4$. By assuming isotropy of the small dissipative eddies, the dissipation tensor ϵ_{ij} is modelled as $\epsilon_{ij} = \frac{2}{3}\delta_{ij}\rho\epsilon$.

When k is needed, FLUENT solves a transport equation for k in order to obtain boundary conditions for the Reynolds stresses, and computes k from $k = \frac{1}{2}\overline{u_i'u_i'}$ for regions away from walls or bulk flow regions. The transport equation for k is identical to Eq. (3.14), except that $\sigma_k = 0.82$. ϵ is also obtained by solving a transport equation identical to Eq. (3.24) for core regions, while for near-wall regions ϵ is computed from wall functions (see Section 3.2.6). The Reynolds stresses at the wall-adjacent cells are calculated from the following equations which are based on the log-law and the assumption of equilibrium:

$$\overline{u'^2} = 1.098k, \quad \overline{v'^2} = 0.247k, \quad \overline{w'^2} = 0.655k, \quad -\overline{u'v'} = 0.255k \tag{3.41}$$

Since the FRSM solves the exact transport equations for stress components where history and non-local effects are accounted for, this type of model can in principle deal with any complex strain field and provide the most advanced turbulence models to date (i.e. the state of the art). Whenever non-isotropic effects are important, the FRSM should be considered. However, the FRSM is complex and difficult to implement. Also it is not without modelling assumption. To simplify the FRSM, an alternative form known as algebraic Reynolds stress model (ARSM) has been developed (see Rodi, 1976).

- **Algebraic Reynolds Stress Model (ARSM) and Explicit Algebraic Stress Model (EASM)**

ARSM is an economical way of accounting for anisotropy of Reynolds stresses without the need to solve a full set of transport equations for the Reynolds stresses. Rodi (1976) proposes the idea of algebraic stress closure by means of an equilibrium hypothesis, in which the Reynolds stress convection and diffusion terms are neglected. For a general ARSM form, two assumptions are made. These are that the sum of the convection and diffusion terms of the Reynolds stresses is proportional to the sum of the convection and diffusion terms of the turbulent kinetic energy (k); and that the anisotropic Reynolds stress b_{ij} given in Eq. (3.40) is constant along a streamline. After introducing these assumptions into Eq. (3.34) and some rearrangement, an implicit algebraic equation for Reynolds stress is obtained (see Gatski and Speziale, 1993; Abid *et al.*, 1995).

Owing to the presence of the Reynolds stresses on both sides of the algebraic equations, this type of model is difficult to implement in complex flows. It also suffers from some numerical problems due to the need for successive matrix inversions at each iteration. Therefore, many researchers have attempted to solve the algebraic stress equations explicitly. Gatski and Speziale (1993) (GS) adopt Pope's (1975) methodology for obtaining explicit equations. This is refered to as Explicit Algebraic Stress Model (EASM). For GS's EASM, the Reynolds stresses are expressed as an explicit function of the mean strain rate and the vorticity tensor, given by

$$\begin{aligned} -\rho\overline{u_i'u_j'} = -\frac{2}{3}\rho k\delta_{ij} + 2\mu_t^*[(S_{ij} - \frac{1}{3}S_{kk}\delta_{ij}) + \alpha_3\frac{k}{\epsilon}(S_{ik}\Omega_{kj} \\ +S_{jk}\Omega_{ki}) - \alpha_4\frac{k}{\epsilon}(S_{ik}S_{kj} - \frac{1}{3}S_{kl}S_{kl}\delta_{ij})] \end{aligned} \tag{3.42}$$

with

$$\mu_t^* = \rho\frac{3(1+\eta^2)\alpha_1}{3+\eta^2+6\eta^2\xi^2+6\xi^2}\frac{k^2}{\epsilon} \tag{3.43}$$

$$\eta = \frac{1}{2}\alpha_2(S_{ij}S_{ij})^{\frac{1}{2}}\frac{k}{\epsilon}, \quad \xi = \frac{1}{2}\alpha_3(\Omega_{ij}\Omega_{ij})^{\frac{1}{2}}\frac{k}{\epsilon} \tag{3.44}$$

$$\alpha_1 = \left(\frac{4}{3} - C_2\right)\frac{g}{2}, \quad \alpha_2 = (2 - C_3)\frac{g}{2} \tag{3.45}$$

$$\alpha_3 = (2 - C_4)\frac{g}{2}, \quad \alpha_4 = 2\alpha_2, \quad g = \frac{1}{C_1 + C_5 - 1} \tag{3.46}$$

When the SSG (Speziale *et al.*, 1991) pressure-strain correlation model is used, the values of constants $C_1 \sim C_5$ are 3.4, 0.36, 1.25, 0.4, 1.88 respectively.

It should be mentioned that the above GS's EASM is a high-Reynolds-number model that is coupled with the standard $k - \epsilon$ model. When applied to low-Reynolds-number flows, this model needs to be modified by introducing damping functions. In this study, the Abid *et al.* (1995) low-Reynolds-number form is employed. The damping functions and source terms used by Abid *et al.* in Eqs. (3.25-27) are as follows:

$$D = 0, \quad E = 0, \quad f_1 = 1, \quad f_\mu = 1, \quad f_2 = 1 - e^{-\frac{R_y}{12.5}} \quad or \quad f_2 = \left[1 - e^{-\frac{y^+}{6.4}}\right]^2 \tag{3.47}$$

In addition, the Abe *et al.* (AKN) (1994) damping functions are also tested.

3.2.5 Turbulence models for heat fluxes

On analogy with the Boussinesq hypothesis, turbulent heat fluxes can be modelled as

$$-\rho\overline{u_j't'} = \frac{\mu_t}{Pr_t}\frac{\partial T}{\partial x_j} \tag{3.48}$$

where Pr_t is the prescribed turbulent Prandtl number which is normally assumed to be a constant (for air, $Pr_t = 0.9$ for wall-bounded flows). This model is usually called the "eddy diffusivity" model.

However, the assumption of constant Pr_t in turbulent flows is not accurate. The experiments from Hishida *et al* (1986) show that Pr_t varies across the wall region. Therefore, to improve heat transfer predictability, models without the use of Pr_t might be considered, such as the second-moment differential-equation models for the heat fluxes like the Reynolds stresses in FRSM. Nevertheless, such models are complex and some terms also need to be modelled. To simplify this type of model, Daly and Harlow (1970) introduces the Generalized Gradient Diffusion Hypothesis (GGDH) which takes the following form:

$$-\rho\overline{u_j't'} = c_t\overline{u_j'u_k'}\frac{k}{\epsilon}\frac{\partial T}{\partial x_j} \tag{3.49}$$

where $c_t = 0.3$. Launder (1988) reviews some strategies for computing heat fluxes showing results from the GGDH approach that are in better agreement with experiments than those using the eddy-diffusivity model.

Obviously, when the Reynolds stresses are computed with sufficient accuracy, the heat fluxes will be consequently predicted accurately from the GGDH model. Hence, non-linear EVMs or EASM with the GGDH method might be an economic combination when predicting both the flow field and heat transfer.

3.2.6 Near-wall modelling

As a wall is approached, turbulent fluctuations are suppressed. Close to the wall, viscous damping reduces tangential velocity fluctuations while kinematic blocking decreases normal fluctuations. Accurate representation of the flow in the near-wall region, therefore, play an important part in successful prediction of wall-bounded turbulent flows, especially for heat transfer. There are two basic near-wall treatment approaches which are briefly described below. Fig. 3.2 schematically depicts these two approaches.

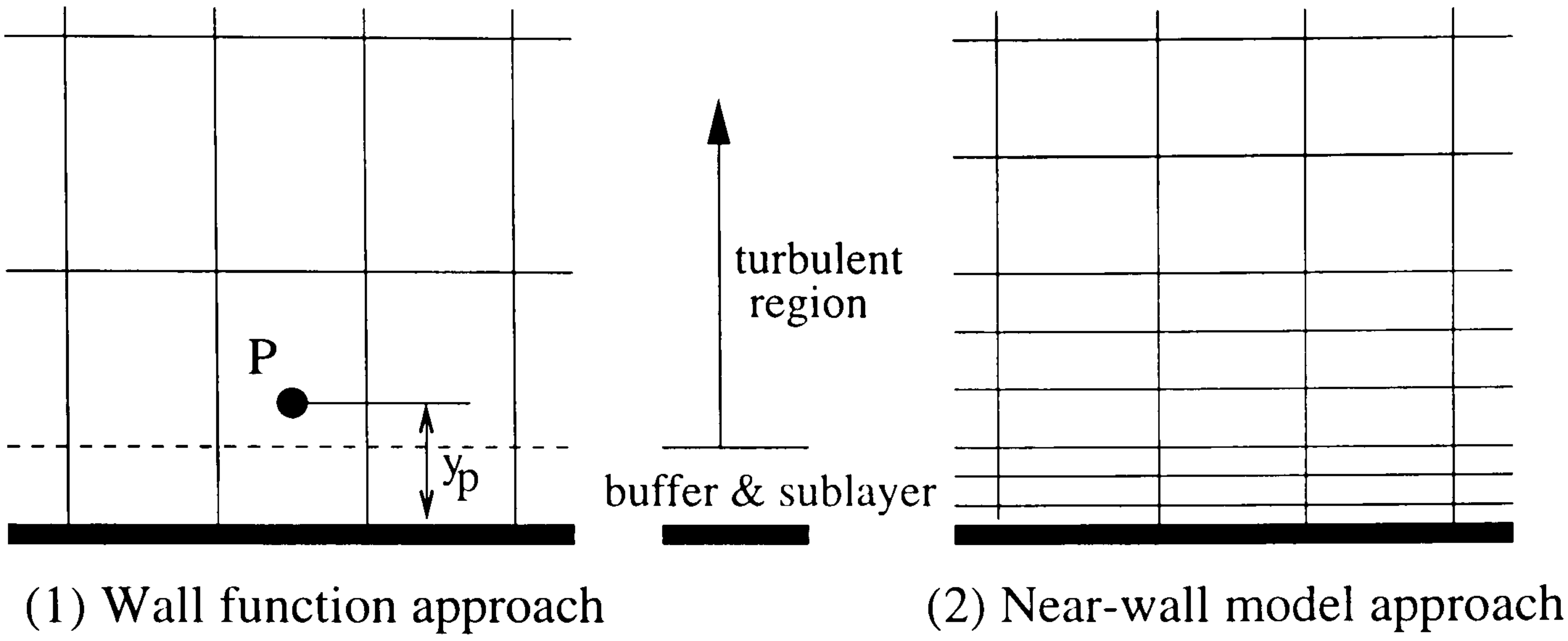

Figure 3.2: Near-wall treatments.

(1) Wall functions

In the near-wall region, the inner region (viscous sublayer, buffer layer and log-law region) is not resolved. Instead, it is bridged with semi-empirical formulae called "wall functions". In the log-law region, the mean velocity is given by

$$U^+ = \frac{U}{u_\tau} = \frac{1}{\kappa} ln(Ey^+) \tag{3.50}$$

where $\kappa = 0.42$, $E = 9.8$ (for smooth walls), $u_\tau = \sqrt{\tau_w/\rho}$ and $y^+ = \rho u_\tau y/\mu$. Here, the widely used wall functions proposed by Launder and Spalding (1974) are used, which read

$$U^* = \frac{1}{\kappa} ln(Ey^*), \quad \epsilon_p = \frac{c_\mu^{3/4} k_p^{3/2}}{\kappa y_p} \tag{3.51}$$

where

$$U^* = \frac{U_p c_\mu^{1/4} k_p^{1/2}}{\tau_w/\rho}, \quad y^* = \frac{\rho c_\mu^{1/4} k_p^{1/2} y_p}{\mu} \tag{3.52}$$

The above formulae are valid for $y_p^* > 30 \sim 60$, namely the log-law layer; but in practice, when $y_p^* > 11.5$, these equations are usually employed.

It should be noted that in Eq. (3.52) y^* is used rather than y^+. In equilibrium turbulent boundary layers, $y^+ \approx y^*$. The k equation is solved in the whole domain including the wall-adjacent cells (the boundary condition for k at the wall is $\partial k/\partial y = 0$), while ϵ is not solved at the wall-adjacent cells, but obtained from Eq. (3.51).

For the thermal boundary layer, the mean temperature is obtained in the same way as the velocity:

$$T^+ = \frac{T_w - T}{T_\tau} = \frac{1}{\kappa_T} ln(\tilde{E} y^+) \tag{3.53}$$

where $T_\tau = q_w/\rho c_p u_\tau$, T_w is the wall temperature and $\tilde{E}$ modelling constant. From Eq. (3.50), we can obtain

$$lny^+ = \kappa U^+ - lnE \tag{3.54}$$

Substituting Eq. (3.54) into Eq. (3.53), the following equation can be obtained

$$T^+ = \frac{\kappa}{\kappa_T}\left(U^+ + \frac{ln(\tilde{E}/E)}{\kappa}\right) = Pr_t\left(U^+ + C_h\right) \tag{3.55}$$

where $C_h = ln(\tilde{E}/E)/\kappa$ is a function of Pr and Pr_t given by Jayatillaka (1969) as

$$C_h = 9.24\left[\left(\frac{Pr}{Pr_t}\right)^{\frac{3}{4}} - 1\right]\left[1 + 0.28e^{-0.007\frac{Pr}{Pr_t}}\right] \tag{3.56}$$

(2) Near-wall model approach

There are two types of treatment: one-layer, and two-layer approaches. For the one-layer method, low-Reynolds-number models are used to resolve the flow through to the wall. In the two-layer zonal model, in the near-wall region low-Reynolds-number models are employed, e.g. the Wolfshtein $k - l$ model; in the fully turbulent region high-Reynolds-number models are applied such as the standard $k - \epsilon$, FRSM and EASM. In this study, several combinations will be investigated involving $k - l/k - \epsilon$, $k - l$/EASM and so on.

In this approach, the near-wall grid should be fine (see Fig. 3.2 (2)). As mentioned before, y^+ at the first off-wall nodes should be less than unity for most of low-Reynolds-number models.

3.3 LES

LES has been widely studied and increasingly employed in engineering since Deardorff (1970) first applied LES to a fully developed turbulent channel flow. For problems such as massively separated flows, combustion and noise studies, LES has advantages over URANS method (see section 3.1.3).

LES consists of three key aspects, namely a filtering operation, a subgrid scale stress approximation and numerical solution. This is discussed in detail in the following sections.

3.3.1 Filtered governing equations

In LES, a spatial scale separation between large and small scales is considered. Large-scale eddies are then resolved and small-scale eddies are modelled. Scale separation is defined by means of filtering to determine the size of small scales (Piomelli, 1999).

(1) Filtering and energy spectrum

A filtered or resolved flow variable, denoted by an overbar, is defined by the filtering operation

$$\overline{f}(x) = \int_D f(x')G(x,x';\Delta)dx' \tag{3.57}$$

where D is the whole flow domain, G is the filter function and Δ the filter width. Eddies of size greater than Δ are large or resolved eddies. Those smaller than Δ are small, unresolved or subgrid scales (SGS) eddies. Generally speaking, Δ would be a length scale characterizing the smallest structures of interest in the flow. There are three commonly used filter functions, namely the spectral or sharp Fourier cutoff filter, Gaussian, and box or top-hat filters. With the cutoff filter, only the eddies with wavenumber $k > \pi/\Delta$ contribute to the subgrid scale field. For the Gaussian filter, a wide range of scales contributes to the subgrid scale field. With the top-hat filter, the situation is intermediate between the former two filters. Therefore, the structure of the subgrid scales depends strongly on the type of filter used (Piomelli, 1988).

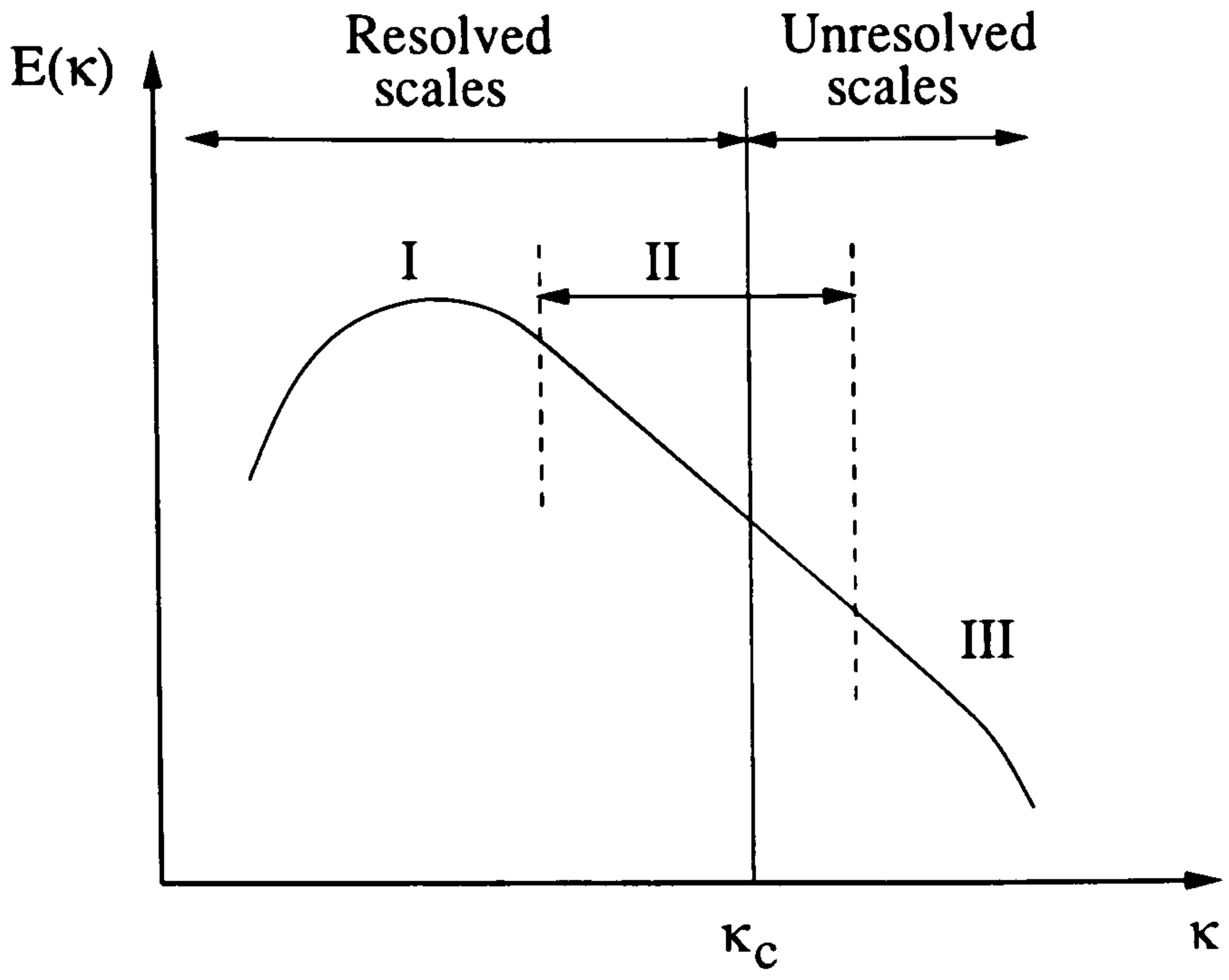

Figure 3.3: Energy spectrum: Region I: the large scale region; II: the inertial range and III: the dissipation range.

The scale separation is illustrated in Fig. 3.3 in spectral space. The cutoff wave number $\kappa_c = \pi/\Delta$ is generally located in the inertial region (Region II where the Kolmogorov spectrum law or -5/3 law holds). Eddies with wave number greater than κ_c are resolved; those with wave number smaller than κ_c are modelled statistically.

(2) Filtered governing equations

By applying a filtering operation, Eq. (3.57), to the governing equations for incompressible flow, the following filtered equations can be obtained

$$\frac{\partial \overline{u}_j}{\partial x_j} = 0 \tag{3.58}$$

$$\rho \frac{\partial \overline{u}_i}{\partial t} + \rho \frac{\partial \left(\overline{u_i u_j}\right)}{\partial x_j} = -\frac{\partial \overline{p}}{\partial x_i} + \frac{\partial}{\partial x_j}\left[\mu \frac{\partial \overline{u}_i}{\partial x_j}\right] \tag{3.59}$$

$$\rho \frac{\partial \overline{T}}{\partial t} + \rho \frac{\partial \left(\overline{u_j t}\right)}{\partial x_j} = \frac{\partial}{\partial x_j}\left[\frac{\mu}{Pr}\frac{\partial \overline{T}}{\partial x_j}\right] \tag{3.60}$$

Decomposing velocities into filtered and fluctuating parts, i.e. $u_i = \overline{u}_i + u'_i$, the non-linear term $\overline{u_i u_j}$ appearing in Eq. (3.59) can then be expressed as (Leonard, 1974)

$$\begin{aligned}\overline{u_i u_j} &= \overline{(\overline{u}_i + u'_i)(\overline{u}_j + u'_j)} \\ &= \overline{\overline{u}_i\,\overline{u}_j} + \overline{\overline{u}_i u'_j} + \overline{\overline{u}_j u'_i} + \overline{u'_i u'_j} \\ &= \underbrace{(\overline{\overline{u}_i\,\overline{u}_j} - \overline{u}_i\,\overline{u}_j)}_{L_{ij}} + \overline{u}_i\,\overline{u}_j + \underbrace{\overline{\overline{u}_i u'_j} + \overline{\overline{u}_j u'_i}}_{C_{ij}} + \underbrace{\overline{u'_i u'_j}}_{R_{ij}}\end{aligned} \tag{3.61}$$

where L_{ij} is the Leonard stress tensor, representing interactions among the large scales; C_{ij} is the cross-stress tensor, representing interactions between large and small scales; and the last term R_{ij} is the subgrid-scale Reynolds stress tensor. This reflects interactions between subgrid scales. Substituting Eq. (3.61) into Eq. (3.59), the resulting equation is

$$\rho\frac{\partial \overline{u}_i}{\partial t} + \rho\frac{\partial(\overline{u}_i\,\overline{u}_j)}{\partial x_j} = -\frac{\partial \overline{p}}{\partial x_i} + \frac{\partial}{\partial x_j}\left[\mu\frac{\partial \overline{u}_i}{\partial x_j}\right] - \rho\frac{\partial \tau_{ij}}{\partial x_j} \tag{3.62}$$

where τ_{ij} is the subgrid-scale stresses, taking the following form

$$\tau_{ij} = L_{ij} + C_{ij} + R_{ij} = \overline{u_i u_j} - \overline{u}_i\,\overline{u}_j \tag{3.63}$$

On analogy with the above procedure, the governing equation for temperature can be obtained as

$$\rho\frac{\partial \overline{T}}{\partial t} + \rho\frac{\partial(\overline{u}_j\overline{T})}{\partial x_j} = \frac{\partial}{\partial x_j}\left[\frac{\mu}{Pr}\frac{\partial \overline{T}}{\partial x_j}\right] - \rho\frac{\partial h_j}{\partial x_j} \tag{3.64}$$

where h_j is the subgrid-scale heat fluxes given by

$$h_j = \overline{u_j t} - \overline{u}_j\,\overline{T} \tag{3.65}$$

It is τ_{ij} and h_i that need to be modelled. Because the SGS energy generally accounts for a much smaller part of the total flow energy than the RANS turbulent energy, the model accuracy may be less crucial in LES than in RANS computations.

As can be seen, the structures of the governing equations (Eqs. (3.58), (3.62) and (3.64)) in LES are very similar to those (Eqs. (3.6-8)) in RANS. However, the underlying physics is different.

3.3.2 Subgrid scale modelling

The main task of a subgrid-scale model is to simulate energy transfer between the resolved large eddies and the unresolved subgrid-scale eddies. Ideally a turbulent energy cascade process requires a SGS model to be capable of reflecting both the forward- and backward-cascade processes. Owing to the forward-cascade process being dominant and the backward-cascade process being weak in the flow, the latter is neglected in most SGS models proposed in the literature. There are various ways of modelling subgrid-scale terms. No matter what strategy is used, the SGS Reynolds stresses τ_{ij} are eventually linked to the resolved variables, with or without some adjustable parameters. The following will briefly discuss several basic or popular SGS models.

(1) Eddy viscosity models

For models based on the eddy viscosity concept, the SGS stresses τ_{ij} are related to the large-scale strain rate tensor $\overline{S}_{ij}$ by the SGS kinematic eddy viscosity, ν_{sgs} or ν_t, i.e.

$$\tau_{ij} - \frac{\tau_{kk}}{3}\delta_{ij} = -2\nu_t\overline{S}_{ij} \tag{3.66}$$

where $\overline{S}_{ij} = \frac{1}{2}\left(\frac{\partial\overline{u}_i}{\partial x_j} + \frac{\partial\overline{u}_j}{\partial x_i}\right)$. By dimensional analysis similar to Eq. (3.12) in RANS method, the SGS kinematic eddy viscosity (for simplicity called the SGS eddy viscosity below) can be expressed as

$$\nu_t \propto V_{sgs}l_{sgs} \tag{3.67}$$

where V_{sgs} and l_{sgs} are the SGS velocity and length scales, respectively. The task of this type of model is to define these two scales. In general, the length scale is related to the filter width Δ (for real space, the cubic root of a cell volume is usually employed), while the SGS velocity scale can be defined in different ways.

- **Smagorinsky model**

This model is the oldest, simplest and best known, subgrid-scale model proposed by Smagorinsky (1963). The model forms the basis of the majority of SGS models. In this model, the length scale l_{sgs} is proportional to Δ, defined as $l_{sgs} = C_s\Delta$, and the SGS velocity scale, V_{sgs}, is computed by

$$V_{sgs} = l_{sgs}|\overline{S}| \tag{3.68}$$

Thus the eddy viscosity can be written as

$$\nu_t = l_{sgs}V_{sgs} = (C_s\Delta)^2|\overline{S}| \tag{3.69}$$

where C_s is the Smagorinsky constant and $|\overline{S}| = \sqrt{2\overline{S}_{ij}\ \overline{S}_{ij}}$. The filter width Δ is usually taken to be $\Delta = (\Delta x\,\Delta y\ \Delta z)^{1/3}$. The values of the constant C_s are flow dependent. The commonly used values of C_s are between $0.065 \sim 0.2$ (Ferziger, 1996) (the former corresponding to channel flow, and the latter to isotropic flow). As can be seen, the structure of the model is similar to Prandtl's mixing-length RANS model.

The Smagorinsky model is easy to implement. However, the model suffers from the drawback that it dissipates too much energy from the resolved scales (Piomelli, 1988; Rodi *et al.*, 1997). Also, the Smagorinsky constant C_s must be optimized for an individual flow. Near-wall treatment is needed to damp the length scale, and thus ν_t. Various types of *ad hoc* corrections that are difficult to justify and hard to apply in complex geometries (Rodi *et al.*, 1997) are frequently used. A traditional method is to introduce damping functions such as the van Driest (1965), which is expressed as

$$f = 1 - e^{y^+/25} \tag{3.70}$$

The eddy viscosity thus becoming

$$\nu_t = (fC_s\Delta)^2|\overline{S}| \tag{3.71}$$

- **Yoshizawa one-equation SGS model**

Proposed by Lilly (1992), the SGS characteristic velocity scale is defined by

$$V_{sgs} = k_{sgs}^{\frac{1}{2}} = \tau_{kk}^{\frac{1}{2}} = \sqrt{\frac{1}{2}\left(\overline{u}_i - \langle\overline{u}_i\rangle\right)^2} \tag{3.72}$$

where k_{sgs} denotes the SGS turbulent kinetic energy and $\langle\overline{u_i}\rangle$ represents time-averaged velocities. Thus

$$\nu_t = \nu_{sgs} = C_e l_{sgs} V_{sgs} = C_k \Delta k_{sgs}^{\frac{1}{2}} \tag{3.73}$$

where C_k is a constant. The transport equation for k_{sgs} in the Yoshizawa (1993) model, which is similar to Eq. (3.14) in RANS, is expressed as

$$\rho\frac{\partial k_{sgs}}{\partial t} + \rho\frac{\partial}{\partial x_j}\left(\overline{u}_j k_{sgs}\right) = \frac{\partial}{\partial x_j}\left[(\mu + \mu_{sgs})\frac{\partial k_{sgs}}{\partial x_j}\right] + P_{k_{sgs}} - C_\epsilon \rho \frac{k_{sgs}^{1.5}}{\Delta} \tag{3.74}$$

where

$$P_{k_{sgs}} = 2\mu_{sgs}\overline{S}_{ij}\overline{S}_{ij} \quad \text{and} \quad \mu_{sgs} = \rho\, C_k \Delta\, k_{sgs}^{1/2}$$

Using analytical theory of turbulence, Yoshizawa (1993) proposes $C_\epsilon = 1.05$ and $C_k = 0.07$.

Since this model contains more information relating to the subgrid scales, it is theoretically better capable of dealing with large-scale intermittency than the Smagorinsky model (Sagaut, 2000). However, it is computationally more expensive requiring solution of an additional transport equation for k_{sgs}.

(2) Dynamic SGS models

To address the drawbacks of a constant C_s value, several models have been proposed. The most successful is the dynamic model of Germano *et al.* (1991). In reality, it is not a model, but is instead a procedure by which the model coefficient, C, is computed dynamically as the calculation progresses, rather than being a prescribed value. Now the constant, C, becomes time- and space-dependent. Consequently, the SGS eddy viscosity is computed by

$$\nu_t = C\Delta^2|\overline{S}| \tag{3.75}$$

With this procedure, two filters are employed: a grid filter, Δ, and a test filter, $\widehat{\Delta}$ with width greater than Δ (typically $\widehat{\Delta} = 2\Delta$). Applying the test filter, $\widehat{\Delta}$, into the filtered Navier-Stokes equations using Δ , the resulting stress tensor on the test level is

$$T_{ij} = \widehat{\overline{u_i u_j}} - \widehat{\overline{u}}_i\widehat{\overline{u}}_j \tag{3.76}$$

where T_{ij} is the subtest-scale stresses. T_{ij} are related to the SGS stresses τ_{ij} via the Germano identity (Germano *et al.*, 1991)

$$Y_{ij} = T_{ij} - \widehat{\tau}_{ij} = \widehat{\overline{u}_i\,\overline{u}_j} - \widehat{\overline{u}}_i\,\widehat{\overline{u}}_j \tag{3.77}$$

which represents the contribution from the region between test-filter and grid-filter scales as shown in Fig. 3.4. The stress, Y_{ij}, can be calculated explicitly from the resolved large-scale variables.

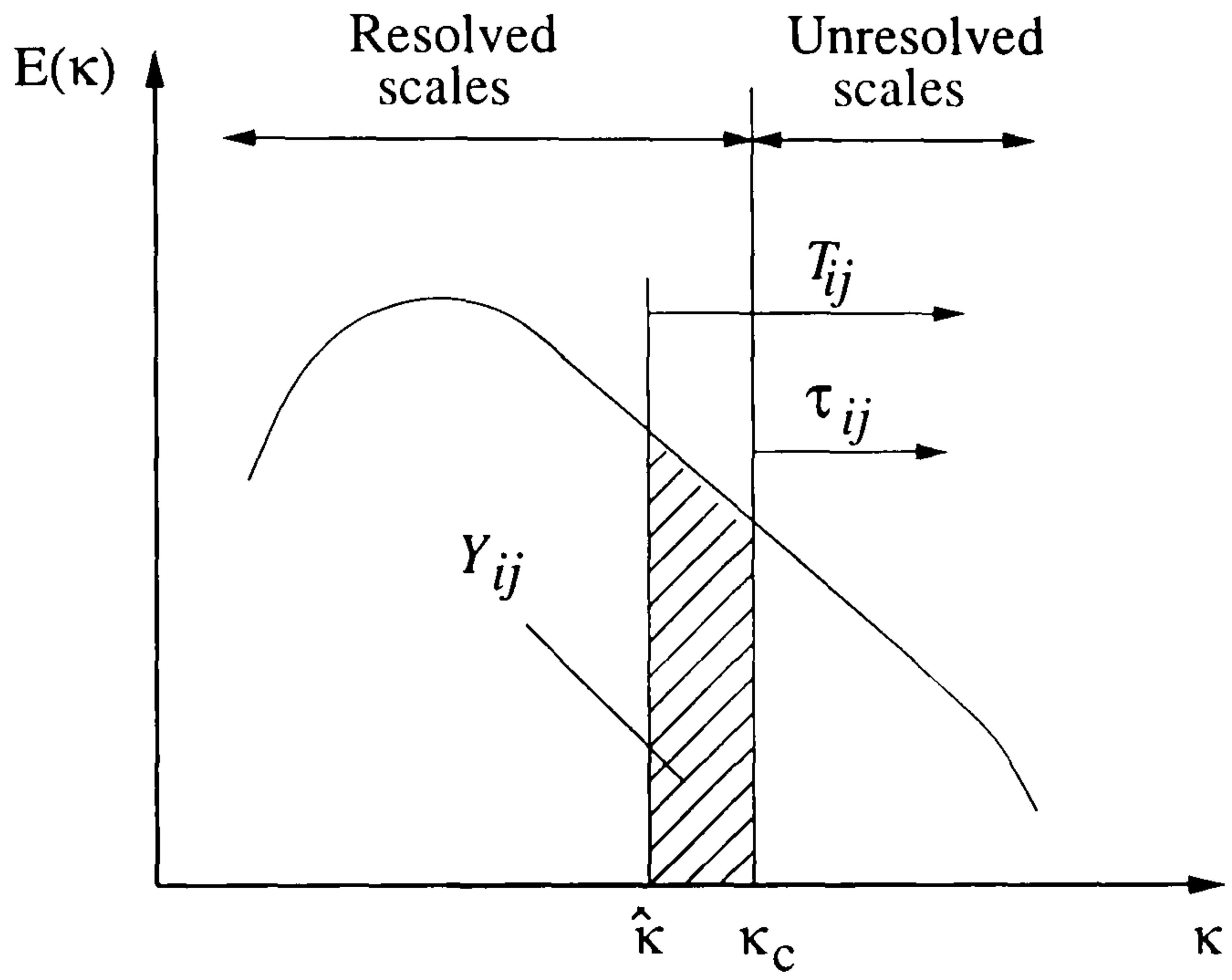

Figure 3.4: Energy spectrum: Grid- and test-filter for the dynamic model.

On the original LES level, the Smagorinsky model gives

$$\tau_{ij} - \frac{1}{3}\tau_{kk}\delta_{ij} = -2C\Delta^2|\overline{S}|\overline{S}_{ij} \tag{3.78}$$

On the test filter level, the Smagorinsky model gives

$$T_{ij} - \frac{1}{3}T_{kk}\delta_{ij} = -2C\widehat{\Delta}^2|\widehat{\overline{S}}|\widehat{\overline{S}}_{ij} \tag{3.79}$$

Substituting Eqs. (3.77-79) into Eq. (3.76) to yield

$$Y_{ij} - \frac{1}{3}Y_{kk}\delta_{ij} = -2CM_{ij} \tag{3.80}$$

with

$$M_{ij} = \widehat{\Delta}^2|\widehat{\overline{S}}|\widehat{\overline{S}}_{ij} - \Delta^2\widehat{|\overline{S}|\overline{S}_{ij}} \tag{3.81}$$

Owing to six independent equations being available for one unknown C (Eq. (3.80), the constant C is overdetermined. Lilly (1992) improves this computation in the least-square sense based on the error $e_{ij} = Y_{ij} - T_{ij} + \widehat{\tau}_{ij}$. This leads to

$$C = -\frac{1}{2}\frac{Y_{ij}M_{ij}}{M_{mn}M_{mn}} \tag{3.82}$$

This dynamic procedure to determine the model coefficient C has several advantages over the standard Smagorinsky model such as avoiding special treatment near walls. However, the dynamic SGS model still has significant problems, for example, large fluctuations in C result in unstable computations, excessive energy back-scattering (due to introduction of the scale-invariance assumption) and so on. Many remedies to these drawbacks have been developed in the literature (see Piomelli, 1999). Many of these involves averaging in homogeneous flow direction. For the CPU unit studied here, this is not possible.

In addition to the above-reviewed SGS models, there is another reasonably popular one called the "scale similarity" model proposed by Bardina *et al.* (1980). This assumes that the interaction between resolved and SGS eddies takes place between the smallest resolved scales immediately above the cutoff, and the largest SGS eddies close to the cutoff. The largest SGS component can be obtained by filtering the SGS velocities, i.e. twice filtering the velocities $(\overline{u_i'} = \overline{u_i} - \overline{\overline{u_i}})$. Thus the terms, C_{ij} and R_{ij} in Eq. (3.61) can be modelled. Consequently, the SGS stresses can then be computed. The Bardina *et al.* (1980) scale similarity model underestimates energy dissipation. To improve the behaviour, this model is always used in conjunction with the dissipative Smagorinsky model. This leads to the so-called mixed model (Bardina *et al*, 1980).

In this work, both the Smagorinsky and Yoshizawa models are employed.

(3) SGS heat fluxes modelling

Similar to the turbulent heat fluxes in RANS, the eddy diffusivity concept is employed in LES. The SGS heat fluxes are modelled using the local resolved temperature gradients, giving by

$$h_j = -\alpha_t \frac{\partial \overline{T}}{\partial x_j} = -\frac{\nu_t}{Pr_t}\frac{\partial \overline{T}}{\partial x_j} \tag{3.83}$$

where α_t is the SGS eddy diffusivity, and Pr_t the SGS turbulent Prandtl number. A wide range of values for Pr_t have been proposed in the literature ranging from 0.25 to 0.85. Here, the value of 0.4 (see Tucker and Davidson, 2003b) is assumed.

3.3.3 Wall models

Resolving the wall layer requires a fine grid to capture near-wall streaks and it is thus computationally costly. In order to reduce costs, approximate boundary conditions or wall models may be used. If near-wall streaks are not resolved and modelled instead, a much coarser grid could be used in the streamwise and spanwise directions saying $\Delta x^+ \approx 100 \sim 600$ and $\Delta z^+ \approx 100 \sim 300$ (if resolving near-wall regions, $\Delta x^+ \approx 50 \sim 150$ and $\Delta z^+ \approx 15 \sim 40$) (see Piomelli and Balaras (2002)). The cell spacing in the wall-normal direction depends on the near-wall treatment used.

Piomelli and Balaras (2002) and Cabot and Moin (1999) review wall-layer models. Following Piomelli *et al.* (2003), wall-layer models can be classified into two types: equilibrium laws and zonal models. Equilibrium laws assume that the dynamics of the wall-layer are universal and that some generalized law-of-the-wall holds. The wall shear stress is then calculated using this law and the velocity in the outer layer. This approach is quite identical to wall functions in RANS simulations and allows the first grid point to be located in the inner part of the logarithmic layer ($y^+ \approx 30 \sim 50$).

Zonal approaches are hybrid RANS/LES methods. In the near-wall region, the RANS (or URANS) is employed, and LES in the core region. To date two methodologies have been proposed. One is the Balaras *et al.* (1996) two-layer model (see the left figure in Fig. 3.5). With this approach, in the outer flow the filtered governing equations are solved using the wall shear stress as the boundary condition. In the inner layer where the grid is refined and embedded under the outer coarser LES mesh, RANS-type boundary-layer equations for the mean velocity are resolved, and the wall shear stress is then obtained. This method permits the first LES grid point to be positioned in a region of $20 < y^+ < 100$.

The other is zonal LES method mentioned in Section 3.1. This technique will be

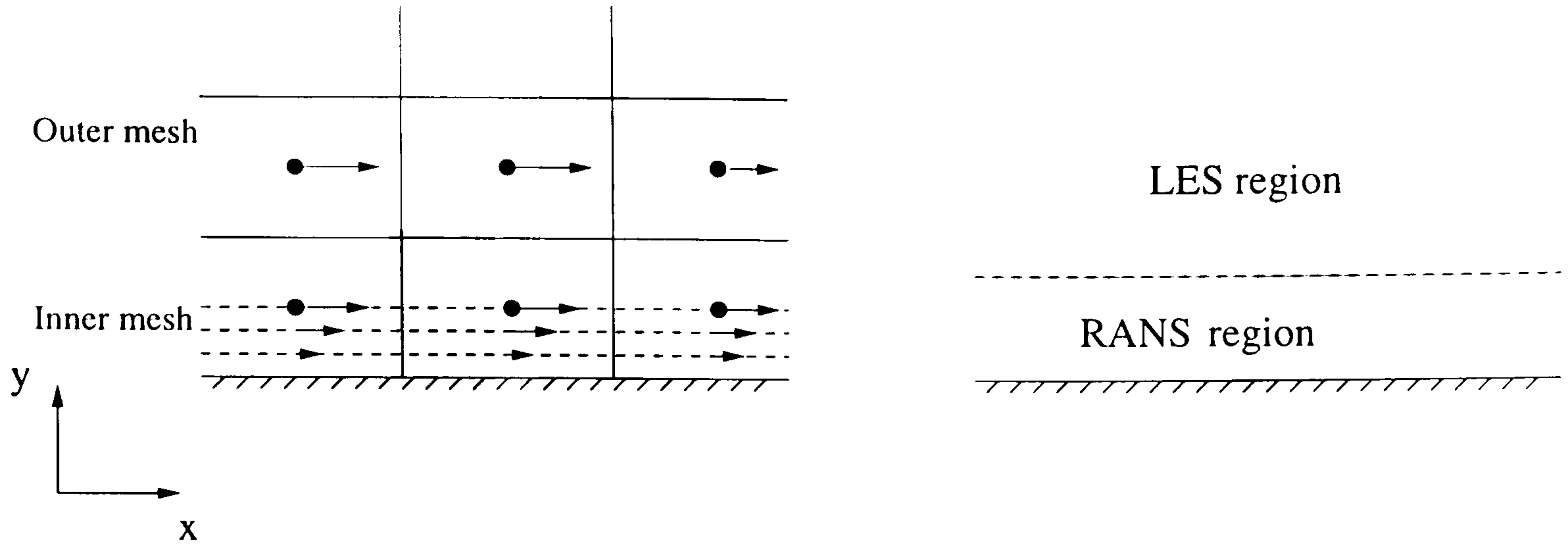

Figure 3.5: Zonal approaches of near-wall treatment: left - two-layer model; right - RANS/LES.

discussed in the next section in more detail. Fig. 3.5 schematically shows the above two hybrid RANS/LES methods near the wall.

In this study, neither the law-of-the-wall method nor the two-layer model is employed. For simplicity, near-wall treatment is achieved by means of applying different length scales. For the Smagorinsky model, the length scale is defined by

$$l_{sgs} = \min(C_s\Delta, \kappa y_{\min}) \tag{3.84}$$

where κ=0.42 is von Karman's constant (Moin *et al.*, 1987) and y_{min} is the distance from the nearest wall. For Yoshizawa's one-equation model, the filter width is defined by

$$l_{sgs,\mu} = \min(\Delta, l_{\mu,\mathrm{RANS}}), \quad l_{sgs,\epsilon} = \min(\Delta, l_{\epsilon,\mathrm{RANS}}) \tag{3.85}$$

where $l_{\mu,\mathrm{RANS}}$ and $l_{\epsilon,\mathrm{RANS}}$ are the same as those in Wolfshtein's $k - l$ model (see Section 3.2.2).

3.4 Zonal LES

An approach which combines LES in the core region with RANS (which more accurately should be called URANS) in the near-wall region is generally called hybrid RANS/LES or zonal LES. This methodology is introduced by Spalart *et al.* (1997). In their paper, they term this method Detached Eddy Simulation (DES). DES has been verified for various cases by researchers and successfully applied to a number of engineering flows. Nikitin *et al.* (2000) employ DES for plain channel flow with LES grid. They perform several calculations with a wide range of Reynolds numbers ($180 \leq Re_\tau \leq 80{,}000$) and obtain acceptable results. Travin *et al.* (1999) investigate performance of DES for the flow past a circular cylinder. The numerical results show good agreement with experimental data. Shur *et al.* (1999) apply DES to flow over a high-incidence aerofoil and gain promising results.

In addition to the S-A based DES, various combinations of RANS and SGS models have been developed in the literature. Hence, in this study, DES refers to the S-A based hybrid RANS/LES, while other RANS/LES combinations are still called hybrid RANS/LES or zonal LES (ZLES).

Davidson and Peng (2001) couple a two-equation $k-\omega$ model (Peng *et al.*, 1997) for RANS region with the Yoshizawa (1993) one-equation $k-l$ SGS model for the LES region. They apply this approach to a fully developed channel flow and 2D hill flow. Temmerman *et al.* (2002, 2003) combine the Wolfshtein (1969) one-equation $k-l$ RANS model with both the Smagorinsky (1963) and Yoshizawa SGS model in their studies. Tucker and Davidson (2003b) test another combination, namely the Wolfshtein $k-l$ RANS model and Yoshizawa $k-l$ SGS model for a plain channel flow and 3D ribbed channel flow. Hamba (2001) also carries out a hybrid simulation for a channel flow using a two-equation $k-\epsilon$ RANS model and the Yoshizawa $k-l$ SGS model.

Although the hybrid method has had notable success in terms of accuracy and cost, there is a common problem that no matter which model is used in the two regions (RANS and LES regions), there is a mismatch of the mean velocity between the RANS and LES regions. This means that a shift exists in the mean velocity profile. Another incorrect phenomenon is that non-physical wall streaks can be formed in the RANS region for a channel flow. From Nikitin *et al.*'s study (2000) on a channel flow, DES results show that the position of shift in the mean velocity profile depends more on the grid resolution than the modelling approach.

In DES, the mode switching between RANS and LES takes place when the length scale changes from a RANS one (the distance to the nearest wall) to an LES one (the maximum cell dimension). No special boundary condition is required at the interface of RANS and LES regions. However, for other combinations of RANS and SGS models, physical boundary conditions for some variables must be imposed at the RANS/LES interface to keep consistency between the two different regions. This depends on the model used. In this study, the $k-l$ based RANS/LES of Tucker and Davidson (2003b) is employed. The turbulence length scale is smoothed to avoid a steep drop in it at the interface. In the following, the S-A based DES will be first reviewed. An outline of the $k-l$ based zonal LES will follow.

3.4.1 Detached-eddy Simulation (DES)

From the methodology of hybrid RANS/LES, the time- or ensemble-averaged continuity and Navier-Stokes equations are used in the RANS region. For the LES region, the filtered equations are employed. Here, general governing equations for both RANS and LES modes are written as

$$\frac{\partial \overline{u}_j}{\partial x_j} = 0 \tag{3.86}$$

$$\rho\frac{\partial \overline{u}_i}{\partial t} + \rho\frac{\partial\left(\overline{u}_i\,\overline{u}_j\right)}{\partial x_j} = \rho\delta_{1j}\beta - \frac{\partial \overline{p}}{\partial x_i} + \frac{\partial}{\partial x_j}\left[\left(\mu + \mu_T\right)\frac{\partial \overline{u}_i}{\partial x_j}\right] \tag{3.87}$$

where the parameter β is the constant pressure gradient in the periodic direction (see Patankar *et al.*, 1977). If boundary conditions are not periodic, β=0. In RANS mode, variables with overbar represent the time-averaged ones and $\mu_T = \mu_t$. In LES mode, variables with overbar denote the filtered ones and $\mu_T = \mu_{sgs}$.

In the DES approach, a single equation for a turbulence quantity is used. For the S-A RANS model, d appearing in the destruction term in Eq. (3.17) is the distance to the nearest wall and is called the RANS length scale. d is replaced with $d_{LES} = C_{DES}\Delta$, termed the LES length scale for the LES region. Hence, DES uses two length scales, defined above. The transport equation for the working variable, $\widetilde{\nu}$, is rewritten as

$$\rho\frac{D\widetilde{\nu}}{Dt} = G_\nu + \frac{1}{\sigma_{\widetilde{\nu}}}\left[\frac{\partial}{\partial x_j}\left\{\left(\mu + \rho\widetilde{\nu}\right)\frac{\partial\widetilde{\nu}}{\partial x_j}\right\} + C_{b2}\rho\left(\frac{\partial\widetilde{\nu}}{\partial x_j}\right)^2\right] - C_{w1}\rho f_w\left(\frac{\widetilde{\nu}}{\widetilde{d}}\right)^2 \tag{3.88}$$

where $\widetilde{d}$=min(d_{RANS}, d_{LES})=min($d, C_{DES}\Delta$) in which Δ = max(Δx, Δy, Δz) and the coefficient $C_{DES} = 0.65$ (Shur *et al.*, 1999). Except for the destruction term, the other terms and coefficients are the same as those in the original transport equation given in Eq. (3.17). At walls, $\widetilde{\nu} = 0$.

For a given level of accuracy, the mesh is denser in the near-wall region than in the core region. Generally, the first grid point is always located at $y^+ < 1$. Where $\widetilde{d} = d$ is called RANS region in which the original transport equation holds. A region away from the wall in which $\widetilde{d} = C_{DES}\Delta$ is termed LES region where the Smagorinsky-like model takes effect. When the length scale is switched from d to $C_{DES}\Delta$, the destruction term in Eq. (3.88) is increased, and consequently the the eddy viscosity becomes smaller than its equivalent in RANS.

3.4.2 Hybrid *k-l* based RANS/LES

(1) Governing equations

The transport equation for the modelled turbulent kinetic energy, k, for both RANS and LES modes is expressed as

$$\rho\frac{\partial k}{\partial t} + \rho\frac{\partial}{\partial x_j}\left(\overline{u}_j k\right) = \frac{\partial}{\partial x_j}\left[(\mu + \mu_T)\frac{\partial k}{\partial x_j}\right] + P_k - \epsilon \tag{3.89}$$

where the turbulent production term $P_k = 2\mu_T\overline{S}_{ij}\overline{S}_{ij}$.

Except for different physical meanings for variables in RANS and LES regions, the other differences between the RANS and SGS models lie in the definitions for the dissipation, ϵ, and the turbulent viscosity, μ_T. In the present study, Wolfshtein's (1969) one-equation $k - l$ model is used in the RANS region. Within this model, the formulae for variables are rewritten below for comparison with the SGS model,

$$\epsilon = \frac{k^{\frac{3}{2}}}{l_\epsilon}, \quad \mu_T = \rho c_\mu l_\mu k^{1/2} \tag{3.90}$$

$$l_\epsilon = c_{\epsilon 0}\, y\left(1 - e^{-A_\epsilon y^*/c_\mu^{1/4}}\right), \quad l_\mu = c_{\mu 0}\, y\left(1 - e^{-A_\mu y^*/c_\mu^{1/4}}\right) \tag{3.91}$$

For the other constants see Section 3.2.2. The Yoshizawa SGS $k_{sgs} - l$ model (1993) is employed in the LES region, wherein

$$\epsilon = C_\epsilon \rho \frac{k_{sgs}^{1.5}}{\Delta}, \quad \mu_T = \rho\, C_k \Delta\, k_{sgs}^{1/2} \tag{3.92}$$

where $\Delta = (\Delta x \Delta y \Delta z)^{1/3}$ is the filter width, $C_\epsilon = 1.05$ and $C_k = 0.07$.

(2) Smoothing of length scale

As mentioned before, without very careful grid design, there is discontinuity at the interface between the $k - l$ RANS and LES regions for variables in ZLES with y^+_{int} specified. The underlying reason for this is the drastic change of turbulent viscosity at the interface (see Chapter 6). To smooth this steep change or make variables at two sides of the interface compatible, a specific technique is required. In this work, the simple smoothing method of Tucker and Davidson (2003b) for length scales is followed, rather than damping the turbulent viscosity as pursued by Temmerman *et al.* (2002, 2003). Using a weighted averaging function, a smoothed length scale for one-dimensional flow is computed by

$$l_j^{new} = \frac{l_{j+1}^{old} dy_{j-1} + l_j^{old}(dy_{j+1} + dy_{j-1}) + l_{j-1}^{old} dy_{j+1}}{2(dy_{j+1} + dy_{j-1})} \tag{3.93}$$

where dy denotes grid spacing in the y direction between two nodes among nodes $j - 1$, j and $j + 1$; and the 'new' and 'old' superscripts represent the current and previous iterations respectively. For three-dimensional flows, the values of length scales at 27 nodes are involved.

Unlike DES, determination of the RANS/LES interface for this type of model should be prescribed. In general, the dimensionless wall distance, y^+, is used. How much the optimal value of y^+ at the interface should be set is debatable. Defining the interface within the logarithmic region is reasonable.

This approach is tested in a plain channel flow first and then applied to a complex geometry flow, CPU case.

3.4.3 Heat fluxes modelling

In RANS regions, Eq. (3.48) is used. Eq. (3.83) is employed in LES regions. Because of the use of different values of Pr_t in these two regions, the harmonic mean for Pr_t is used in the discretization of temperature equation at the interfaces between RANS and LES regions.

3.5 Summary

This chapter has described the main properties of turbulence and its modelling techniques, including DNS, LES, zonal LES and RANS. Comparisons between these approaches have also been given. The numerical accuracies and complexities of the four methods decrease successively. However, the computational costs for them also decline in succession. The turbulence models used in the present study in RANS have been reviewed together with the subgrid models employed in LES. In addition, near-wall treatments for RANS and LES have been addressed. Two types of hybrid RANS/LES have been discussed, namely the S-A based DES and $k-l$ based zonal LES. In addition, this chapter has briefly introduced heat flux modelling in RANS and LES.

Chapter 4

Numerical methods

4.1 Introduction

The momentum, energy and transport equations for turbulent quantities are differential and non-linear. As a result, except for very simple idealized cases, it is impossible to obtain analytical solutions for these equations. Instead, numerical solution techniques need to be employed such as finite difference, finite volume and spectral methods. Among these numerical methods, the finite volume method is the most well-established and verified general-purpose CFD technique. The most attractive feature of this method is the underlying physical conservation of quantities such as mass, momentum and energy. The conservation of a general variable ϕ within a finite volume can be expressed as a balance between the various processes.

In this study, the finite volume method is used. The following sections outline this method.

4.2 Finite Volume method (FVM)

The finite volume method consists of three steps, viz. the control volume integration, formation of a system of algebraic equations by means of discretization, and solution of the algebraic equations by an iterative method.

When FVM is applied to discretise differential equations, the computational domain is subdivided into a number of non-overlapping control volumes. In the framework of the structured control volume or cell, there are two possible grid-point arrangements. One is the cell-vertex scheme, in which control volume faces are located midway between the grid points as shown in Fig. 4.1. In this method, fluxes across faces are well approximated. However, the grid point is not at the geometric centre of the control volume for a non-uniform grid. This means that the variable value at a grid point cannot represent adequately the value for the whole control volume. The other arrangement is the cell-centred approach where grid points lie at the centres of the control volumes. The stored value at a grid point can represent the value for the complete cell well, but control-volume-face flux values are not modelled well. If a uniform grid is used, both methods are the same.

There are two types of grids or meshes in terms of variable deployment or placement, namely staggered and collocated grids. For a staggered grid, scalar variables such as pressure (P), temperature (T) and turbulent kinetic energy (k) etc. are defined at the nodes of a control volume, whereas velocity components or variables relevant to velocities are arranged at the scalar cell faces in between the nodes (see Fig. 4.1). With a collocated grid, scalar variables and velocities are defined at the same nodes. Here, in this study, all of the grids used are structured and staggered. Staggered grids are superior for LES, having better conservation properties.

After generating the grid, integration and discretization of differential equations follow. To discuss the discretization methods applied in this study, a transport equation for a general property ϕ is considered, which is written in the Cartesian coordinate system as

$$\underbrace{\frac{\partial(\rho\phi)}{\partial t}}_{\text{Temporal term}} + \underbrace{\frac{\partial(\rho U_i\phi)}{\partial x_i}}_{\text{Convection term}} = \underbrace{\frac{\partial}{\partial x_i}\left(\Gamma_\phi\frac{\partial\phi}{\partial x_i}\right)}_{\text{Diffusion term}} + \underbrace{S_\phi}_{\text{Source term}} \tag{4.1}$$

where Γ_ϕ and S_ϕ are the diffusion coefficient and the source term respectively. The temporal term represents the rate of change at a local point and is zero for steady flows. The integration of Eq. (4.1) over a three-dimensional control volume CV and a finite time step Δt yields

$$\int_{CV}\left(\int_t^{t+\Delta t}\left(\frac{\partial(\rho\phi)}{\partial t}\right)dt\right)dV+\int_t^{t+\Delta t}\left(\int_{CV}\left(\frac{\partial(\rho U_i\phi)}{\partial x_i}\right)dV\right)dt$$
$$=\int_t^{t+\Delta t}\left(\int_{CV}\left(\frac{\partial}{\partial x_i}\left(\Gamma_\phi\frac{\partial\phi}{\partial x_i}\right)\right)dV\right)dt+\int_t^{t+\Delta t}\int_{CV}S_\phi dV dt \tag{4.2}$$

In general, for simplicity the source term is treated as constant. Therefore, there is no need to approximate this term. If the source term is a function of the variable ϕ, it may be approximated in the following linear form

$$\int_{CV}S_\phi dV=S_u+S_p\phi_P \tag{4.3}$$

For spatial and temporal terms, there are several discretization schemes available. Firstly, the numerical schemes used for spatial terms are reviewed, and secondly the temporal schemes. To illustrate the discretisation procedure, a two-dimensional coordinate system is considered. The staggered grid for this is shown in Fig. 4.1. The uppercase letters E, W, N and S denote respectively the East, West, North and South nodes of the central node P (used to store scalar variables). The lowercase letters represent the scalar control volume faces, or the vector variable grid nodes.

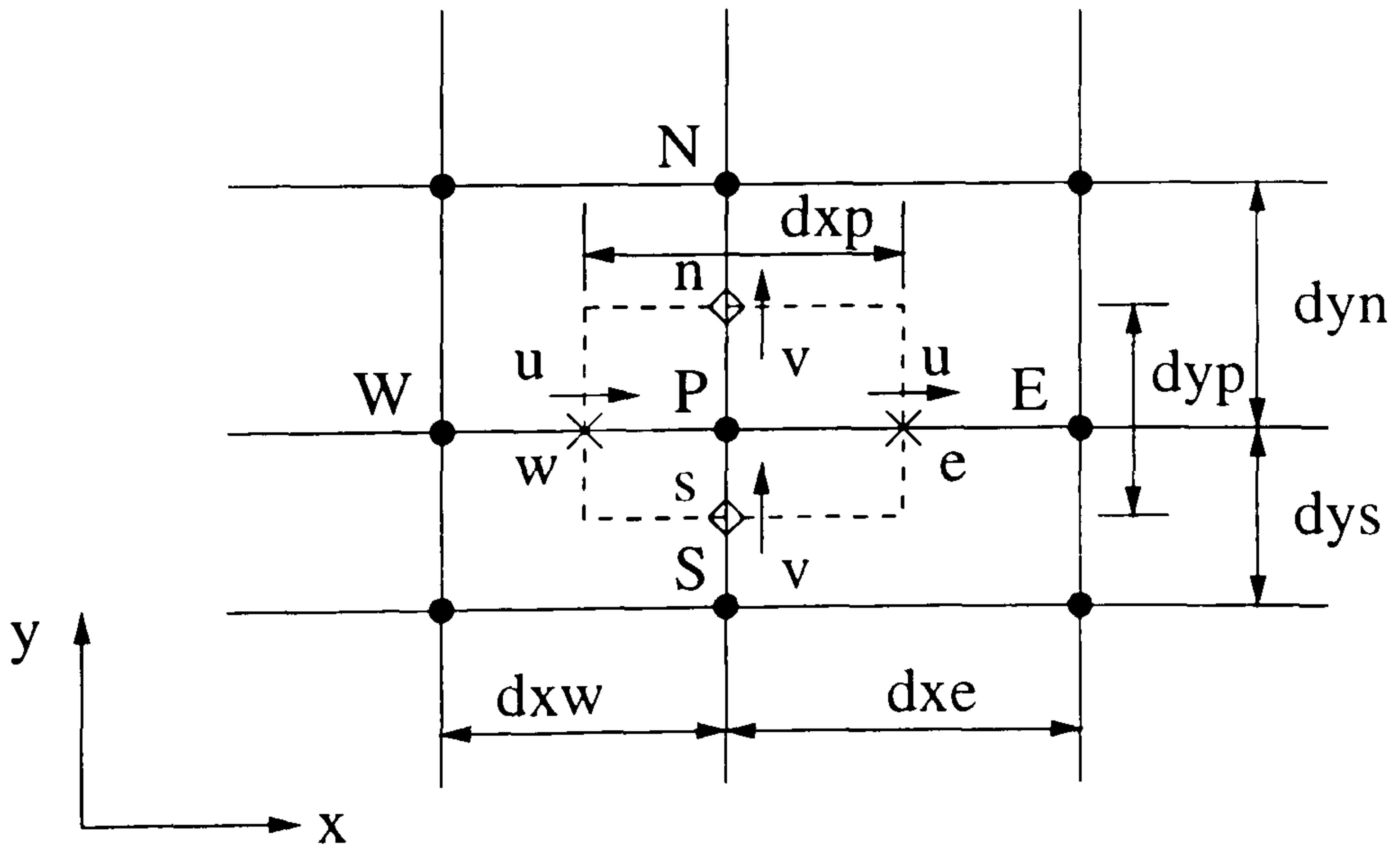

Figure 4.1: Schematic diagram of a staggered grid: circle symbol for scalar variable; x for u velocity; square for v velocity.

4.2.1 Numerical treatment of spatial terms

The common way of calculating gradients for the diffusion terms is the second-order central differencing scheme. Using this, the diffusion term in Eq. (4.2) for two-dimensional problems is discretised as

$$\int_{CV}\left(\frac{\partial}{\partial x_i}\left(\Gamma_\phi\frac{\partial\phi}{\partial x_i}\right)\right)dV=\int_w^e\left(\frac{\partial}{\partial x}\left(\Gamma_\phi\frac{\partial\phi}{\partial x}\right)\right)dydzdx+\int_s^n\left(\frac{\partial}{\partial y}\left(\Gamma_\phi\frac{\partial\phi}{\partial y}\right)\right)dxdzdy$$

$$=(\Gamma_\phi A)_e\frac{\phi_E-\phi_P}{dxe}-(\Gamma_\phi A)_w\frac{\phi_P-\phi_W}{dxw}+(\Gamma_\phi A)_n\frac{\phi_N-\phi_P}{dyn}-(\Gamma_\phi A)_s\frac{\phi_P-\phi_s}{dys}$$

$$=d_e\phi_E+d_w\phi_W+d_n\phi_N+d_s\phi_S-(d_e-d_w+d_n-d_s)\phi_P \qquad (4.4)$$

where $d_e=\frac{(\Gamma_\phi A)_e}{dxe}$, $d_w=\frac{(\Gamma_\phi A)_w}{dxw}$, $d_n=\frac{(\Gamma_\phi A)_n}{dyn}$, and $d_s=\frac{(\Gamma_\phi A)_s}{dys}$ are called diffusion coefficients.

As for treatment of the convective terms, a number of approximation methods can be used, ranging from low- to high-order accuracy schemes. To a large extent, discretisation of these terms determines the accuracy, stability and boundedness of solution. Integrating the x direction convective term over a control volume yields

$$\int_{CV}\left(\frac{\partial(\rho U\phi)}{\partial x}\right)dV=\int_w^e\frac{\partial(\rho U\phi)}{\partial x}dydzdx+\int_s^n\frac{\partial(\rho V\phi)}{\partial y}dydzdx$$

$$=(\rho U\phi A)_e-(\rho U\phi A)_w+(\rho V\phi A)_n-(\rho V\phi A)_s$$

$$=c_e\phi_e-c_w\phi_w+c_n\phi_n-c_s\phi_s \qquad (4.5)$$

where $c_e=(\rho UA)_e$, $c_w=(\rho UA)_w$, $c_n=(\rho VA)_n$ and $c_s=(\rho VA)_s$ are called convective coefficients.

A brief review of the schemes considered in this study is given below.

- **First-order Upwind Differencing Scheme (UDS)**

Upwind schemes of any order can be generated. Values of ϕ at control-volume faces are determined by upstream-biased values that depend on the flow direction. If the flow goes from the west to east (see Fig. 4.1), then for the first-order upwinding $\phi_w=\phi_W$, $\phi_e=\phi_P$,

$\phi_n = \phi_P$, $\phi_s = \phi_S$. This scheme is based on the first-order backward-differencing formula. Hence accuracy is only of the first order. Consequently solutions suffer from extreme false diffusion. This damps flow unsteadiness and thus causes excessive smoothing of variable profiles. Therefore, this scheme is not suitable for RANS or LES.

- **Second-order Central Differencing Scheme (CDS)**

Schemes of any order can be generated. For the second-order scheme, the cell-face values of ϕ are determined as

$$\phi_e = \frac{\phi_P + \phi_E}{2},\ \phi_w = \frac{\phi_P + \phi_W}{2},\ \phi_n = \frac{\phi_P + \phi_N}{2},\ \phi_s = \frac{\phi_P + \phi_S}{2} \qquad (4.6)$$

This approximation is the spatial equivalent of the Crank-Nicholson temporal scheme (see Section 4.2.2). However, the use of this scheme is subject to one condition: the absolute value of cell or grid Peclet number Pe ($=c/d$, i.e. convection coefficient/diffusion coefficient) should be less than 2 to ensure that all coefficients are positive, and thus the solution is stable and accurate. Otherwise, the CDS leads to over- and under-shoots and is unstable.

- **The Hybrid Differencing Scheme (HDS)**

This approach is a combination of the central and upwind differencing schemes. When the absolute value of Peclet number, Pe, at a face is smaller than 2, the centre-difference scheme is employed. Otherwise, the upwind differencing scheme is used. Therefore, the HDS possesses the advantage of second-order accuracy of the CDS, and inherits the shortcoming of high numerical diffusion for large values of grid Peclet number. In reality for practical flows $P_e > 2$ at most grid points. Hence, use of this scheme should generally be avoided. Here its use was restricted to the turbulence transport equations.

- **The COntrolled Numerical Diffusion with Internal Feedback (CONDIF) Scheme**

This scheme is proposed by Runchal (1987). It is a modification of CDS, introducing a controlled amount of numerical diffusion (R_{max}) based on the ratio (R) of the gradients of the variable at adjacent cell faces. If the absolute value of grid Peclet number, P_e, is less than or equal to 2, the original CDS is used. For the case where the absolute value of P_e exceeds 2, the modified CDS is applied if R is positive; otherwise the first-order UDS is used. The parameter R in the x direction is expressed as

$$R = \frac{\phi_E - \phi_P}{\phi_P - \phi_W} \tag{4.7}$$

In the same way, we can calculate the values of R in other directions.

With modification of the CDS, for the west face of a cell (see Fig. 4.1) the coefficient c_w is replaced by

$$\frac{\text{abs}(c_w) + c_w}{4} + R * \frac{\text{abs}(c_e) + c_e}{4} \tag{4.8}$$

For the east face of a cell the coefficient c_e is computed from

$$\frac{\text{abs}(c_e) - c_e}{4} + \frac{\text{abs}(c_w) - c_w}{4 * R} \tag{4.9}$$

Similarly for the south and north faces of a cell c_s and c_n are modified, becoming respectively $(\text{abs}(c_s) + c_s)/4 + R * (\text{abs}(c_n) + c_n)/4$ and $(\text{abs}(c_n) - c_n/4 + (\text{abs}(c_s) - c_s)/(4 * R)$. Consequently, all these coefficients are positive. In the case where R becomes zero or infinity, when ϕ is locally constant such as $\phi_P = \phi_W$ or ϕ_E, a limit on the R is imposed, i.e.

$$1/R_{\text{max}} \leq R \leq R_{\text{max}} \tag{4.10}$$

For practical applications, a reasonable value of R_{max} lies between 4 and 10. In this study, R=5 is chosen.

From the foregoing discussed methodology, it can be seen that this numerical method is essentially a hybrid scheme. But it is more accurate than the HDS because the proportion of CDS used in the whole computational domain is much larger than that in the HDS. If R is large, 90% of solution will be CDS. However, the rate of convergence is generally lower than that for the HDS.

For steady problems, there is no temporal term in Eq. (4.1). Only spatial terms exist. Thus in the steady cases, using any of the schemes mentioned above, after rearrangement, the discretised equation of Eq. (4.1) can be written as

$$a_P\phi_P = \sum a_{nb}\phi_{nb} + S_u \tag{4.11}$$

where nb denotes the neighbouring nodes around the central point P and a_{nb} are the neighbouring coefficients which are combinations of convection and diffusion coefficients. a_{nb} represent

$$a_{nb} = \begin{cases} a_W, a_E & \text{for} \quad \text{1D} \\ a_W, a_E, a_S, a_N & \text{for} \quad \text{2D} \\ a_W, a_E, a_S, a_N, a_F, a_B & \text{for} \quad \text{3D} \end{cases}$$

4.2.2 Numerical schemes for temporal discretisation

For unsteady flows, the temporal term appearing in Eq. (4.1) must be retained in the discretisation process. For time integration, assumptions need to be made about how variables will change with time. The commonly used assumption is expressed mathematically as

$$\frac{1}{\Delta t}\int_t^{t+\Delta t} \phi dt \simeq W\phi^{new} + (1-W)\phi^{old} \tag{4.12}$$

where W is the weighting parameter, ϕ^{new} and ϕ^{old} denote the values at new time level $(t+\Delta t)$ and old time level (t) respectively. Depending on the value of W, there are three widely used schemes viz.

$$W = \begin{cases} 0 & \text{Explicit Scheme} \\ 0.5 & \text{Crank-Nicholson Scheme} \\ 1 & \text{Implicit Scheme} \end{cases}$$

When substituting Eq. (4.12) into Eq. (4.2) and applying any of the differencing methods for spatial terms, we can obtain a discretized equation. Although schemes with $0.5 \leq W \leq 1$ are unconditionally stable for all values of the time step (Δt), including the Crank-Nicholson and implicit schemes, it is more important to ensure that all coefficients are positive for physically realistic and bounded results. To do this, a time-step limitation is necessary for the Crank-Nicholson scheme, as for the explicit scheme. Otherwise, stable solutions cannot be obtained. For the implicit scheme, there is no limitation on the time step because all coefficients are positive and thus the solution is stable. However to ensure the accuracy of results, small time steps are required.

The Crank-Nicholson scheme is second-order accurate in time, whereas the implicit and explicit schemes are both first-order. In this study, only the Crank-Nicholson and implicit schemes are used.

For unsteady flows, by integrating the Eq. (4.1) over a control volume and Δt, and by employing the numerical methods for spatial and temporal terms discussed above, the Eq. (4.1) can now be discretised to become a system of linear algebraic equations. The resulting algebraic equation can be written in the same form as Eq. (4.11). The terms associated with time are incorporated into the coefficients and source term. Therefore, from now on, the Eq. (4.11) form can be considered applicable for both steady and unsteady flows.

4.2.3 Pressure-correction algorithm

The momentum equations couple velocities with pressure. In general, pressure fields are previously unknown in most flows. For incompressible flows, the pressure-velocity linkage can be resolved by adopting an iterative solution strategy. The method used here is the **SIMPLE** (Semi-Implicit Method for Pressure-Linked Equations) algorithm of Patankar and Spalding (see Versteeg and Malalasekera, 1995). The algorithm is essentially a guess-and-correct procedure. The method can be illustrated briefly by considering the u-momentum equation.

The resulting discretised u-momentum equation, omitting the source term, can be written as

$$a_P U_P = \sum a_{nb} U_{nb} + (P_W - P_P) A \tag{4.13}$$

Starting the iteration process with an estimated pressure field, P^*, the estimated velocity component U^* can be obtained from Eq. (4.13) as follows

$$a_P U_P^* = \sum a_{nb} U_{nb}^* + (P_W^* - P_P^*) A \tag{4.14}$$

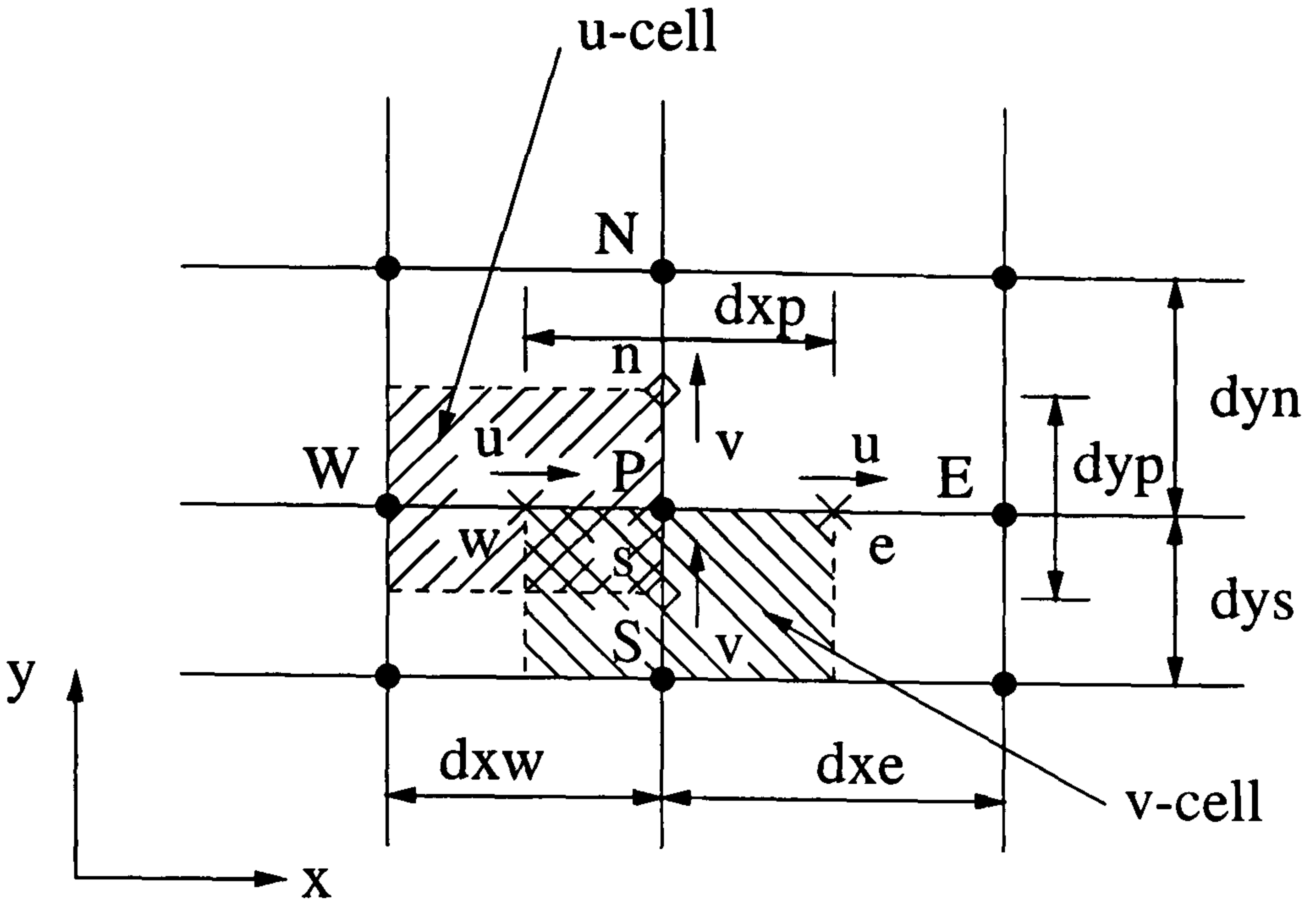

Figure 4.2: Control volumes for u and v.

Subtracting Eq. (4.14) from Eq. (4.13) gives the following velocity-correction equation

$$a_P U'_P = \sum a_{nb} U'_{nb} + \Delta P' A \tag{4.15}$$

For the SIMPLE method, the term, $\sum a_{nb} U'_{nb}$, is neglected. Thus the velocity correction, U'_P, is obtained as

$$U'_P = d_P \Delta P' \tag{4.16}$$

where $d_P = A/a_P$. The correct U velocity is then given by

$$U_P = U^*_P + U'_P = U^*_P + d_P \Delta P' \tag{4.17}$$

Using the same procedure as above for v-velocity in 2D, as well as for v- and w-velocities in 3D, the correct V- and W velocities can be obtained. The obtained velocity field should satisfy the continuity equation (Eq. (3.6)). Substitution of Eq. (4.17) and equations for V and W into Eq. (3.6) yields

$$a_{P,P} P'_P = \sum a_{nb,P} P'_{nb} + S \tag{4.18}$$

where S is the source term. By solving Eq. (4.18), the pressure correction field P' can be obtained at all grid points. The new and improved pressure at the grid point P is then computed as

$$P^{new} = P^{*} + \alpha_P P' \tag{4.19}$$

where α_P $(0 < \alpha_P \leq 1)$ is the pressure under-relaxation factor. The use of α_P helps obtain stable computation. The velocity component is updated using Eq. (4.17).

In practical computations, velocities are also under-relaxed, for example, for u velocity,

$$U^{new} = \alpha_u U^{(n)} + (1 - \alpha_u) U^{(n-1)} \tag{4.20}$$

where α_u $(0 < \alpha_u \leq 1)$ is the u-velocity under-relaxation factor , U^n is the *nth* corrected velocity without relaxation, and $U^{(n-1)}$ represents its value obtained in the previous iteration.

Generally, two kinds of boundary conditions exist for the pressure-correction equation (Eq. (4.18)). Either the pressure at the boundary is given, or the velocity is specified. To avoid errors creeping in either with time (for unsteady cases) or with iteration, a number of sweeps are desirable with the same time step, or inside one iteration. The whole procedure needs to be repeated a sufficient number of iterations until a converged solution is obtained. It might be thought that for this unsteady-flow-based thesis the PISO or fractional-step schemes might be more applicable. However, as can be seen in Tucker and Davidson (2003b) and Chung *et al.* (2003), where a range of pressure schemes are applied to zonal LES and Tollmien-Schlichting wave propagation, SIMPLE is perfectly adequate. This is also noted in Tucker (2001).

4.2.4 Solution of discretised equations

Discretisation of the differential equations governing fluid flow and heat transfer results in a system of linear algebraic equations which have to be solved. Through the use of lagging coefficients, these non-linear equations can be linearized. The methods for solving linear systems can be classified broadly under two categories: direct and iterative methods. Partly, since variables must be lagged, the iterative method is preferable. Except for conventional iterative methods, the multigrid method of Brandt (1972, 1977) is another possible technique. With conventional methods, high-frequency errors are effectively damped, whereas low-frequency errors are poorly damped. With the multigrid method the errors are damped over the whole frequency range in every circle, by means of transferring residuals from the finest to the coarsest grid and back for corrections. Therefore the multigrid algorithm is a more effective method for enhancing convergence rate and for saving computing time. Following Hirsch (1988) and Tucker (2001), the method is briefly outlined below.

- **The multigrid method**

The discretised equation sets can be written as

$$[A_m][\phi_m] = [S_m] \tag{4.21}$$

where $[\phi_m]$, $[A_m]$ and $[S_m]$ denote the solution, equation coefficient and source term matrices respectively. The subscript m indicates the current grid level with m=1 referring to the finest grid. Setting $[\phi_m] = [\phi_m^a] + [\phi_m^c]$ and introducing the residual $[R_m] = [S_m] - [A_m][\phi_m^a]$, Eq. (4.21) can be re-written as

$$[A_m][\phi_m^a + \phi_m^c] = [R_m] + [A_m][\phi_m^a] \tag{4.22}$$

where $[\phi_m^a]$ and $[\phi_m^c]$ represent approximate and correction values to $[\phi_m]$ respectively. For linear problems, Eq. (4.22) can be simplified as

$$[A_m][\phi_m^c] = [R_m] \tag{4.23}$$

On a coarser mesh denoted by m+1, the residual equation is given by

$$[A_{m+1}][\phi_{m+1}^c] = [R_{m+1}] \tag{4.24}$$

where the residual $[R_{m+1}]$ on a coarser mesh is obtained from the residual $[R_m]$ on a finer mesh by means of restriction. Since solutions start from the finest mesh, $[R_{m+1}]$ is then known. According to Eq. (4.24), the correction $[\phi_{m+1}^c]$ on the coarsest mesh can be obtained. The following procedure is to calculate the correction $[\phi_m^c]$ on a finer mesh by interpolating or prolongating. Consequently the improved values of the variable ϕ

on the finest mesh are $[\phi_m] = [\phi_m^a] + [\phi_m^c]$. A converged solution can be obtained after repeating the whole procedure for a number of iterations.

A coarse mesh can be achieved by removing every second line in the different co-ordinate directions. For practical applications, three grid levels are appropriate. However as noted by Tucker (1990) and others, turbulence quantities such as k and ϵ generally show poor multigrid convergence. Therefore for these, m=1 is used. Turbulence values required at $m > 1$ are restricted. For three-dimensional simulations, a 27-point distance weighted averaging is used for scalar variables when transferring residuals from a fine to coarse grid. For staggered variables such as velocities, 18 points are used. When transferring the corrections from a coarse to fine grid, bilinear or linear interpolation can be used.

- **TDMA solver**

For general CFD problems, a popular solver is the Thomas algorithm or Tri-Diagonal Matrix Algorithm (**TDMA**). Whatever the dimensions of the flow considered, each discretised equation can be re-arranged in the following form

$$a_W\phi_{i-1} + a_P\phi_i + a_E\phi_{i+1} = Q_i \tag{4.25}$$

The left hand side of Eq. (4.25) contains only the variable ϕ at its own node (i) and its immediate left (i-1) and right (i+1) neighbours or two other neighbours in other directions. Q_i on the right hand side of Eq. (4.25) represents the sum of the temporarily known source term and the variable values on other nodes. Then the corresponding matrix A, consisting of the coefficients a_W, a_P and a_E, has non-zero terms only on its main and first off-diagonal locations. Such a matrix is called tri-diagonal. This type of system can usually be solved by forward elimination and back-substitution.

In two-dimensional computations, the TDMA method is applied line-by-line on a selected sweep direction (x or y direction). For three-dimensional situations, a line-by-line calculation procedure is applied on a selected plane, and then the calculation is moved to the next plane, until finally the whole domain is computed.

When periodic boundary conditions are employed, the aforementioned standard TDMA needs to be modified. The modified algorithm is called the Cyclic TDMA (CTDMA) (Patankar *et al.*, 1977) which is a special case of Gaussian elimination. The method, along with the TDMA, is given in Appendix A.

To obtain a converged solution, the procedure of iteration is needed. For numerical stability, the Courant-Friedrichs-Lewy or **CFL** condition needs to be satisfied, expressed by

$$0 < C_i = \frac{u_i \Delta t}{\Delta x_i} \leq 1 \tag{4.26}$$

where the subscript i indicates the coordinate, Δx grid spacing, and C is called the Courant number. The restriction implies that a fluid particle should not convect more than one grid cell per time step.

As for convergence criteria, predictions studied here use either normalized residual levels, absolute residual drops or root mean square (*rms*) changes of variables. The absolute residual is defined as

$$R = \sum_{\text{all nodes}} \left| \sum a_{nb}\phi_{nb} + S_u - a_P\phi_p \right| \tag{4.27}$$

If Eq. (4.27) is divided by a correct scaling value, a normalized residual can be obtained. For example, if Eq. (4.27) is divided by a total system inflow momentum, the normalized residual for velocities is achieved.

The normalized root mean square change of the variable ϕ is computed from

$$rms_\phi = \sqrt{\frac{\sum \left(\phi^{new} - \phi^{old}\right)^2}{\sum \left(\phi^{new}\right)^2}} \tag{4.28}$$

where ϕ^{new} and ϕ^{old} represent the values at current and previous iterations respectively. In this study, when rms_ϕ is less than 1 x 10^{-5} and the normalised residuals are less than 1% for most cases (for the CPU case, the normalised residuals are limited to 2%), solutions are converged.

4.3 Calculation of normal wall distances

Some of the turbulence models discussed in Chapter 3 require distances from the nearest walls, d. For simple-geometry flows such as plane-channel flows, it is easy to economically calculate wall-normal distances using search procedures. For complex geometries, this is not that easy. Therefore, Tucker (1998) develops Spalding's (1994) differential-equation method to calculate d. The procedure is as follows. First, a Poisson equation given in Eq. (4.29) is solved. Second, d is calculated using Eq. (4.30).

$$\nabla^2 L = -1 \tag{4.29}$$

$$d = -\sum_{j=1}^{3} \left|\frac{\partial L}{\partial x_j}\right| \pm \sqrt{\left(\sum_{j=1}^{3} \left|\frac{\partial L}{\partial x_j}\right|\right)^2 + 2L} \tag{4.30}$$

At solid walls L=0 and $\partial L/\partial n$=0 where n is the normal direction. Eq. (4.30) has negative and positive roots corresponding to the nearest (d_{min}) and furthest (d_{max}) normal-wall distances. The approximate distance between two surfaces is equal to d_{min} + d_{max}.

In addition, Tucker (2003c) explores two other differential-equation-based methods to achieve wall distances, namely Eikonal and Hamilton-Jacobi. The Eikonal is a direct exact wall-distance equation. It has the following form

$$|\nabla d| = 1 \tag{4.31}$$

Solution of the Eikonal equation is described in Tucker (2003c). A Laplacian scaled by d can be added to the right-hand side of Eq. (4.31). This gives the following Hamilton-Jacobi equation

$$|\nabla d| = 1 + Cd\,\nabla^2 d \tag{4.32}$$

where C is a constant. The Cd function ensures that near walls the Eikonal equation holds, and hence accurate wall distances are recovered. However, the Laplacian also ensures that for sharp convex features d is overestimated, and for sharp concave features it is underestimated. These treatments can lead to superior modeling (see Tucker, 2003c). For example, underestimating d around sharp concave features ensures the added turbulence damping effect of multiple walls is accounted for (see Mompean *et al.*, 1996). Also around sharp convex features such as wires turbulence destruction terms can be excessively active. Overestimating d can alleviate this problem. The Poisson equation naturally provides wall distances that have similar traits to the Hamilton-Jacobi equation.

The above three approaches are tested and compared with each other in computations for a 3D square duct flow. This is intended to explore the sharp-concave-feature aspect noted above, i.e. the duct corners form concave surfaces. For all other cases presented in this thesis, the Poisson equation method is used.

4.4 Summary

This chapter has discussed the commonly used FVM. It has outlined basic discretisation algorithms for convective and diffusion terms and for temporal terms applied in this study. For diffusion terms, the CDS is always used without exception. The UDS, CDS, HDS and CONDIF schemes for convective terms have been discussed together with three algorithms for temporal discretizations including the explicit, Crank-Nicholson and implicit. For stability reasons, just the latter two are used here. To solve coupled velocity and pressure, the SIMPLE method has been chosen. This procedure has been outlined and explained.

The multigrid algorithm has been introduced in addition to conventional iterative methods. An outline has been given of the solution method used here for systems of algebraic equations (standard TDMA or the CTDMA depending on boundary conditions considered).

Three differential-equation-based wall-distance computation methods have been reviewed. Solutions from the three equations differ from each other. The Eikonal equation gives exact wall distances. However, the Poisson and Hamilton-Jacobi equations are able to account for the damping effect of multiple walls and excessive turbulence destruction caused by sharp convex features.

Chapter 5

Heat transfer experimental setup and procedure

5.1 Introduction

This chapter will describe the experimental apparatus used. In the study, two approaches to measure temperatures are applied. One is the use of surface thermocouples, which will be referred to as Experiment 1. The other method is the application of infrared thermography. This will be described as Experiment 2. When using the infrared imaging system, in order to enhance radiation the surface to be investigated is painted black. Importantly, as part of this chapter, the uncertainty in temperature and Nusselt number is addressed.

A brief description of the experimental rig and the calculation of convective heat flux will be given in Section 5.2. Section 5.3 describes the procedures for Experiment 1 and presents the data and their uncertainty. The principle of the infrared thermography and procedures for Experiment 2 will be explained in Section 5.4. Also in Section 5.4, the experimental data and the factors that affect the accuracy of temperature measurement are given.

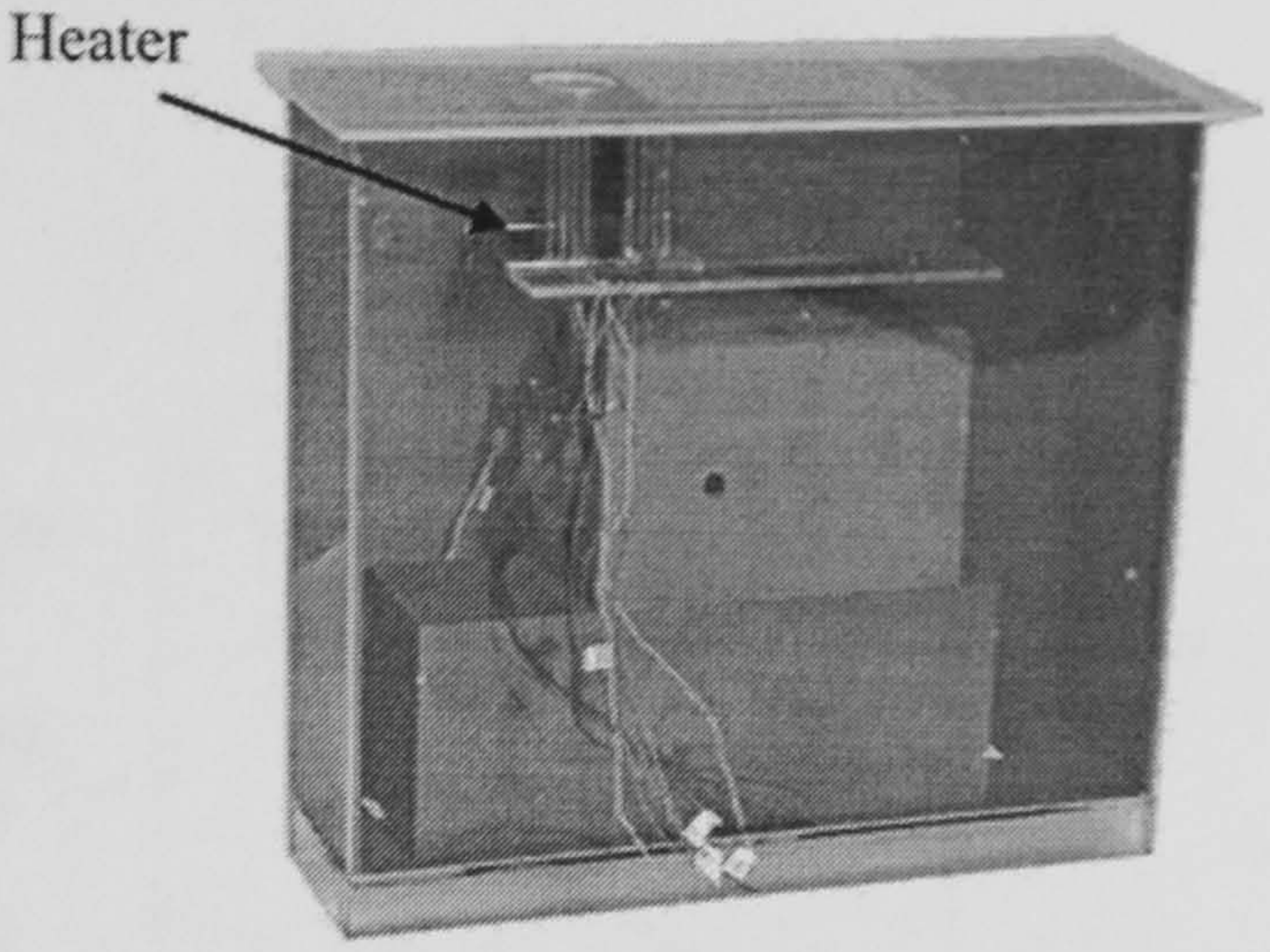

Figure 5.1: Electronics system with a heater.

5.2 Experimental rig and convective heat flux calculation

The idealized electronics system shown in Fig. 5.1 (Fig. 5.2 is a physical model for it) is investigated. In order to simulate the thermal condition generated by printed circuit boards, a stainless steel (Fe/Cr18/Ni10) foil heater is mounted on a horizontal surface (see Fig. 5.2). The heater element is 120 mm × 112 mm × 0.025 mm in width (b), length (l) and thickness (h), respectively. To obtain a uniform direct current distribution, and hence a constant heat flux boundary condition, two brass semi-cylinders of 12 mm diameter are used. The foil heater and the brass bars are clamped together by screws at two ends. Fig. 5.3 shows this setup.

In order to accurately measure heat flux, two approaches are used: direct heat flux measurement, and theoretical calculation.

A RdF Micro-Foil heat flux sensor is employed to directly measure the heat flux. This sensor is a differential thermocouple-type sensor. As shown in Fig. 5.4, it utilizes a thin-foil-type thermopile bonded to both sides of a known thermal barrier. The difference in temperature across the thermal barrier is proportional to heat flow through the sensor. The material of the barrier is Kapton polyimide which has a nominal emissivity of 0.7. The sensor attached to the surface of the foil heater using Kapton tape is approximately 20 mm long, 25 mm wide and 0.3 mm thick. A millivoltmeter is used to read the signal

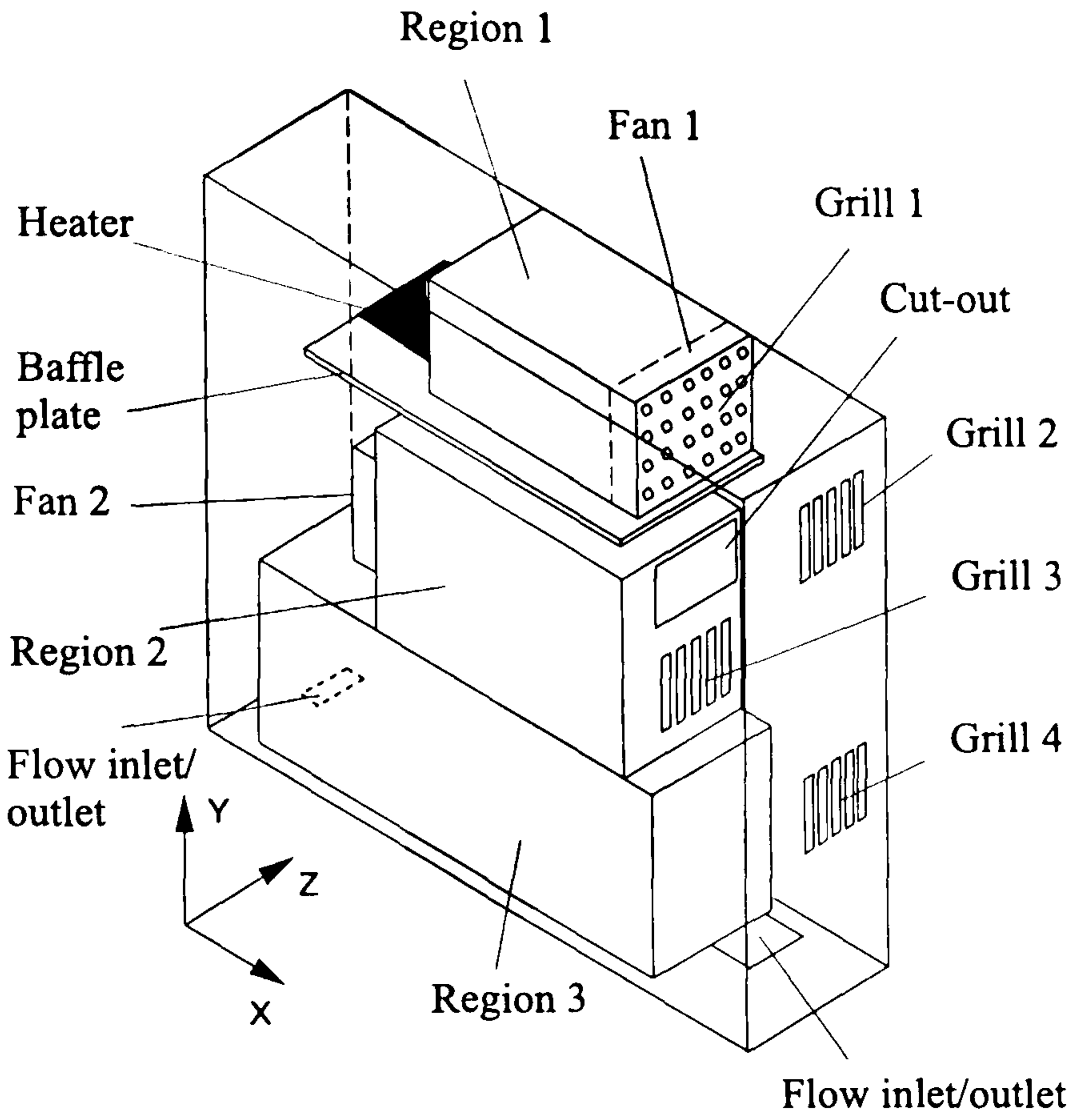

Figure 5.2: Physical model for the electronics system.

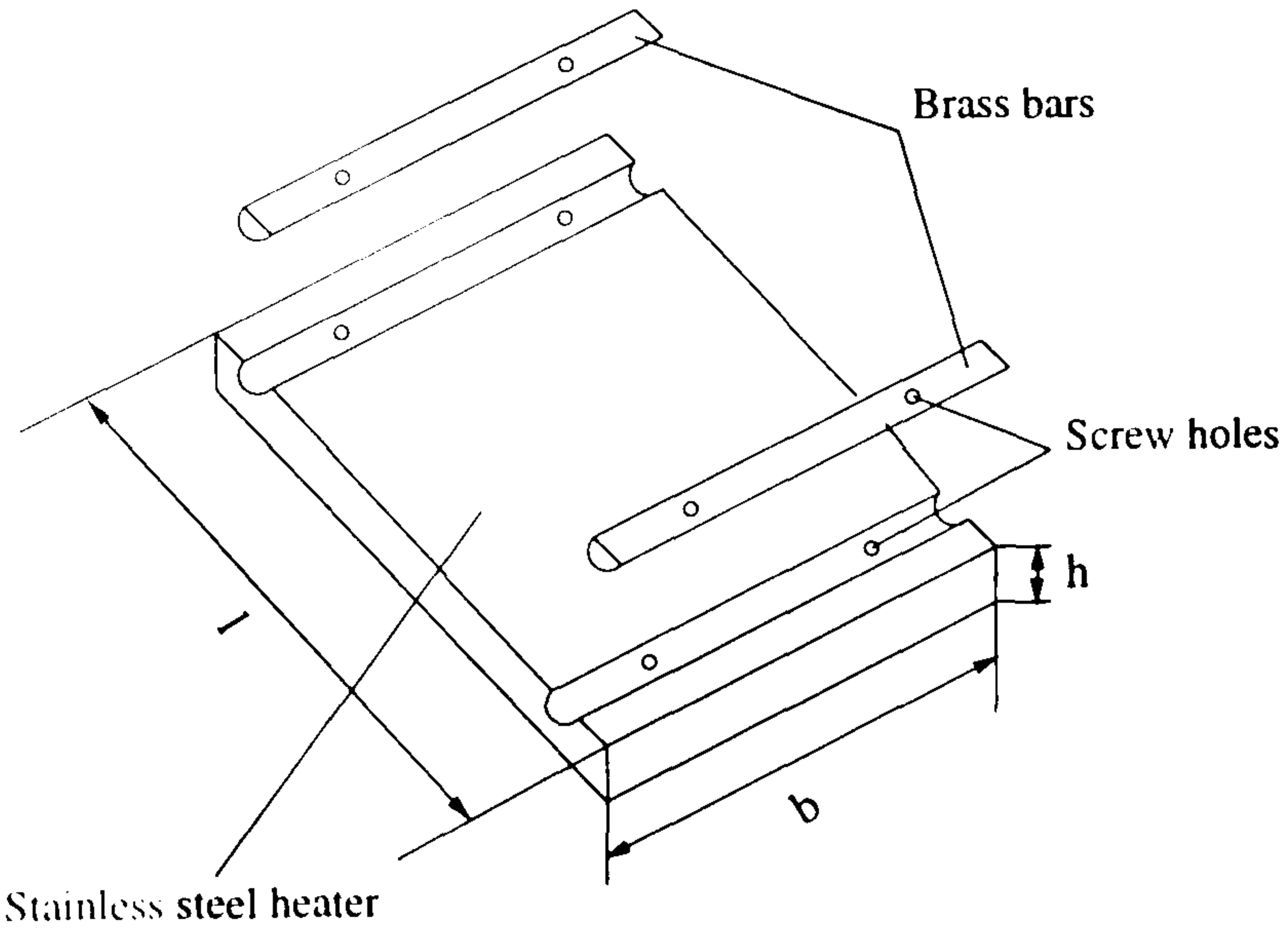

Figure 5.3: Heater assembly diagram.

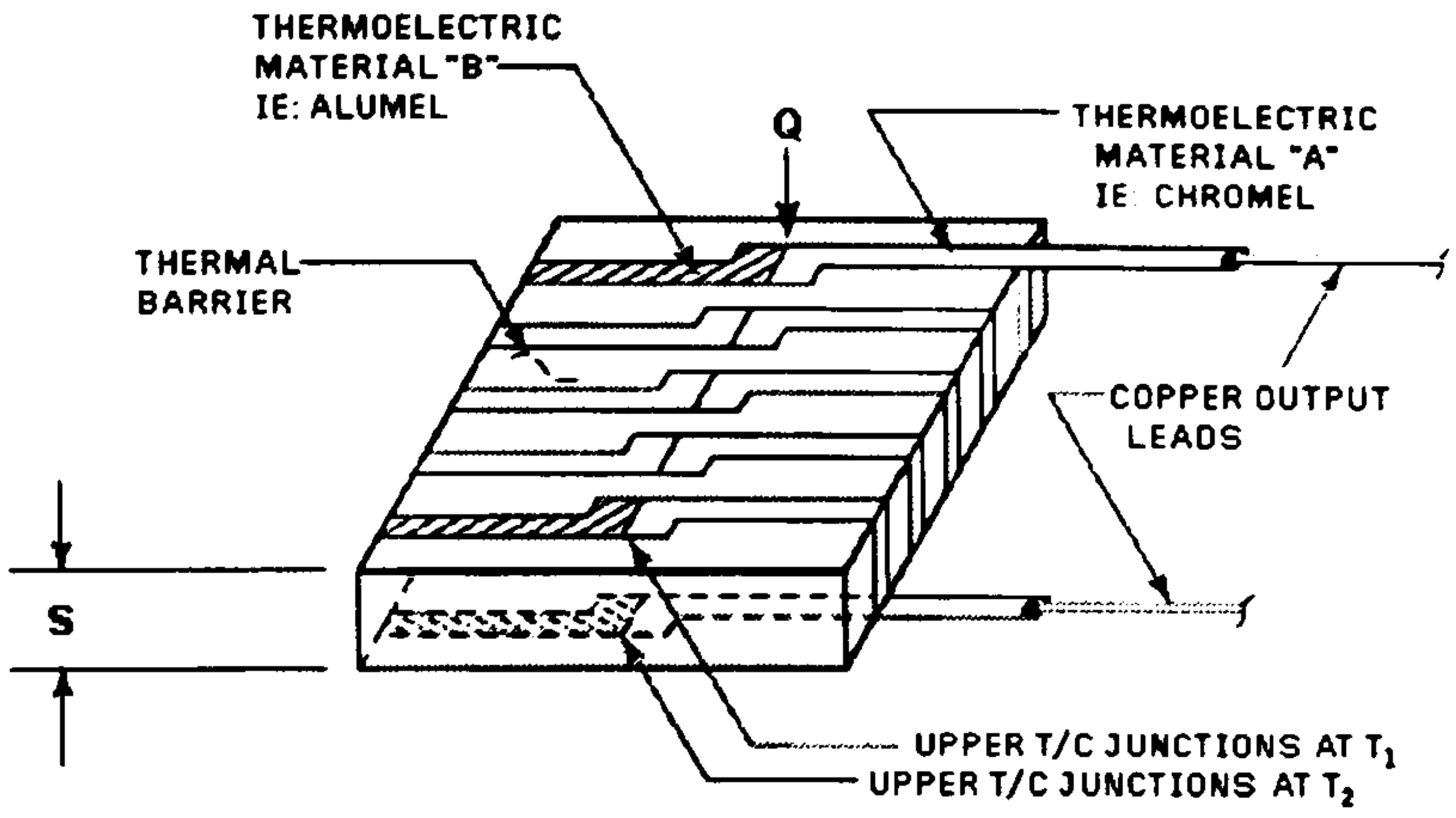

Figure 5.4: Heater flux sensor from RdF Corporation.

output from the sensor.

The total local heat flux, q_{tot1}, from the fluxmeter consists of the local convective and radiative heat fluxes. q_{tot1} is determined by the following formula

$$q_{tot1} = V/(\mu_q C) \tag{5.1}$$

where V is the output voltage from the heat flux sensor, C=1.1065 μV/(W/m^2) is a coefficient calibrated at 21°C and μ_q the temperature modification factor. The local convective heat flux, q_{conv1}, is expressed as

$$q_{conv1} = q_{tot1} - q_{rad1} \tag{5.2}$$

where q_{rad1} is the local radiative heat flux which is determined by

$$q_{rad1} = \frac{\sigma(T_s^4 - T_{up}^4)}{\frac{1}{\varepsilon_s} + \frac{1}{\varepsilon_{up}} - 1} \tag{5.3}$$

where σ, T_s and T_{up} represent the Stefan-Boltzmann constant (5.67× 10^{-9}), the sensor surface and top cover temperatures, respectively (see Fig. 5.5). ε_s and ε_{up} are emissivities of the sensor and top cover (perspex) respectively.

In theory, the electric heat flux generation, q_{tot2}, of the heater element can be determined by means of its resistance and heating current (I). The local convective heat flux then can be arrived at by subtracting conduction of the baffle plate, q_{cond2} , and the radiation, q_{rad2}, heat losses from q_{tot2}, i.e.

$$q_{conv2} = q_{tot2} - q_{cond2} - q_{rad2} \tag{5.4}$$

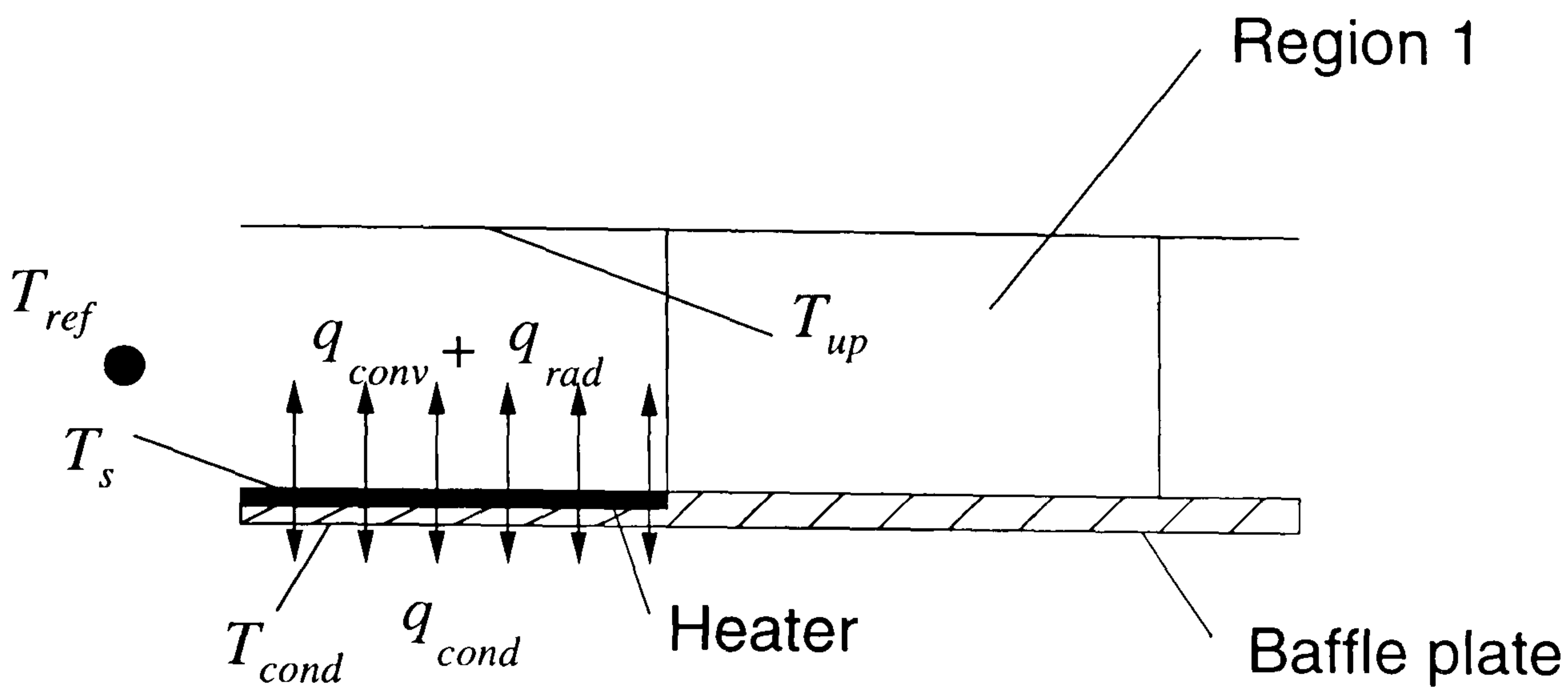

Figure 5.5: Diagram of variables defined.

where

$$q_{tot2} = I^2 R \frac{l}{bh} / bl, \quad q_{cond2} = k\frac{dT}{dh} = k\frac{T_s - T_{cond}}{h} \tag{5.5}$$

in which R is the electrical resistivity of stainless steel, k and h are the conductivity and thickness of the baffle plate made from perspex respectively. The formulation for q_{rad2} is the same as Eq. (5.3) with ε_s being the emissivity of polished stainless steel. The positions for T_s, T_{cond}, T_{up} and other variables are illustrated in Fig. 5.5.

When calculating the radiative heat loss, the averaged surface temperature, $T_{up,ave}$, over the bottom wall of the upper perspex cover will be used. The convective heat flux, q_{conv2}, will be used, with q_{conv1} as a reference.

5.3 Experiment 1 – measurement using thermocouples

5.3.1 Experimental procedure

Eight RdF surface chromel-alumel thermocouples are attached to the underside of the foil heater (since the foil is thin, hence the underside temperatures can accurately represent upper-surface values) by means of tape. Five thermocouples are put in the x direction at even intervals, labelled as TX1, TX2, TX3, TX4 and TX5 as shown in Fig. 5.6. The

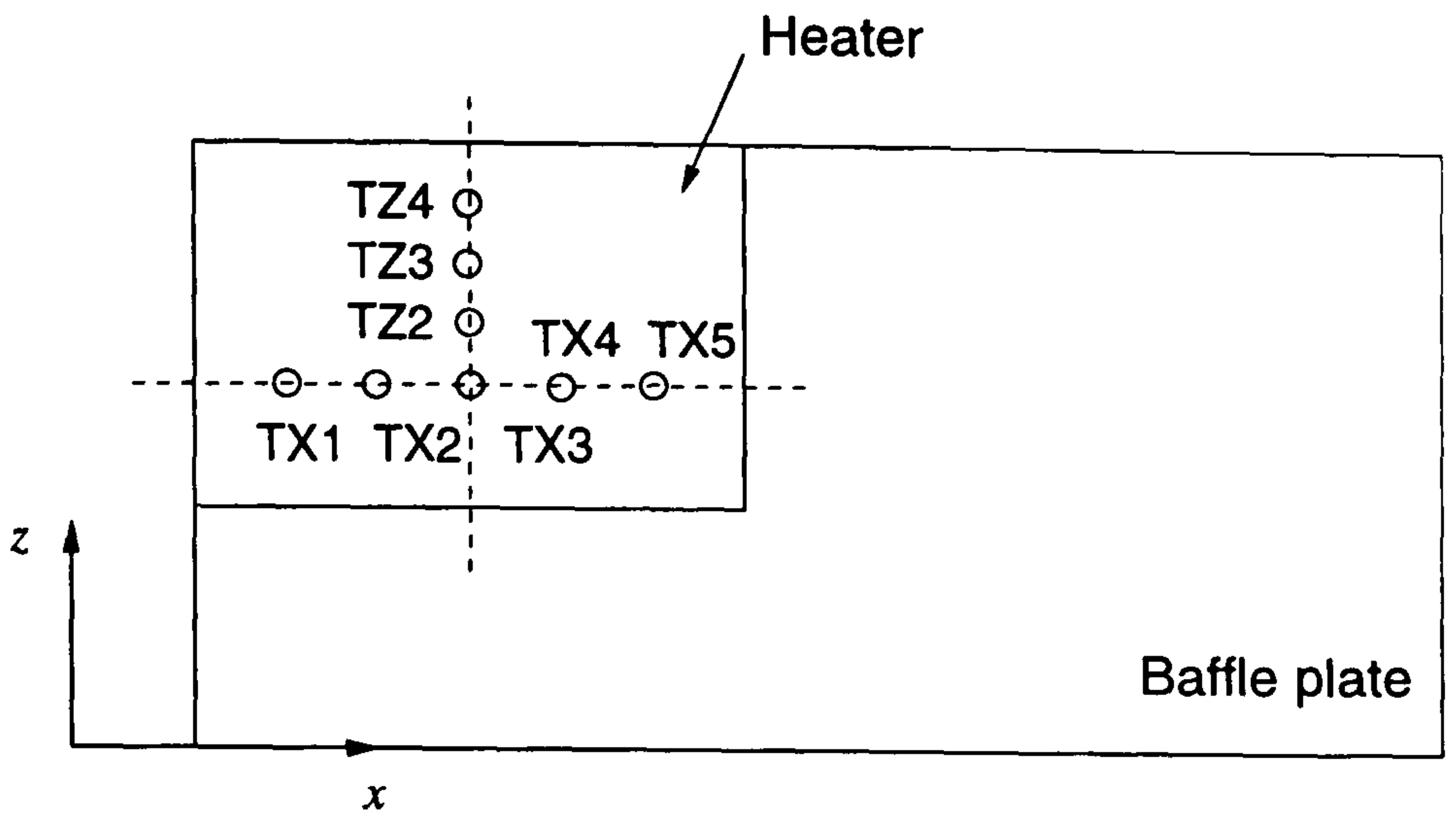

Figure 5.6: Positions of thermocouples (not to scale).

remaining three thermocouples are in the z direction and are denoted by TZ2, TZ3 and TZ4 (see Fig. 5.6). The positions of these are given in Table 5.1. Each of the 12.7 μm thick foil sensors is embedded in a thin laminate of glass-reinforced polymer which is 20 mm long and 10 mm wide. The foil sensors can eliminate the effect of the heating current on the sensors.

At a reference point chosen in the upstream of the baffle plate, the temperature is measured by a stainless-steel thermocouple probe named T_{ref} (see Fig. 5.5). The position of the reference point is 0.07 m, 0.57 m and 0.12 m in the x, y and z directions respectively. The thermocouple measuring T_{cond} is adjacent to location TX3. The position of T_{cond} is also given in Table 5.1.

The measurement system thus comprises a heater, thermocouples, a heat fluxmeter, a power supply, a millivoltmeter and data-acquisition system with eight input channels.

Before the final experiment can be done, it is very important to check whether the electrical distribution in the stainless-steel heater is uniform. By observing readings from the data-acquisition system (before coating with black paint), and from thermal images obtained from JADE camera (after coating with black paint) (see section 5.4), at the commencement of heating, the temperature is almost the same over the whole surface of heater. As heating progresses, the temperature changes at the surface owing to natural convection and conduction of surrounding material. Thus the heating effect can be regarded as uniform. According to data provided by the manufacturer, the accuracy

Table 5.1: Thermocouple positions.

Thermocouple		x (m)	y (m)	z (m)
Thermocouple in the x direction	TX1	0.165	0.5	0.12
	TX2	0.185	0.5	0.12
	TX3	0.205	0.5	0.12
	TX4	0.225	0.5	0.12
	TX5	0.245	0.5	0.12
Thermocouple in the z direction	TZ1 =TX3	0.205	0.5	0.12
	TZ2	0.205	0.5	0.14
	TZ3	0.205	0.5	0.16
	TZ4	0.205	0.5	0.18
Thermocouple at the reference point	T_{ref}	0.07	0.57	0.12
Thermocouple at the under side of the plate	T_{cond}	0.205	0.492	0.12

of the thermocouples is expected to be ±0.5%.

The experimental procedure is summarized below:

(1) Switch on power for the heater and fans; set the supply current for the heater to I=12.6 A;

(2) Leave the whole system running until the quasi-steady state is reached (this process takes around one hour). When the data displayed on the monitor have stabilized, the data from both the data logger and thermometer are regarded as the final experimental temperature data;

(3) Record the data from T_{ref}, T_{cond} and voltmeter connected to the heat fluxmeter.

5.3.2 Experimental data and calculation of Nu

(1) Calculation of the convective heat flux

The physical properties of the perspex of the baffle plate and the stainless steel are presented in Table 5.2 together with the heat flux results. q_{tot2}, q_{cond2} and q_{conv2} are obtained from Eq. (5.5) and Eq. (5.4) respectively. Temperature measurements are

Table 5.2: Physical properties of perspex and stainless steel and calculation results.

Thermal conductivity of perspex	k=0.1875 J/kg· k
Emissivity of polished stainless steel	ε=0.17
Emissivity of perspex	ε=0.8
Electrical resistivity of stainless steel	R=71 $\mu\Omega$· cm
Heating current for the foil heater	I=12.6 A
Total heat flux of the heater, q_{tot2}	313 W/m^2
Conduction of the baffle plate, q_{cond2}	84.4 W/m^2
Radiation of the heater, q_{rad2}	10.1 W/m^2
Convective heat flux , q_{conv2}	218.5 W/m^2

given in Table 5.3.

The reference, convective heat flux, q_{conv1}, obtained from the heat flux meter is calculated as follows. The output voltage of the meter is 0.28 mV. The temperature modification factor, μ_q=0.983 is obtained from a modification chart provided by the manufacturer. Substitution of V and μ_q into Eq. (5.1) gives q_{conv1}=254.4 W/m^2. According to Eq. (5.3), q_{rad1}=39.2 W/m^2 (where the emissivity of the Kapton tape is 0.7). Thus

$$q_{conv1} = q_{tot1} - q_{rad1} = 218\,\mathrm{W/m^2} \tag{5.6}$$

Comparing q_{conv1} and q_{conv2}, it can be found that q_{conv2} calculated from electric heat generation and q_{conv1} from the heat flux sensor are almost equal. The uncertainty of the heat flux sensor can almost be treated as the uncertainty of the convective heat flux, i.e. 3 %. In the following calculations, the convective heat flux, q_{conv2}, is used.

(2) Calculation of Nusselt number

The local Nusselt number based on the hydraulic diameter of the geometry is defined as

$$Nu = D_h \frac{q_{conv}}{T_s - T_{ref}} \frac{1}{k} \tag{5.7}$$

where D_h is the hydraulic diameter of the geometry shown in Fig. 5.1 and T_s is the surface temperature at a measured location. D_h is calculated from $D_h = 4y_{max}z_{max}/(2(y_{max} +$

Table 5.3: Temperature measurements and Nu results.

Location	Temperature(°C)	Nu_x
Ambient temperature, T_{amb}	21.5	–
TX1	33.7	248.2
TX2	32.7	275.1
TX3	31.9	301.3
TX4	31.2	328.7
TX5	30.8	346.8
TZ1	31.9	301.3
TZ2	32.2	291.0
TZ3	33.6	250.6
TZ4	34.4	232.2
T_{ref}	23.5	–
T_{cond}	28.3	–
$T_{up,ave}$	23.0	–
Average surface temperature of the heater, $T_{s,ave}$	32.6	–
Average Nu_{ave}	–	284.2

z_{max})) (D_h=0.3048 m). The conductivity of air at ambient temperature is k=0.02637 W/m·K. The resulting local Nusselt numbers at the eight measured locations shown in Fig. 5.5 are summarized in Table 5.3.

When using local coordinate values instead of D_h, Nu_x is expressed as

$$Nu_x = X\frac{q_{conv}}{T_s - T_{ref}}\frac{1}{k} \tag{5.8}$$

In Eq. (5.8), $X = x - x_0$, which is a reference coordinate value, x representing the x-coordinate values of the measured points, and x_0 the x-coordinate value of the starting point of the heater. The resulting Nu_x in the x direction is presented in Table 5.4 and shown in Fig. 5.7.

Table 5.4: Local Nusselt number results.

Location	TX1	TX2	TX3	TX4	TX5
Nu_x	16.3	36.1	59.3	86.2	113.7

Table 5.5: Accuracy of equipment

System component	Relative accuracy	Absolute error
Data acquisition and thermocouples	±1%	±0.2°C
Heater flux sensor	±3%	$\pm$ 6.54 W/m^2

(3) Uncertainty analysis

Table 5.5 presents relative accuracy and absolute errors for the equipment used. Hence, uncertainty of temperature and heat flux measurement is $\delta T=\pm 0.2$°C and $\delta q_{conv}=\pm 6.54$ W/m^2.

For Nu, uncertainty can be calculated as follows (Moffat, 1988): by differentiating Eq. (5.7), the following can be obtained

$$(\delta Nu)^2 = \left(\frac{\partial Nu}{\partial T_s}\delta T_s\right)^2 + \left(\frac{\partial Nu}{\partial T_{ref}}\delta T_{ref}\right)^2 + \left(\frac{\partial Nu}{\partial q_{conv}}\delta q_{conv}\right)^2 \tag{5.9}$$

where

$$\frac{\partial Nu}{\partial T_s} = -\frac{D_h q_{conv}}{k}\frac{1}{(T_s - T_{ref})^2} \tag{5.10}$$

$$\frac{\partial Nu}{\partial T_{ref}} = \frac{D_h q_{conv}}{k}\frac{1}{(T_s - T_{ref})^2} \tag{5.11}$$

$$\frac{\partial Nu}{\partial q_{conv}} = -\frac{D_h}{k}\frac{1}{T_s - T_{ref}} \tag{5.12}$$

Substituting the data for all variables into Eq. (5.9), δNu can be obtained, i.e. $\delta Nu=\pm 13$. Thus the relative accuracy is

$$\delta Nu/Nu_{ave} = \pm 5\% \tag{5.13}$$

5.4 Experiment 2 – measurement using the infrared imaging system

Owing to the limited space and the dimensions of the thermocouple, it is impracticable to mount many thermocouples on the foil heater. Therefore, the full thermal field on the surface of the heater cannot be obtained. Even for a specific line, the points measured are sparse. In order to make up for these drawbacks, infrared thermography is applied.

The principle of infrared thermography is based on the theory of heat radiation, i.e. the radiative energy emitted by a body is a function of the body's temperature. The radiation wavelengths at low temperatures up to 500-600°C lie deep in the infrared region (0.75$\sim$1000 μm). As the temperature of a body increases, the energy of infrared radiation at all wavelengths will also increase. By detecting this heat radiation, the temperature of the body will be known.

Infrared non-intrusive measurements provide large contiguous sets of surface-temperature data. These are useful for comparison with simulations.

The infrared system used here is the JADE thermography system from the CEDIP company. The JADE infrared imaging system operates in midwave (MWIR 3 $\sim$ 5 μm). This means that the measurement of radiation is made in the wavelength band of 3 $\sim$ 5 μm. The system uses focal plane array (FPA) technologies and uncooled microbolometers. It consists of an infrared lens, a detector, a beam splitter, an imaging lens, an imaging plane and processing unit as shown in Fig. 5.8. The lens material is sapphire. The focal length of the lens is 50 mm. The image frame is of 128 × 128 pixels. Because the heater is located in the flow, a special window that can transmit infrared radiation is required. The optical material of the window is calcium fluoride (CaF_2). The window provided by Cystran Ltd is 70 mm in diameter and 3 mm in thickness. As can be seen from Fig. 5.9, a 3 mm thick window has a transmissivity of approximate 95% in the midwave range.

A new upper cover with a hole cut is fitted with the CaF_2 window. Fig. 5.10 shows the positions of the infrared camera and CaF_2 window. Before making measurements,

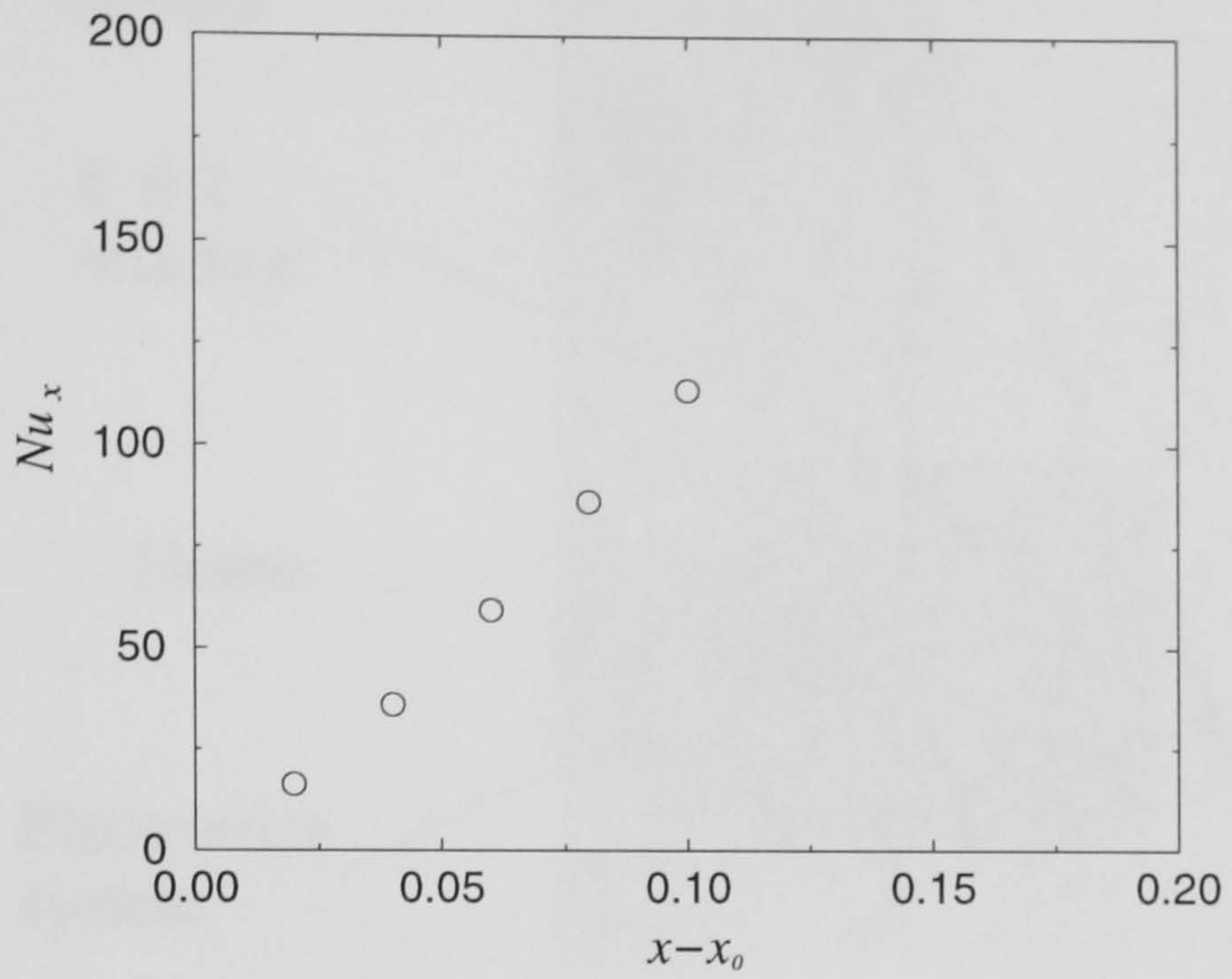

Figure 5.7: Local Nu_x distribution.

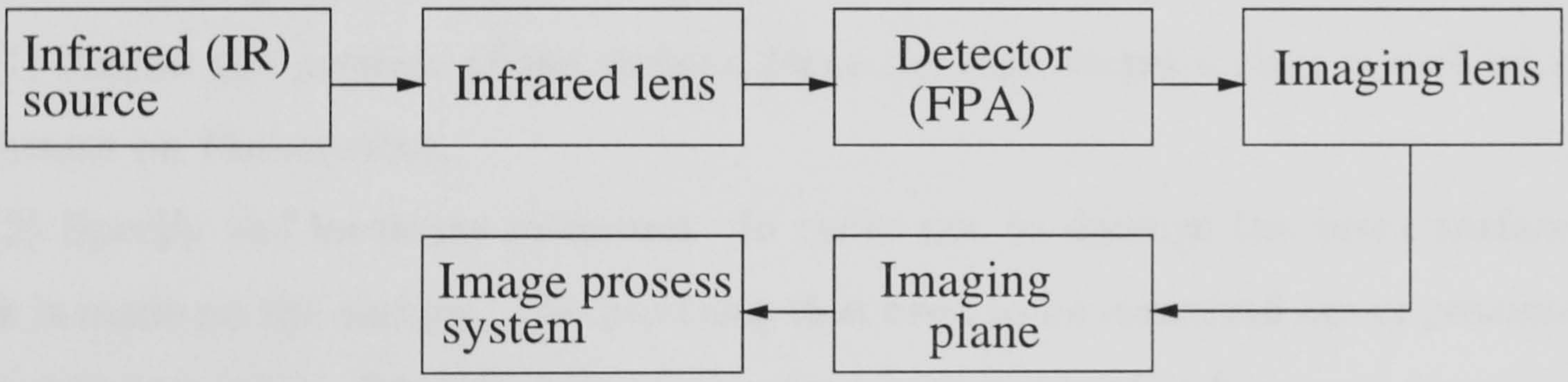

Figure 5.8: Block diagram of infrared imaging system.

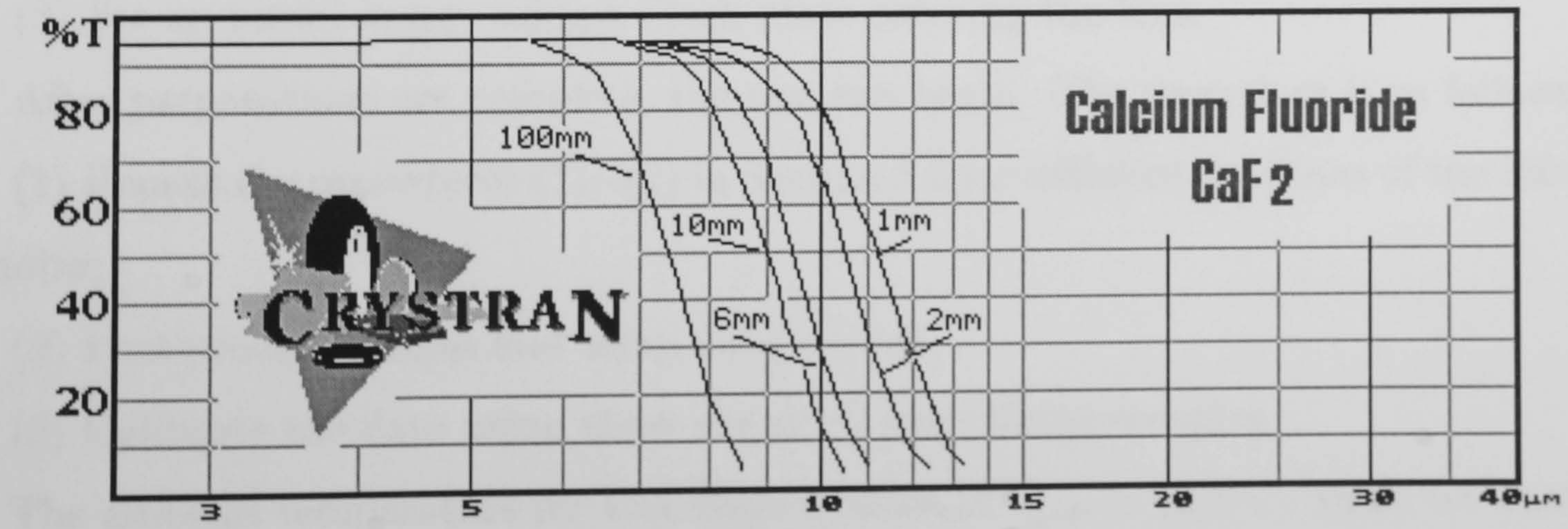

Figure 5.9: CaF_2 transmission range.

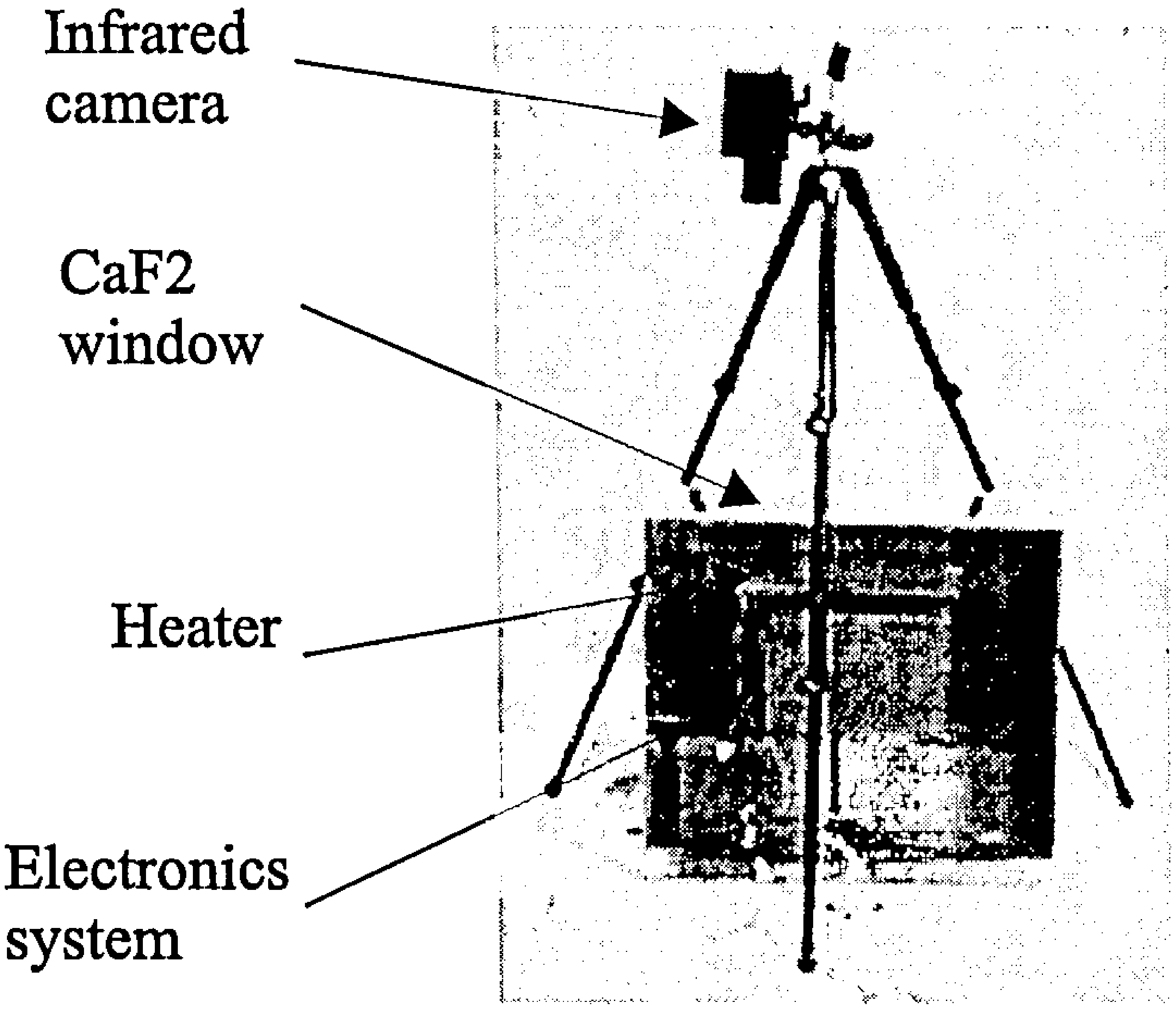

Figure 5.10: Arrangement of the infrared camera and CaF_2 window.

the following preparations had to be made.

(1) Adjust the position of the camera, focus the lens, to get a clear overall image of the heater on the monitor;

(2) Specify the locations measured. In order not to damage the black surface, no mark is made on the surface. The positions that need to be measured are approximately defined by two rulers. The pixels for particular locations are then known on the monitor. Once the monitored positions are established, the camera position cannot be changed. Otherwise, the positions for the monitored points on the image will be changed;

(3) Set an initial image using a black plate covering the lens.

After preparations are complete, the test can begin. The procedure is as follows:

(1) Repeat the procedures (1)∼(2) in Section 5.3 for different positions of the infrared window;

(2) Post-process images and temperature plots;

(3) Calibrate the data using those obtained from thermocouples.

The ambient temperature for this measurement is $T_{amb} = 20.2°C$. Table 5.6 summarizes the experimental data.

It can be seen from Table 5.6 that the temperature measurements from the camera

Table 5.6: Temperature data.

Location	Temperature reading from thermocouple(°C)	Temperature reading from IR camera(°C)
TX1	30.9	28.7
TX2	30.3	28.3
TX3	29.8	27.6
TX4	29.2	27.1
TX5	28.8	27.1
TZ1	29.8	27.9
TZ2	29.5	27.7
TZ3	30.5	28.7
TZ4	32.5	30.7

are lower than those obtained from the thermocouples. The factors which degrade the signal for the infrared camera and cause temperature difference are as follows:

(a) During transmission of the radiation in atmosphere, two phenomena occur, which are:

- Thermal gradients and turbulence created inhomogeneities;
- Absorption of radiation by gas or by water molecules present in the air.

(b) Surface emission, i.e. emissivity of the object, not being a perfect black body;

(c) Image degradation caused by the optical system (for example, defocussing of the object measured);

(d) Use of an optical window, which can drop the temperature of the transmitted light by around 1°C.

By comparing the IR data with the thermocouple data, final results for the IR data should consider the average temperature difference of 1.8°C. It should be mentioned that owing to the black paint on the surface of the heater, radiation from it is increased, and convective heat flux is reduced, for the same heating current. Therefore, the temperature data from the thermocouples in Table 5.6 are lower than those in Table 5.3.

In this measurement, the CaF_2 window used is small and cannot cover the whole heater. Therefore, the whole thermal field image over the heater cannot be obtained in one go. Also it is difficult to correctly measure T_{up} (temperature on the bottom side of the upper cover) owing to the CaF_2 window being on the upper cover. Thus T_{up} is not measured. Hence q_{conv} cannot then be calculated. However, the obtained temperature distribution on the surface of the heater is very useful to justify whether the temperature pattern obtained from the thermocouples is correct. By comparison, the temperature profiles obtained from the thermocouples (Experiment 1) are almost the same as those from the infrared camera at the locations studied.

For comparison between simulations and measurements, the experimental data presented in Table 5.3 will be used. The data in Table 5.6 are treated as a reference.

5.5 Summary

Two temperature-measurement approaches, namely thermocouple and infrared imaging systems have been discussed in this chapter. The experimental setup and procedures have been outlined. Convective heat flux calculated from theory is consistent with that from the heat flux meter. The temperature distributions over the surface of the heater obtained from the thermocouples are almost the same as those from the infrared camera after modification. The temperature and local Nu data obtained from the thermocouples for the heater without black paint have been presented and will be used, while the data from the infrared camera are treated as a reference. The uncertainty of Nu is around $\pm 5\%$.

Chapter 6

Turbulence model validation cases

6.1 Introduction

The basic program used in this study is the in-house NEAT code (Tucker, 2000) code. Using this code as a basis, new turbulence models outlined in Chapter 3 have been added. These include the Spalart-Allmaras (1994) model (S-A), low-Reynolds-number versions of the two-equation $k - \epsilon$ (CH, LS and LS + Yap (LSY) defined in Chapter 3), the Craft *et al.* (1993) nonlinear two-equation cubic model (Cubic), and the Gatski and Speziale (1993) explicit algebraic stress model (EASM). In addition, zonal or two-layer models are also investigated. For zonal models, the one-equation $k - l$ model is used in the near-wall regions, and the high-Reynolds-number model EASM, or other model, is applied in the regions away from the wall. Out of interest, the high-Reynolds-number version of the original cubic model is tested, i.e. the standard $k - \epsilon$ model, coupled with the cubic form of the Reynolds stresses. This combination is denoted by HCubic. To validate the modified program, and to assess performance of various turbulence models employed here, benchmark test cases are required. For (U)RANS, four cases are selected. These are two-dimensional fully-developed channel, backward-facing step and ribbed-duct flows. In addition, a square-duct flow is examined. For LES and ZLES predictions, a three-dimensional fully-developed channel flow is used.

This chapter will describe details of the test cases and present the results obtained

Table 6.1: Flow parameters for plain channel flow.

Re_c	32000
L x H x W	4 x 0.0635 x 1 m^3
U_{in}	1/7 power law, i.e. $U = U_{max}(y/h)^{1/7}$
T_{in}, T_w	300K , 310K
k_{in}	$k = 1.5(U_{ref}T_i)^2$, $U_{ref} = U_b$, $T_i = 5\%$
ϵ_{in}	$\epsilon = C_\mu^{3/4} k_{in}^{1.5}/l$, $l = 0.07H$

from (U)RANS, LES and hybrid RANS/LES approaches.

6.2 (U)RANS validation

6.2.1 Fully-developed channel flow

- **Case description**

The flow parameters are summarized in Table 6.1. The Reynolds number, Re_c, is based on the channel half height, h, and centreline velocity, U_{max}. If based on the hydraulic diameter (D_h) and bulk mean velocity (U_b), the Reynolds number $Re_{D_h} = 105000$. The experimental data of Laufer (1954) are used.

To ensure independence of inlet conditions, the channel is sufficiently long compared with its height (here $L/H = 63$). Inlet boundary conditions are also shown in Table 6.1. At the outlet, a zero-gradient, differential boundary condition is applied for all variables except for axial velocity. The outlet velocity is computed to conserve mass flow rate. For heat transfer predictions, a constant wall temperature is used. For this flow, only low-Reynolds-number models are tested. The grid used is 151 × 111 (x, y) with uniform distribution in the x direction and non-uniform in the y direction. Solutions are grid independent.

The predicted friction coefficient, C_f, is defined as

$$C_f = \frac{\tau_w}{\frac{1}{2}\rho U_b^2} \tag{6.1}$$

The dimensionless temperature, T^+, and Nu are defined respectively by

$$T^+ = \frac{\rho C_p (T_w - T) u_\tau}{q_w}, \quad Nu = \frac{D_h}{T_w - T_b} \frac{\partial T}{\partial y} \tag{6.2}$$

where u_τ is the friction velocity and q_w the wall heat flux.

The chosen Nu correlation for comparison is the Dittus-Boelter (1930), given by

$$Nu = 0.023 Re_{D_h}^{0.8} Pr^{0.4} \tag{6.3}$$

The dimensionless temperature correlation is computed by the Kader (1981) expression:

$$T^+ = Pr\, y^+ e^{-\Gamma} + \left\{ 2.12 \ln \left[(1 + y^+) \frac{1.5(2 - \frac{y}{h})}{1 + 2(1 - \frac{y}{h})^2} \right] + \beta(Pr) \right\} e^{-\frac{1}{\Gamma}} \tag{6.4}$$

where

$$\Gamma = \frac{10^{-2} (Pr y^+)^4}{1 + 5 Pr^3 y^+}, \quad \beta(Pr) = \left(3.85 Pr^{1/3} - 1.3\right)^2 + 2.12 \ln Pr \tag{6.5}$$

- **Results and discussion**

Table 6.2 presents the predicted wall shear stress, τ_w, friction coefficient, C_f, and the Nusselt number, Nu, together with the experimental data of C_f and correlation data of Nu (where errors in C_f and Nu are computed by $(C_{f,exp} - C_{f,num})/C_{f,exp} \times 100\%$ and $(Nu_{corre} - Nu_{num})/Nu_{corre} \times 100\%$ respectively). For comparison, the $k - l$ and zonal $k - l/k - \epsilon$ models are included. In Table 6.2, EASM-1 and EASM-2 are low Reynolds number versions of the original high-Reynolds-number EASM form. In the EASM-1, Abid *et al.*'s (1995) damping function is used. Abe *et al.*'s (1994) (AKN) damping functions are employed in the EASM-2. For zonal models, the interface between the $k - l$ and extended model is determined at $y^+ = 60$.

From the table, it can be observed that most of the models tested underpredict C_f and N_u, while the S-A model overpredicts C_f and N_u . Both the EASM-1 and EASM-2 give lower errors than other models for both C_f and Nu. The $k - l$ model gives the lowest values of C_f and Nu. The $k - l/k - \epsilon$ model predicts the same values of C_f and Nu as the $k - l$/HCubic model. The results from the LS with Yap correction (LSY)

Table 6.2: Wall shear stress, friction coefficient and Nusselt number results

Model	τ_w	C_f	Error in C_f	Nu	Error in Nu
Experimental data	0.5449	0.00491	-	-	-
Correlation	-	-	-	207.4	-
CH	0.5031	0.00453	-7.7	195.5	-5.7
$k-l$	0.4850	0.00437	-10.9	184.7	-10.9
LS	0.4949	0.00446	-9.2	194.2	-6.4
LSY	0.4950	0.00446	-9.2	194.6	-6.2
S-A	0.5743	0.00517	5.3	226.5	9.2
Cubic	0.5060	0.00456	-7.1	199.5	-3.8
EASM-1	0.5224	0.00471	-4.1	202.8	-2.2
EASM-2	0.5420	0.00488	-0.6	209.2	0.9
$k-l$/HCubic	0.5050	0.00455	-7.3	196.9	-5.1
$k-l$/EASM	0.4870	0.00439	-10.6	195.9	-5.5
$k-l/k-\epsilon$	0.5048	0.00455	-7.3	196.9	-5.1

are almost the same as those from LS without correction (this result differs from that of Heyerichs and Pollard (1996), where C_f obtained from LSY is larger than that from LS). This verifies that Yap correction does not take effect for plain channel flow without separation.

Fig. 6.1 compares velocity distributions near the wall for linear and nonlinear models. It can be seen clearly that the $k-l$ profile deviates from the log law in the core region. Overall, the predicted velocity profiles from all models are in good agreement with the measurements of Laufer (1954). The dimensionless temperature profiles are shown in Fig. 6.2. Except that there is a little undershoot in the log law region for EASM-1 and EASM-2 models, and same rise in the $k-l$ profile in the core region, the profiles generally match the correlation data well. The velocity and temperature profiles for the $k-l/k-\epsilon$ model are virtually the same as the $k-l$/HCubic model and hence are not shown.

Fig. 6.3 compares the normalized streamwise velocity fluctuations, u', for the linear

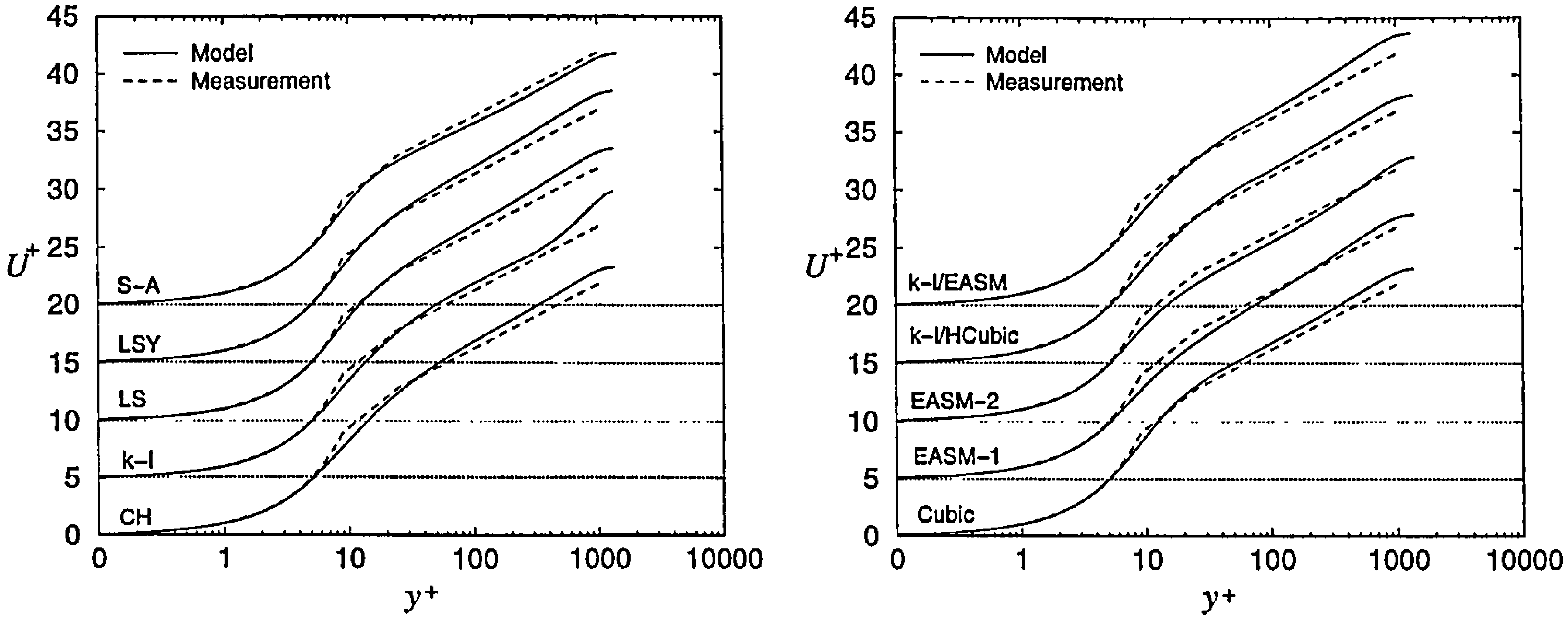

Figure 6.1: Velocity distributions for the linear (left) and nonlinear (right) models.

and nonlinear models. Fluctuations in the spanwise (w') and wall-normal (v') directions are shown in Fig. 6.4. In Figs. 6.3-5, $C = U_{max}$. The three components are calculated from

$$u' = \left(\frac{-\tau_{xx}}{\rho}\right)^{1/2}, \quad v' = \left(\frac{-\tau_{yy}}{\rho}\right)^{1/2}, \quad w' = \left(\frac{-\tau_{zz}}{\rho}\right)^{1/2} \tag{6.6}$$

where $\tau_{xx} = -\rho\overline{u'u'}$, $\tau_{yy} = -\rho\overline{v'v'}$ and $\tau_{zz} = -\rho\overline{w'w'}$.

From the left figure in Fig. 6.3, the CH gives better predictions than the LS and $k-l$ models for u'. Compared with the LS and $k-l$, as demonstrated in Fig. 6.4 all nonlinear models improve u' predictions. As is well known, linear models based on k cannot distinguish between the three normal Reynolds stresses and hence $u' = v' = w'$. However nonlinear models are capable of predicting individual normal Reynolds stress. Fig. 6.5 compares the predicted v' and w' profiles from different nonlinear models with experimental data. It can be noted from the right-hand figure in Fig. 6.4 that the zonal $k-l$ models show kinks in the u' and v' profiles (ZLES also shows a similar kink as presented in Section 6.4.2). This is because of discontinuity in the variables caused by different models at the interface. Although the models investigated demonstrate a separation between the normal stress components, the difference is not as large as that found in the experimental data (see Fig. 6.4), particularly in the near-wall region. Also,

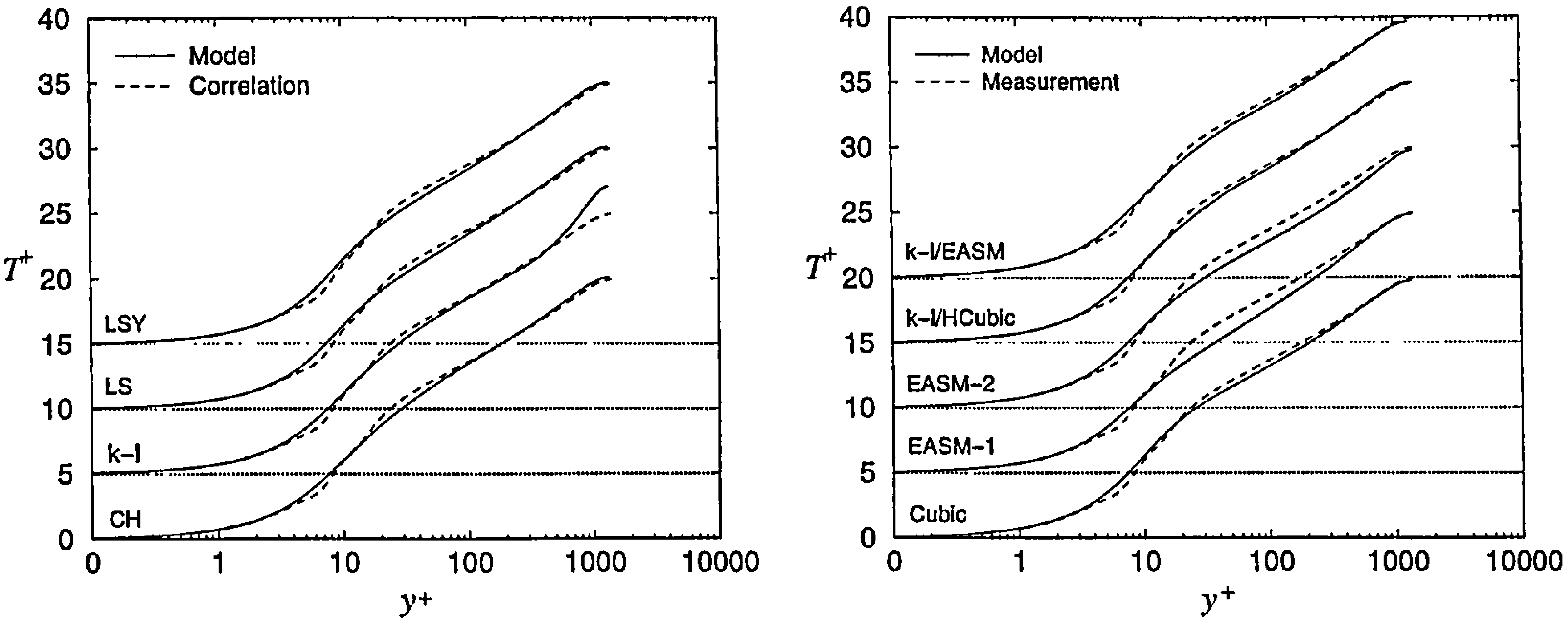

Figure 6.2: Temperature distributions for the linear (left) and nonlinear (right) models.

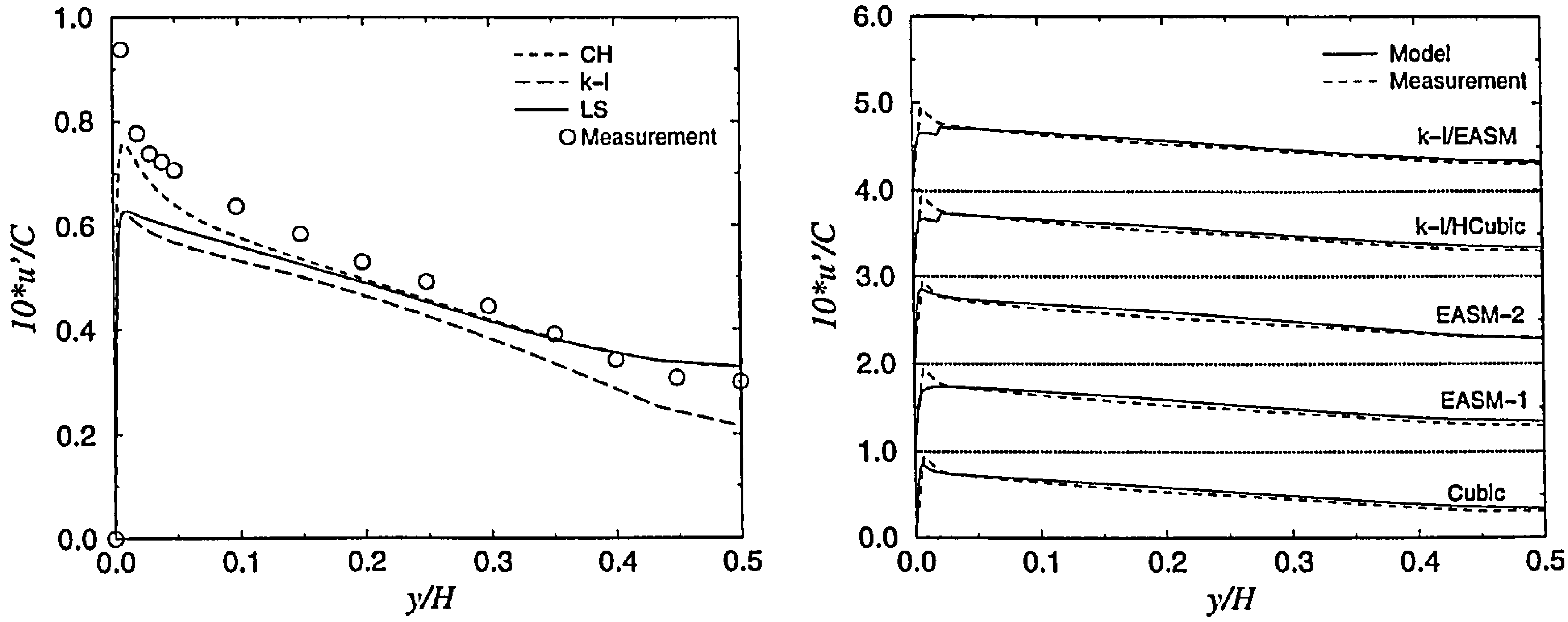

Figure 6.3: Normalized streamwise velocity fluctuation distributions for the linear (left) and nonlinear (right) models.

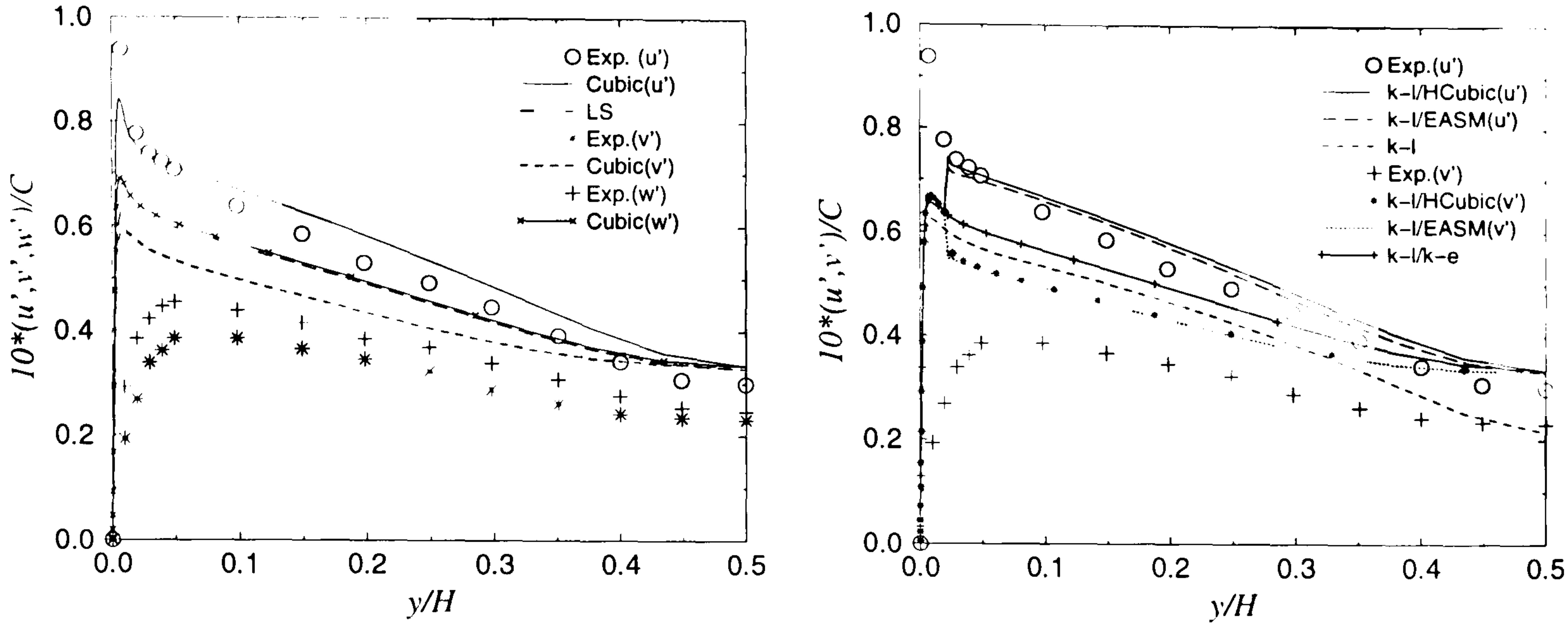

Figure 6.4: Comparison of normalized u', v' ad w' distributions for the LS and Cubic models (left); u' and v' for the zonal models (right).

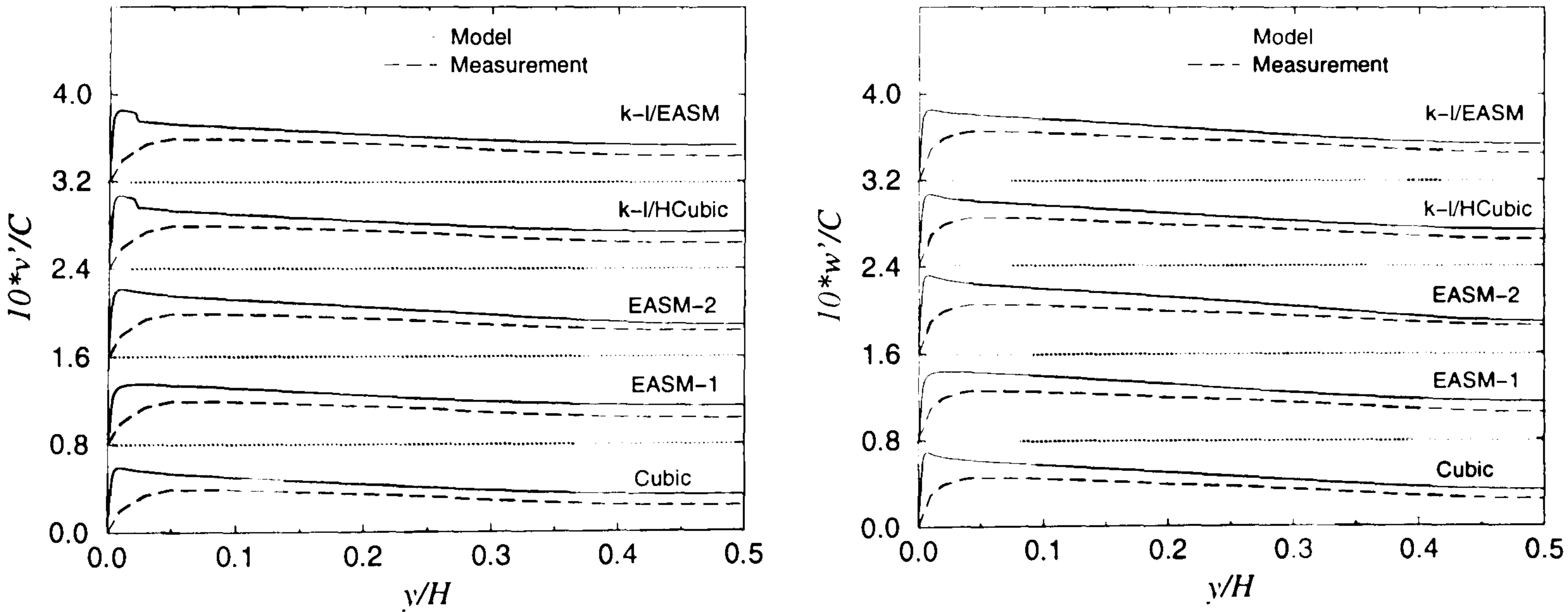

Figure 6.5: Normalized velocity fluctuation distributions in the y (left) and z (right) directions for the nonlinear models.

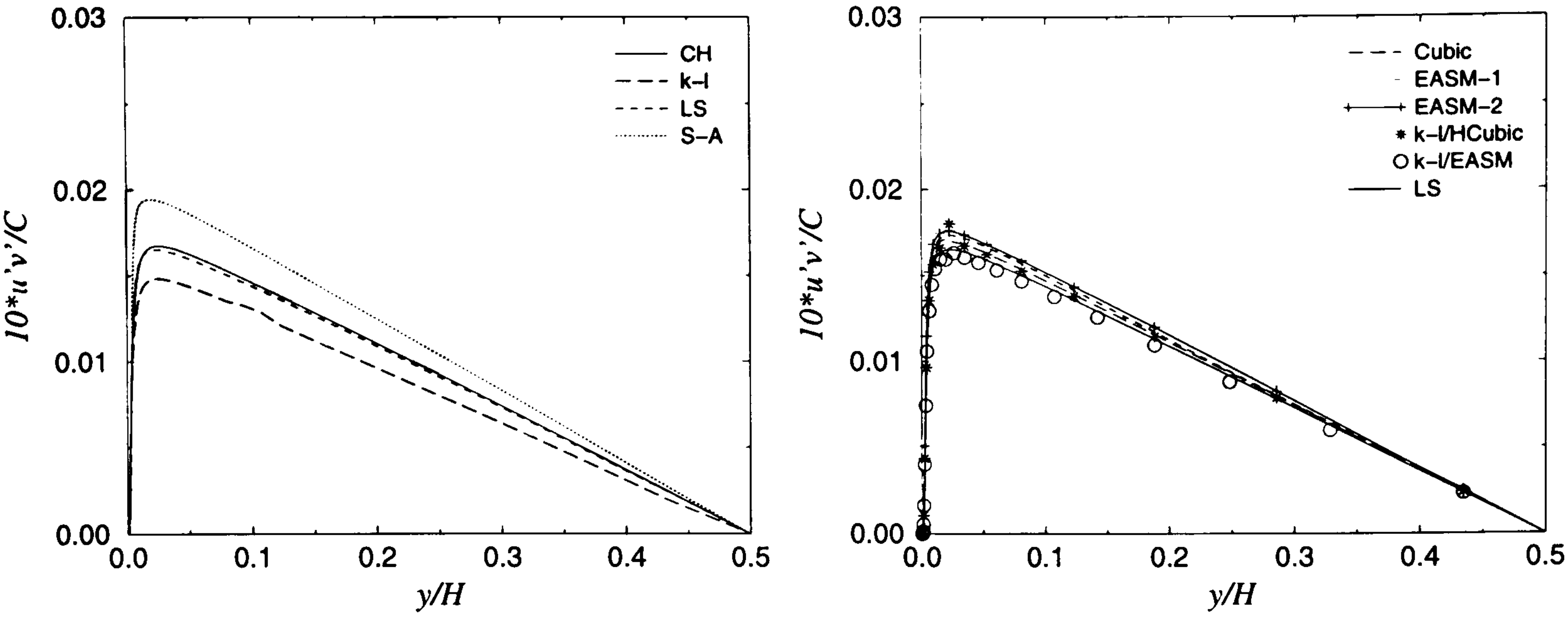

Figure 6.6: Normalized shear stress distributions for the linear (left) and nonlinear (right) models.

the nonlinear models still overpredict v' and w'. Nevertheless, as argued by Craft *et al.* (1993), it is the shear stress that governs mean flow behaviour in the near-wall region. Therefore, the above deficiency is not a big problem. To illustrate the difference of performance between the LS and Cubic models, and between the $k-l$ and zonal models, variations of u' and v' along the channel cross-section are shown separately in Fig. 6.4. As can be observed, the linear zonal $k-l/k-\epsilon$ model improves u' prediction compared with the $k-l$ model, but the nonlinear zonal $k-l$/HCubic and $k-l$/EASM models predict a higher peak value of u' than the $k-l/k-\epsilon$.

Fig. 6.6 presents the shear stress results, where $C = \rho U_{max}^2$. As can be seen, the CH and LS models give similar predictions. The S-A model predicts the highest shear stress, and $k-l$ the lowest. The nolinear models predict slightly higher values of $\overline{u'v'}$ than those from the LS and CH models except for the $k-l$/EASM model. The zonal $k-l/k-\epsilon$ gives a similar distribution of $\overline{u'v'}$ to the $k-l$/HCubic model.

From the results presented above for channel flow, it appears, as expected, that the nonlinear models of cubic model, EASM-1, EASM-2, $k-l$/HCubic and $k-l$/EASM perform better than the linear models for the flow and thermal field in terms of C_f and Nu.

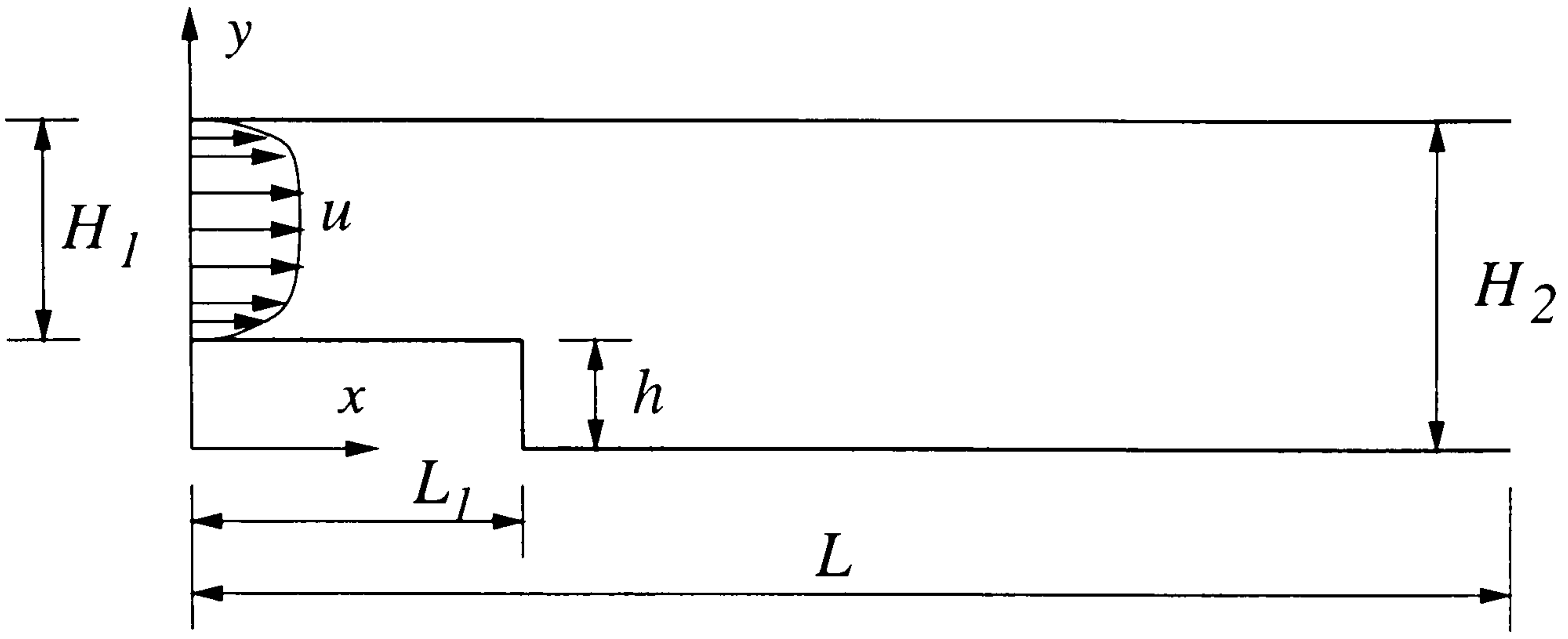

Figure 6.7: Schematic of backward-facing step flow.

Table 6.3: Simulation data for the backward-facing step flow.

Re	132000
H_2/H_1(expansion ratio)	3:2
h(step height)	0.0381 m
L/L_1	1.3025 m/0.3048 m
U_{in}	1/8 power law for near wall region and uniform distribution for core region
k_{in}	$k = 1.5(U_{ref}T_i)^2$, $U_{ref} = U_c$, $T_i = 10\%$
ϵ_{in}	$\epsilon = C_\mu^{3/4}k_{in}^{1.5}/l$, $l = 0.07h$

6.2.2 Backward-facing step flow

- **Case description**

As discussed in the paper by Speziale and Ngo (1988), the flow over a backward-facing step is a primary benchmark for assessing the performance of turbulence models for prediction of separated flows. This case is therefore selected for the validation of the models used in this study. The geometry investigated, shown in Fig. 6.7, is the same as that used by Speziale and Ngo (1988). The simulation data are summarized in Table 6.3. Re is based on H_2 and inlet centreline velocity, U_c.

- **Results and discussion**

A grid-independence study was conducted. For high-Reynolds-number models, three sets of coarse grids: 140 × 40, 202 × 60 and 202 × 80 were tested. Owing to the use of the wall functions, y^+ at first off-wall nodes have to be larger than 11.5 except in the recirculation region. Predictions of velocity profiles obtained from the standard $k - \epsilon$ model at two locations are shown in Fig. 6.8. It can be seen that solutions from the 202 × 60 grid are virtually grid-independent. For low-Reynolds-number models, computations are performed using three grids: 139 × 92, 173 × 160 and 203 × 196. No big difference is found between the results from the last two grids in the case of all the models. It should be pointed out that the grids used are non-uniformly distributed in both the x and y directions. Results from both the 202 × 80 and 203 × 196 grids are used and presented below.

Fig. 6.9 shows the flow pattern computed with the $k - \epsilon$ model. All other models produce a similar flow pattern. Separation occurs at the top corner of the step, a recirculation region then forms, followed by reattachment. L_R represents reattachment length. Table 6.4 summarizes predicted dimensionless reattachment lengths for the models tested.

It is clearly seen that the EASM overpredicts the reattachment length, L_R/h (Speziale's nonlinear $k - \epsilon$ model predicts $L_R/h = 6.4$ and Celenligil and Mellor (1985) predict $L_R/h = 7$ using the Reynolds stress model)(see Speziale and Ngo, 1988). Like the $k - \epsilon$, the HCubic model underpredicts L_R/h. This is not surprising. The empirical constants appearing in the Craft *et al.*'s (1993) cubic model, calibrated in a low-Reynolds-number form, are not well suited to wall-function methods. For linear low-Reynolds-number versions of the standard $k - \epsilon$ model, the CH and LS underpredict the values of L_R/h. However, the LSY improves the prediction of L_R/h. This is owing to the introduction of the Yap term which reduces the turbulence length scale in the separated region (see Chapter 3). The linear one-equation S-A model predicts L_R/h well when compared with experimental data.

Fig. 6.10 gives comparison of velocity predictions with measurements for the $k - \epsilon$,

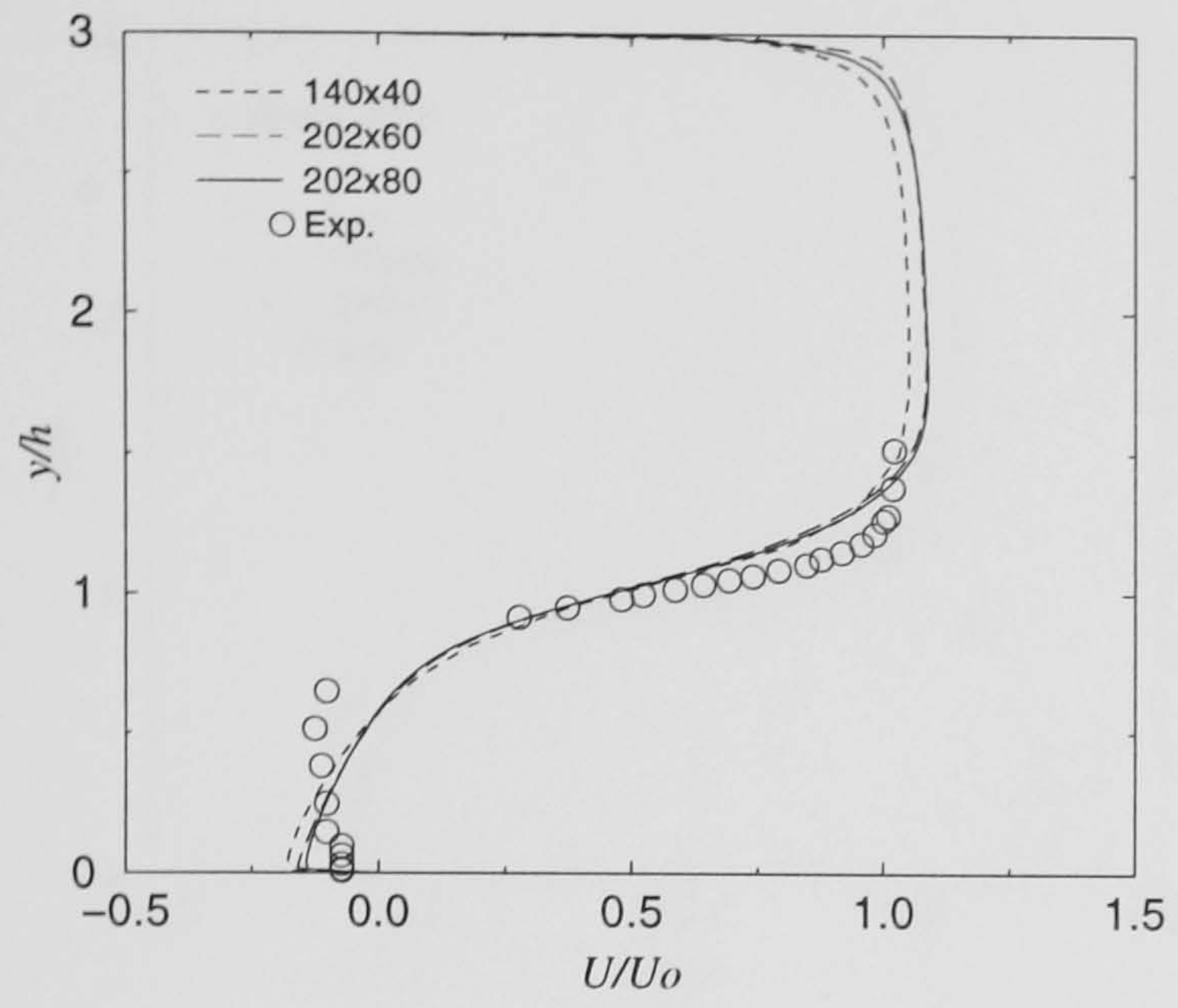

Figure 6.8: Grid independence studies for the $k-\epsilon$ model: left: at $(x-L_1)/h=1.333$; right: at $(x-L_1)/h=6.22$.

HCubic and EASM models at five locations, where $x' = x - L_1$ and U_0 (i.e. U_c) is the maximum inlet velocity. It can be seen that the results obtained from the EASM agree better with experimental data than do the other two models. Also a similar performance can be seen in the dimensionless turbulence intensity $(\overline{u'u'}^{1/2}/U_0)$ and shear stress distributions shown in Fig. 6.11 and Fig. 6.12 respectively, where $C=\rho U_0^2$. The HCubic improves the predictions of turbulence intensity compared with the $k-\epsilon$ model. However, for shear-stress prediction, the results obtained from either the HCubic or $k-\epsilon$ are not in good agreement with measurements for the locations investigated.

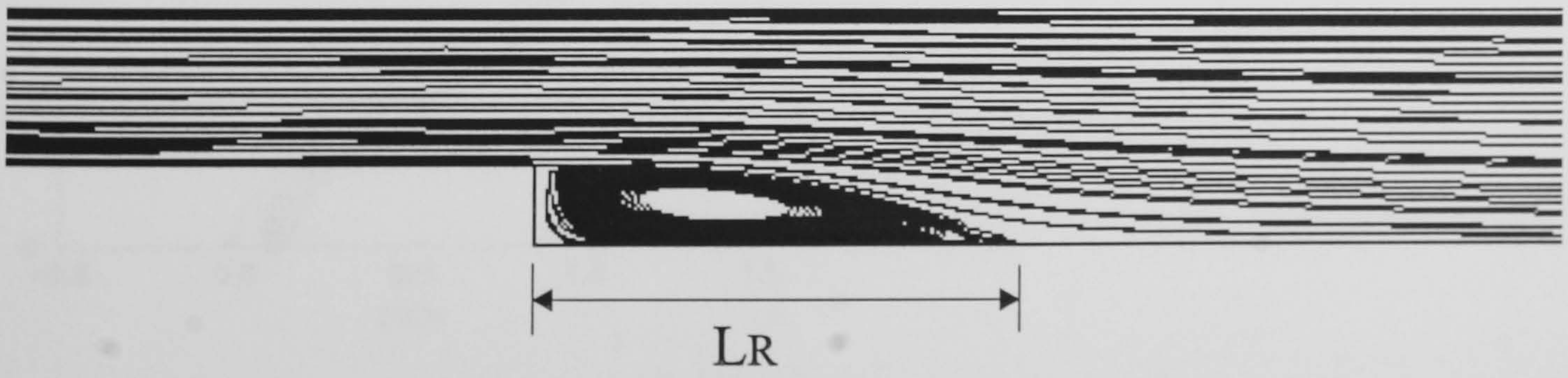

Figure 6.9: Streamline for the $k-\epsilon$ model.

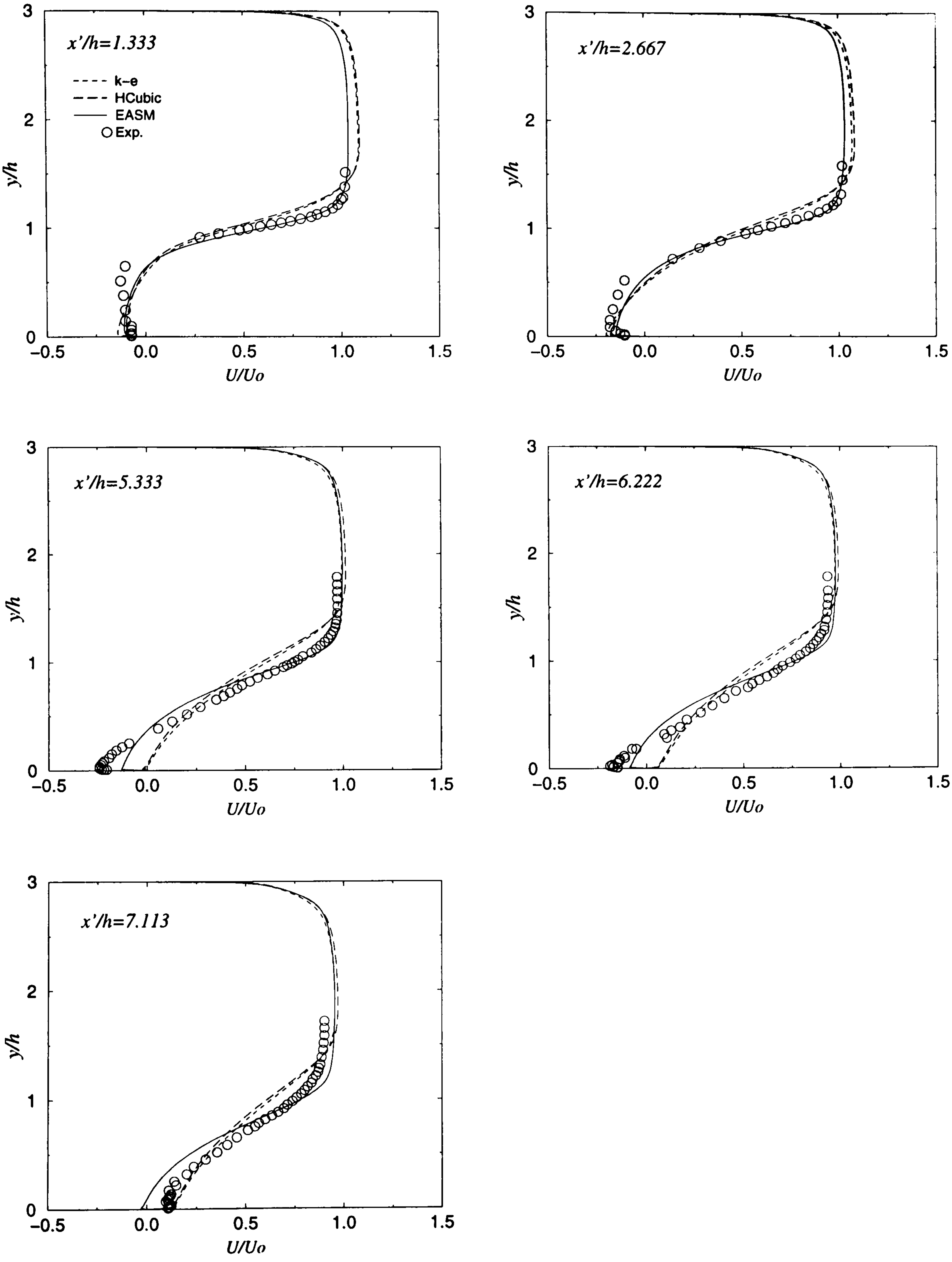

Figure 6.10: Comparison of velocity predictions with measurements for the $k-\epsilon$, HCubic and EASM models.

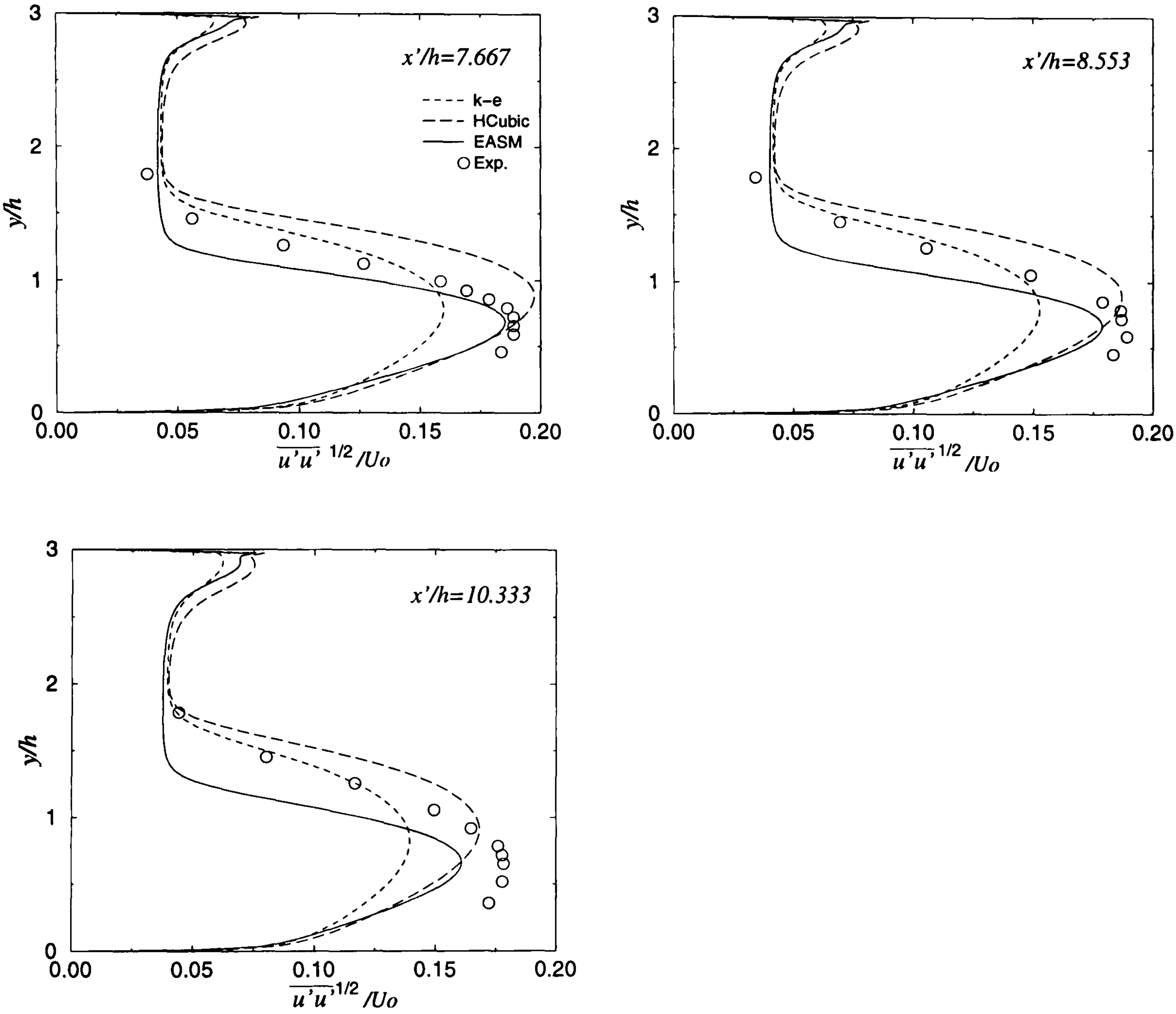

Figure 6.11: Comparison of normalized Reynolds stress predictions with measurements for the $k-\epsilon$, HCubic and EASM models.

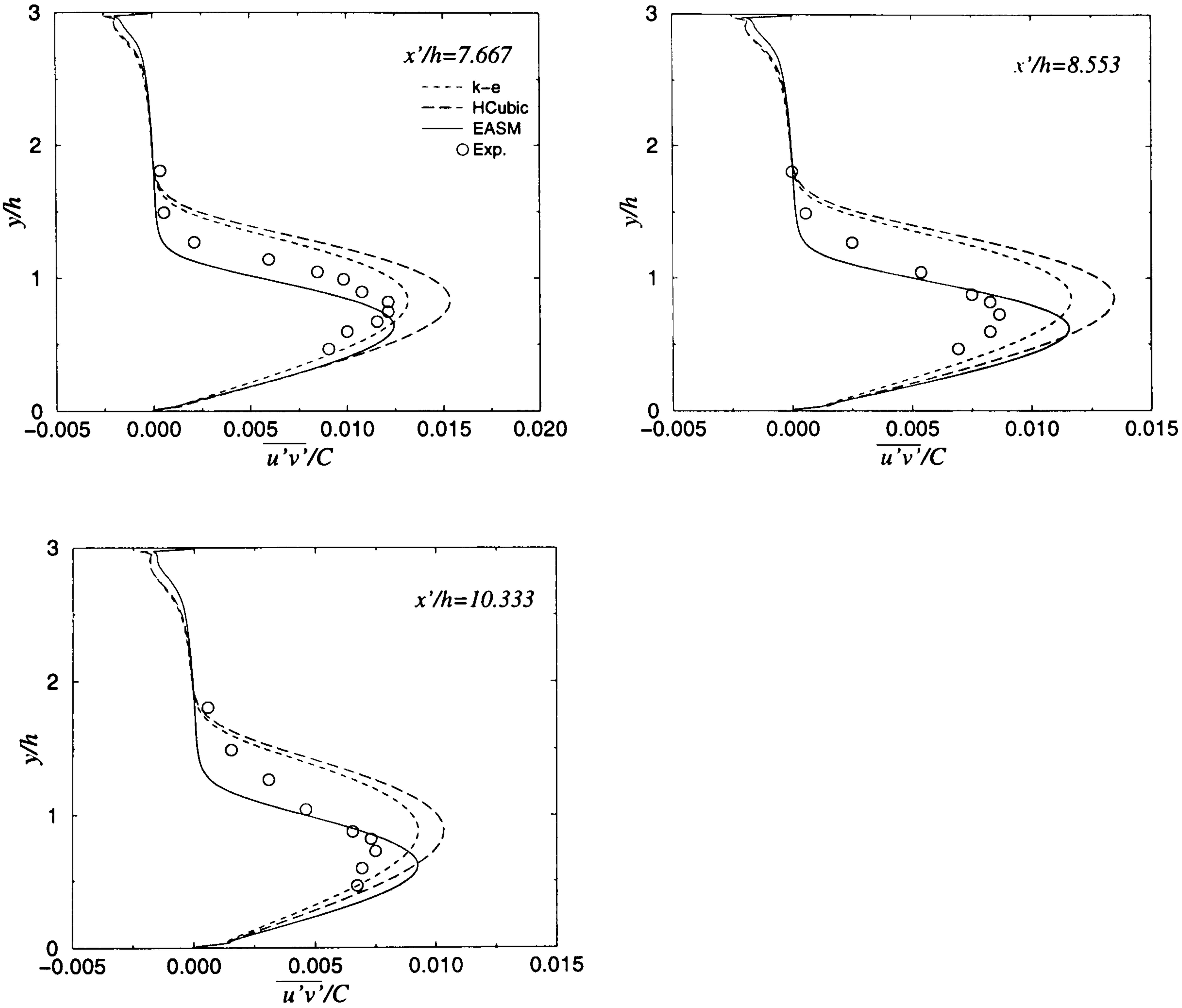

Figure 6.12: Comparison of normalized shear stress predictions with measurements for the $k-\epsilon$, HCubic and EASM models.

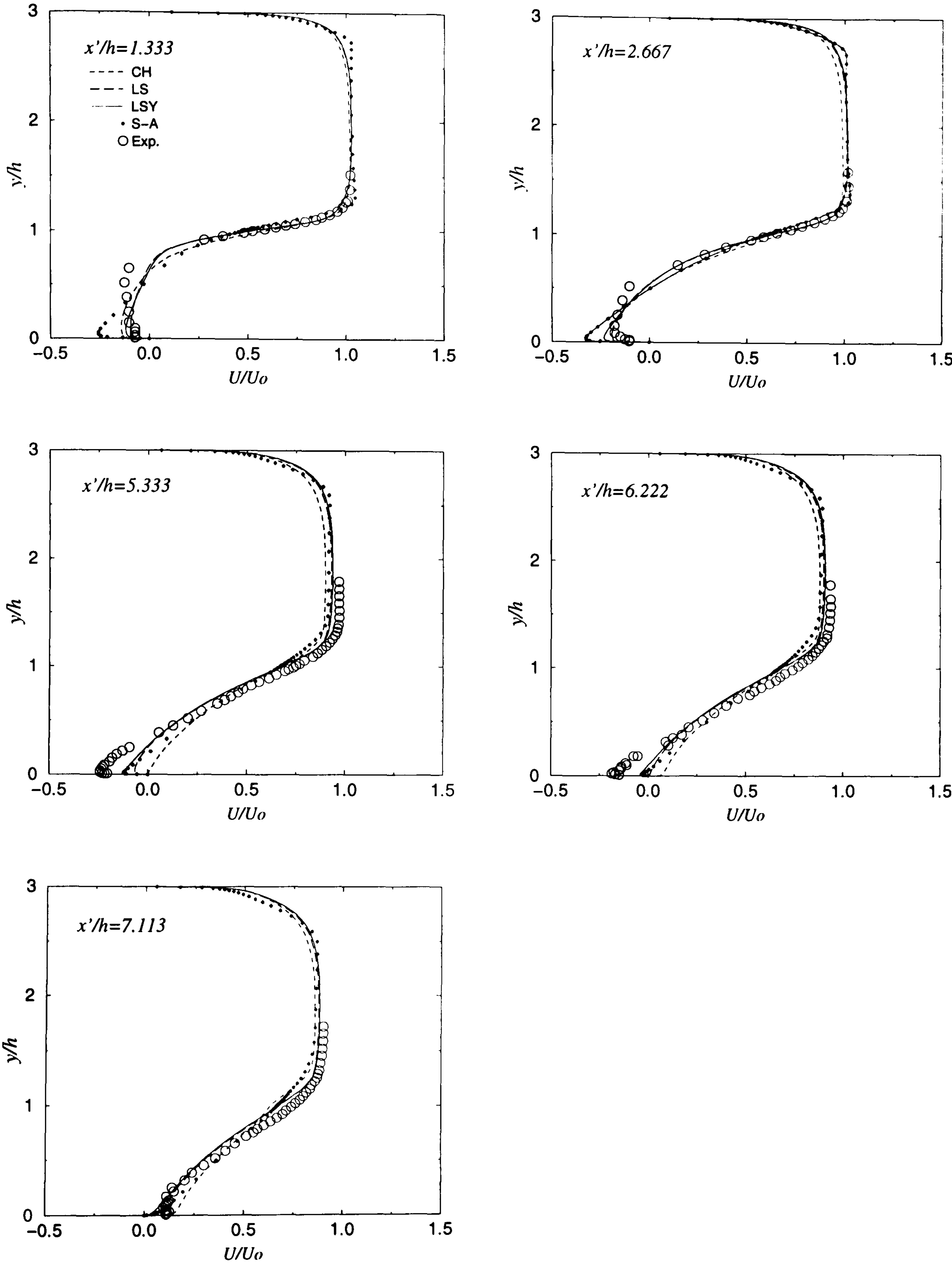

Figure 6.13: Comparison of velocity predictions with measurements for the CH, LS, LSY and S-A models.

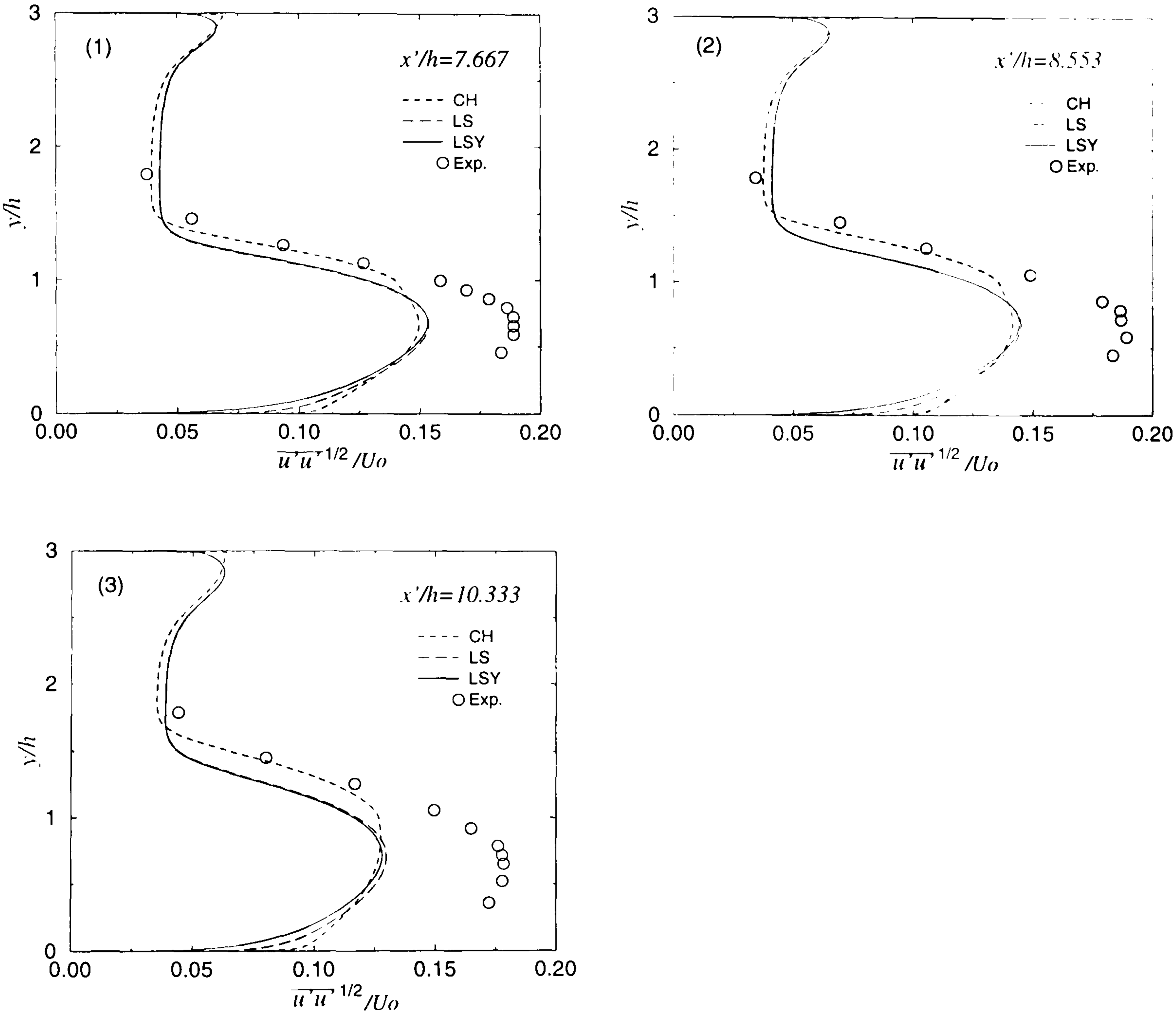

Figure 6.14: Comparison of normalized Reynolds stress predictions with measurements for the CH, LS and LSY models.

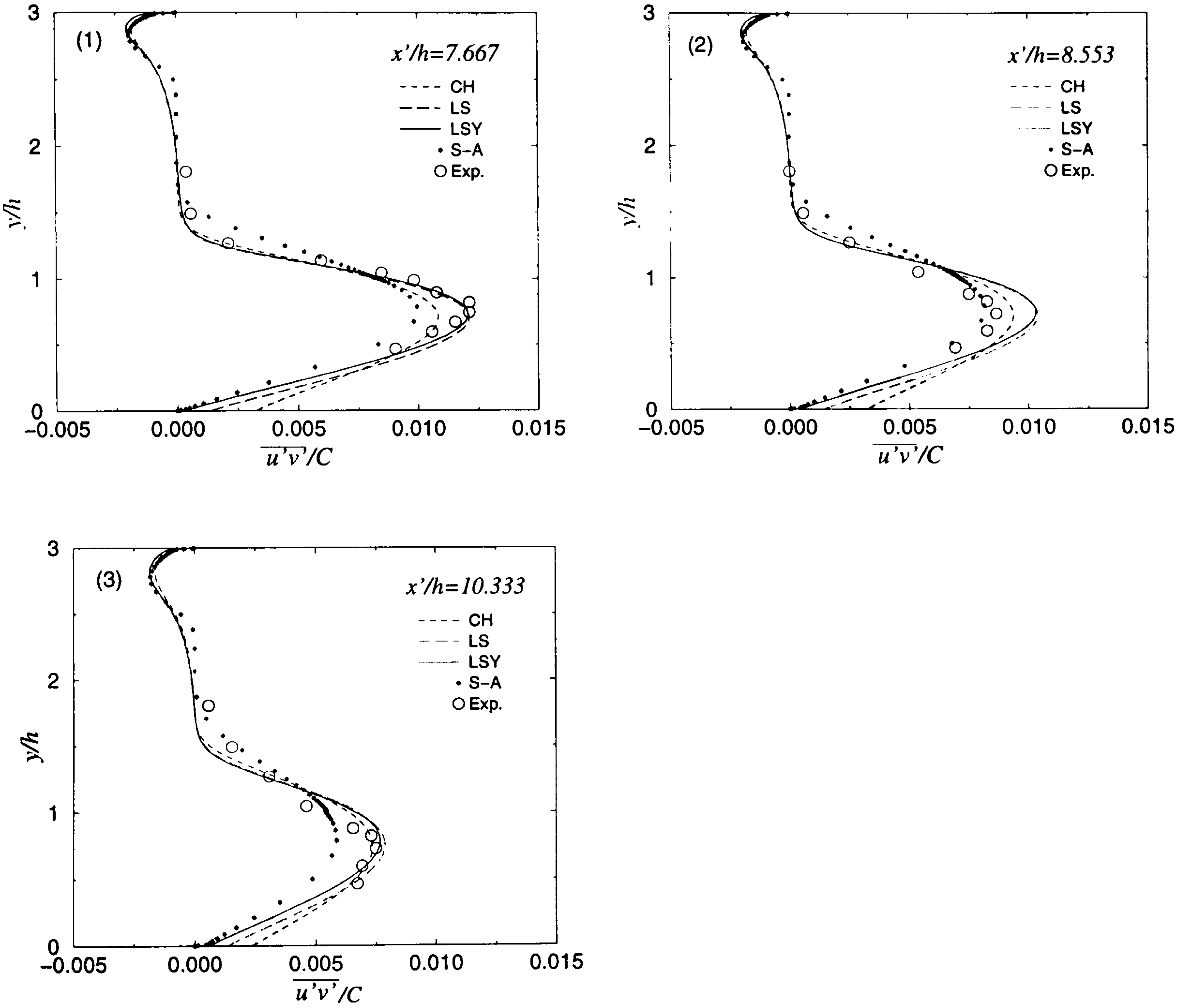

Figure 6.15: Comparison of normalized shear stress predictions with measurements for the CH, LS, LSY and S-A models.

Table 6.4: Predicted reattachment lengths for backward-facing step flow.

Model		L_R/h
High-Reynolds-number models	$k-\epsilon$	5.6
	EASM	7.5
	HCubic	5.7
Low-Reynolds-number models	CH	5.4
	LS	6.1
	LSY	6.9
	S-A	6.6
	$k-l/k-\epsilon$	-
	$k-l$/EASM	-
	$k-l$/HCubic	-
Experimental data		7.0

Comparisons are also made for the low-Reynolds-number models. Velocity distributions obtained from the CH, LS, LSY and S-A models are shown in Fig. 6.13. As can be seen from Fig. 6.13, The LSY performs better than do other models especially in the near-wall region within the recirculation region. The S-A model performs well although it overpredicts the u velocity very near the wall just behind the step. Fig. 6.14 presents the dimensionless turbulence-intensity distributions. Compared with Fig. 6.11, the nonlinear models, EASM and HCubic predict the turbulence intensity better than the linear low-Reynolds-number models as expected. The normalized shear stress predictions from the CH, LS, LSY and S-A models are shown in Fig. 6.15. The S-A model underpredicts $\overline{u'v'}$ in the recirculation region compared with the other models.

The three zonal models, $k-l/k-\epsilon$, $k-l$/EASM and $k-l$/HCubic, have been tried. However, they do not converge well. The same problem occurs for the cubic model. It might be due to high velocity gradient existing in the separation region.

Overall, for this step flow the high-Reynolds-number EASM performs better than the $k-\epsilon$ and HCubic models. As concluded by Heyerichs and Pollard (1996), for low-Reynolds-number versions of the standard $k-\epsilon$ model, the LSY performs better than

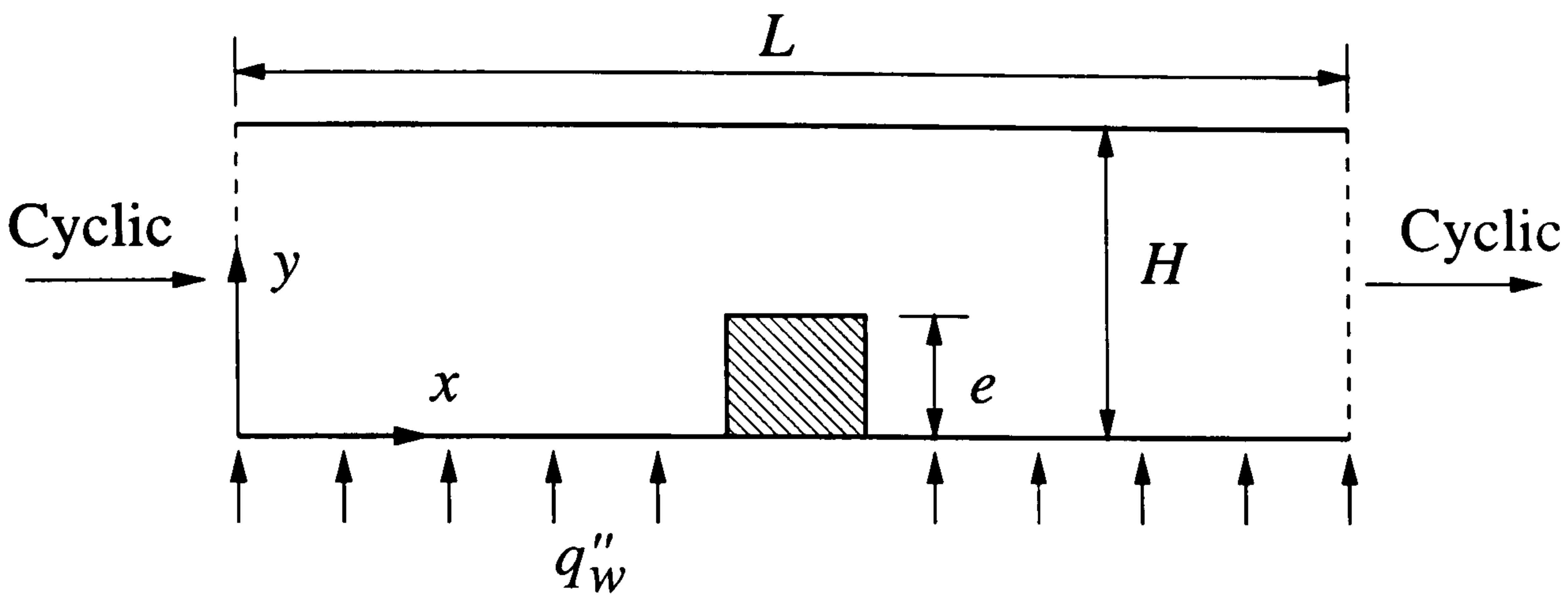

Figure 6.16: Schematic of the ribbed channel flow.

the CH and LS models. The S-A model performs reasonably well.

6.2.3 Ribbed-duct channel flow

- **Case description**

For this case comparison is made with the measurements of Acharya *et al.* (1993). The case is chosen since it is a low-Reynolds-number flow relevant to electronic systems. Owing to the presence of a rib mounted on the bottom wall of the channel, separation occurs in the flow. This flow feature, as with the step case, is a challenge for turbulence models. A schematic of the configuration is shown in Fig. 6.16.

Table 6.5: Flow parameters for the ribbed channel flow.

Re_b	14200
$L \times H \times W$	0.127 × 0.061 × 0.3 m^3
U_b	3.6 m/s^2
e	6.35 mm
D_h	101.6 mm
q''_w	280 W/m^2

The Reynolds number, Re_b, based on the channel height and mean (or bulk) velocity is 14200. The other flow parameters are given in Table 6.5. Periodic boundary conditions are applied for both flow field and temperature in the streamwise direction. On the

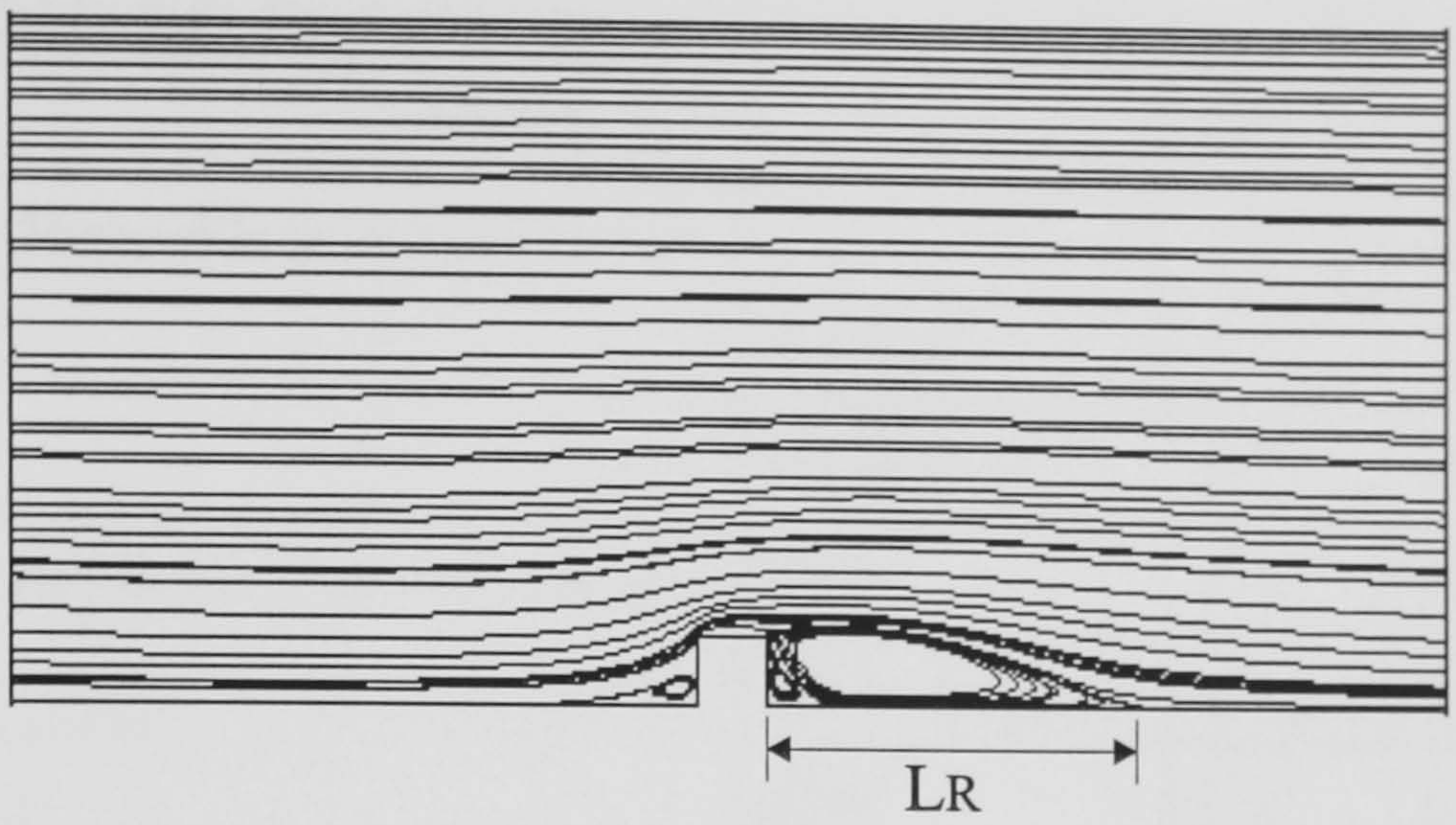

Figure 6.17: Streamline of the ribbed channel flow

surfaces of the rib and top wall of the channel, an adiabatic boundary condition is applied for the temperature prediction.

Regarding grid generation, attention should be paid to some areas such as the separation regions. Here, in the streamwise direction, a two-parameter stretching tanh function is used to create stretched mesh at the inlet and outlet, while in the middle part around the rib, an uniform grid is established. For high-Reynolds-number models, a coarse grid with 139 × 21 (x, y) nodes is used with a uniform distribution in the y direction. For low-Reynolds-number models, a fine grid with 199 × 142 (x, y) nodes is used in which an exponential function is applied to obtain non-uniform grid in the y direction.

For constant heat flux, the local Nusselt number along the bottom wall is defined as

$$Nu = \frac{q''_w D_h}{k(T_w(x) - T_b(x))} \tag{6.7}$$

where $k = \mu c_p / Pr$ is thermal conductivity, $T_w(x)$ is the wall temperature at x and $T_b(x)$ the bulk temperature of the $y - z$ plane at x.

- **Results and discussion**

The mean streamline computed with the S-A model is shown in Fig. 6.17. All other models studied generate a similar flow pattern. As is seen, the flow impinges on the front of the rib, creating a small recirculating region. When leaving the rib, the flow separates

Table 6.6: Predicted parameters for ribbed channel flow.

Model		L_R/h	$\frac{dp}{dx}(\frac{\text{Pa}}{\text{m}})$
High Reynolds number models	$k-\epsilon$	4.6	5.6
	EASM	5.5	5.1
	HCubic	4.7	5.6
Low Reynolds number models	CH	3.1	8.8
	LS	4.0	7.2
	LSY	6.2	5.6
	SA	5.7	5.4
	$k-l/k-\epsilon$	6.3	5.3
	$k-l$/EASM	8.1	4.8
	$k-l$/HCubic	6.4	5.7
	Cubic	8.3	6.1
Experimental data		6±0.7	-

immediately on the top right corner of the rib, generating a low-pressure region and a primary bubble behind the rib.

The predicted reattachment length and pressure gradient are summarised in Table 6.6. The CH and LS models largely underpredict L_R/h, as do the standard $k-\epsilon$ and HCubic models, while the nonlinear $k-l$/EASM and cubic models overpredict L_R/h. The other models give prediction of L_R/h within the experimental uncertainty of the measured data.

(a) Mean velocity predictions

Fig. 6.18 shows the normalized streamwise velocity profiles obtained from the standard $k-\epsilon$, EASM and HCubic models at various locations (where U_o represents the averaged flow velocity). The distributions are very similar to those obtained by the linear and non-linear $k-\epsilon$ models by Acharya *et al.* (1993). In the near-wall regions immediately above the rib and downstream of the rib, all three models underpredict the measured u−velocity with the nonlinear EASM model giving lower velocity predictions

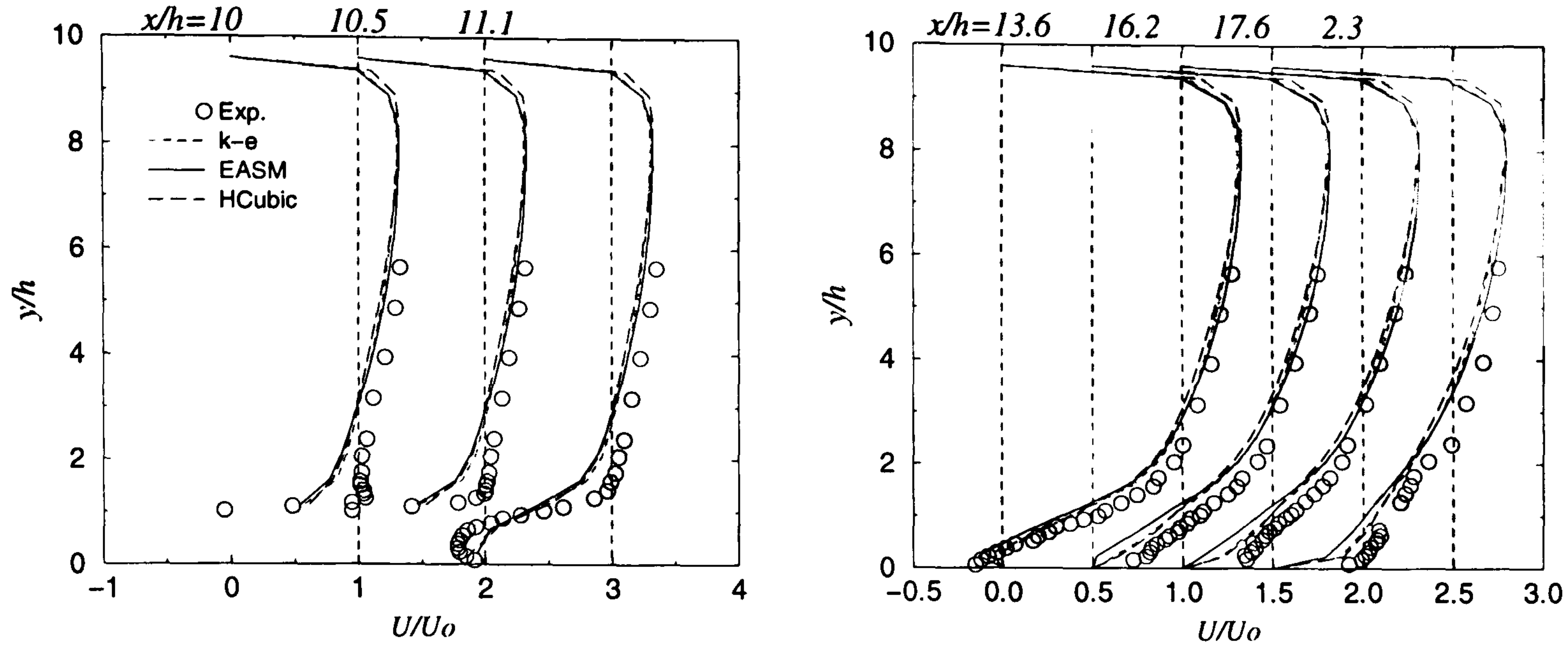

Figure 6.18: Comparison of streamwise velocity predictions with measurements for high-*Re* models at seven locations.

than the $k-\epsilon$ and HCubic models. The lower u-velocity results in overprediction of reattachment length. The HCubic model gives similar results to the $k-\epsilon$ model.

Fig. 6.19 compares the v-velocity distributions. Like the results presented by Acharya *et al.* (1993), all three models give predictions almost identical to each other at all locations, except at x/h=13.6, where the EASM predicts lower v than the other two models in this study.

The linear low-Reynolds-number model predictions from the CH, LS, LSY and S-A are shown in Figs. 6.20-21. For the u and v velocities, the predictions from the four models agree well with the measurements in the core region. Immediately above the rib, all models follow the measurements well except for the CH model. Near the wall around the reattachment point, all models underpredict the measured values. Compared with the predictions shown in Fig. 6.18 and Fig. 6.19, the low-Reynolds-number models generally perform better than the high-Reynolds-number models in the near-wall region. This is because of the use of the wall functions for the high *Re* models.

The u and v results obtained from the zonal and cubic models are shown in Fig. 6.22 and Fig. 6.23 respectively. The distributions are similar to those from the above low-*Re* models except for the cubic model. In the recirculation region, the cubic model predicts much lower values than the zonal models and hence overpredicts reattachment length (see Table 6.6).

(b) Turbulent stresses

Fig. 6.24 and Fig. 6.25 show respectively the streamwise and wall-normal velocity fluctuations from the high *Re* models. The measurements show stress peaks above and behind the rib regions arising from shear-layer turbulence generation. As the flow redevelops, the peak decreases in value. However, the nonlinear models fail to predict the peaks similar to those of the $k-\epsilon$ although the EASM slightly improves the predictions. The HCubic model slighly overpredicts the measured u' values except near the wall. The EASM predicts v' quite well in the core region when compared with the HCubic and $k-\epsilon$ models. The HCubic model largely overpredicts v' in the core region.

For the u' predictions shown in Fig. 6.26, the LSY results are slightly lower than those from the LS and CH models near the wall. The CH and LS models overpredict the v' especially for the CH except for the zone immediately above the rib as presented in Fig.6.27. The LSY model predictions agree well with the measured v' values except in the near-wall region at x/h=11.1.

Comparing Fig. 6.28 with Fig. 6.26, it is found that the performance of the zonal models is similar to the LSY model for the u' predictions. However, for the v' predictions shown in Fig. 6.29, the zonal models generally perform better than the low-*Re* versions of the $k - \epsilon$ model. The cubic model does not perform as well as the zonal and LSY models at x/h=11.1 within the separation region for both the u' and v'.

Like the u' and v' predictions, all models investigated fail to predict the peaks in the turbulent shear stress ($\overline{u'v'}$) shown in Fig. 6.30 except for the CH model at $x/h = 11.1$. In the core region, the results from all models are in good agreement with the measurements except at x/h=10.5.

It should be pointed out that the cubic model gives unsteady Reynolds stresses near the wall within the recovery region. No oscillation has been found for the other models. However, for consistency, mean values have been used for the parameters discussed above.

The low-Reynolds-number versions of EASM, namely the EASM-1 and EASM-2, have also been tested. However, as with the zonal models for the step case, a similar convergence problem occurs for both the EASM-1 and EASM-2.

(c) Heat transfer results

Comparisons between the predicted and measured *Nu* for all models investigated are shown in Fig. 6.31. From Fig. 6.31(a), it can be seen that all the high-*Re* models underpredict *Nu*. Although the nonlinear EASM model improves the predictions of the u' and v', it does not improve *Nu* predictions. Except in the area behind the rib, the HCubic gives similar predictions to the $k-\epsilon$. Also, it should be noted that there is a very high peak at the reattachment point downstream of the rib for each profile. This results from the use of wall functions in which the wall shear stress is used (at the reattachment point the wall shear stress is zero).

From Fig. 6.31(b), it can be seen clearly that the CH and LS models overpredict *Nu*. This is due to the high level of turbulence near the wall predicted by these models. The LSY greatly improves *Nu* compared with the LS. The *Nu* results from the S-A model agree surprisingly well with the measurements.

As is shown in Fig. 6.31(c), all zonal models give better predictions than the high-*Re* models. However, the nonlinear zonal models do not, as in their high-Reynolds-number form, show improvement in *Nu* in comparison with the linear $k - l/k - \epsilon$ model. The cubic model overpredicts *Nu* upstream and downstream of the rib. This may be caused by overprediction of velocity very near to the wall.

As can be seen from Fig. 6.31, all profiles have two peaks, though the peak locations differ depending on the model. This is because of the impingement occuring in front of the rib and reattachment behind the rib.

Overall, the above results from the nonlinear models including the EASM, HCubic and their zonal forms do not show improvement in predicted heat transfer. However, these models improve the u' and v' to some extent for the ribbed channel flow. This is similar to the performance of Speziale's nonlinear model shown in Acharya *et al.* (1993). The CH and LS do not perform well for either the flow field or heat transfer. Compared with the CH and LS models, the LSY improves prediction of velocities and *Nu*. This is

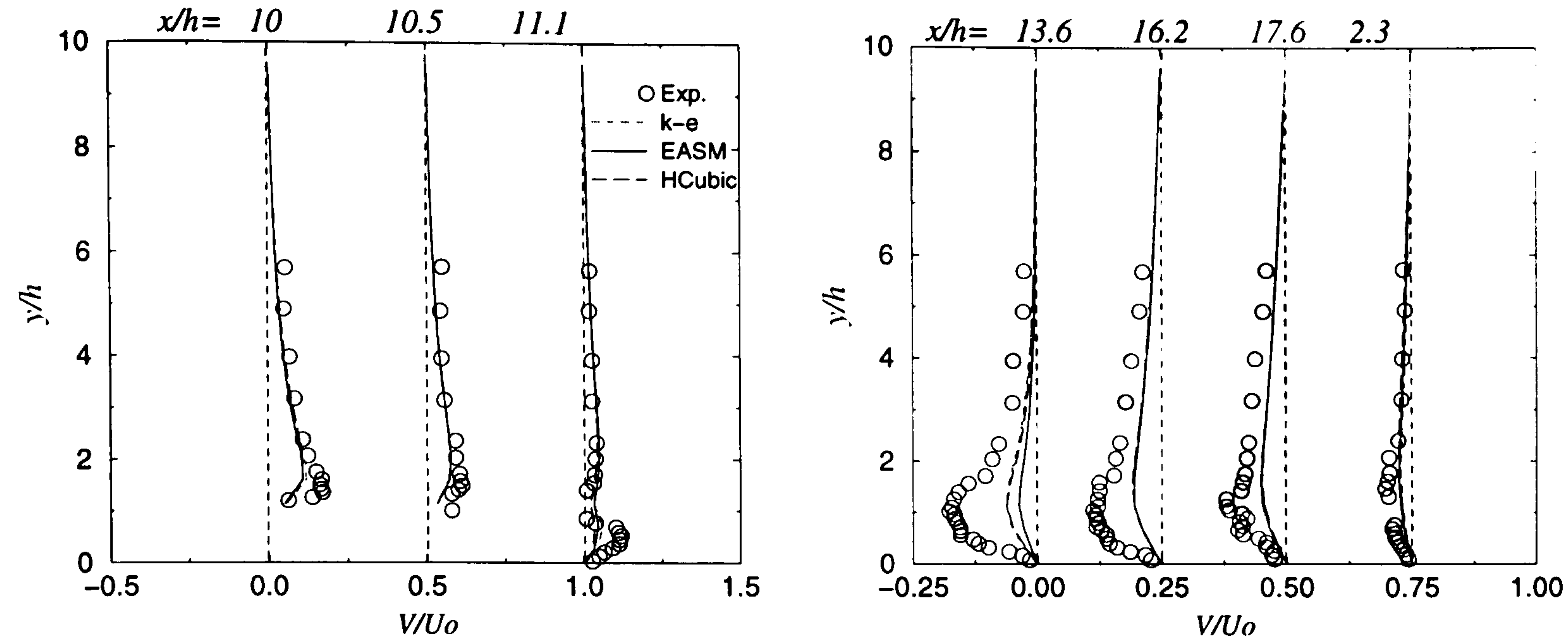

Figure 6.19: Comparison of cross-stream velocity predictions with measurements for high-*Re* models at seven locations.

consistent with that shown in Bredberg *et al.* (2000). Performance of the zonal models is similar to the LSY for velocities. Like Ooi *et al.*'s (2002) work for 3D ribbed-duct flow, the S-A model gives reasonable predictions for both the flow field and heat transfer. However, the u' and v' are not well modeled for the S-A model. The cubic model does not perform well for the near-wall velocities and heat transfer.

6.2.4 Square-duct flow

- **Problem description**

Turbulent flow in a square duct is characteristic of Prandtl motions of the second kind. It is well known that, unlike non-linear models, linear models fail to predict this turbulence-driven secondary flow.

To examine how well some of the non-linear models used in the study predict the secondary motions, a straight square duct case used by Mompean *et al.* (1996) is chosen. Comparison is made with the measurements of Cheesewright *et al.* (1990). The Reynolds number is Re_b=4800 based on the channel height and bulk velocity. Periodic boundary condition is employed in the streamwise x direction. A non-uniform grid with 15 × 33

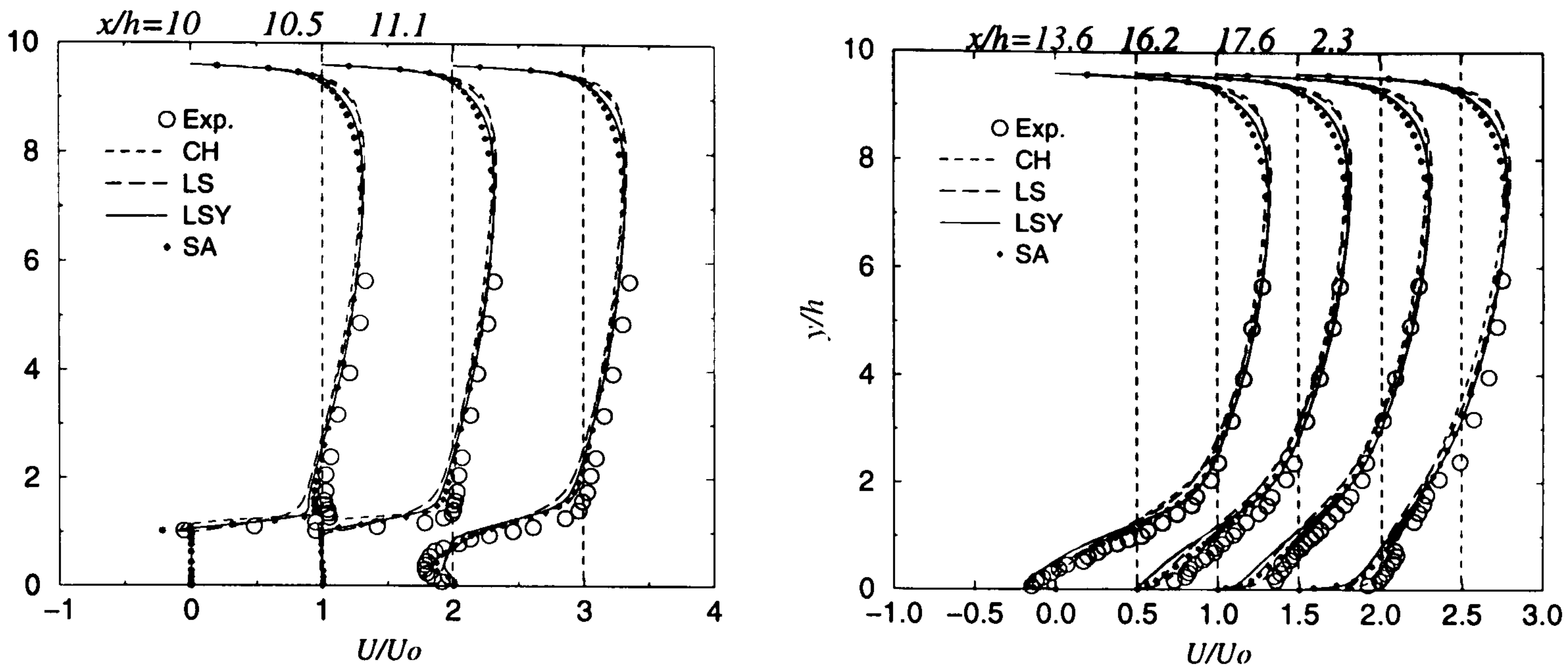

Figure 6.20: Comparison of streamwise velocity predictions with measurements for linear low-*Re* models at seven locations.

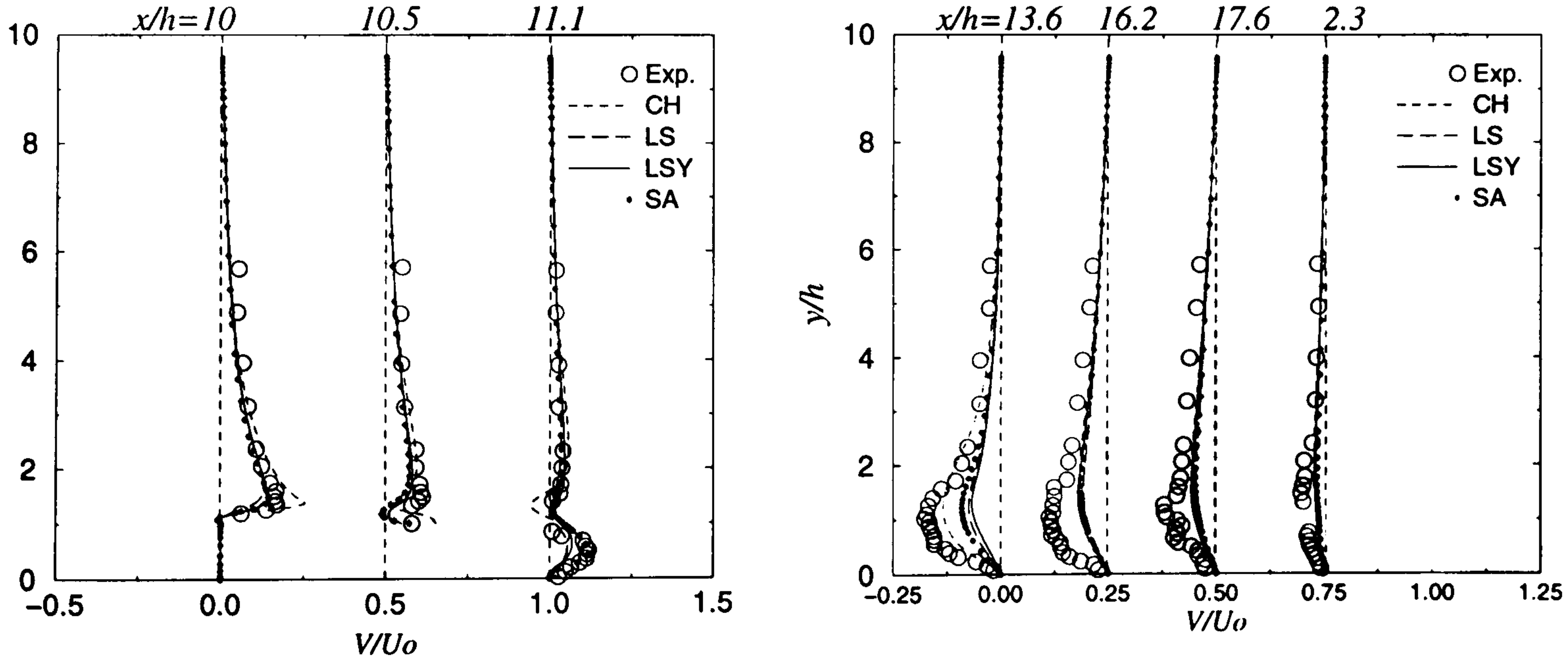

Figure 6.21: Comparison of cross-stream velocity predictions with measurements for linear low-*Re* models at seven locations.

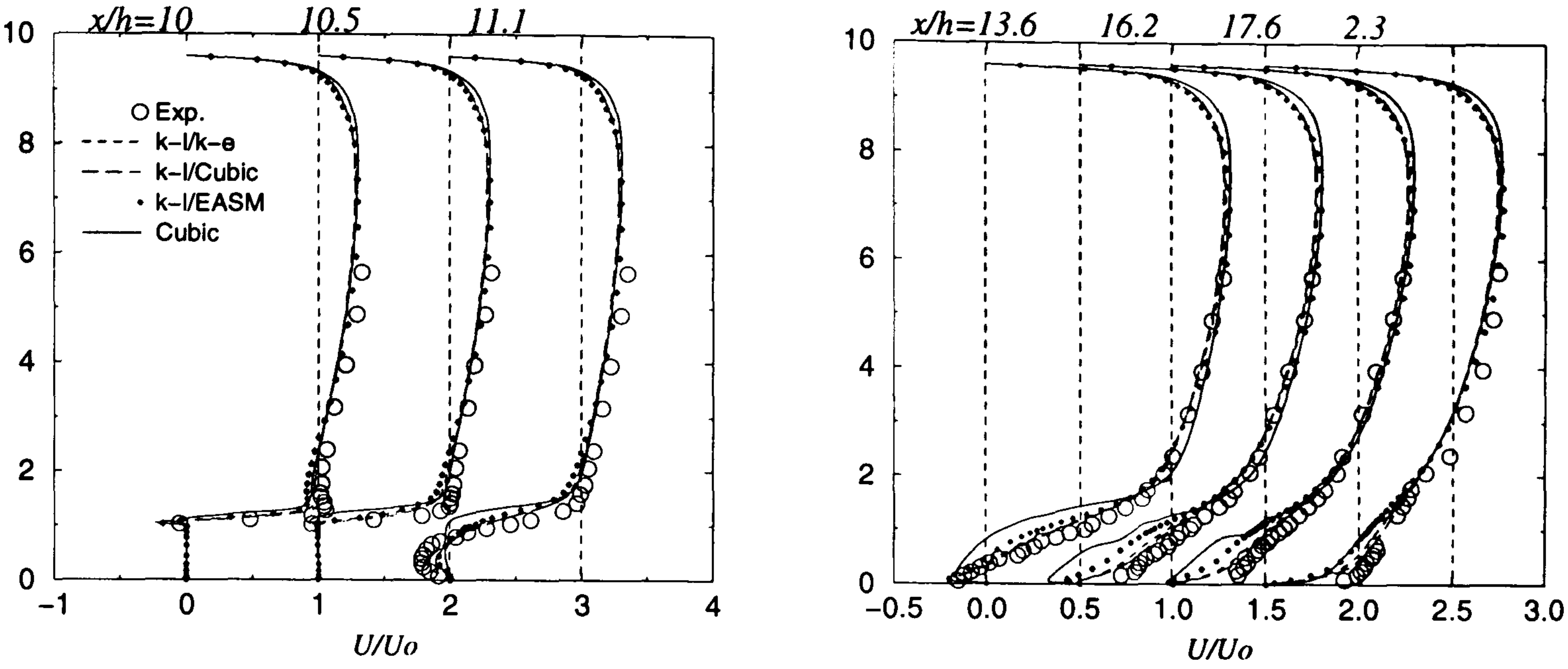

Figure 6.22: Streamwise velocity distributions at seven locations for zonal and cubic models.

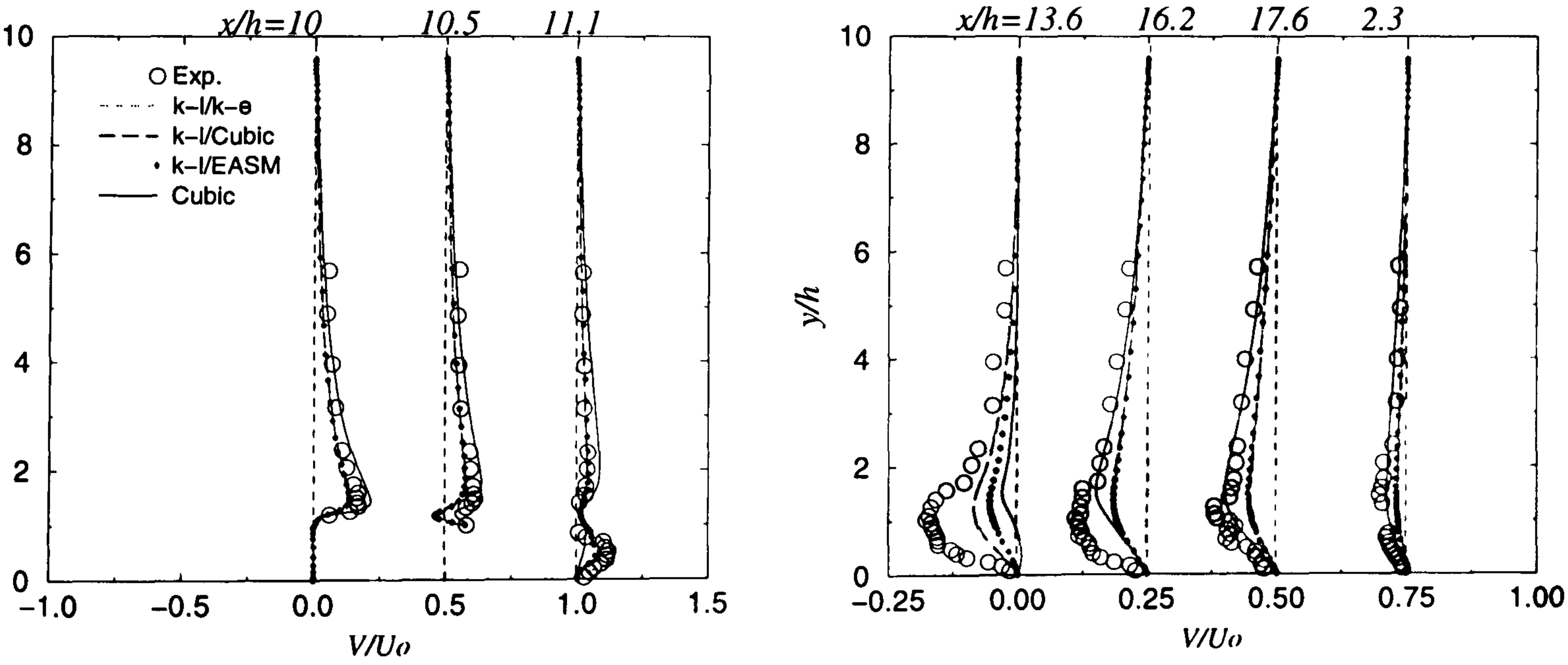

Figure 6.23: Cross-stream velocity fluctuations at seven locations for zonal and cubic models.

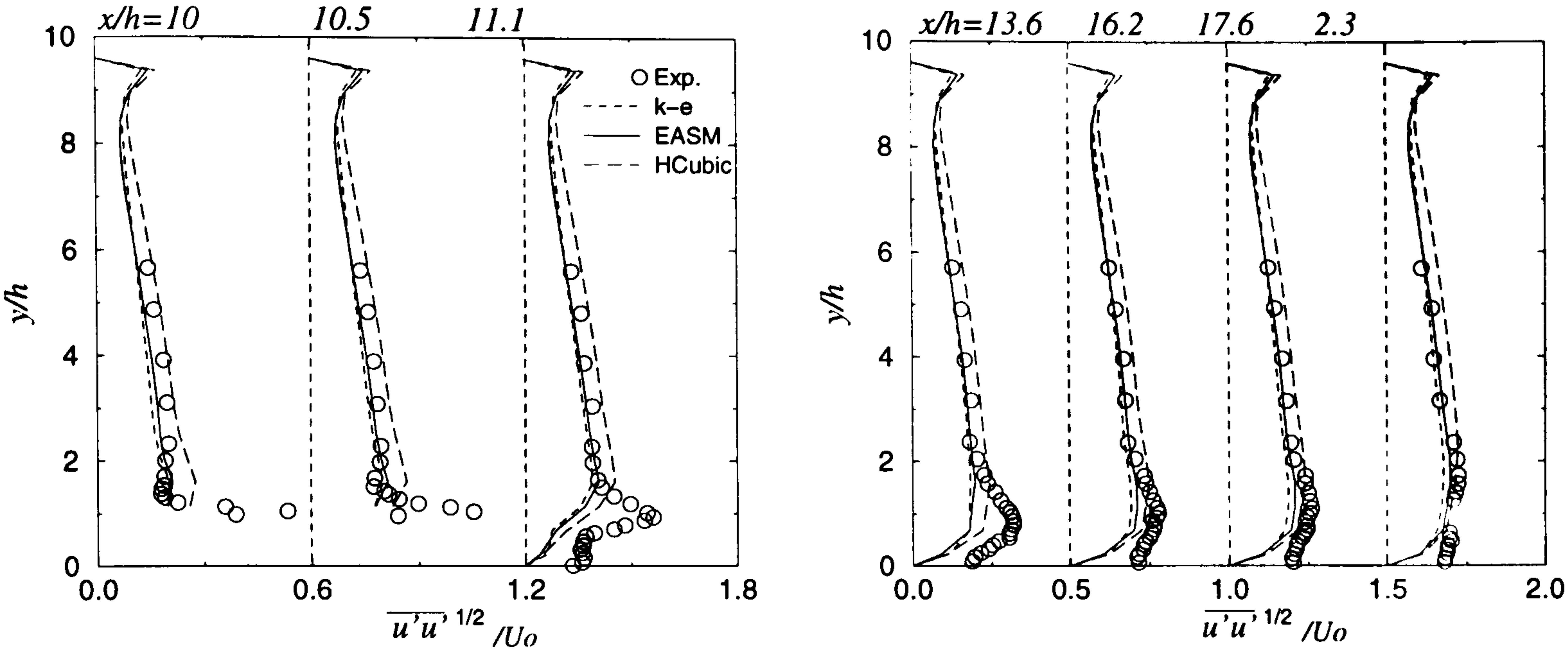

Figure 6.24: Streamwise velocity fluctuations for high-*Re* models at seven locations.

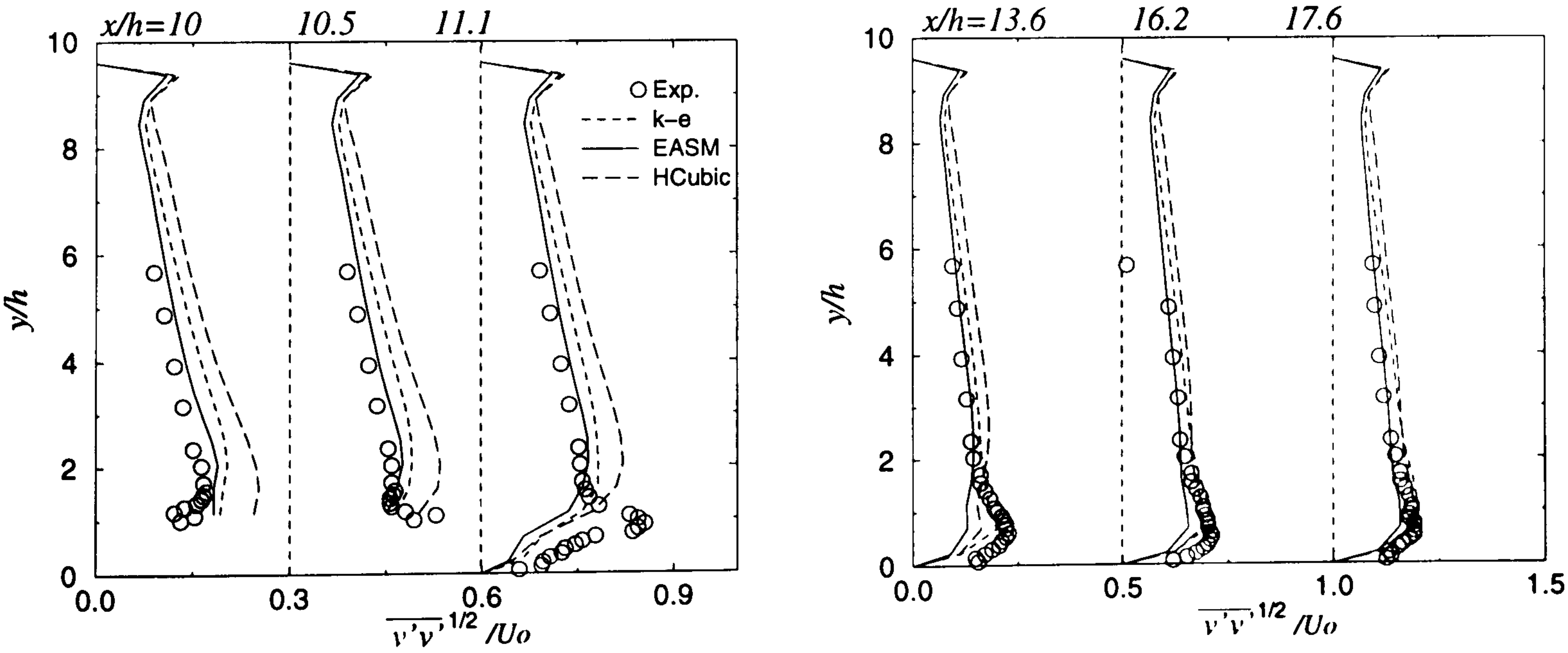

Figure 6.25: Cross-stream velocity fluctuations for high-*Re* models at seven locations.

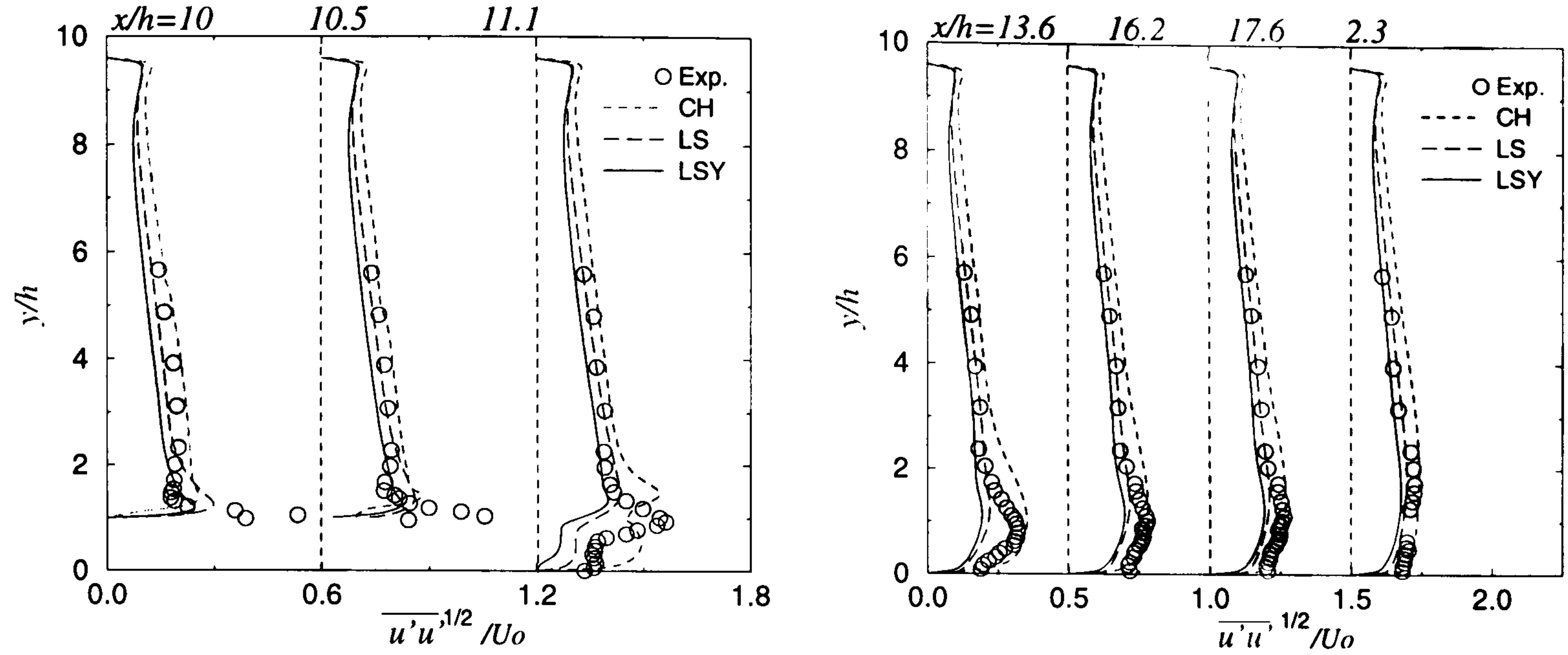

Figure 6.26: Streamwise velocity fluctuations for linear low-*Re* models at seven locations.

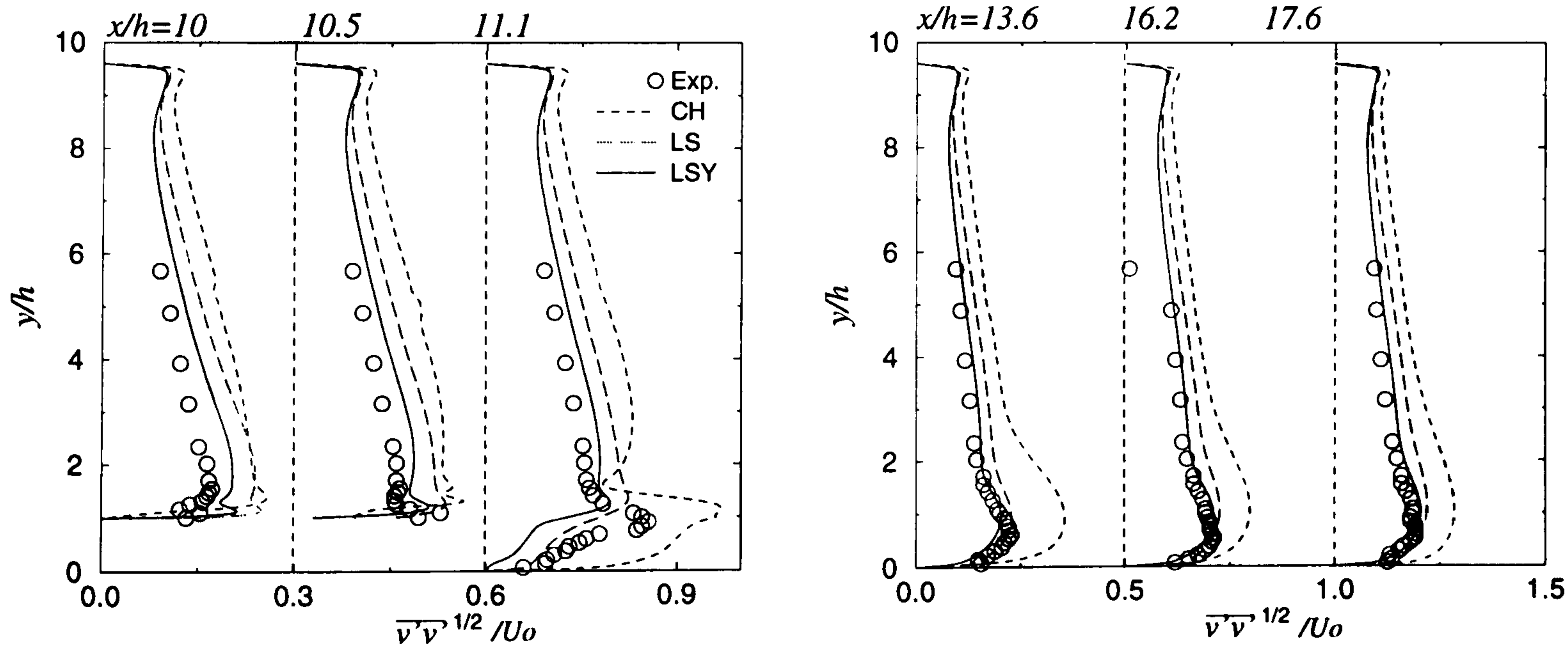

Figure 6.27: Cross-stream velocity fluctuations for linear low-*Re* models at seven locations.

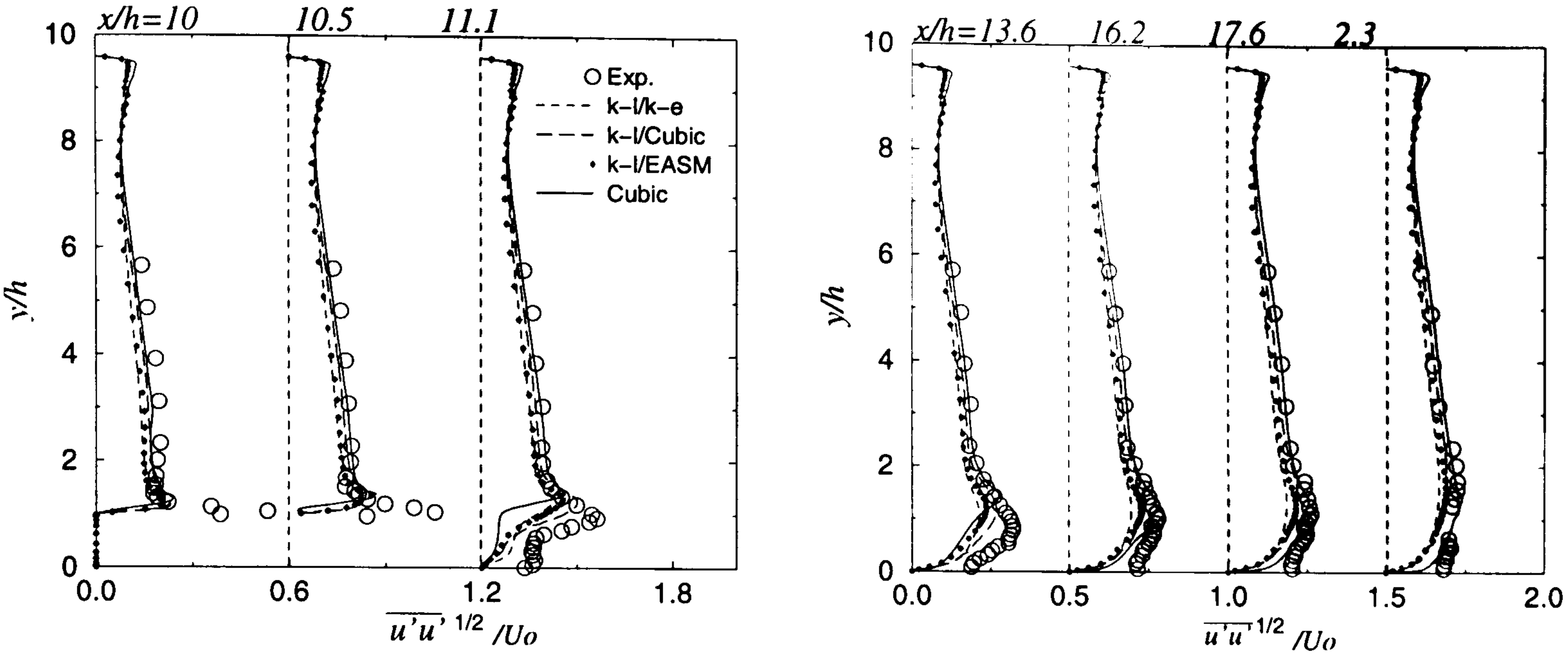

Figure 6.28: Streamwise velocity fluctuations at seven locations for zonal and cubic models.

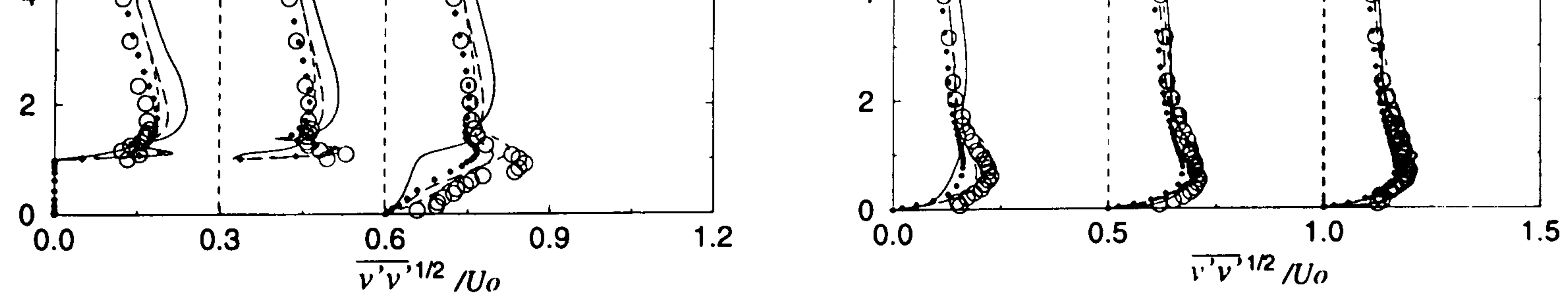

Figure 6.29: Cross-stream velocity fluctuations at seven locations for zonal and cubic models.

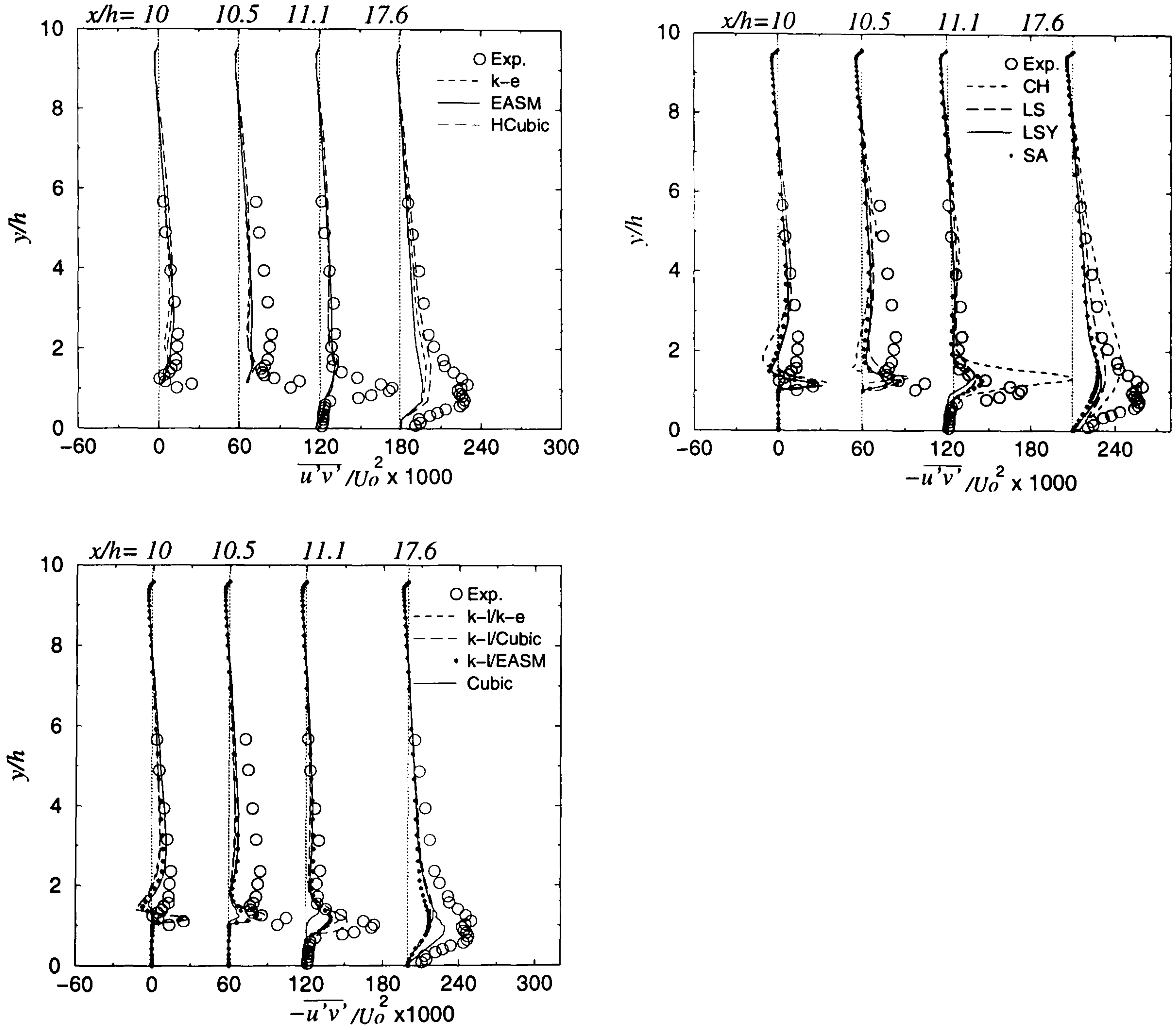

Figure 6.30: Normalized shear stress distributions at four locations.

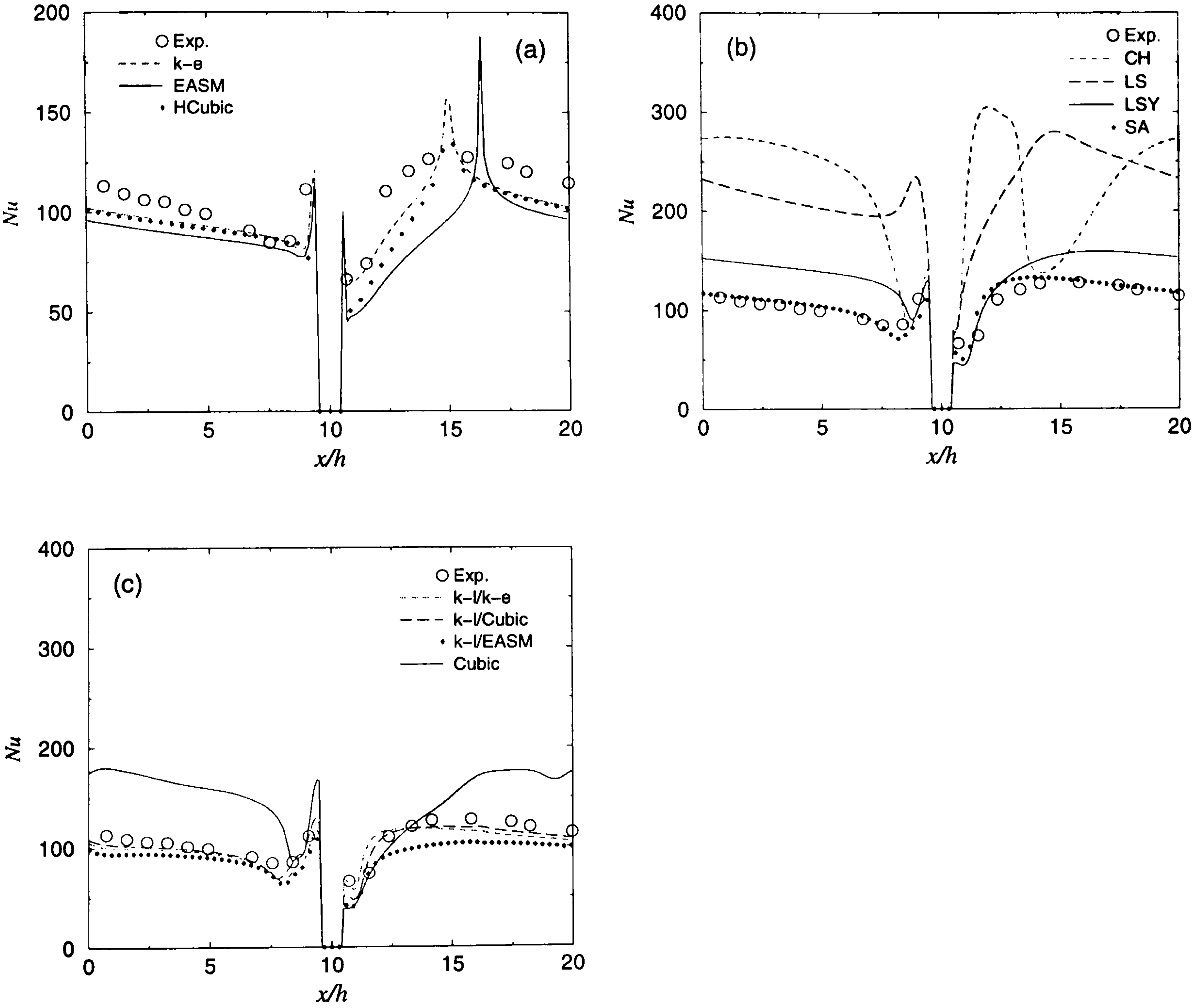

Figure 6.31: Local Nusselt number distributions.

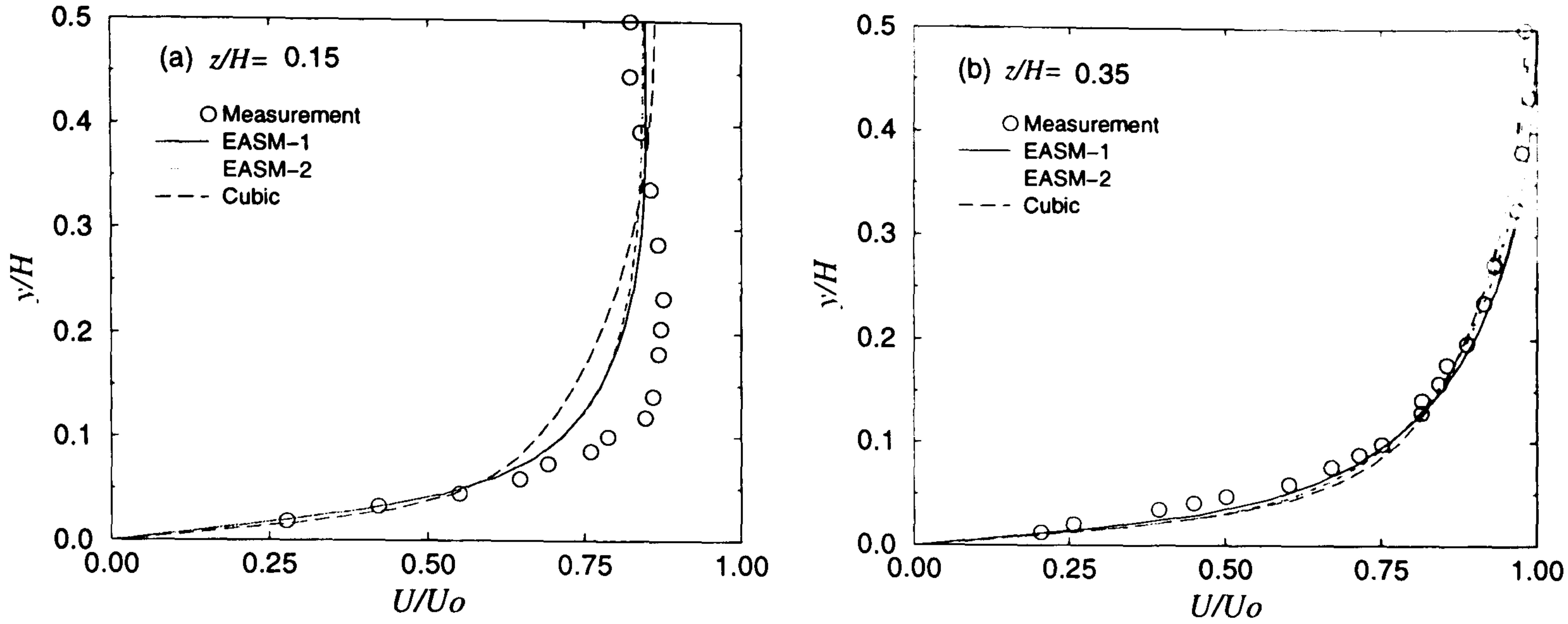

Figure 6.32: Comparison of mean streamwise velocity predictions with measurements for three nonlinear models at two locations.

× 33 (x, y, z) nodes is used.

The investigated models comprise: the cubic model and low-Reynolds-number versions of the EASM, i.e. Abid *et al.* (1995) (EASM-1) and the original high-Reynolds-number model coupled with Abe *et al.*'s (AKN) damping functions (1994) (EASM-2) (see Section 6.2.1). For the EASM-1 and EASM-2, three wall-distance computation methods are tested, namely the Poisson, Eikonal and Hamilton differential equations (see Chapter 4 for details). For the cubic model, only the Poisson equation is used to achieve wall distances.

- **Results and discussion**

The mean streamwise velocity (U) predictions from the EASM-1, EASM-2 and cubic models along two vertical profiles are shown in Fig. 6.32. At z/H=0.15, the three models fail to predict the distortion on U as shown in the measurements. Near the centre line at z/H=0.35, the predicted U velocities are in a good agreement with the measurements for each of the models. The velocity distributions are similar to those presented by Mompean *et al.* (1996).

Fig. 6.33 shows the spanwise velocity (W) distributions again for two vertical profiles.

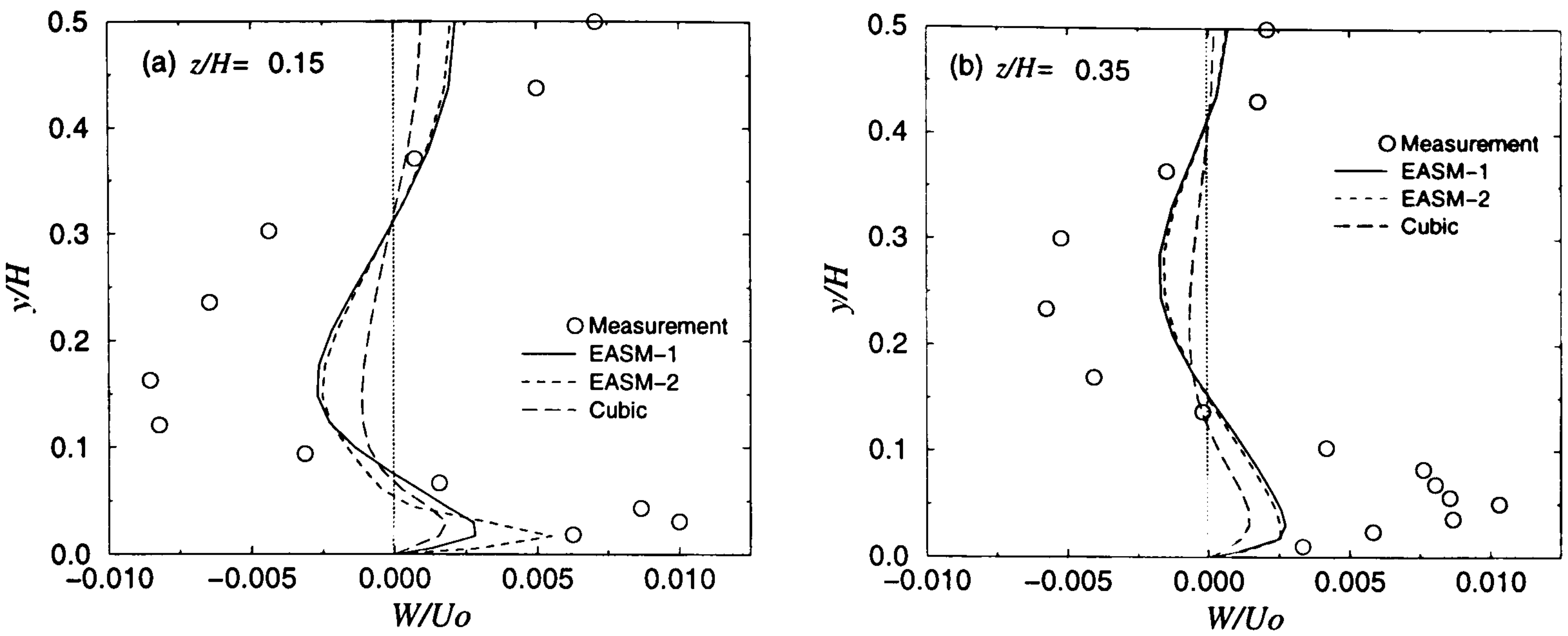

Figure 6.33: Comparison of mean spanwise velocity predictions with measurements for three nonlinear models at two locations.

Generally, the predicted positions of the zero crossings for the three models are similar to each other. This suggests that the computed postions of the secondary vortices within each octant are also similar (see Figs. 6.39-41). However, the agreement between the predictions and measurements at z/H=0.15 is not as good as that at z/H=0.35 (see Fig. 6.33(b)). Also, it is found that the cubic model predicts lower W velocity distributions than both the EASM-1 and EASM-2. Nevertheless, all three models underpredict the magnitude of W velocity in comparison with the measurements.

For the above results, wall distances are computed from the Poisson equation.

Wall distances at a cross-section ($y-z$ plane) computed from the Poisson, Eikonal and Hamilton-Jacobi equations are compared in Fig. 6.34. It is clearly seen that the Poisson method gives smoothing wall distances (Fig. 6.34(a)) at corners in comparison with the other two methods. The Eikonal method gives exact wall distances as discussed in Chapter 4. The Hamilton-Jacobi method gives a solution between the other two methods. These indicate that the turbulence damping influence of both walls is accounted for the best in the Poisson solution, followed by the Hamilton-Jacobi , and least by the Eikonal equation.

Comparisons between different wall-distance computation methods for the U and W

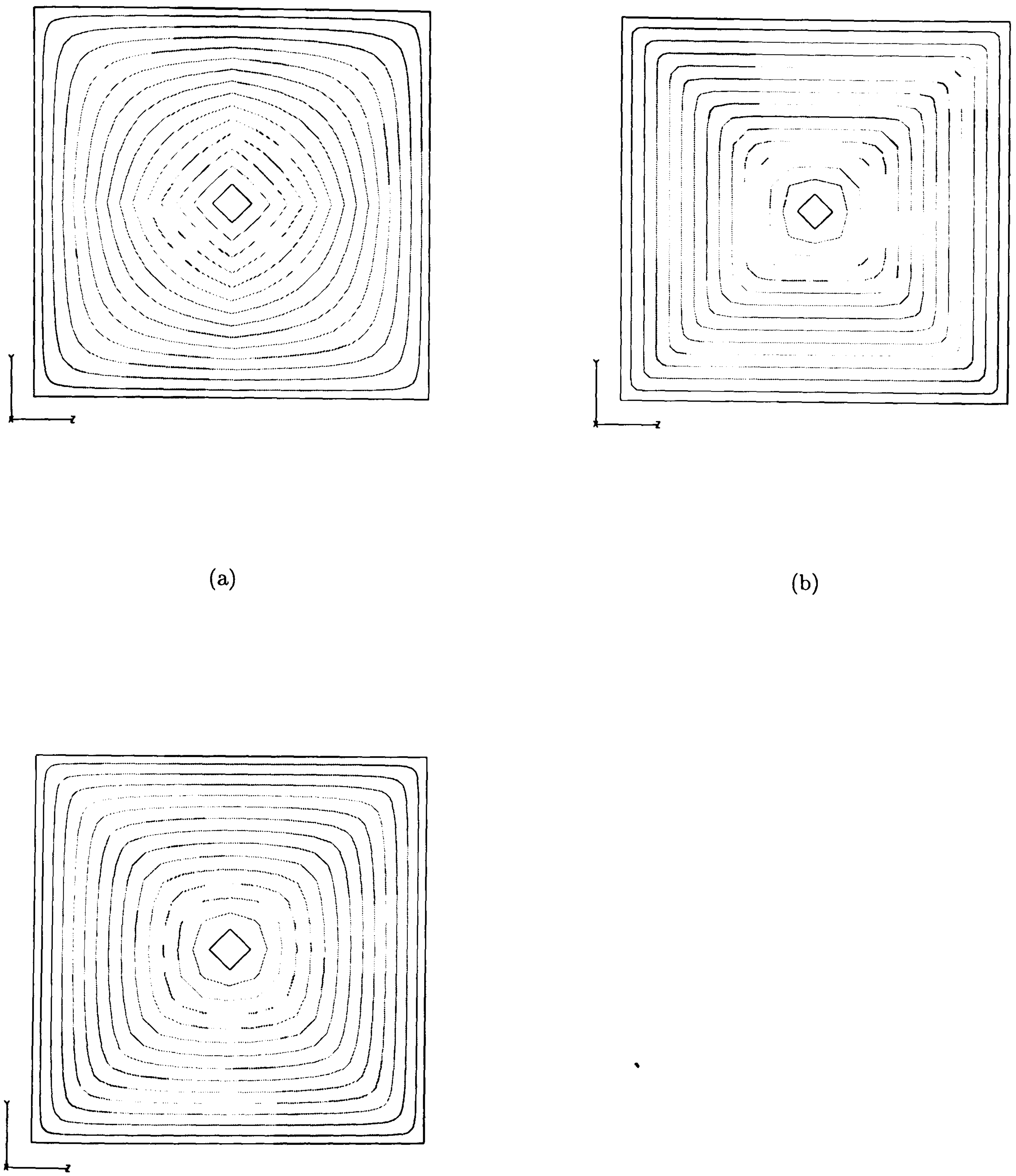

(a)

(b)

(c)

Figure 6.34: Wall-distance contours from the three solutions: (a) Poisson; (b) Eikonal and (c) Hamilton-Jacobi.

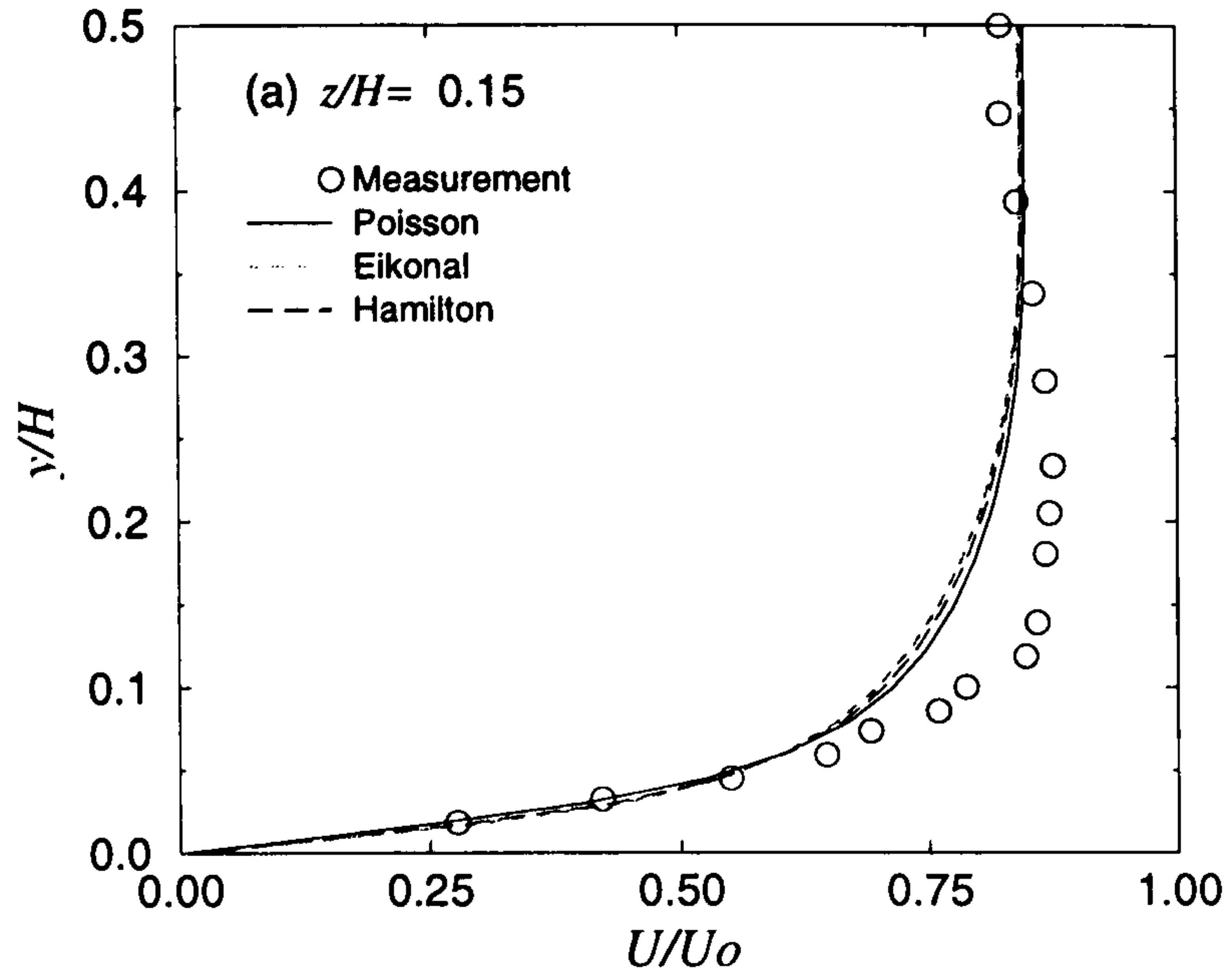

Figure 6.35: Comparison of mean streamwise velocity predictions with measurements for the EASM-1, using three wall-distance methods.

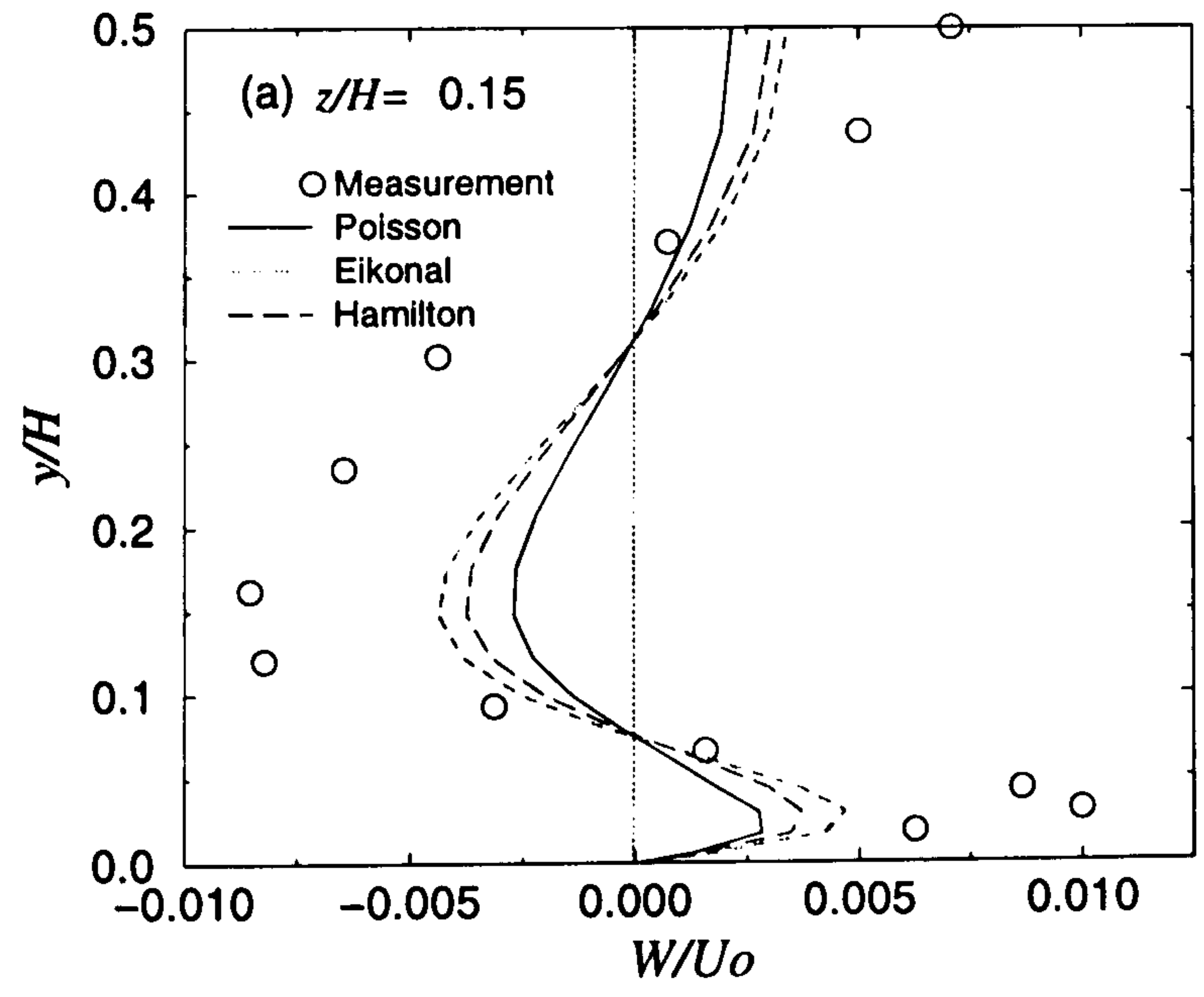

Figure 6.36: Comparison of mean spanwise velocity predictions with measurements for the EASM-1, using three wall-distance methods.

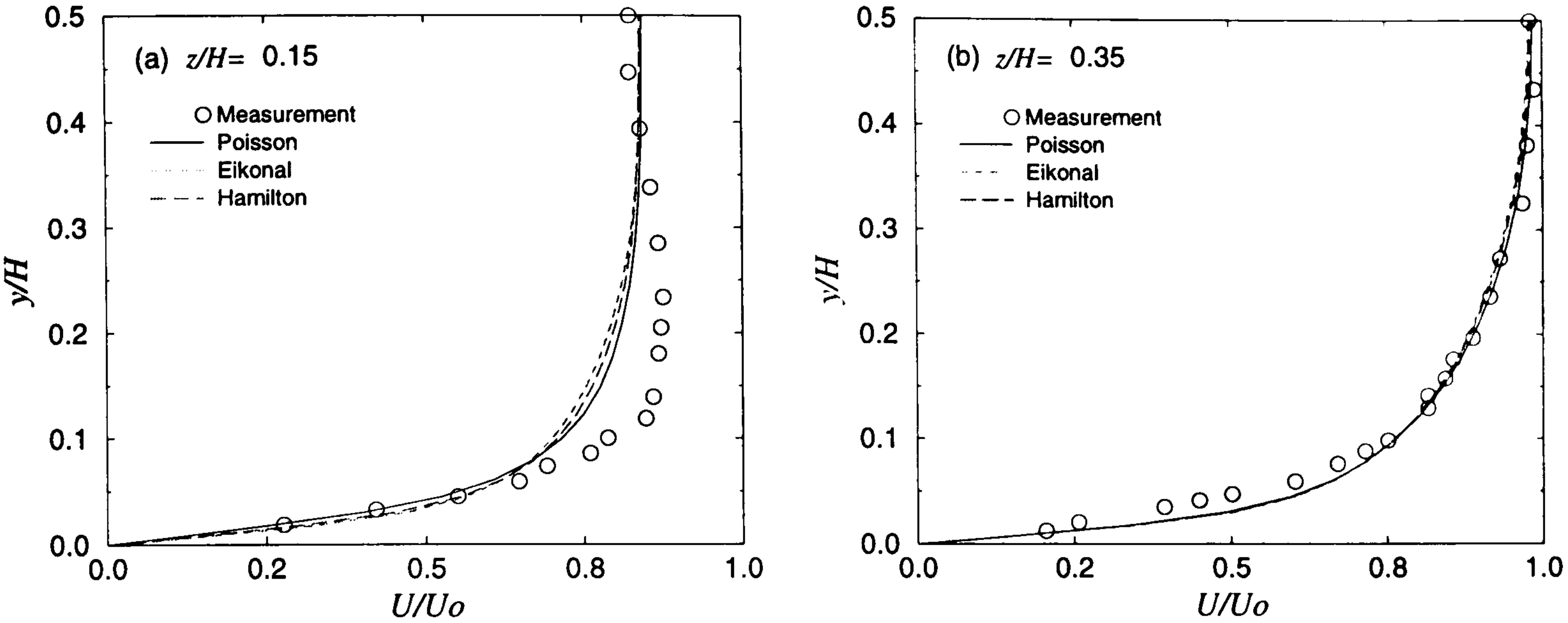

Figure 6.37: Comparison of mean streamwise velocity predictions with measurements for the EASM-2, using three wall-distance methods.

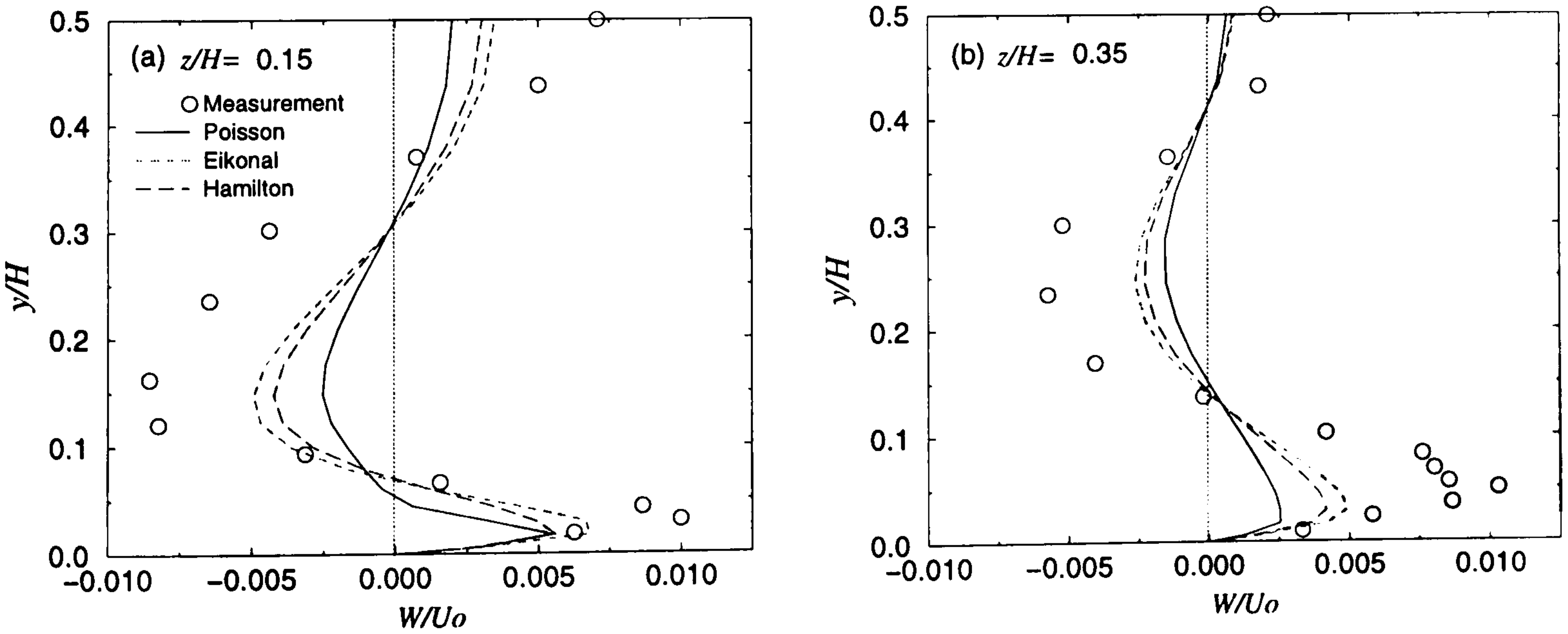

Figure 6.38: Comparison of mean spanwise velocity predictions with measurements for the EASM-2, using three wall-distance methods.

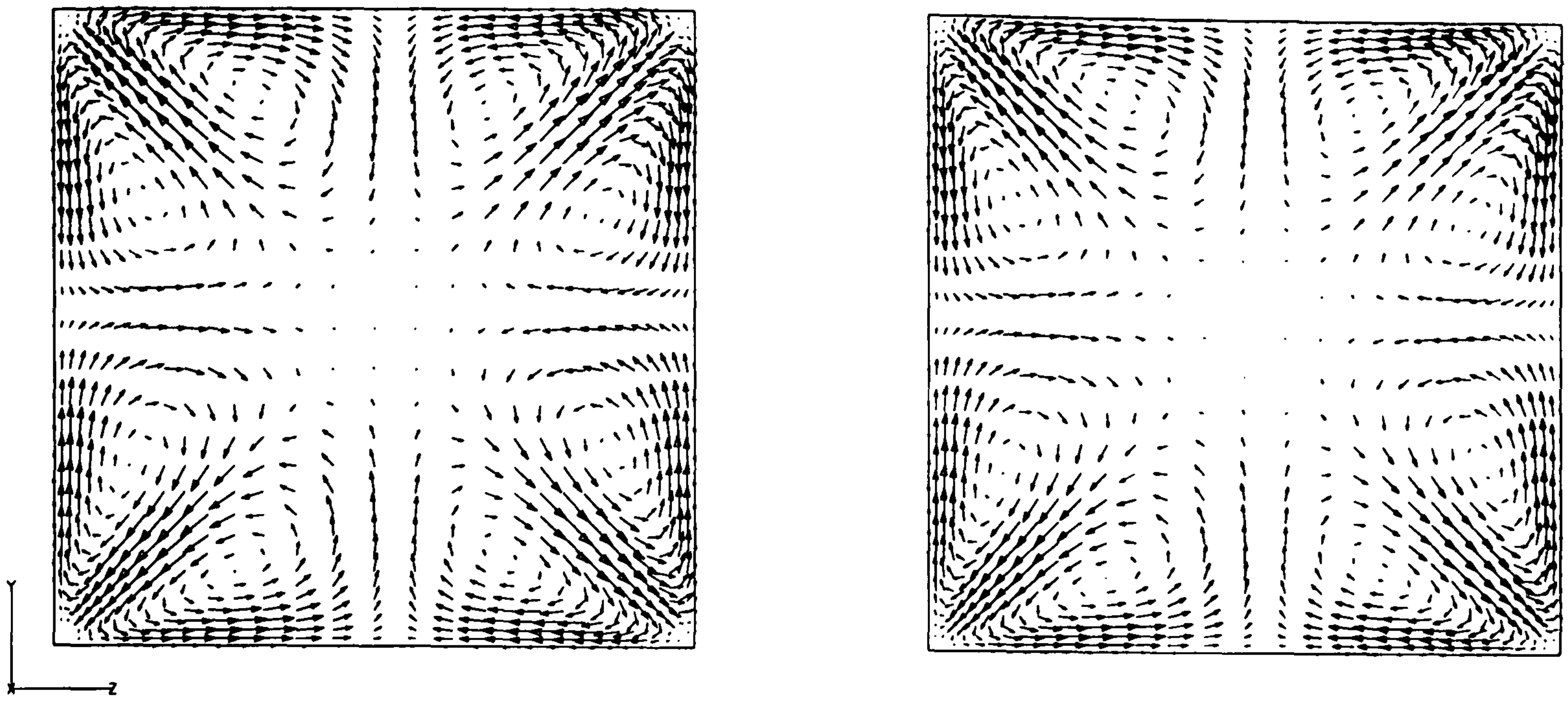

Figure 6.39: Predicted secondary velocity vectors from the EASM-1 (left: using Poisson equation; right: using Eikonal equation).

for the EASM-1 are presented in Fig. 6.35 and Fig. 6.36, respectively. Fig. 6.37 and Fig. 6.38 correpond to the EASM-2. As can be seen from the U velocity distributions, the three wall-distance methods give simliar predictions for the two profiles. However, the Eikonal solution gives the best W velocity predictions for the two profiles. The Poisson solution predicts the weakest W velocity distributions. The Hamilton solution gives the predictions between those from the Eikonal and Poisson solutions. These W results are unexpected because the Poisson method is supposed to give the best predictions owing to more damping involvement at the corners than the other two methods as shown in Fig. 6.34. Although the Eikonal solution improves the W velocity predictions, it still underpredicts the measurements.

For interest, the cubic model without the Yap correction term (see Chapter 3) has been tried. Comparing the two plots in Fig. 6.41, the predicted secondary velocity distributions from the cubic model with and without the Yap term are very similar. The U velocity profiles are also similar (not shown here). However, for W velocity

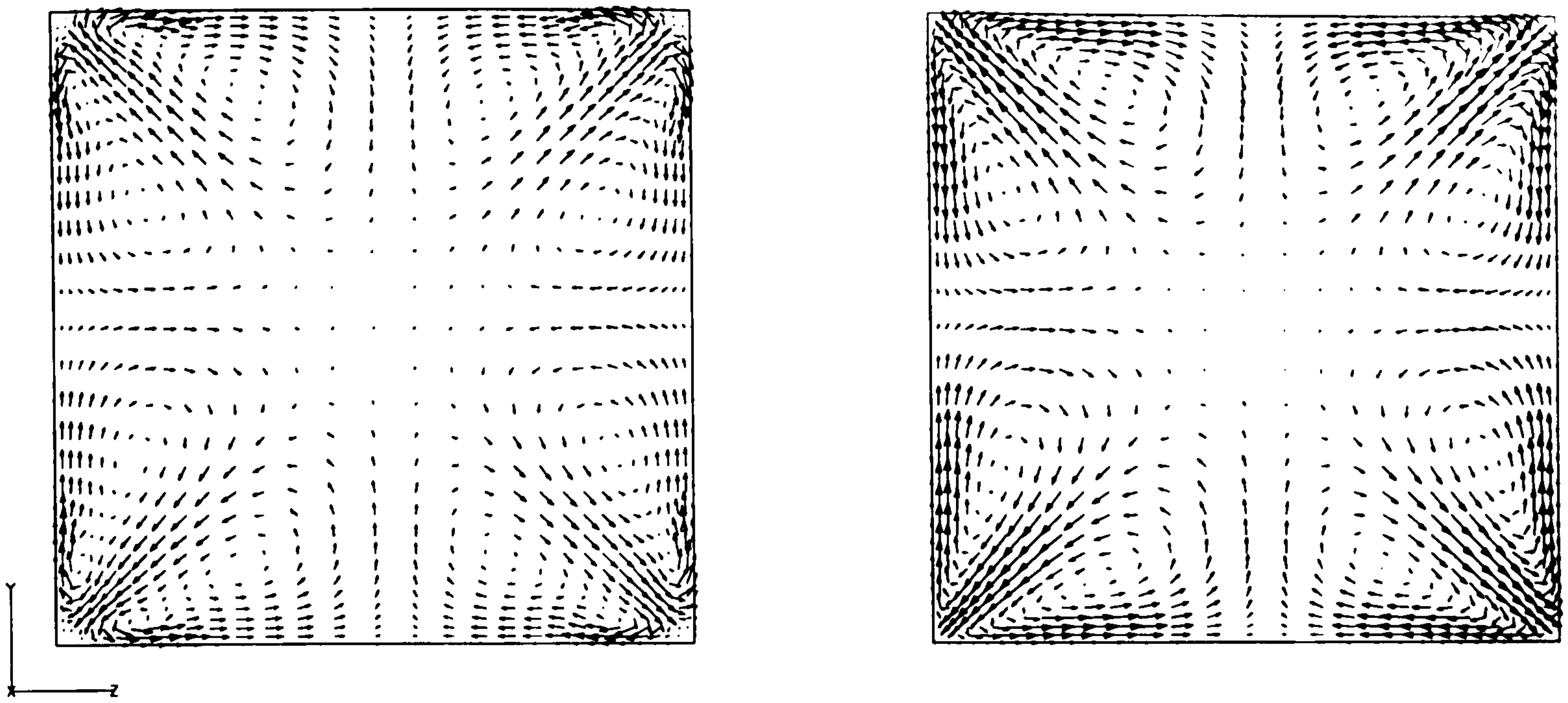

Figure 6.40: Predicted secondary velocity vectors from the EASM-2 (left: using Poisson equation; right: using Eikonal equation).

predictions, the error for the near-wall maximum W at the two profiles is around 30%, with the model without the Yap term giving better prediction. This is not surprising because the Yap term is calibrated for separated flows. There is no separation occuring in this 3D square-duct flow. Therefore, the constants in the Yap term are not well suited to this flow. The results shown in Fig. 6.32 and Fig. 6.33 are from the model without the Yap term.

In addition to the above three nonlinear models, the Speziale nonlinear $k-l$ model was tested. When coupled with the van Driest damping function and the Poisson method for wall distances, this model can capture the secondary flows. However, neither the Eikonal, nor the Hamilton-Jacobi method with a low value of the constant, C (see Eq. (4.32)), is capable of predicting these well. Fig. 6.42 compares the damping functions of Mompean *et al.* (1996) and van Driest (see Eq. (3.70)), in which $d = \sqrt{y^2 + z^2}$. The former uses a search procedure to obtain wall distances, while the latter uses both the

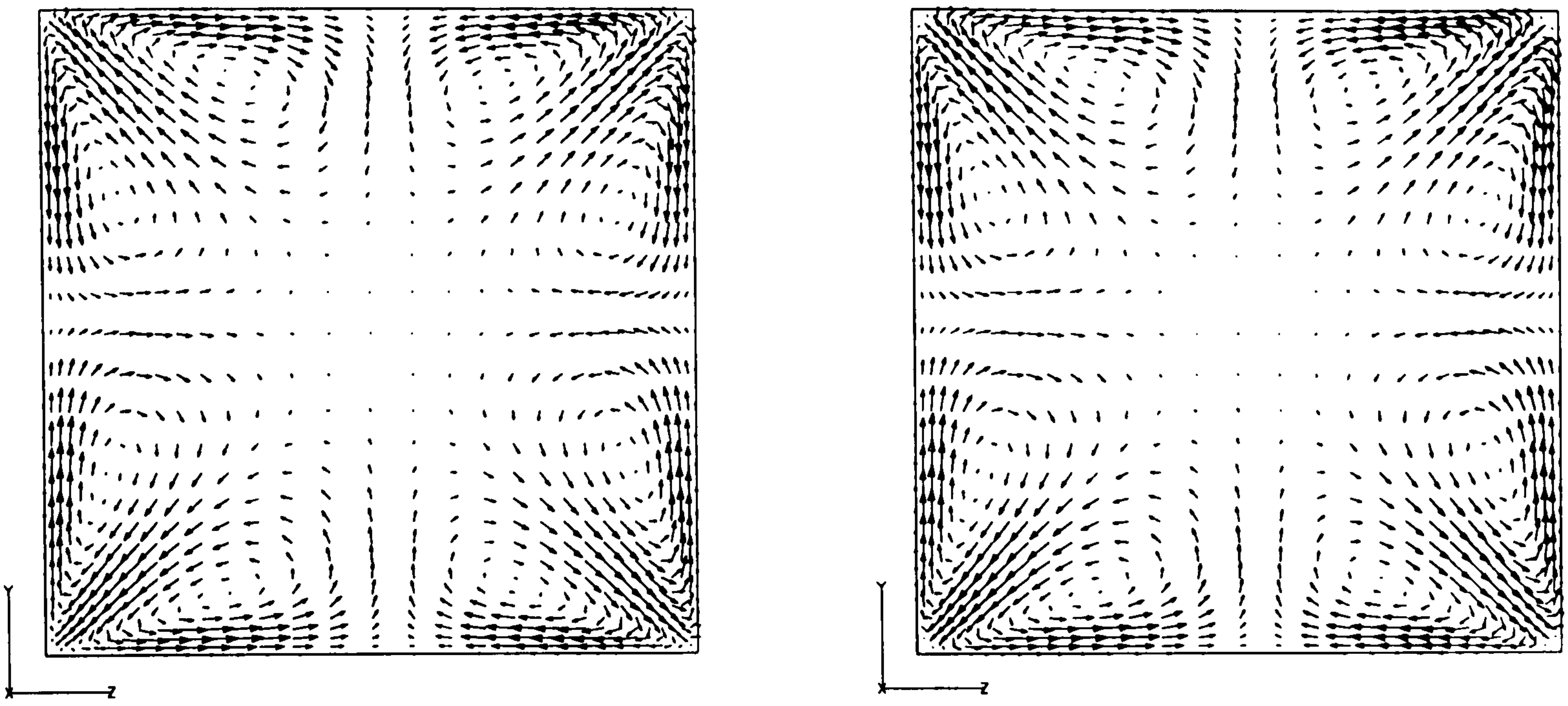

Figure 6.41: Predicted secondary velocity vectors from the cubic model (left: without Yap correction; right: with Yap correction).

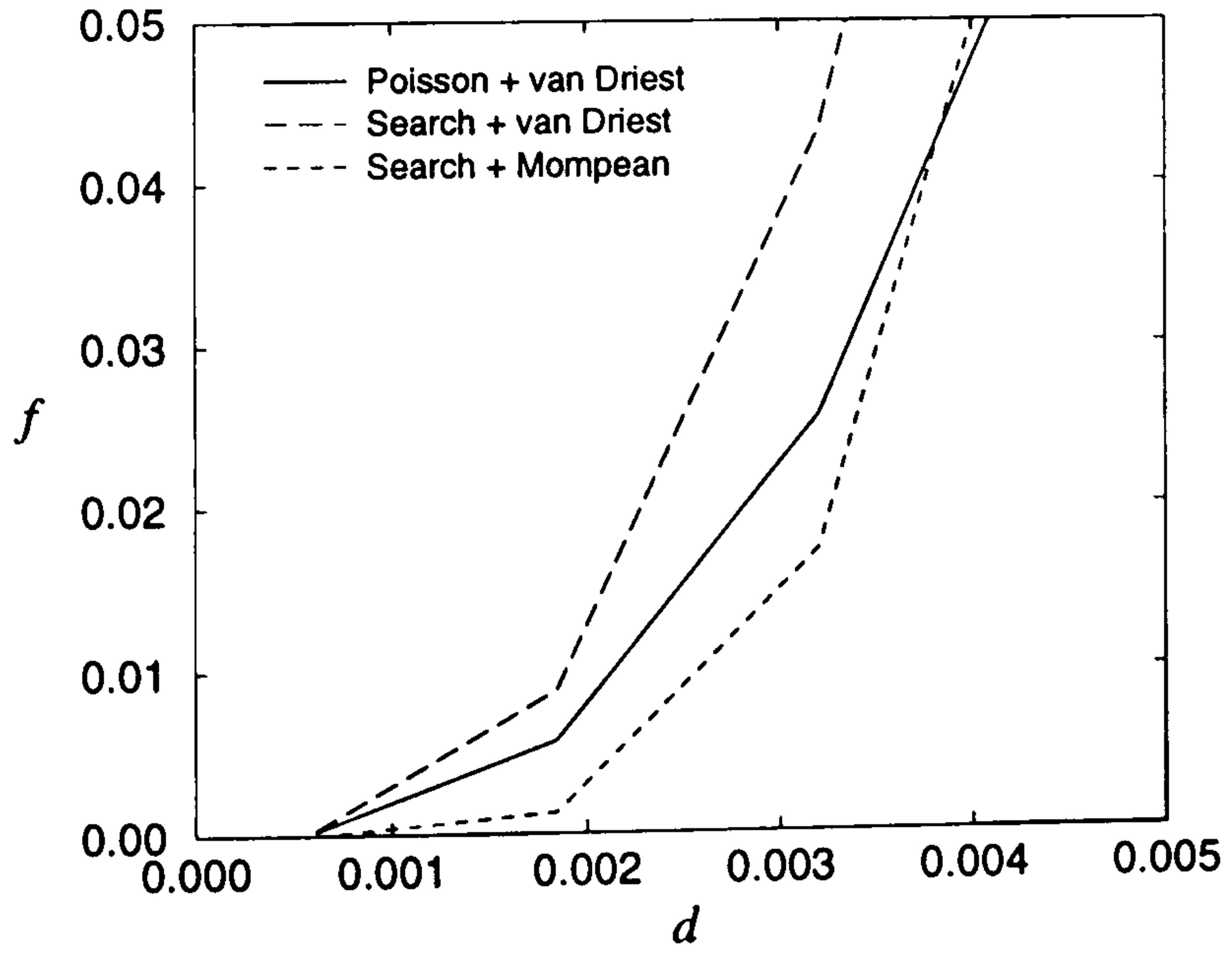

Figure 6.42: Comparison of damping functions along corner bisector.

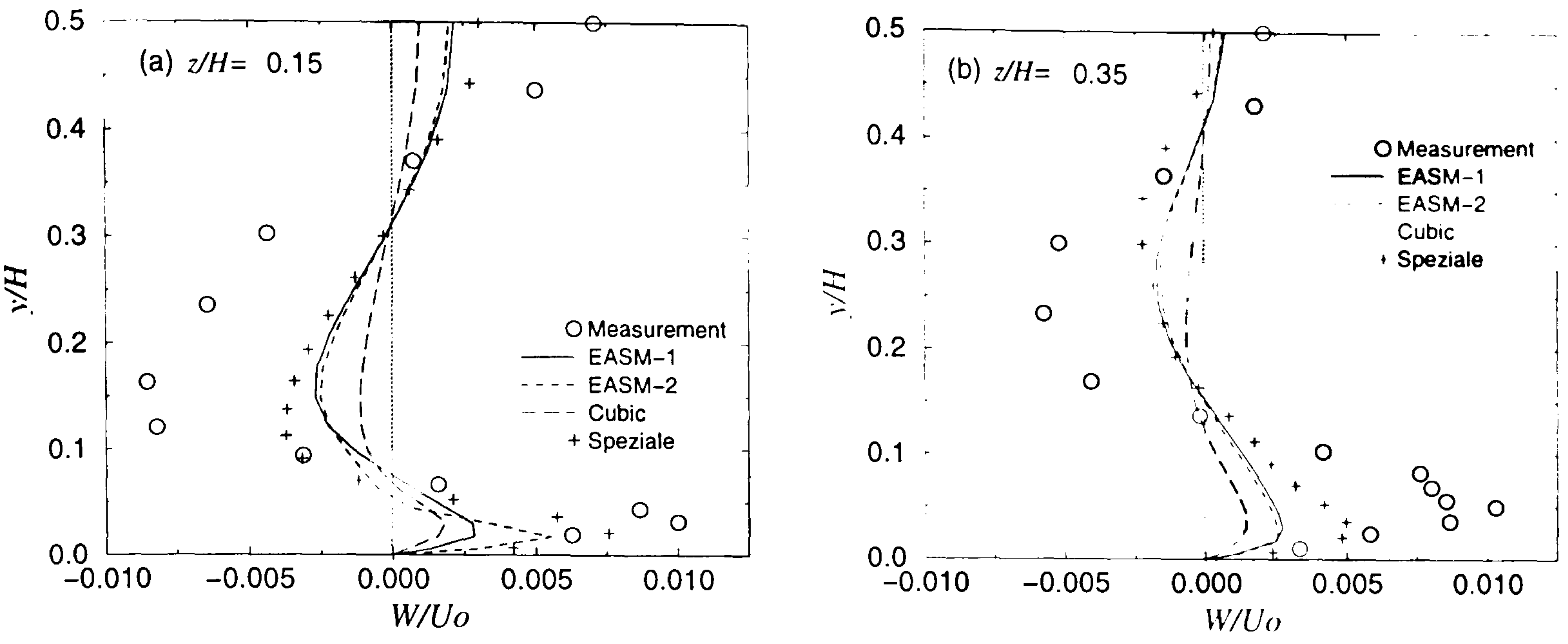

Figure 6.43: Comparison of W-velocity predictions with measurements for nonlinear models at two locations.

Poisson method and search procedure. As can be seen, at the corner, the Mompean *et al.* method (which attempts to match DNS data behaviour) damps more than the van Driest, as would be expected. The Poisson method (and also Hamilton-Jacobi with a large C) gives a wall-distance function that yields damping that is more consistent with the Mompean *et al.*'s.

Fig. 6.43 shows the comparison of W-velocity distributions for the four nonlinear models. As can be seen, the Speziale model with van Driest damping function predicts the near-wall W-velocity best.

Overall, the four nonlinear models tested reasonably capture Prandtl's motions of the second kind. The EASM-1, EASM-2 and Speziale models give better W predictions than the cubic model. Also solutions are sensitive to wall distances and the turbulence damping modelling in the corner regions.

Table 6.7: Flow parameters.

Re_τ	$L_x \times L_y \times L_z$ (m)	ρ (kg/m^3)	μ (N.S/m^2)	u_τ (m/S)	$\frac{dp}{dx}(\beta)$ (Pa/m)
180	$2\pi h \times 2h \times \pi h$ h=1	1	1/180	1	1

Table 6.8: Simulation parameters.

$N_x \times N_y \times N_z$	Δx	Δx^+	Δz^+	Δ
Grid : 65 × 67 × 65	0.01	17.4	8.7	Δy

6.3 LES validation

6.3.1 3D fully-developed channel flow

- **Problem description**

In the current work, a 3D fully developed channel flow with $Re_\tau = 180$ based on the friction velocity and the channel half-height is selected. The benchmark DNS data of Kim *et al.* (1987) are used. The flow domain size is $2\pi h \times 2h \times \pi h$ (x, y, z), where h is the channel half-height. The other flow parameters are given in Table 6.7.

For this channel flow, periodic boundary conditions are used in the streamwise (x) and spanwise (z) directions. No-slip conditions are applied at the walls. Uniform grid spacing is used in the x and z directions. The mesh in the wall-normal direction is stretched with an expansion factor of 1.15 to ensure that the first grid points are at $y^+ < 1$. The simulation parameters are summarized in Table 6.8.

- **Results and discussion**

The SGS models tested are the Smagorinsky and Yoshizawa ones discussed in Chapter 3. Fig. 6.44 compares the resolved mean velocity profiles and the root-mean-square (rms) velocity fluctuations with benchmark data. The rms statistical velocity fluctuation is computed by

$$u_i' = \left(< \overline{u}_i^2 > - < \overline{u}_i >^2\right)^{0.5} \tag{6.8}$$

where $< \bullet >$ donates the space- (in the homogeneous direction) and time-averaging operator.

As can be seen from Fig. 6.44, the predicted law of the wall matches the benchmark data very well for both SGS models. The resolved velocity fluctuations are also in good agreement with the benchmark data except for the Yoshizawa predictions of the v' and w' with slightly lower values.

The results presented above for the channel flow show that the Smagorinsky and Yoshizawa models have been coded correctly.

6.4 Zonal LES validation

The case used is still a 3D fully developed channel flow. The domain size is the same as that applied in LES validation, i.e. $2\pi \times 2 \times \pi$, but a flow with $Re_\tau = 1050$ instead. Again periodic boundary conditions and uniform grids are employed in the x and z directions. The benchmark LES data of Piomelli (1993) are used.

The following presents results and discussions for the S-A based DES and $k - l$ based zonal LES (ZLES).

6.4.1 S-A based DES validation

Simulation parameters are summarized in Table 6.9, where the subscript, 'int', represents the interface of RANS and LES. Grid 1 and Grid 2 have different grid spacing in the streamwise direction. Correponding to these two grids, simulations are denoted by DES-1 and DES-2, respectively.

Fig. 6.45 shows the length scales for full RANS and DES. As can be seen, the modelled LES scale is grid dependent. When defining d_{LES}, the maximum among the grid spacings Δx, Δy and Δz is chosen. To compare performances of DES with RANS

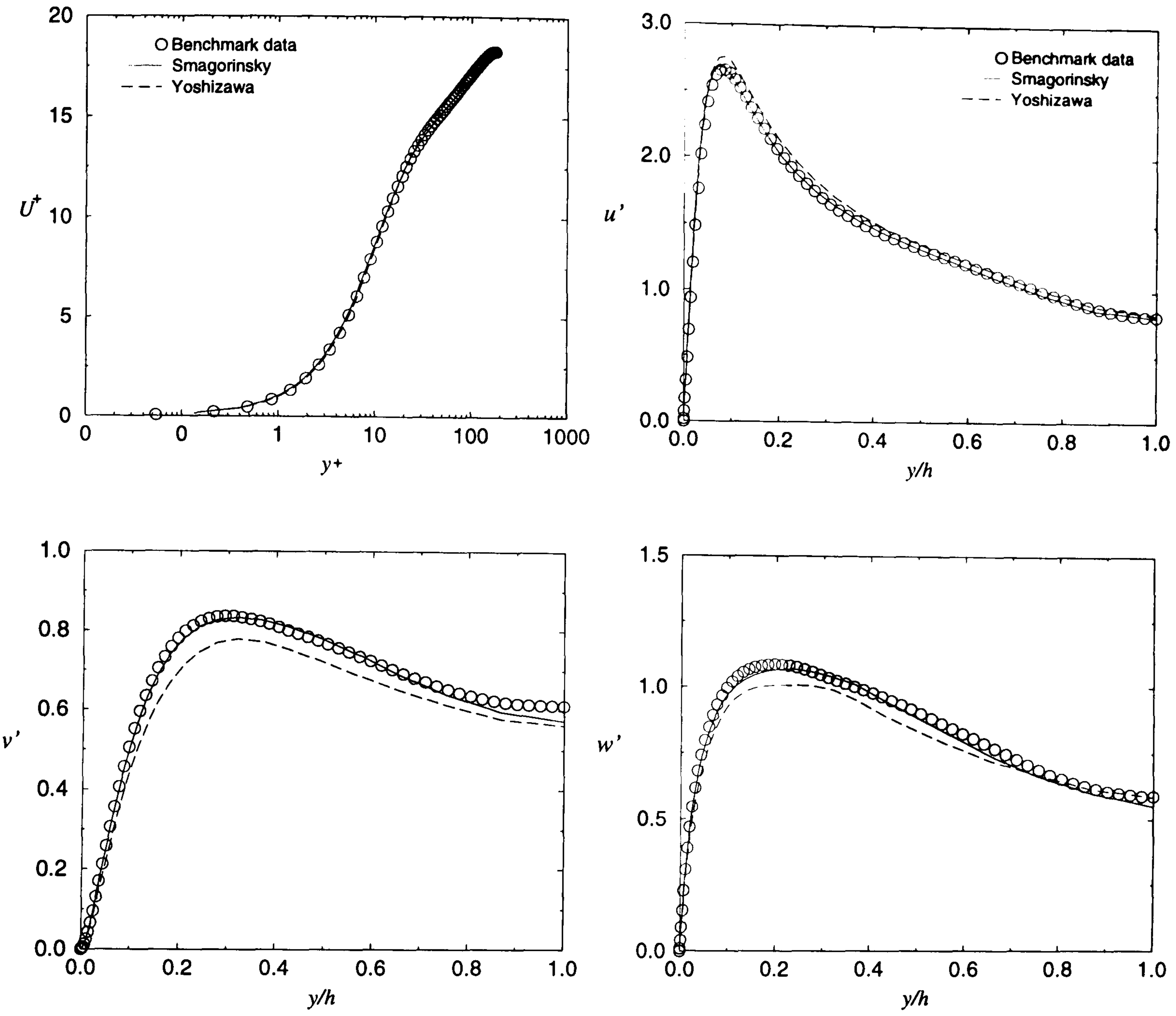

Figure 6.44: Comparisons of resolved mean velocity and of root-mean-square velocity fluctuations with benchmark data.

Table 6.9: Simulation parameters for DES.

$N_x \times N_y \times N_z$	Δx	Δx^+	Δz^+	y_{int}	y^+_{int}
Grid 1: 33 × 65 × 33	0.2	200	100	0.13	138
Grid 2: 65 × 65 × 33	0.1	102	100	0.07	75

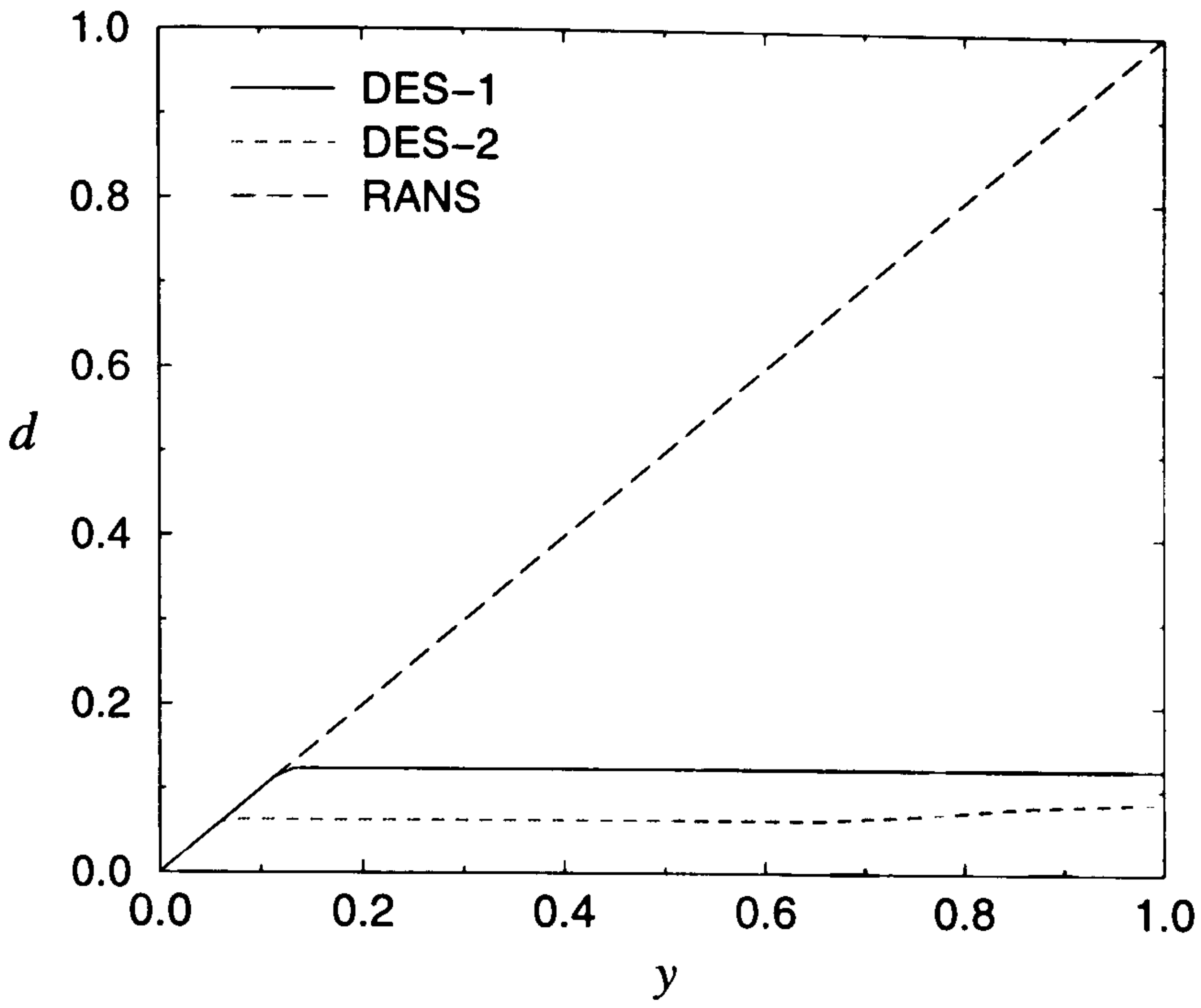

Figure 6.45: Length scales for the S-A RANS and DES

S-A model on the same RANS grid, only DES results from Grid 1 is used in the following parts.

The left frame in Fig. 6.46 shows the mean velocity profiles. The DES profile rises above the log law and displays a shift between modelled log layer and upper layer as reported by Nikitin *et al.* (2000) and Spalart (2000). The studies undertaken by Nikitin *et al.* (2000) and Spalart (2000) show that grid refinement does not sufficiently improve the shift. For Grid 1, $\Delta x/h(h = 1)$ =0.2. Nikitin *et al.* (2000) point out that the resolved turbulence usually 'dies' if $\Delta x/h = 0.2$. This leads to a steady one-dimensional solution as shown in the right figure in Fig. 6.46. Fig. 6.47 compares the eddy viscosity profiles for full S-A RANS and DES-1. It clearly shows that the eddy viscosity in LES region for DES is smaller than that in the same region for the full RANS. This is owing to the length scale becoming smaller.

The reason for the mismatched mean velocity is due to the transition between the LES and RANS regions. The two regions in each side of the interface interact with each other. The eddy viscosity at the LES side of the interface is lower than if it were a RANS region. This change of the eddy viscosity causes a steep velocity gradient (see Hamba, 2001) as shown in Fig. 6.46 (left figure).

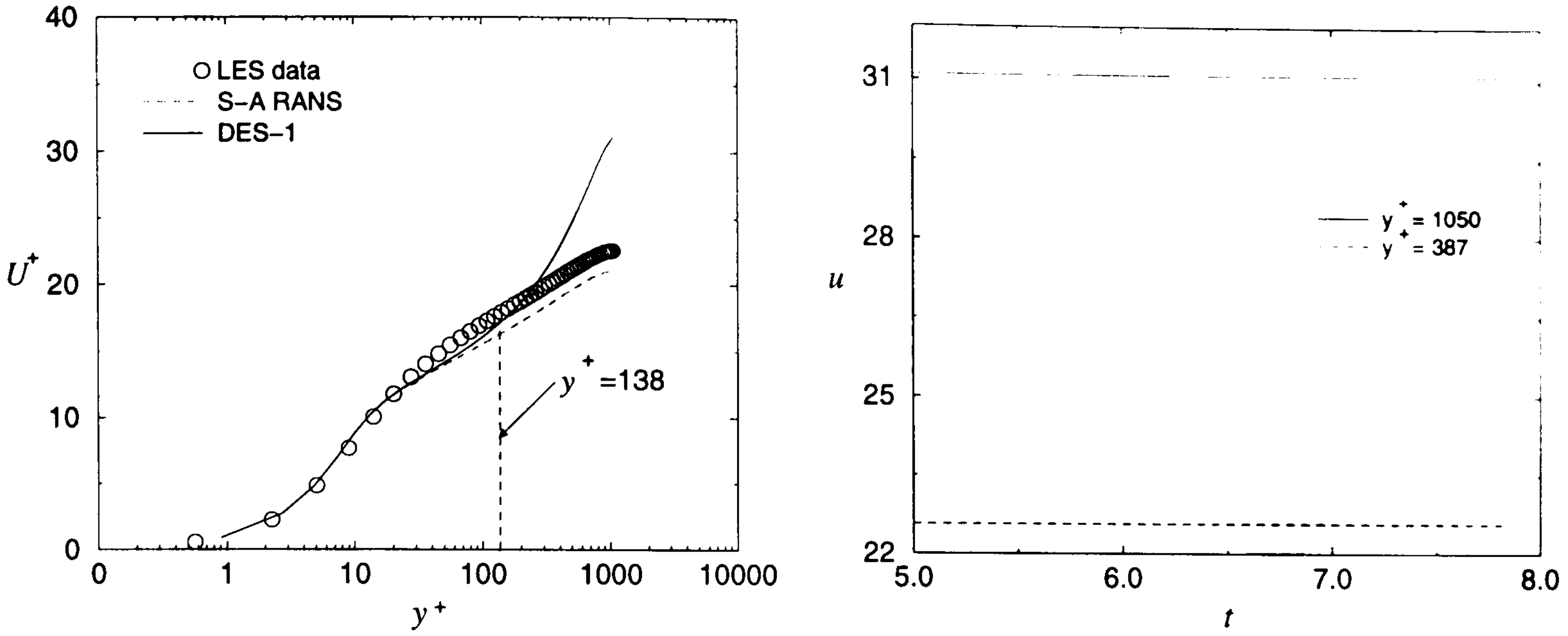

Figure 6.46: Mean velocity profiles (left) and time histories of velocity (right).

To circumvent the mismatching problem in the mean velocity profile, several ideas have been proposed. Piomelli *et al.* (2003) investigate four methods, namely lowering the y^+_{int} (by decreasing the values of C_{DES}), using different filter widths Δ, blending the S-A inner-layer model and the Smagorinsky SGS model and introducing a backscatter model based on stochastic forcing. The former three measures do not effectively correct the mean velocity profile and the shift in the logarithmic layers still remains. However, the last method improves the mean velocity profile and has proved to be successful.

It is not surprising that DES has some problems for a plain channel flow because this approach is not adjusted for this flow (Spalart, 2000). It is initially designed for external flows with separation. Despite this deficiency, fairly accurate results can be obtained for a plain channel flow, provided that a proper grid is used (see Nikitin *et al.* (2000) and Piomelli *et al.* (2003)).

From the above results, it can be found that DES solutions can have grid sensitivity. To achieve reasonable results, in general, near-cubic grid cells in the core region and very flat cells in the near-wall region are required.

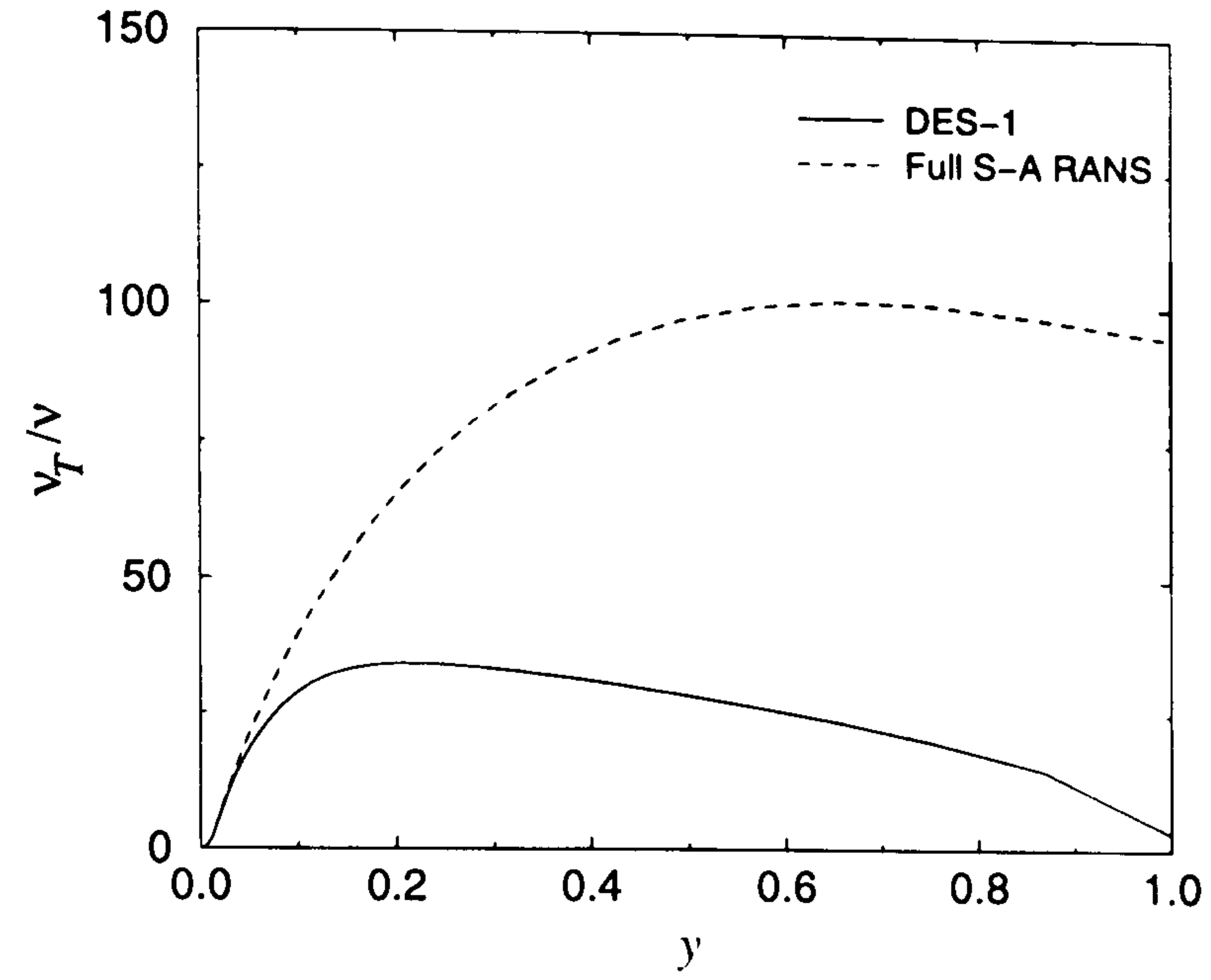

Figure 6.47: Eddy viscosity profiles.

Table 6.10: Simulation parameters for the ZLES.

Case	$N_x \times N_y \times N_z$	Δx	Δx^+	Δz^+	j_{int}	y_{int}	y^+_{int}
Case 1	Grid 1: 33 × 65 × 33	0.2	200	100	14	0.06	63
Case 2	Grid 1: 33 × 65 × 33	0.2	200	100	10	0.03	31

6.4.2 $k - l$ based RANS/LES validation

Simulation parameters are summarized in Table 6.10. As can be seen, the interface setting is prescribed. The values of j_{int}, y_{int} and y^+_{int} represent the starting position for LES in different ways. Hence, the number of cells in the RANS region is $j_{int} - 1$. Two interface settings are investigated, denoted Case 1 and Case2 respectively.

Fig. 6.48 compares the smoothed length scale and turbulent viscosity with and without smoothing for Case 1. As can be seen, without smoothing, the viscosity discontinuously changes from the RANS one to much lower SGS viscosity. The effect of smoothing on the length scale occurs at the interface between RANS and LES regions. This reduces the steep change for the length scale and thus also for the turbulent viscosity.

Fig. 6.49 shows the predicted mean velocity profiles together with the LES data of Poimelli (1993). As can be seen, the law of the wall for both Case 1 and Case 2 is in good agreement with the LES data. However, like DES prediction discussed in the previous

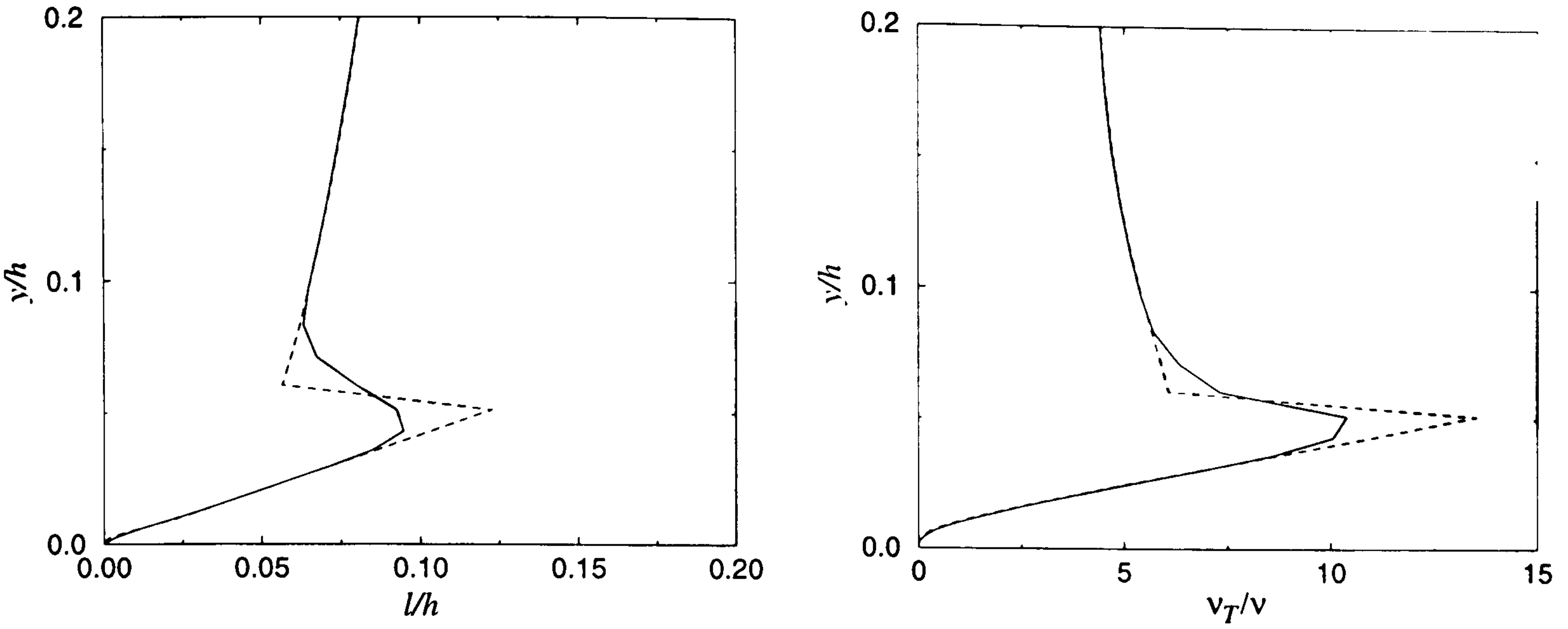

Figure 6.48: Length scales (left) and turbulent/SGS viscosities (right) for Case 1 (Solid line: smoothed variables; dashed line: non-smooth variables).

section, there is a mismatching point near the location of the switching line for each case. This is attributed to the change of turbulence viscosity as shown in Fig. 6.48. From the theoretical point of view, as argued by Piomelli (2003), the eddy viscosity is lower in the LES region than if it were in a RANS region, but the Reynolds-stress-generating scales have not been formed. Therefore, the resolved motions cannot support their share of the shear stress, while the model has already switched to the LES. The only way to reach the equilibrium value of the shear stress is by a velocity gradient increase that balances the eddy-viscosity decrease. It can be seen from Fig. 6.50 that the turbulent viscosity obtained by the full $k - l$ RANS is larger than that obtained either by the zonal LES or by pure LES using the same grid. In the pure LES computation using the same grid as Case 1, the Yoshizawa (1993) SGS $k - l$ model is used. Also it is noted that the modeled viscosity in the RANS region for the hybrid method is larger than that the equivalent LES value (if using a fine grid for pure LES, the viscosity is lower than that shown in Fig. 6.50). This implies that the RANS predicts an excessive level of turbulence in the RANS region within the framework of the hybrid approach because there is near-wall resolved turbulence. This results in the contribution of Temmerman *et al.* (2002, 2003) and Tucker and Davidson (2003b) (see Chapter 3).

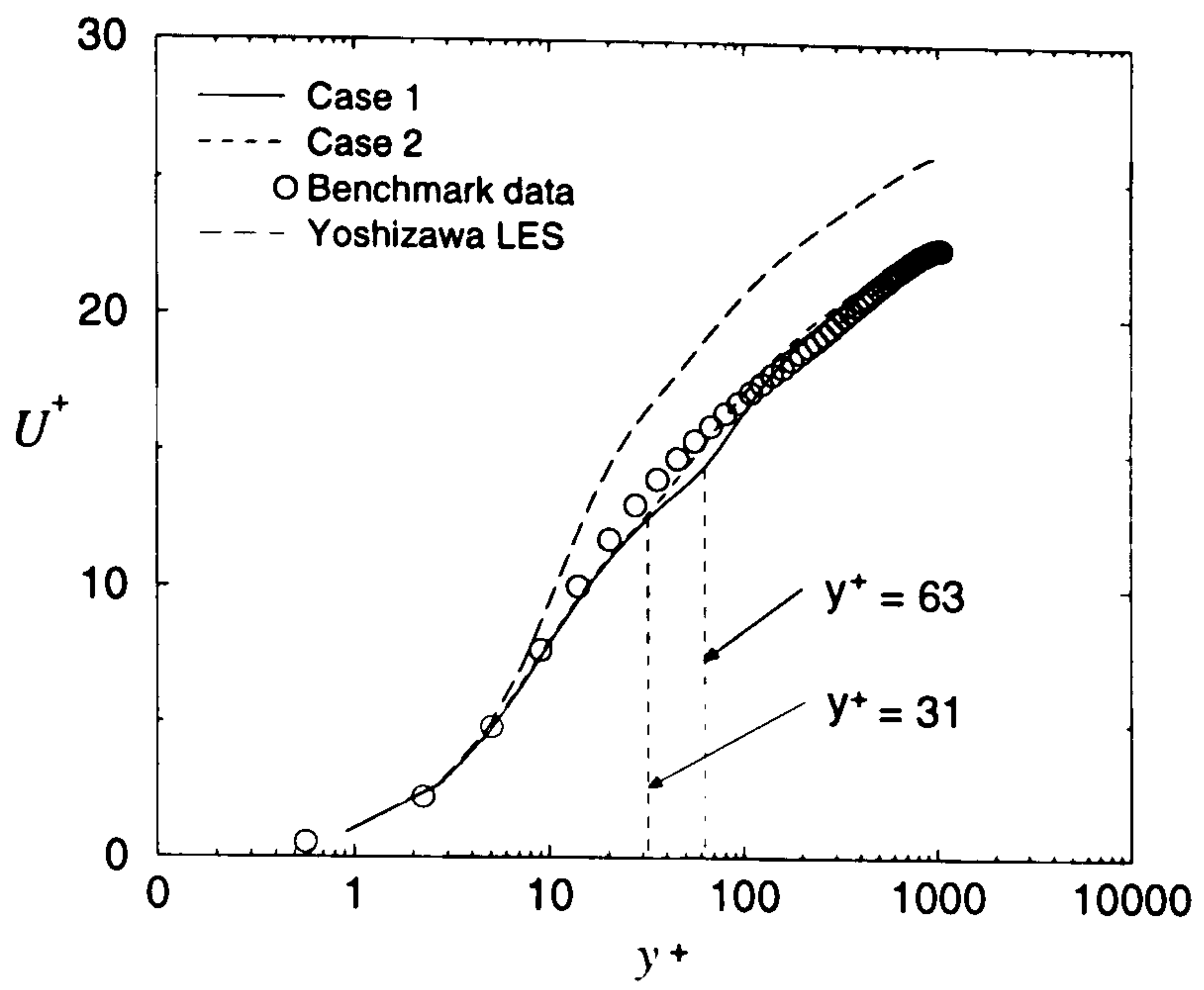

Figure 6.49: Mean velocity profiles

Fig 6.51 presents the resolved, modelled and total turbulent kinetic energy obtained by the ZLES. Owing to the large viscosity provided by the RANS computaion, the resolved k is over-predicted and thus total k is much higher than benchmark LES data especially in the transition regions from the RANS to LES modes for both Cases 1 and 2. The root-mean-square velocity fluctuations are shown in Fig. 6.52. The predicted results are not in good agreement with LES data. As can be seen, the streamwise fluctuations, u', are too large, while the other two fluctuations, v' and w', are too small.

From the results for Cases 1 and 2, it can be found that predictions depend on the position of the RANS/LES interface. In addition, the filter width also affects simulation results (see Tucker and Davidson (2003b), Davidson and Peng (2001)). Another method of defining the RANS/LES interface has been tested in the work of Tucker and Davidson (2003d), i.e. natural length scale change. The process is as follows. Comparing two length scales, i.e. $l_\mu = \min(\Delta, l_{\mu,\mathrm{RANS}})$ and $l_\epsilon = \min(\Delta, l_{\epsilon,\mathrm{RANS}})$, when $l_\mu = l_{\mu,\mathrm{RANS}}$, RANS mode is switched on. Otherwise LES mode holds. It should be noted that the mode change is based on l_μ. From the results shown in their study for the channel flow, no big difference has been found between the results from this interface setting and those from other settings.

To compare the ZLES results with pure LES predictions on coarse grids, the mean

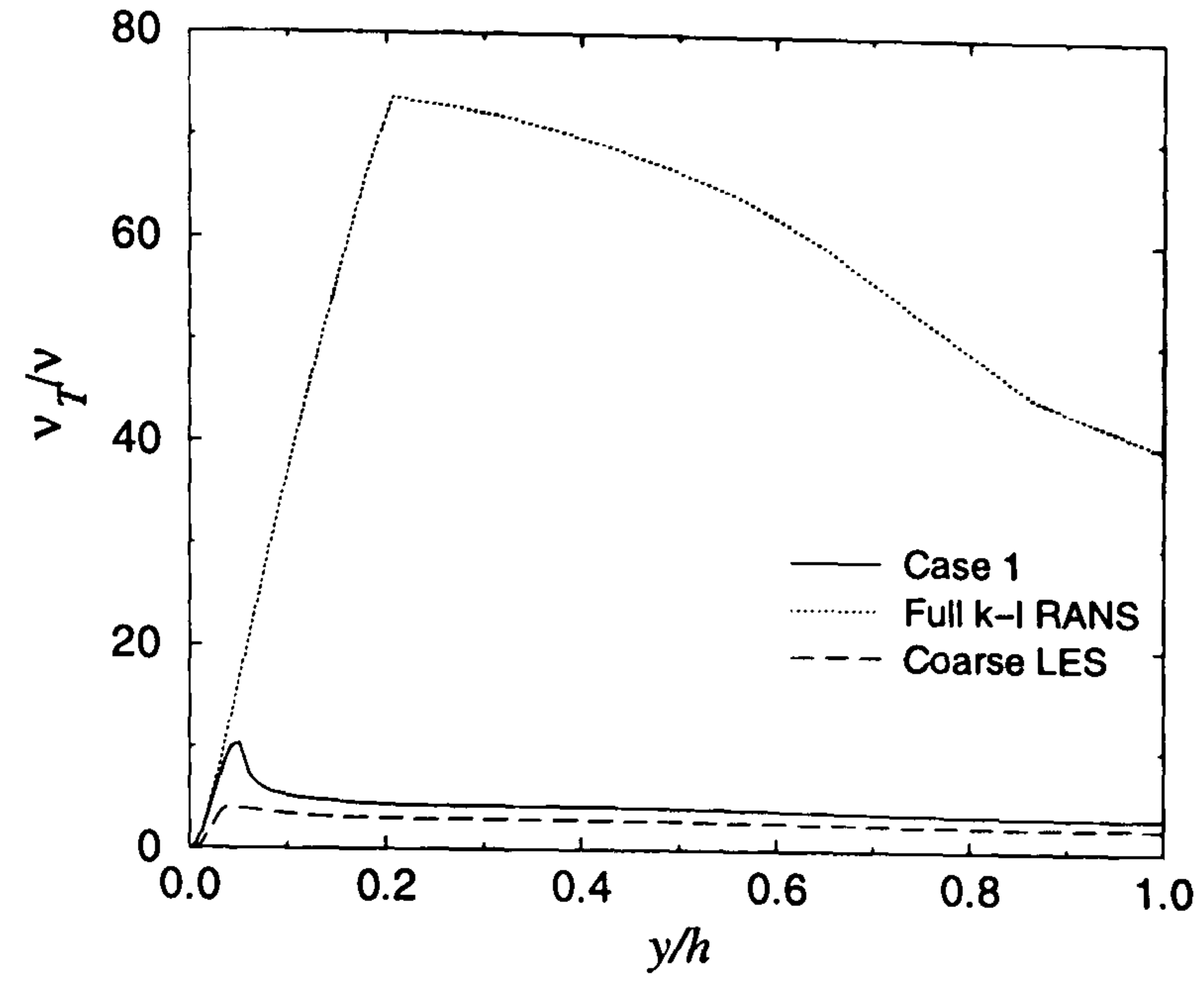

Figure 6.50: Comparison of eddy-viscosity profiles.

velocity distribution from the Yoshizawa LES is also shown in Fig. 6.49. This demonstrates that pure LES does not perform well on coarse grids. However, the ZLES is able to give satisfactory results.

Overall, the general results obtained from the hybrid RANS/LES method for a channel flow in this study are very similar to those published in the literature mentioned before.

6.5 Summary

This chapter has presented and discussed the simulation results from (U)RANS, LES and zonal LES approaches for test cases. Comparisons have been made with either measurements, benchmark data or predictions of other works. For (U)RANS, the implemented turbulence models (namely the S-A, low-Reynolds-number versions of the $k-\epsilon$ (CH, LS and LSY), EASM and its low-Reynolds-number versions, cubic and zonal models) have been carefully tested for three cases. They are two-dimensional plain channel, backward-facing step and ribbed-duct flows. Generally, the level of agreement between predictions and measurements is consistent with that gained by other works. Surprisingly, the nonlinear cubic model did not perform well for the ribbed case. This needs

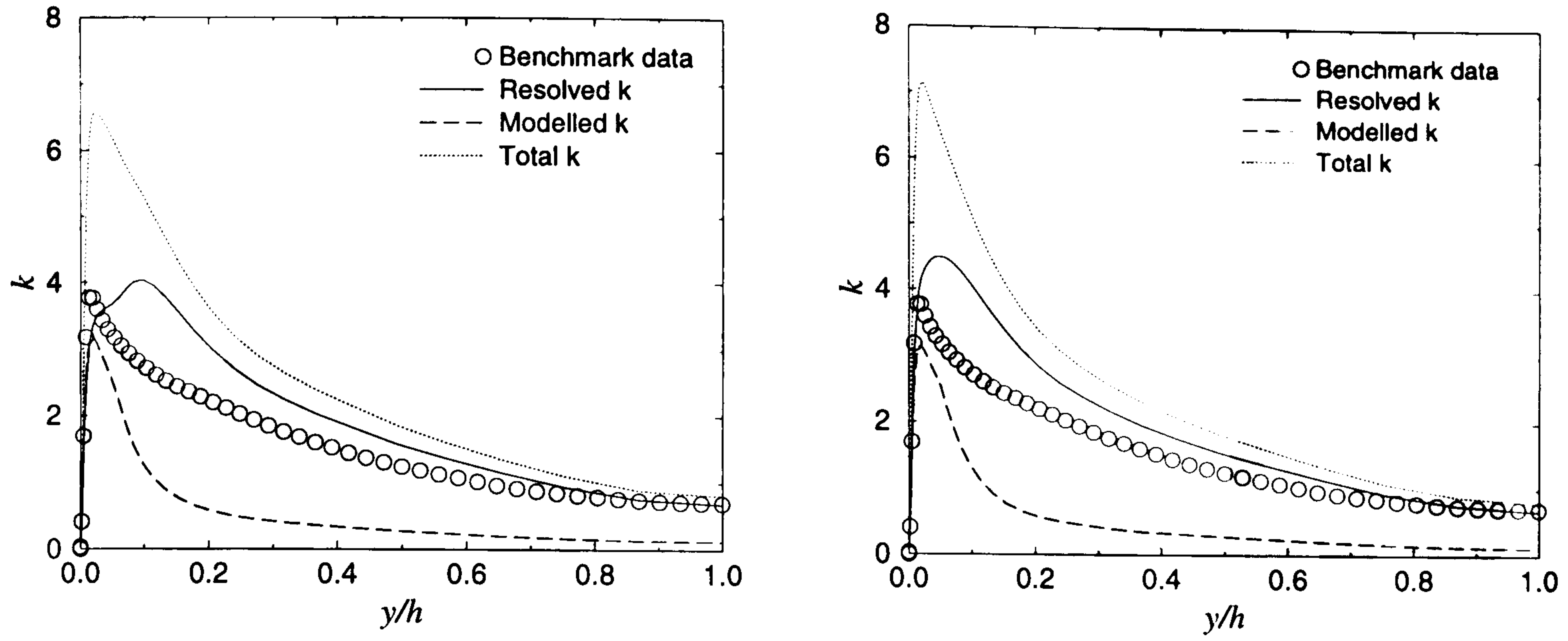

Figure 6.51: Turbulent kinetic energy. Left figure for Case 1; right for Case 2.

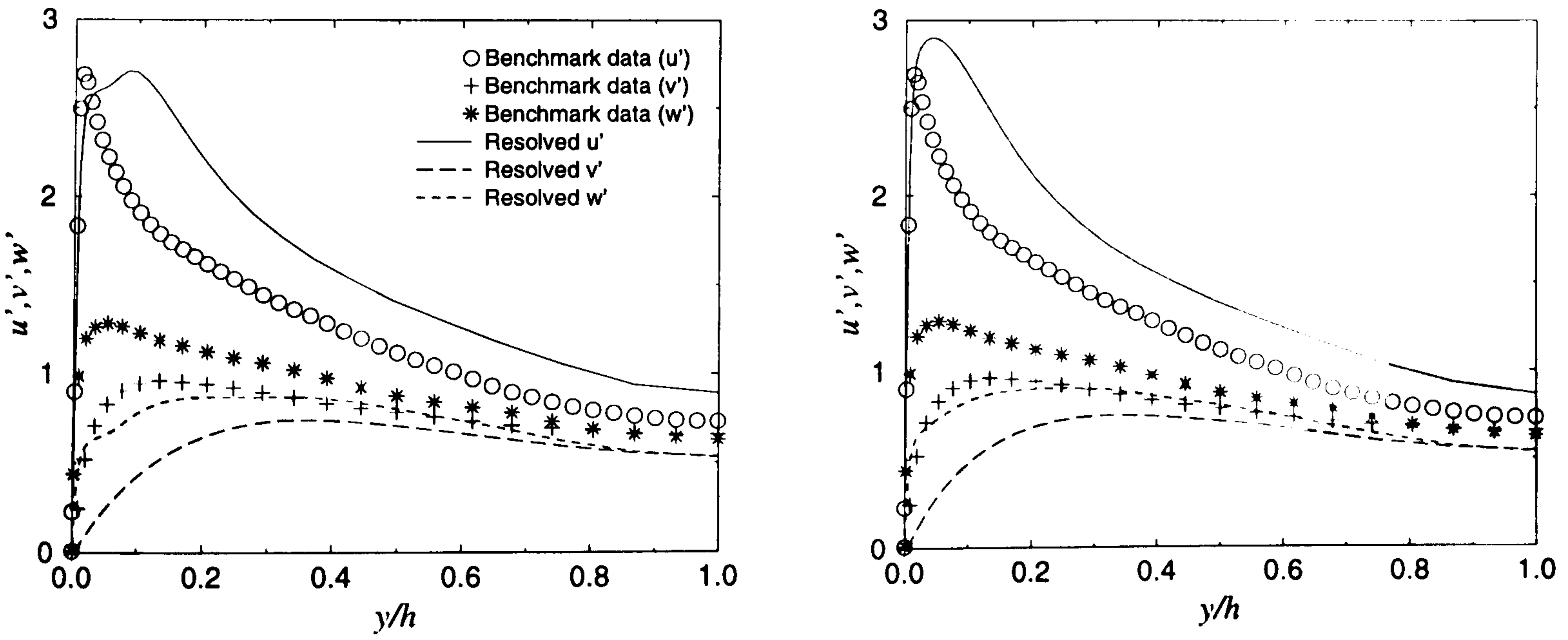

Figure 6.52: Resolved rms velocity fluctuations. Left figure for Case 1; right for Case 2.

further exploration.

For the 3D square-duct flow, the non-linear models including the EASM-1, EASM-2 and cubic models have demonstrated that they can predict Prandtl's motions of the second kind. However, the results are sensitive to wall distances and hence the turbulence damping modelling in the corner regions.

The LES and $k-l$ based ZLES predictions for 3D fully developed channel flows agree well with benchmark data in terms of the mean velocity, turbulent kinetic energy and Reynolds stresses. Also, the ZLES results have demonstrated that the ZLES performs better than pure LES on coarse grids. However, the S-A based DES does not predict the mean velocity profile well.

The results show that the models have been correctly coded and validated.

Chapter 7

Computation of unsteady complex geometry flow

7.1 Introduction

The composition and features of electronics cooling systems have been discussed in Chapter 2. Approaches to modelling turbulence have been introduced in Chapter 3. Also, in Chapter 3, the advantages and disadvantages of three techniques of turbulence modelling, i.e. URANS, ZLES and LES, have been discussed. The turbulence models have been validated in Chapter 6. This chapter deals with the complex flow in the idealized electronic system shown in Fig. 5.2. Simulation results obtained by using URANS, ZLES and LES, are compared with measurements.

7.2 Numerical description of the problem

7.2.1 The configuration under study

The geometry shown in Fig. 5.2 is representative of an electronic central processor unit (CPU). It consists of three, main, hollow, block-like components, labelled regions 1, 2 and 3, from which printed circuit boards have been removed. Two fans are mounted on the vertical walls of regions 1 and 2 respectively. These fans drive the air flow. There are also four grills in the geometry. The geometrical features bring about unsteady flow separation, recirculation and reattachment over a wide range of geometrical scales. Understandably it is a big challenge to model a flow having such complex flow physics. Addtionally, the geometrical complexity gives rise to problem definition issues such as the modelling of losses and turbulence structures introduced by grills.

The maximum dimensions of the geometry are 0.75 m × 0.64 m × 0.2 m in the x, y and z directions respectively.

7.2.2 Boundary conditions

The boundary conditions applying to this case are now outlined. At inflow boundaries, the total pressure is fixed, the normal velocity set to conserve mass and the remaining velocity components made zero. At flow outlets, the pressure is again fixed, the normal velocity being set to conserve mass, with the gradients of all other variables set to zero. Prior to start-up it is not known which are inflow and outflow boundaries among the Grill 2, Grill 4 and the other two openings (i.e. flow inlet/outlet holes) shown in Fig. 5.2. The above boundary conditions are therefore set automatically depending on the flow directions at each iteration.

At solid walls, the no-slip boundary condition is employed for velocities. The settings of turbulence parameters at walls are dependent on the turbulence models used (see Chapter 3 for detail). It is found by Tucker (2000) that the results are insensitive to specified values for turbulence intensity, ranging from 0 to 10% at inlets.

The slotted Grills 1 to 4 are modelled using specified loss coefficients. Energy loss for the grills is calculated from

$$E_l = \frac{1}{2} K \rho u_j^2 \tag{7.1}$$

where E_l is the loss of energy per unit volume of fluid with a local velocity u_j passing through the grill. Acceptable K values found by Tucker (2000), which are K=2 for Grill 1 and K=1 for others, are used here.

Fans are considered to be infinitely thin and the discontinuous pressure-rise across them is specified as a function of the velocity through the fan. Here, as can be seen in

Table 7.1: Fan constants.

	a (Jm^{-3})	b (Jsm^{-4})	c (Js^{2}m^{-5})
Fan 1	59.39	-11.869	0.4655
Fan 2	58.94	-11.495	0.5379

Fig. 5.2, the fans are fixed in the $y - z$ planes. Hence the pressure rise is a function of u. A quadratic relationship between pressure-rise and u is used and is given below

$$E_i = a + bu + cu^2 \tag{7.2}$$

where E_i is the energy input equivalent to the pressure-rise per unit volume and the constants, a, b and c, are given in Table 7.1.

These constants are obtained by making least-square fits to the manufacturer's data. For Fan 1, measurements are made for an input voltage of 15 V. However, data are only available for inputs of 12 and 13.8 V. Hence, linear extrapolation is used. Fan 2 is 50 % obstructed. To account for this, based on tests carried out by the fan manufacturer, a loss coefficient of K=1 is used.

For numerical methods of solving governing equations and transport equations for turbulent variables see Chapter 4.

7.2.3 Modelling techniques and grids employed

For URANS predictions, the following models are investigated: high-Reynolds-number models involving the RSM, EASM and HCubic (i.e. the high-Reynolds-number $k - \epsilon$ model coupled with the cubic form of the Reynolds stresses) and zonal models of $k - l$/EASM and $k - l$/HCubic. Within the RSM, EASM and HCubic models, the two-equation $k - \epsilon$ model is used as a base model. For the zonal RANS method, the interface between the linear $k - l$ (avoiding taking models out of standard calibration ranges) and either the nonlinear EASM or HCubic model is set at y^*_{int} =60. For interest, the popular aerospace-orientated S-A model is also tested.

It should be mentioned that owing to the limitation of computing resources and high demands for near-wall meshes, the nonlinear low-Reynolds-number EASM-1, EASM-2 and cubic models were not tested for the CPU case. Instead the $k-l$ based zonal models, which on computational economy grounds are of the most practical use, are considered. This is because incorporating the $k-l$ model places less stringent demands on first off-wall grid node locations.

ZLES computations are tested using four interface settings between RANS and LES. These include locally instantaneous values of y^+_{int} set to 30, 60 and a mean value of 30, as well as using natural-length-scale compatibility discussed in Chapter 3. When $y^+ > y^+_{int}$, LES with the Yoshizawa one-equation SGS model is applied. Otherwise, the one-equation $k-l$ RANS model is used.

Except for the RSM computation carried out in Fluent (using the second-order upwind scheme for convective spatial terms and the fully implicit scheme for temporal terms), all the simulations are carried out using the in-house code.

For spatial discretization, the second-order central differencing scheme (CDS) is used for zonal URANS, ZLES and LES computations. Owing to stability problems, the CONDIF (essentially it is a stabilised CDS scheme) is employed for the standard $k-\epsilon$, EASM and HCubic high-Reynolds-number models, and also for the S-A model (CDS was tried, but did not converge well). The Crank-Nicholson time scheme is used in the ZLES and LES, and the fully implicit scheme for URANS.

Two grids are used in this study. One is a coarser grid, with 101 (x) × 89 (y) × 45 (z) nodes for high-Reynolds-number models. The other is a relatively fine grid, with 105 (x) × 99 (y) × 51 (z) nodes for low-Reynolds-number models. At first off-wall nodes y^+_{ave} is around 2 and 15 for low- and high-Reynolds-number turbulence models, respectively. For low-Re-model heat-transfer predictions, y^+_{ave} at the first off-wall nodes above the heater are less than 1.

7.2.4 Calculation of turbulence intensities and percentage errors

The Fig. 5.2 geometry flow is unsteady and, surprisingly, to an extent cyclic, i.e. to an extent the flow has a coherent unsteadiness with superimposed stochastic components (see section 7.3.2). Consequently, the instantaneous u-velocity can be expressed as $u = U + \tilde{u} + u'$ (see Eq. (3.9)). Measurements of turbulence intensity to be compared have not been corrected to remove the coherent flow unsteadiness. These intensities can be expressed as

$$T_i' = \frac{\sqrt{\overline{(\tilde{u}+u')^2}}}{U} = \frac{\sqrt{\overline{\tilde{u}\tilde{u}} + \overline{2\tilde{u}u'} + \overline{u'^2}}}{U} \tag{7.3}$$

According to Nishimura *et al.* (2000), the cross term of coherent and turbulence fluctuations, $\overline{\tilde{u}u'} \approx 0$. Therefore, in simulations, the following two forms of turbulence intensity are used, given by

$$T_i = \frac{\sqrt{\overline{u'u'}}}{U}, \quad T_i' \approx \frac{\sqrt{\overline{\tilde{u}\tilde{u}} + \overline{u'u'}}}{U} \tag{7.4}$$

The latter, which includes both the coherent and stochastic unsteadiness, is refered to here as the total intensity. In T_i the periodic fluctuation ($\tilde{u}$) is ignored/filtered out and only the turbulent fluctuation (u') is considered. For URANS, the contribution of the predicted unsteadiness component to the total intensity, T_i', is explored.

For profiles where predictions and measurements are compared, percentage errors for u-velocity and intensity are given. The following experimental data point summations are made

$$\text{Error}_U = \frac{\sum_{\text{exp}} |U_{\text{exp}} - U_{\text{num}}|}{\sum_{\text{exp}} |U_{\text{exp}}|}, \quad \text{Error}_{T_i} = \frac{\sum_{\text{exp}} |T'_{i,\text{exp}} - T_{i,\text{num}}|}{\sum_{\text{exp}} |T'_{i,\text{exp}}|} \tag{7.5}$$

where the subscripts, 'exp' and 'num', represent experimental data and numerical values respectively. At points where numerical data points do not coincide exactly with measurements, a stiff quadratic spline interpolation is used.

7.3 Results and discussion

Comparisons between predictions and LDA measurements are made for the six profiles/lines shown in Fig. 7.1. The exact locations of these lines, normalized by the maximum dimension in each direction for the system shown in Fig. 5.2, are given in

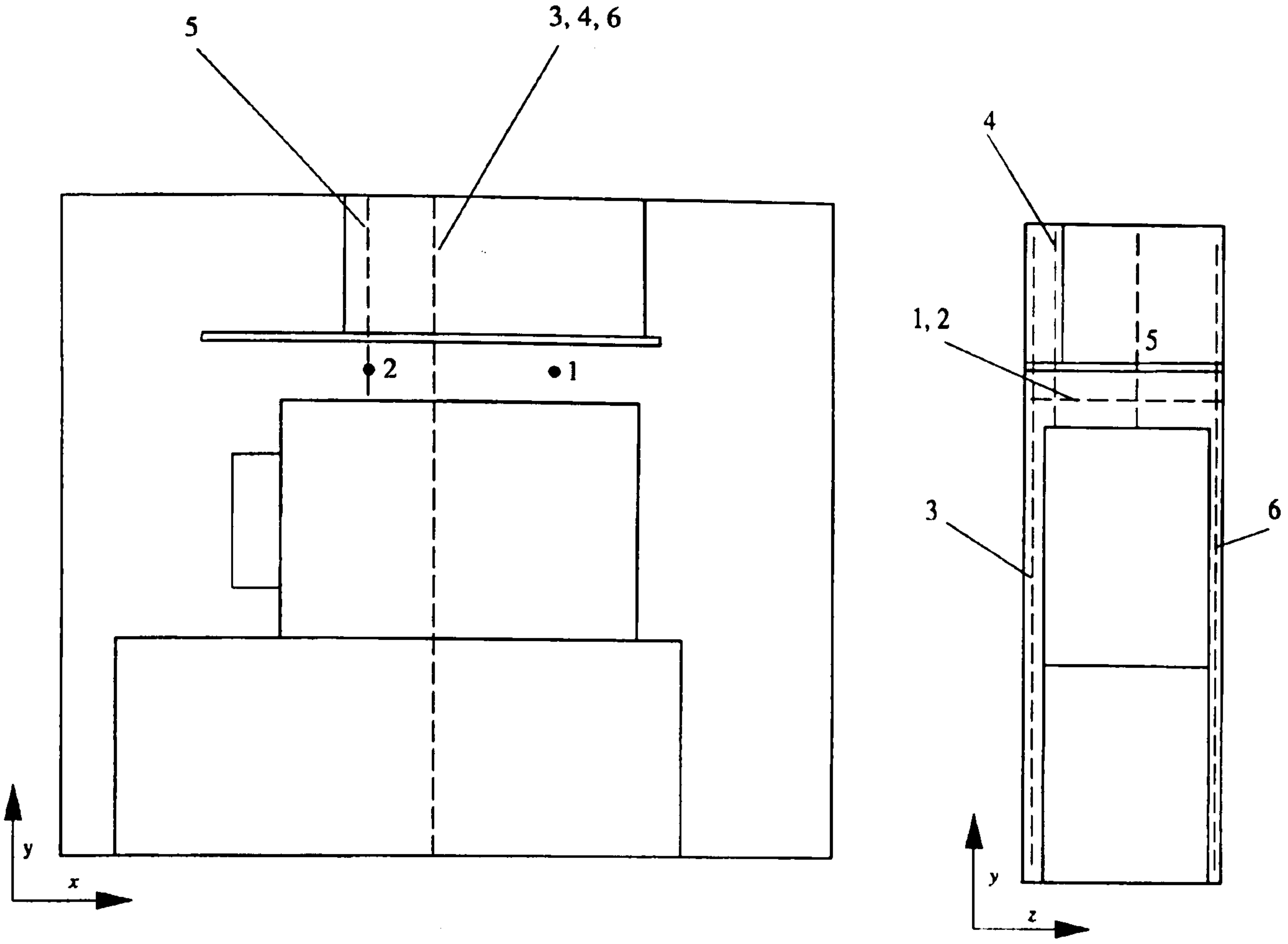

Figure 7.1: Positions of velocity and turbulence intensity profiles.

Table 7.2. The LDA measurements have an estimated uncertainty of ±5% (see Tucker and Pan, 2000). For temporal velocity variation comparisons, thermistor-based measurements with a ±10% error for six points on profiles 1-6 are used (see also Tucker and Pan, 2000).

7.3.1 Temporal velocity variations

Fig. 7.2 shows predicted u−velocity variations from two discretization schemes for the S-A model at two points. Frame (a) corresponds to the central point of Profile 1 and Frame (b) to the central point of Profile 5. As can be seen, the hybrid scheme (dashed line) gives a steady solution, while CONDIF (full line) predicts unsteadiness. As pointed out by Tucker *et al.* (2003a), the hybrid scheme has a strong damping effect on fluctuations.

Fig. 7.3 compares u-velocity variations against time for the zonal non-linear models, ZLES and LES at the central point of Profile 5. It can be seen that, as expected, the unsteadiness predicted by the $k-l$/EASM and $k-l$/HCubic models is much weaker

Table 7.2: Locations of profiles investigated.

Position	Profile 1	Profile 2	Profile 3	Profile 4	Profile 5	Profile 6
X/L	0.53	0.37	0.41	0.41	0.37	0.41
Y/H	0.73	0.73	0~1	0.7~1.0	0.7~1.0	0~0.8
Z/W	0~1.0	0~1.0	0.06	0.1	0.57	0.96

than for both ZLES and LES. Also the fluctuation for LES (which has a lower URANS element) is stronger than that for ZLES. This feature can also be observed in Fig. 7.4.

Fig. 7.4 shows the average predicted u-velocity amplitude against average turbulent viscosity for the different turbulence models. The amplitude averages are based on velocity time traces at the centres of the profiles 1-6 shown in Fig. 7.1. The turbulent viscosity is computed from a volume average over the complete domain. The data represented by open and closed circle symbols are taken from Tucker *et al.* (2003a). Each symbol represents a separate model. As can be seen, linear model amplitudes vary significantly. As might be expected these decrease with increasing turbulent viscosity, μ_t. However, this clear trend does not hold for non-linear models including $k-l$/EASM, $k-l$/HCubic, Speziale's non-linear model and RSM. This is understandable since a significant fraction of the modelled turbulence is not accounted for through diffusive modelling terms. These latter predict relatively low amplitudes compared with some linear models. The ZLES and Smagorinsky LES amplitudes have an error of around just 20%. However, the LES with the Yoshiziwa SGS model is in the closest agreement.

7.3.2 Flow structure

Fig. 7.5 shows mid $x-y$ plane instantaneous streamlines obtained from ZLES ($y^+_{int,ave}$=30) at different times. The structure of the complex flow illustrates the occurrence of massive separation, reattachment together with strong streamline curvature and numerous vortical structures. As can be seen from the plots, the flow pattern changes with time. The flow around the baffle plate where the heater is mounted is turned through 180° and then separation occurs.

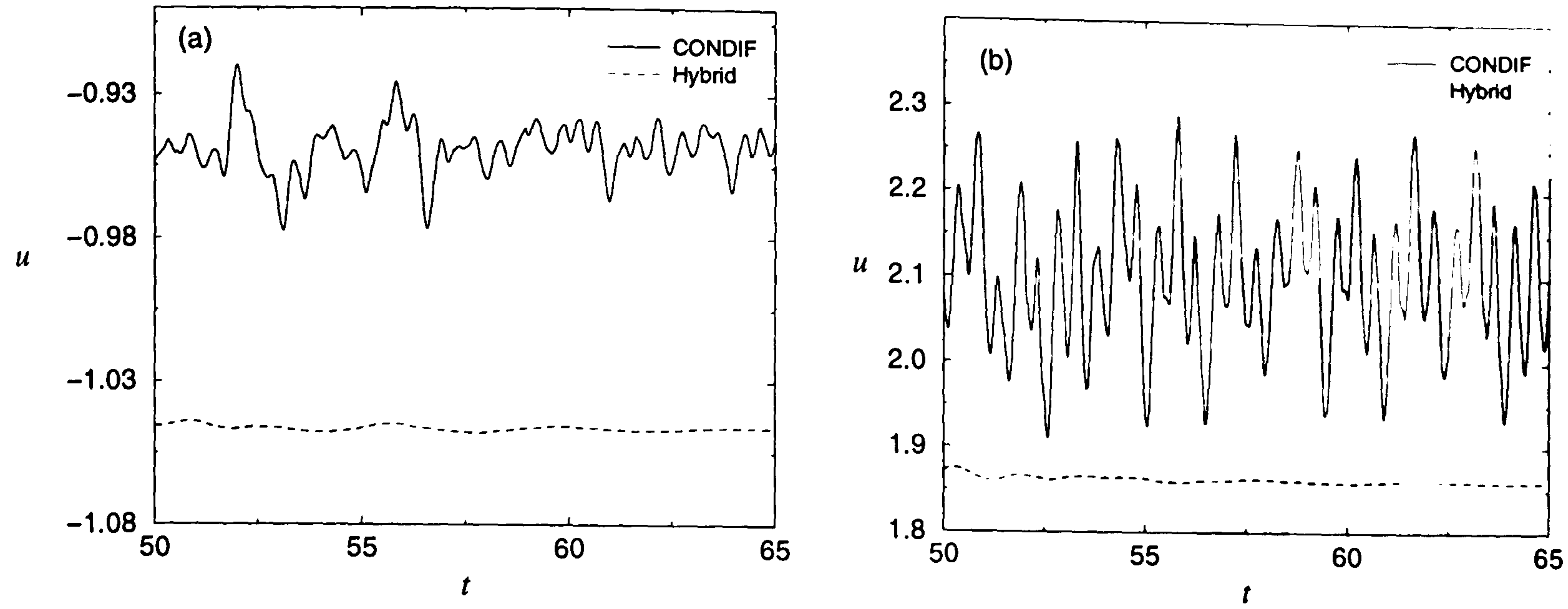

Figure 7.2: Comparison of two discretization schemes at $Z \simeq 0.5$ for the S-A model: (a) for Profile 1 and (b) for Profile 5.

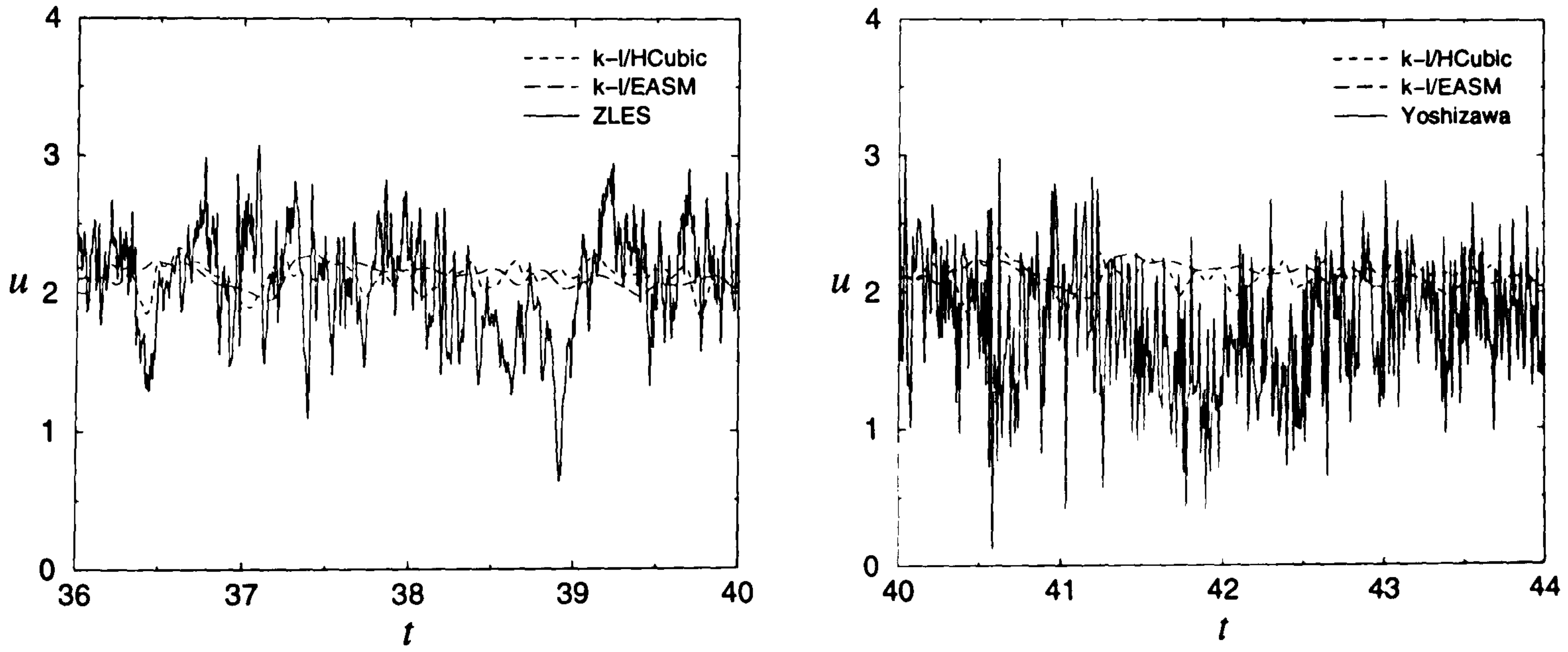

Figure 7.3: Time histories of velocity at the central point of Profile 5.

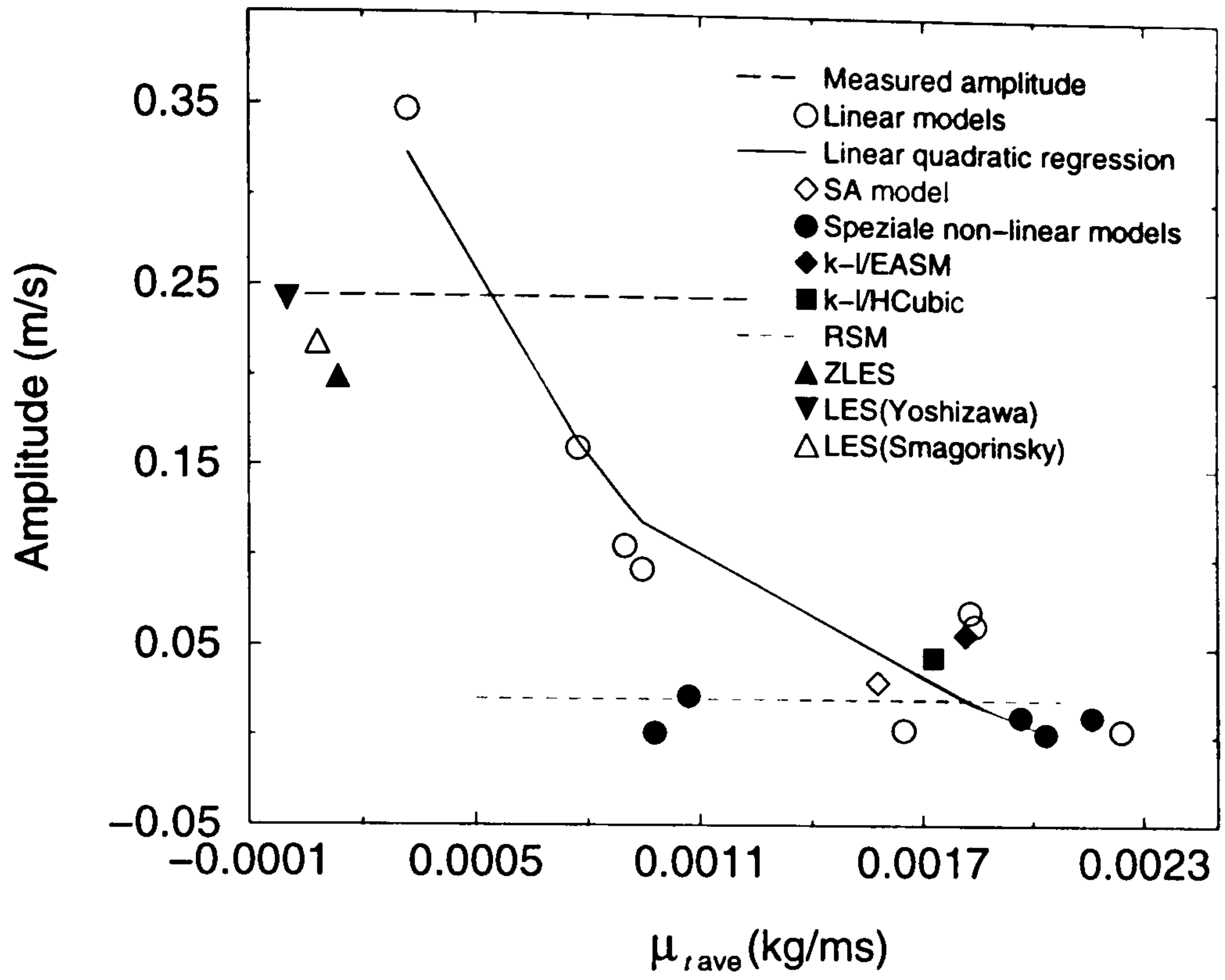

Figure 7.4: Variation of unsteadiness amplitude with turbulent intensity.

Observation shows that the flow has a cyclic element. The vortex arising from separation above the baffle plate is generated and then tends to collapse. This process is repeated in time. Tucker and Pan (2000) present this cyclic flow behaviour. In reality once vortices are generated, they should convect away with the mean flow as shown in a sharp 180° bend flow predictions of Chung *et al.* (2003). However, the ZLES results do not capture this physical phenomenon very well. This might be due to the use of URANS model in the near-wall regions which introduces a region where the modelled turbulent viscosity is high. Some of this convect into the LES region. Numerical dissipation is also likely to play a role in the rapid vortex destruction.

Comparing Fig. 7.5 with Fig. 7.6 (b), the ZLES, as would be expected, shows more unsteadiness activity than the zonal $k - l$/EASM URANS model.

Fig. 7.6 (a) shows the flow pattern from the Yoshizawa-based LES (the Smagorinsky SGS model gives a similar result). As expected the LES (with the lower overall modelled turbulence viscosity levels) predicts finer flow structures than the ZLES shown in Fig. 7.5.

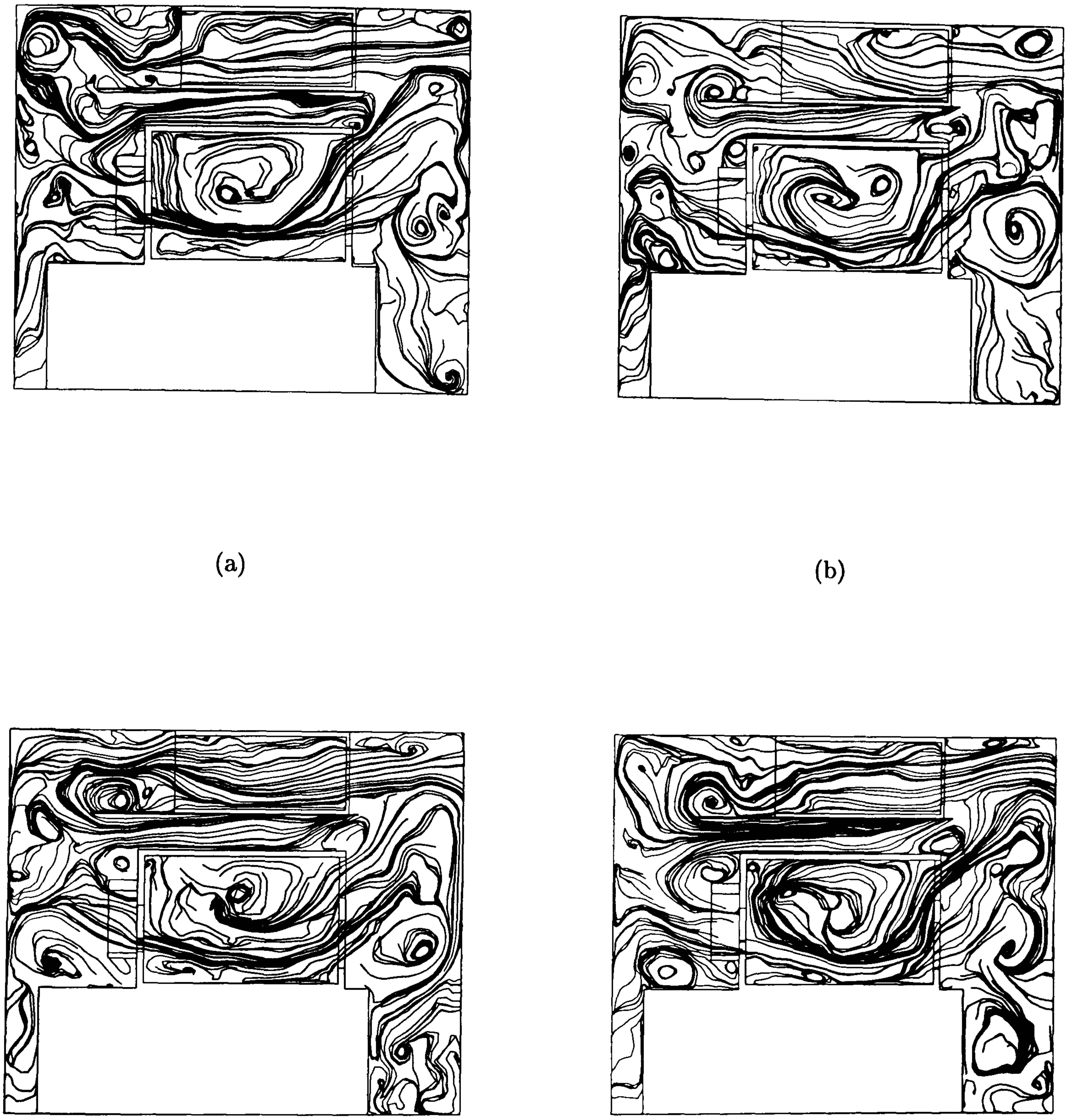

(a) (b)

(c) (d)

Figure 7.5: Mid $x - y$ plane instantaneous streamlines from ZLES at different times (time interval 0.5s).

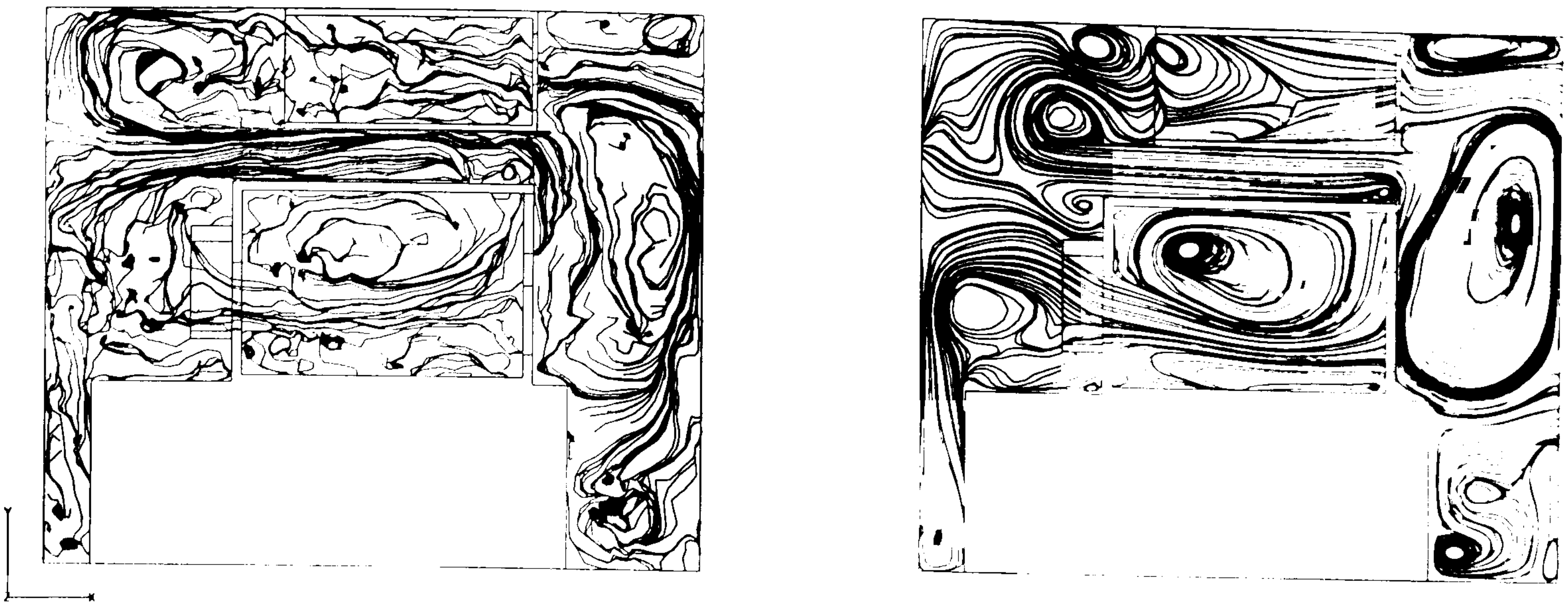

(a) (b)

Figure 7.6: Mid x-y plane instantaneous streamlines: (a): from Yoshizawa model; (b): from $k-l$/EASM.

7.3.3 Velocity and intensity magnitude comparisons

Fig. 7.7 plots the predicted U velocities against those measured for profiles 1-6. The left-hand figure gives the zonal linear $k-l/k-\epsilon$, non-linear $k-l$/EASM and $k-l$/HCubic model results. The right-hand figure shows the results obtained from the ZLES and LES with the Smagorinsky and Yoshizawa models. Fig. 7.8 is the equivalent plot to Fig. 7.7 but for turbulent intensities. The predictions from high-Reynolds-number models, i.e. $k-\epsilon$, EASM and RSM are shown in Fig. 7.9. Given perfect agreement, the points would fall on the 45° reference line. As can be seen, intensities, like velocities, are mostly underpredicted (most points falling beneath the reference line).

The percentage errors in velocity and intensity for each profile and model are summarized in Tables 7.3-8, where the symbols, '-' and '+', represent under- and over-predictions, respectively. Tables 7.3, 7.4 and 7.5 present URANS, zonal LES and LES velocity error results, respectively. It can be seen from Table 7.3 that for the $k-\epsilon$ group, the EASM model performs better than both the standard $k-\epsilon$ and HCubic, while the

HCubic performs slightly better than the standard $k-\epsilon$. The RSM in its high-Reynolds-number form does not perform as well as might be expected (see later discussion). Zonal URANS models improve velocity predictions in comparison with high-Reynolds-number models. For the present complex flow, the $k-l$/EASM performs better than the other two zonal models, i.e. $k-l$/HCubic and $k-l/k-\epsilon$. Although the one-equation S-A model predictions are not as good as zonal models, the performance is better than the standard $k-\epsilon$ model. However, the computational cost of the S-A is about twice that of the $k-\epsilon$. Because of instability, relative to the $k-l$ model, the S-A requires around 50% more computing time.

According to Table 7.4, the four interface settings in the ZLES computations give similar results. For the LES predictions shown in Table 7.5, the Yoshizawa SGS model gives a slightly higher average error than Smagorinsky. The tables suggest that ZLES generally has slightly better accuracy (≈1%) than LES. This is perhaps to be expected as the current grids are slightly coarse for LES (for example, at the top wall of the system, average $\Delta z^+ \simeq 40$).

Comparing ZLES with URANS results, the ZLES performs better than the other URANS predictions except for the $k-l$/EASM.

Intensity errors are given in Tables 7.6-8. The URANS results are summarized in Table 7.6. The data in parentheses represent average errors for T_i', and the others for T_i. When coherent unsteadiness is included, intensities are slightly improved (1%) for zonal URANS models. For high-Re models T_i' is virtually identical to T_i owing to small predicted unsteadiness. Generally, the zonal URANS models do not improve T_i predictions as much as for U. Table 7.6 suggests that the RSM gives the lowest URANS-model average error. As can be seen from Table 7.7, the natural-length-scale-based ZLES gives the most accurate intensities. The average ZLES error is the largest at y_{int}^+=60. This is due to the fact that the LES area diminishes and RANS extent rises with increasing y_{int}^+. This leads to unsteadiness damping.

Comparison of Tables 7.6 and 7.7 shows the ZLES method gives better intensity predictions than the zonal URANS.

As with U, the Yoshizawa LES model (see Table 7.8) gives a larger average error

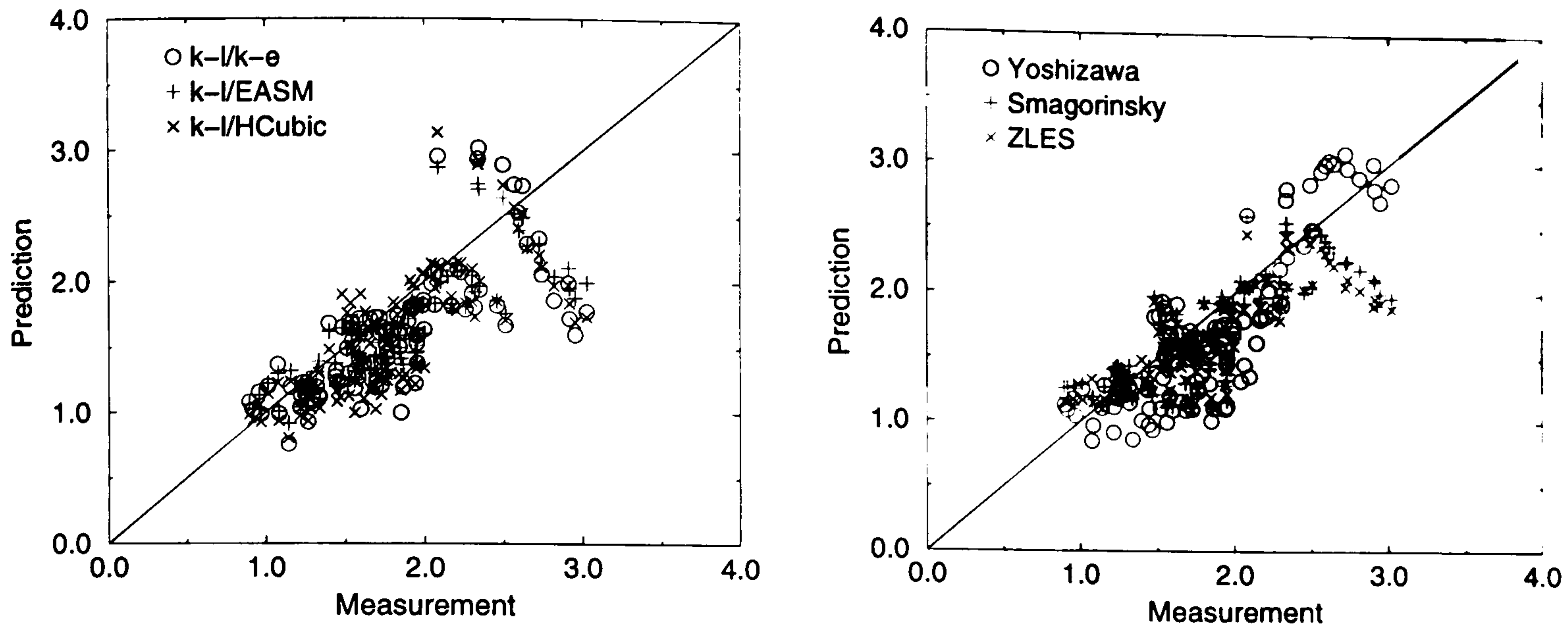

Figure 7.7: Plots of measured against predicted U velocities for profiles 1-6.

than the Smagorinsky.

Velocity distributions for profiles 1-6 are shown in Figs. 7.10, 7.11, 7.12 and 7.13 for high and low-Reynolds-number URANS, ZLES and LES, respectively. Velocities are normalized by the average axial velocities of the two fans ($U_0 \approx 4.5m/s$). Spatial coordinates are normalized by the maximum dimension in each direction. Figs. 7.14, 7.15, 7.16 and 7.17 present turbulent intensity distributions again for the URANS, ZLES and LES (Note: in these plots, the LDA data are T_i'. For URANS, T_i is used and T_i' for ZLES and LES). As can be seen from these plots, each model does not perform consistently for all locations investigated. Some models predict correct trends in one area, but not in others. This is especially true for Profiles 3 and 4.

A possible reason for the RSM, EASM and HCubic models not performing particularly well for velocities with the present complex flow may be the use of wall function (see Chapter 3). The wall function is not suitable for the present nonequilibrium system. Also both the RSM and EASM models may not properly reproduce streamline-curvature effects (see Spalart, 2001). Furthermore, like other turbulence models, these advanced models still contain many empirical terms and their theoretical basis for unsteady flows is tenuous.

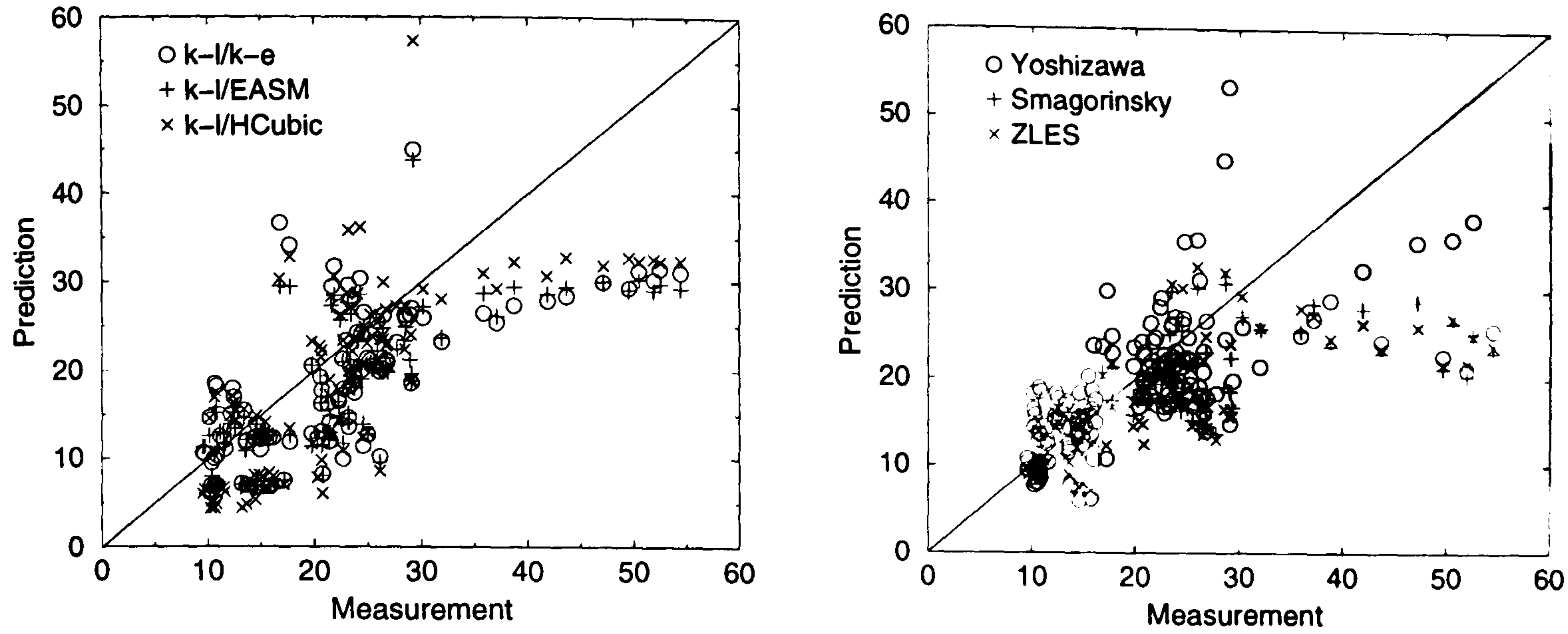

Figure 7.8: Plots of measured against predicted intensities for profiles 1-6.

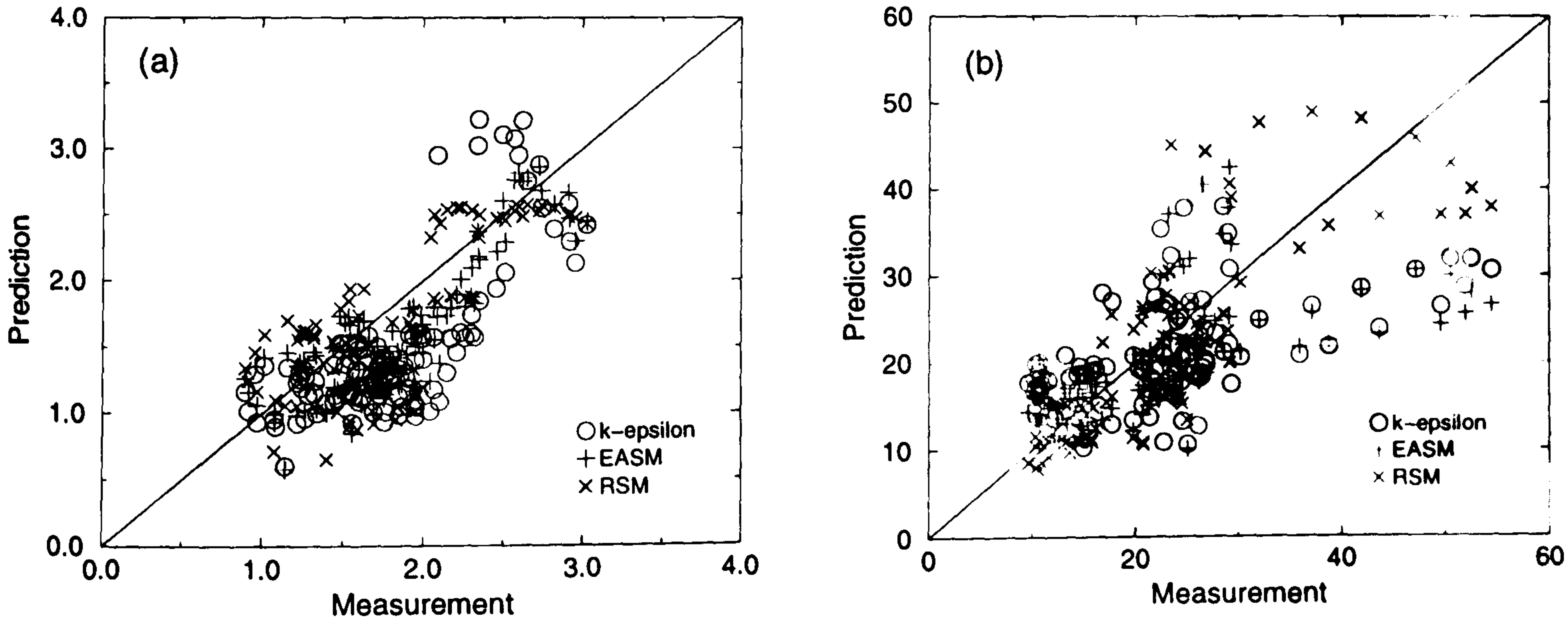

Figure 7.9: Plots of measured against predicted U velocities (Frame (a)) and intensities (Frame (b)) for profiles 1-6.

Table 7.3: Percentage errors in velocity for URANS models.

Model	Profile 1	Profile 2	Profile 3	Profile 4	Profile 5	Profile 6	Average
$k-\epsilon$	-27	-19	-20	-16	-31	-34	-25
HCubic	-26	-18	-22	-17	-28	-33	-24
EASM	-25	-20	-17	-16	-30	-30	-22
RSM (Fluent)	-32	-22	-14	-14	+16	-37	-23
S-A	-24	-18	-19	-18	-13	-24	-19
$k-l/k-\epsilon$	-21	-16	-17	-21	-16	-13	-17
$k-l$/HCubic	-24	-24	-18	-22	-13	-11	-19
$k-l$/EASM	-17	- 14	-13	-17	-11	-15	-15

Table 7.4: Percentage errors in velocity for ZLES.

Model	Profile 1	Profile 2	Profile 3	Profile 4	Profile 5	Profile 6	Average
y^+_{int} =30	-21	-16	-14	-16	-8	-15	-15
y^+_{int}=60	-19	-14	-17	-18	-8	-16	-15
$y^+_{int,ave}$=30	-22	-19	-14	-16	-8	-16	-16
$l = l_{min}$	-22	-18	-14	-16	-7	-16	-16

Table 7.5: Percentage errors in velocity for LES.

SGS model	Profile 1	Profile 2	Profile 3	Profile 4	Profile 5	Profile 6	Average
Yoshizawa	-27	-21	+14	+9	-12	-20	-17
Smagorinsky	-22	-17	-13	-13	-8	-18	-15

Table 7.6: Percentage errors in turbulent intensity for URANS models.

Model	Profile 1	Profile 2	Profile 3	Profile 4	Profile 5	Profile 6	Average
$k-\epsilon$	-35	-24	+35	+24	+37	+43	+33 (+33)
HCubic	-39	-24	+50	+33	+41	+49	+40 (+40)
EASM	-37	-23	+28	+26	+30	+35	+30(+30)
RSM	-20	-15	-19	+26	-22	-38	-23(-22)
$k-l/k-\epsilon$	-32	-21	-25	-28	-29	-49	-31 (-30)
$k-l$/HCubic	-24	-14	-39	-26	-34	-57	-32 (-31)
$k-l$/EASM	-32	-22	-22	-24	-26	-49	-29 (-27)

Table 7.7: Percentage errors in turbulence intensity (T_i') for ZLES.

Model	Profile 1	Profile 2	Profile 3	Profile 4	Profile 5	Profile 6	Average
y_{int}^+=30	-37	-24	-17	-14	-32	-27	-25
y_{int}^+=60	-38	-27	-18	-14	-35	-28	-27
$y_{int,ave}^+$=30	-34	-19	-17	-17	-30	-19	-23
$l = l_{min}$	-34	-16	-18	-17	-25	-20	-22

Table 7.8: Percentage errors in turbulence intensity (T_i') for LES.

SGS model	Profile 1	Profile 2	Profile 3	Profile 4	Profile 5	Profile 6	Average
Yoshizawa	-35	-15	+15	+29	+40	+20	+26
Smagorinsky	-37	-21	-15	+14	-29	-26	-24

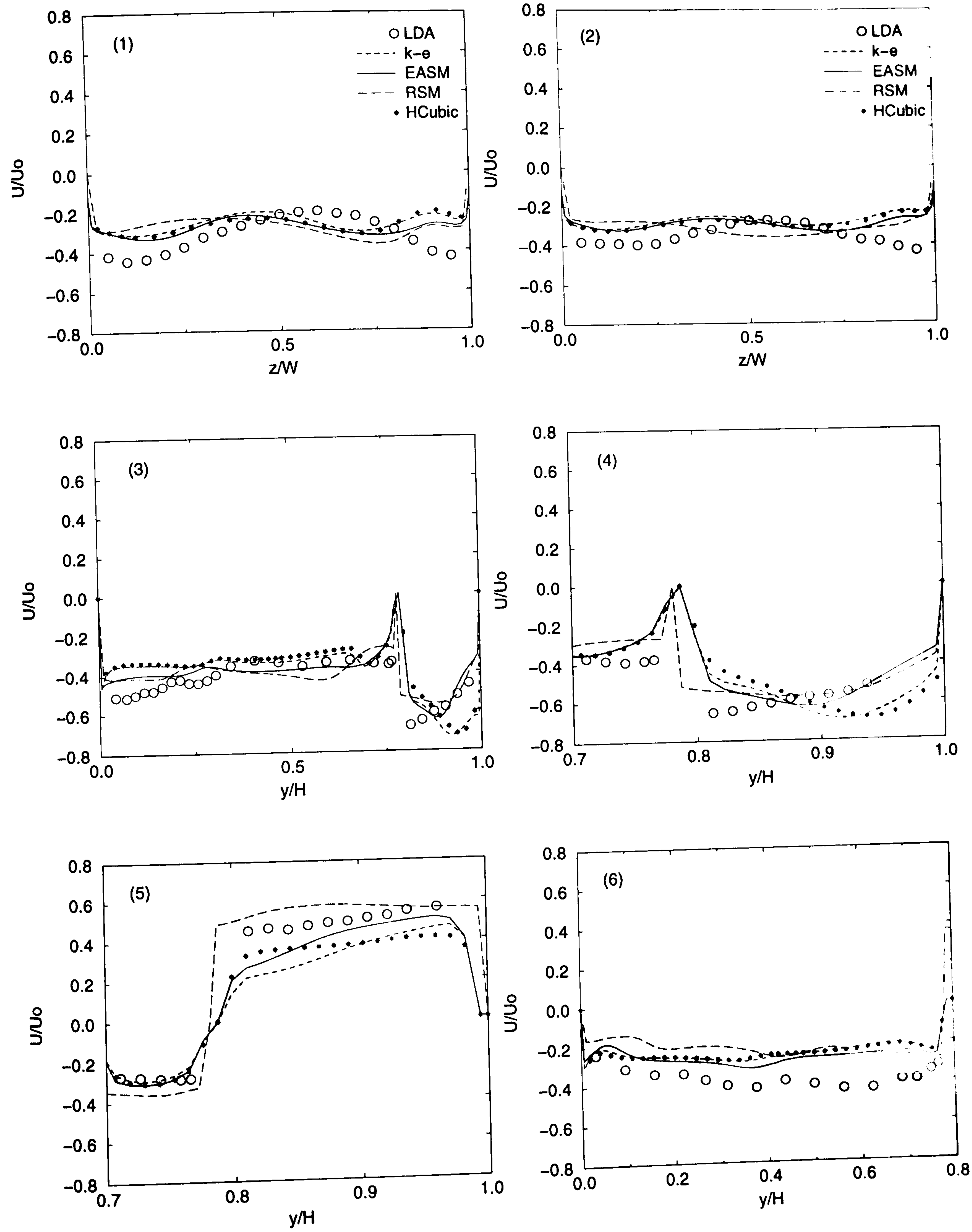

Figure 7.10: Comparison of U-velocity predictions with measurements for high-Reynolds-number URANS models.

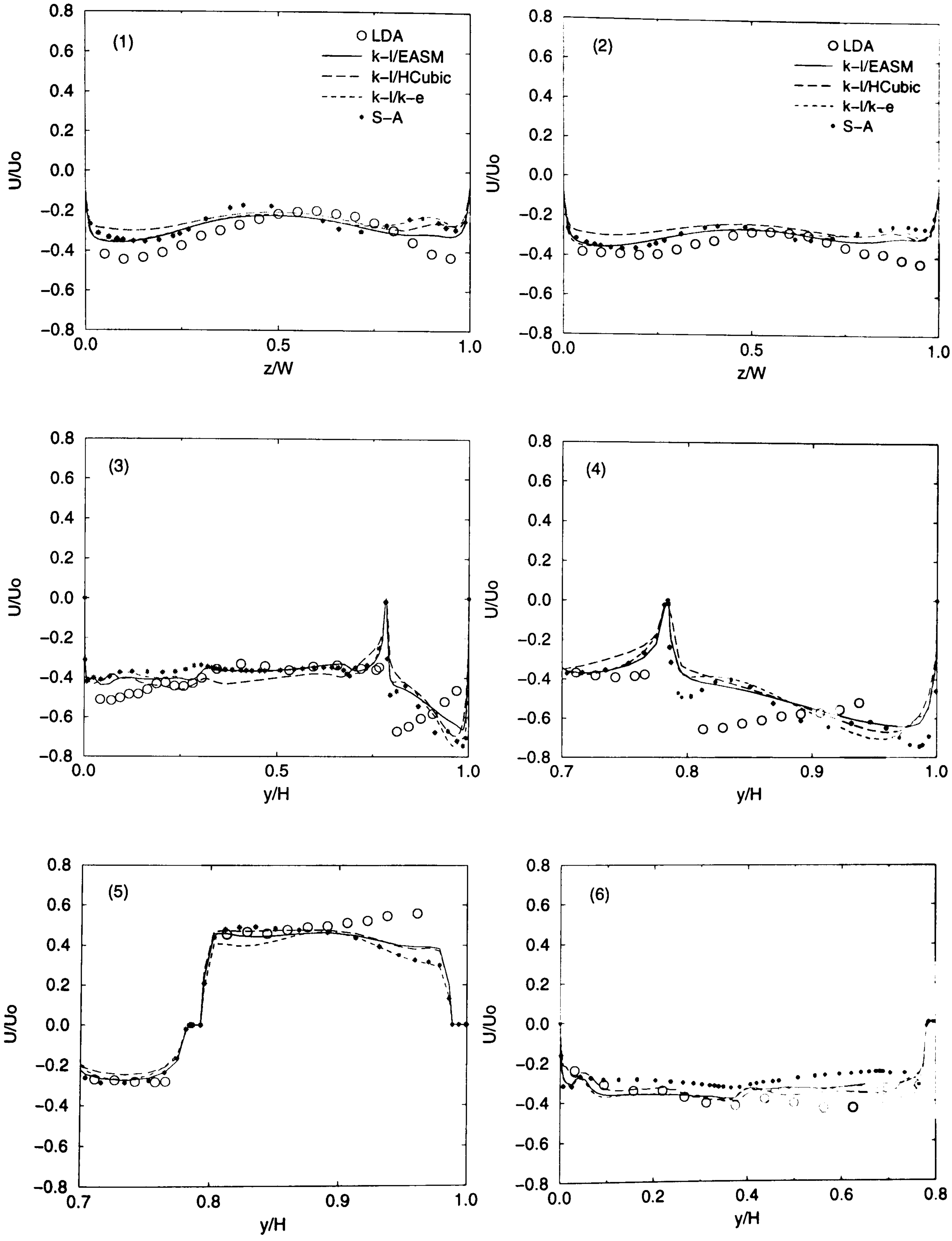

Figure 7.11: Comparison of U-velocity predictions with measurements for low-Reynolds-number URANS models.

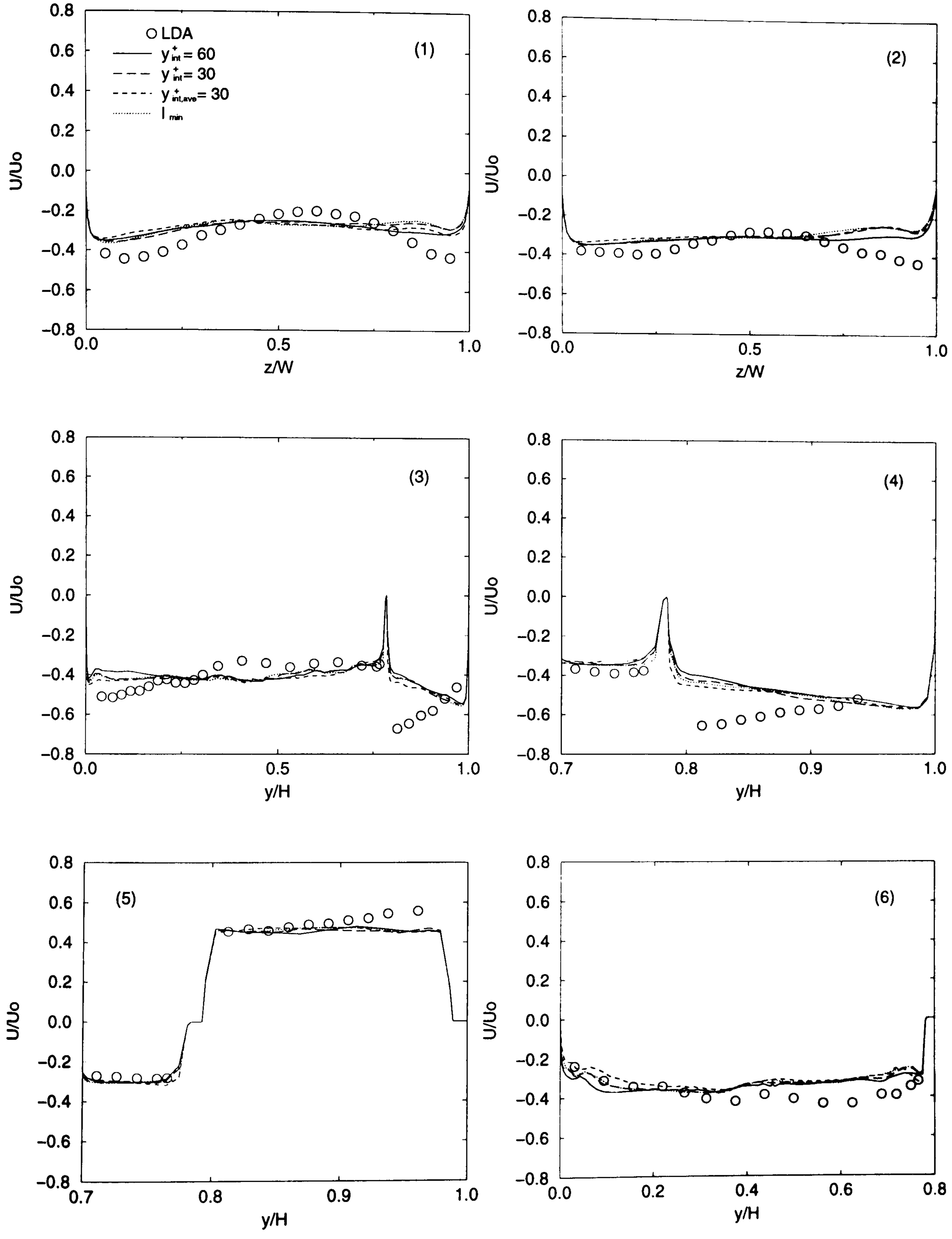

Figure 7.12: Comparison of U-velocity predictions with measurements for ZLES.

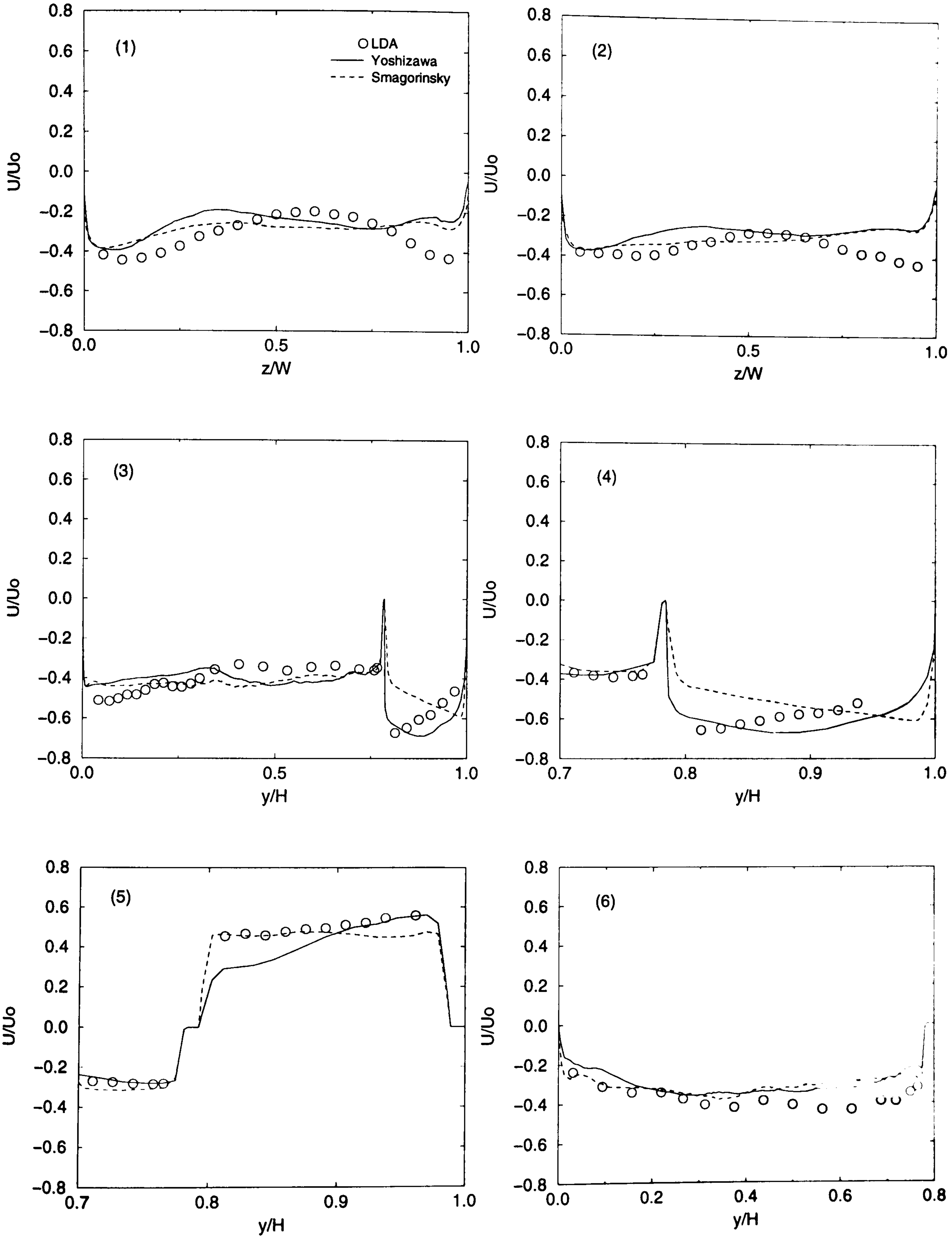

Figure 7.13: Comparison of U-velocity predictions with measurements for LES.

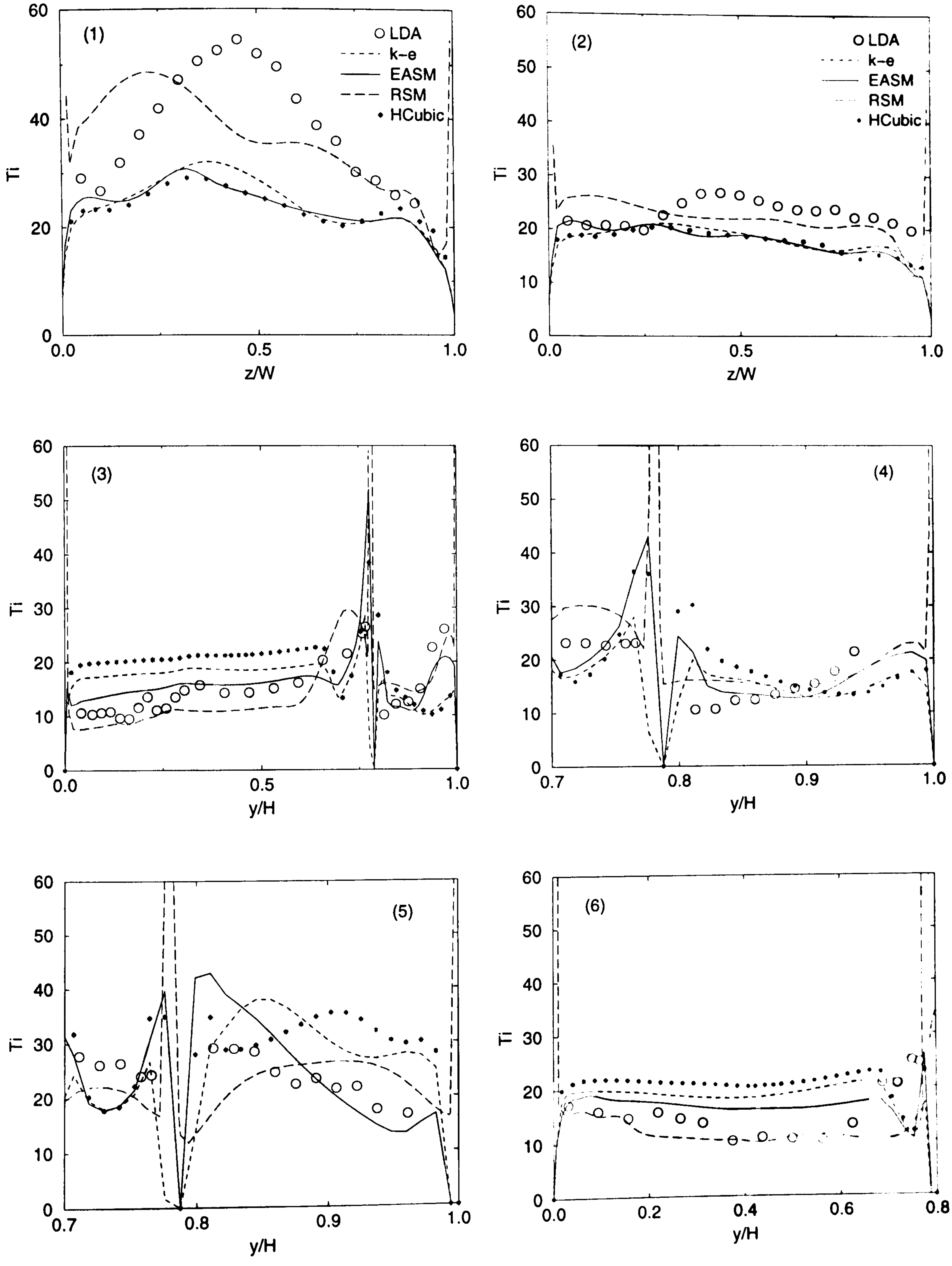

Figure 7.14: Comparison of intensity predictions with measurements for high-Reynolds-number URANS models.

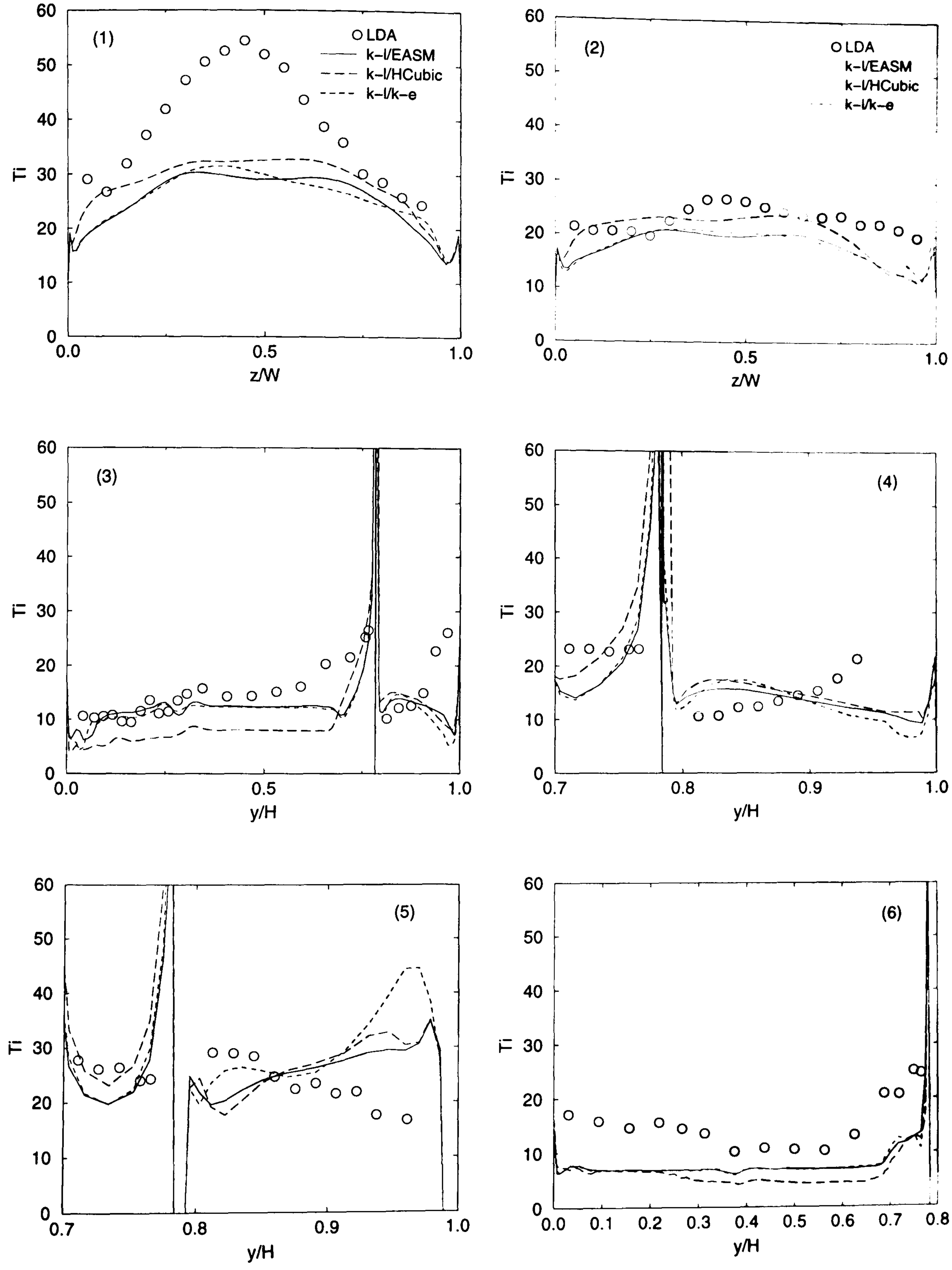

Figure 7.15: Comparison of intensity predictions with measurements for low-Reynolds-number URANS models.

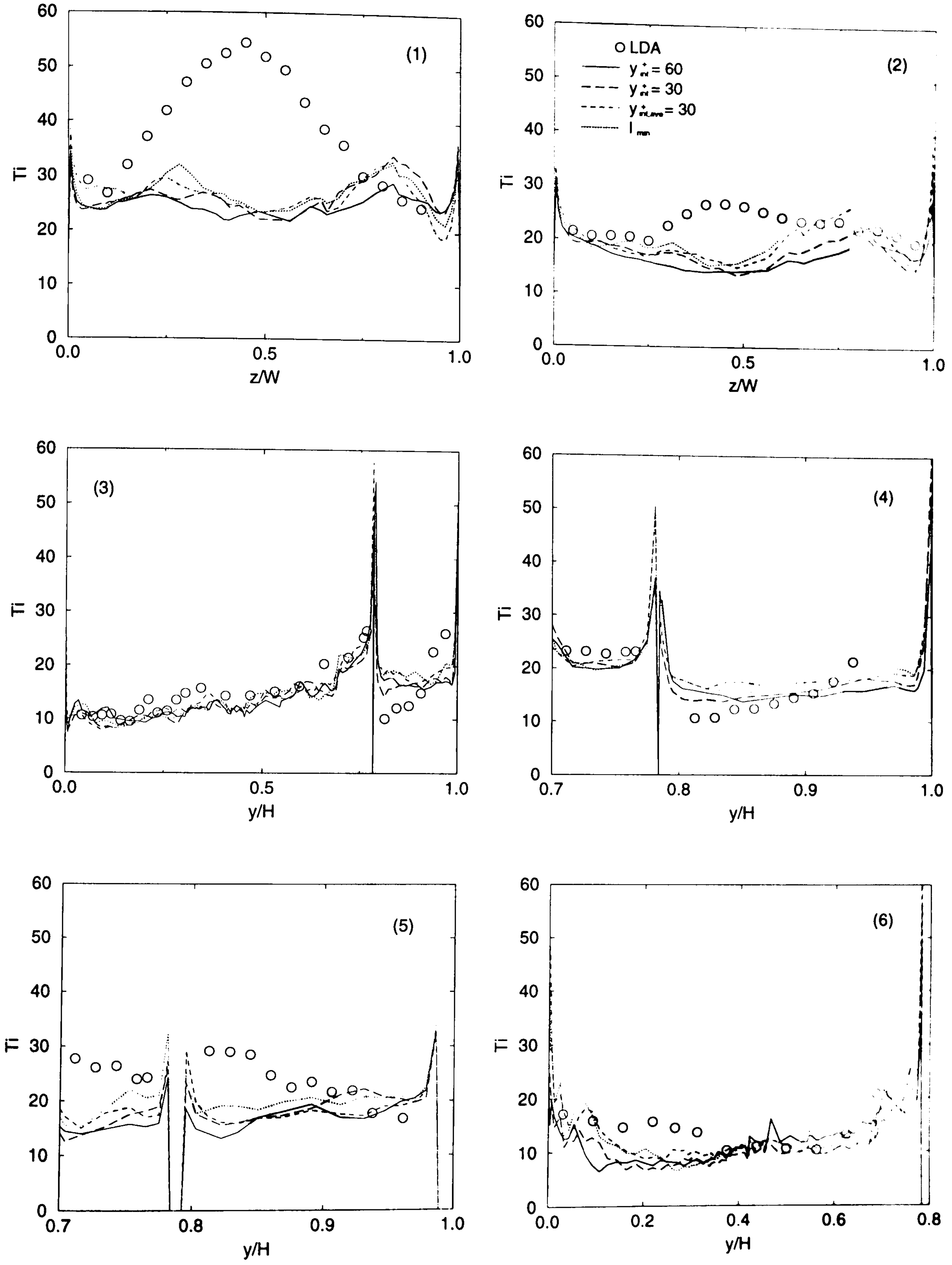

Figure 7.16: Comparison of intensity predictions with measurements for ZLES.

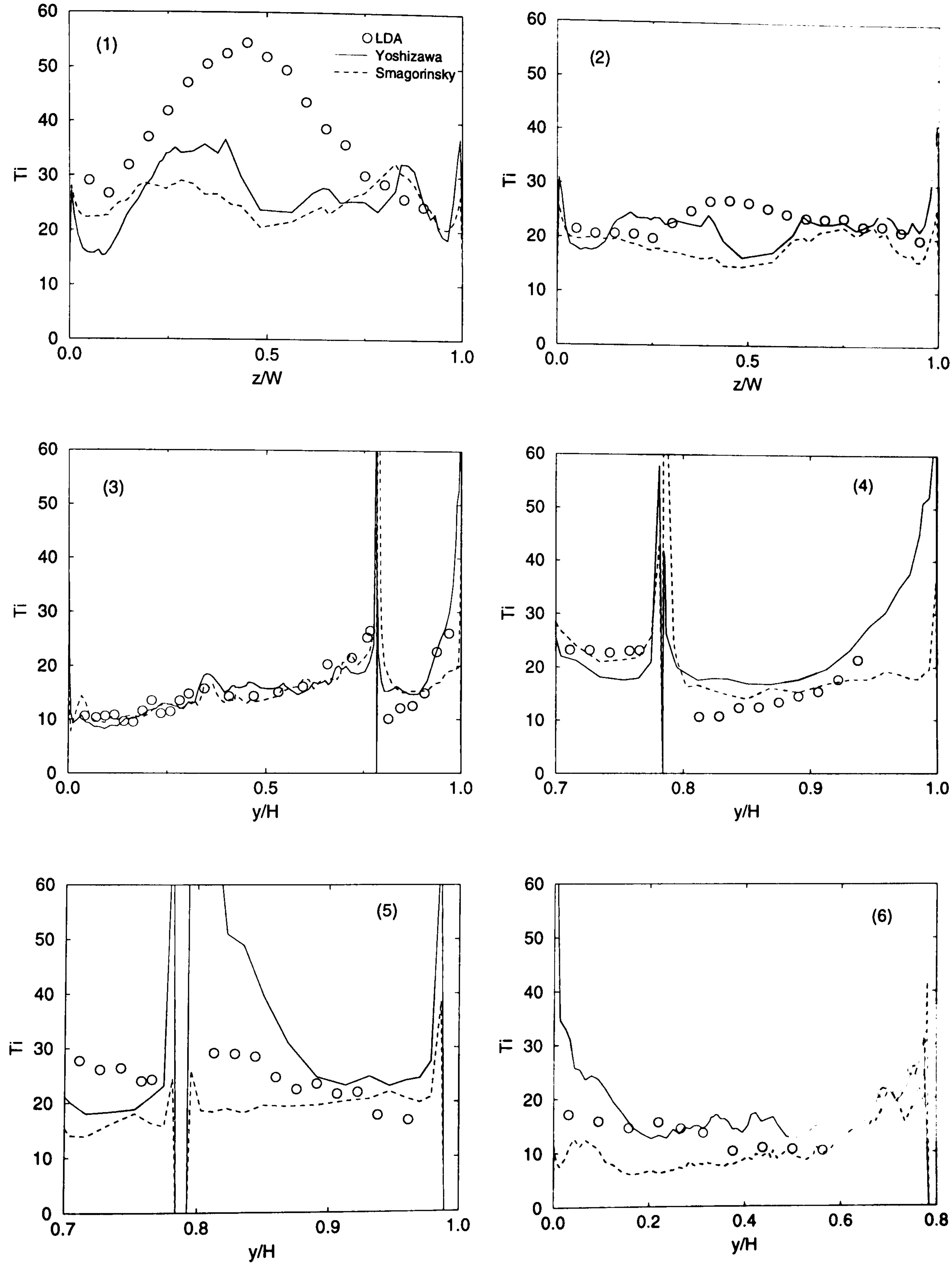

Figure 7.17: Comparison of intensity predictions with measurements for LES.

7.3.4 Heat transfer results

The location of the heater and other details for experimental data of temperature and Nusselt number have been given in Chapter 5.

The local Nusselt number, Nu_x, is shown in Fig. 7.18. Nu_x is determined by

$$Nu_x = \frac{q''X}{k(T_{w(X)} - T_{ref})} \tag{7.6}$$

where q'' is the heat flux, k the thermal conductivity, $T_{w(X)}$ the local surface temperature at X along the centreline of the heater ($X(= x - x_0)$ is a reference coordinate value, where $X = 0$ corresponds to the edge (x_0) of the heater). Also, T_{ref} is the temperature at the reference point just upstream of the heated surface (see Chapter 5). Frame (a) shows high-Reynolds-number EASM and HCubic model results; (b) low-Reynolds-number $k-l$/EASM, $k-l$/HCubic, $k-l/k-\epsilon$ and S-A; (c) ZLES at the four y^+_{int} settings and (d) LES results. As a reference, the Nu_x results for turbulent flow over a flat plate, calculated by Eq. (7.7), is also shown in Frames (c) and (d) in Fig. 7.18.

$$Nu_x = 0.0308 Re_x^{0.8} Pr^{1/3} \tag{7.7}$$

In Eq. (7.7), the inflow velocity is approximately determined by the bulk average velocity through Fan 1 (see Fig. 5.2).

As can be seen from the plots, the models investigated perform differently. Nu_x is overpredicted by the low-Reynolds-number URANS models and underpredicted by both the ZLES and LES.

Surprisingly the EASM and HCubic models using the wall function for temperature (see Chapter 3) appear to perform best. Thermistor-based measurements suggest the velocity profiles for these models over the heated-surface region have totally the wrong trends.

As with velocities, the ZLES predicts similar Nu_x results for each interface setting. Also the ZLES results seem in fairly close agreement with correlation data for a turbulent flat plate. It is important to note that the CPU Nu_x measurements are much higher than those for a flat plate given by Eq. (7.7). This is to be expected. As the work of Chung *et al.* (2003) shows, large coherent convecting vortex structures should be generated as a result of sharply turning the flow and these should dramatically increase heat transfer. The Fig. 7.5 ZLES streamline plots suggest that in the current predictions the vortex structures exhibit excessive dampimg. This excessive damping is consistent with the low ZLES Nu_x values. The hybrid MILES-RANS approach of Tucker (2004) might well increase the resolved ZLES activity and would be worth testing for future work. An encouraging feature of the ZLES and LES results is that they show a consistent behaviour, i.e. they all give similar Nu_x levels and distributions. In a design context this behaviour is more manageable and in stark contrast to the URANS results. For the latter Nu_x appears to have much stronger model dependence.

In a sharp-bend study, Chung *et al.* (2003) find the order-of-magnitude Nu changes for minor Re perturbations when modelling sharply turned flows intended to be a prototype of the study here.

In addition to the substantial turbulence modelling errors, there are other factors causing the large Nu_x discrepancy (see Fig. 7.18), which are:

- The complex system has significant problem-definition uncertainties;
- There is ±5% Nu_x measurement error (see Chapter 5);
- Tucker and Pan (2000) suggest some grid-convergence error.

7.4 Conclusions

Predictions for the complex geometry, non-isothermal flow obtained from URANS, ZLES and LES have been presented. Normal-wall distances were evaluated using a Poisson differential-equation-based technique (see Chapter 4). Performances of the advanced URANS models, ZLES and LES were assessed in terms of unsteadiness amplitude, velocity, turbulence intensity and local Nusselt number accuracies. For velocities, the zonal $k - l$/EASM model results were most accurate compared to the other URANS models. Although the $k - l$/EASM model improved intensity predictions relative to the other two zonal models, the error was still large. Despite the RSM giving the lowest intensity error, overall the advanced high-Reynolds-number EASM, HCubic and RSM models did not perform as well as expected. This may be due to the use of the wall functions. Also,

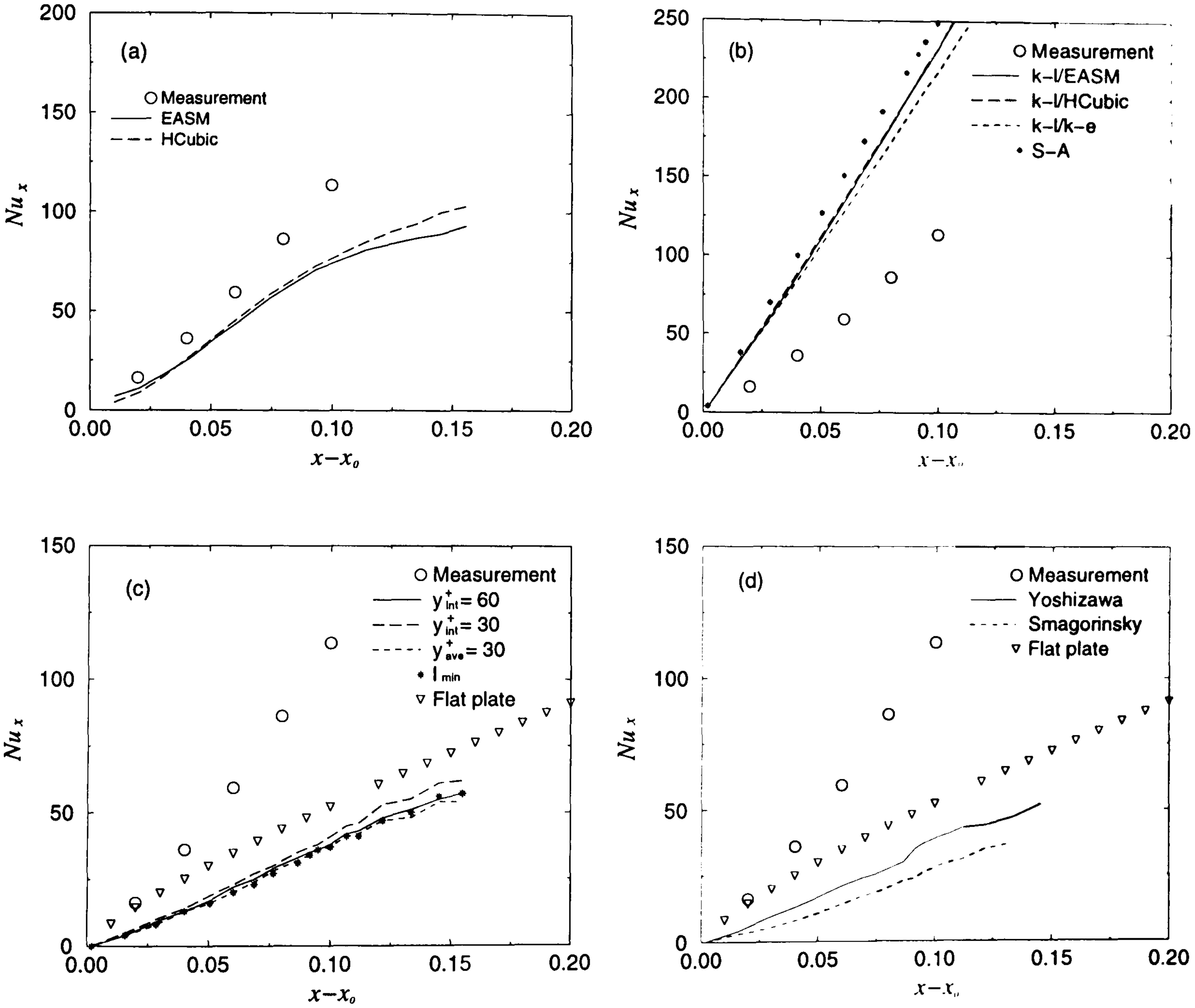

Figure 7.18: Local Nu_x distributions for various models.

many existing empirical terms may not be well suited to this unsteady complex flow. For example, in the RSM, the empirical terms in the pressure-strain and dissipation areas are controversial.

The grids employed are not perhaps LES suitable. This is reflected by the ZLES, where introduction of the 'RANS' model shows slightly improved accuracy relative to the Yoshizawa LES. However, unlike this unusual case with relatively high-Reynolds-numbers, most realistic electronics systems run at lower Reynolds numbers. Hence, LES might be applicable and perform well. For the present case, both the ZLES and LES gave better coherent unsteadiness component predictions than any of the URANS models. Even so, all models underpredicted turbulence intensity except for the $k - \epsilon$ based high-Reynolds-number models. This is not surprising since this model is well known for its excessively dissipative behaviour. Overall, ZLES gave better predictions compared with the URANS in terms of velocity and intensity.

For heat transfer, the high-Reynolds-number EASM and HCubic models show best agreement with measurements. However, since they gave velocity profiles with the wrong trend in the heat-transfer region, this is surprising. Although the ZLES, LES and the low-Reynolds-number URANS models have performed well for velocities, their predicted heat transfer results were relatively poor. The turbulence modelling errors, problem-definition uncertainties and grid-convergence errors are all attributed to the large Nu discrepancies.

However, it is encouraging that the LES and ZLES Nu results, although involving a range of modelling approaches, show a more consistent behaviour. This is to be expected. These approaches rely less heavily on modelling. The consistent behaviour is more manageable in a design context. The ZLES and LES results might be improved using less dissipative procedures such as a hybrid MILES-RANS approach or through use of fine grids and high-order discretization.

The ZLES and LES are about five times more computationally expensive than the non-linear models. Although this difference in expense is not as high as might be expected (a key reason being that the non-linear models are expensive to converge), it is still problematic in a design context.

Chapter 8

Conclusion and future work

This thesis has outlined predictions obtained from URANS, ZLES and LES covering different electronic-system-related geometry flows, ranging from relatively simple to a highly complex CPU geometry. The performance of nonlinear models has been compared with that of linear models for all cases investigated. In the CPU case, assessment is given of the performance of URANS, ZLES and LES. The following summarizes the main conclusions drawn in the present study for the various cases.

- **2D channel flow**. The nonlinear low-Reynolds-number models, viz. EASM-1, EASM-2 and cubic models have performed better than any linear model (i.e. CH, LS, LSY and S-A) and zonal models (i.e. $k - l/k - \epsilon$, $k - l$/EASM and $k - l$/HCubic) in terms of C_f, Nu and normal Reynolds stresses.

- **2D step flow**. Regarding velocity distribution and Reynolds stress predictions, the high-Reynolds-number EASM performs better than the standard $k - \epsilon$ and HCubic models. The $k - \epsilon$ and HCubic models behave similarly. Reattchment length is overpredicted by the EASM, while the other two models underpredict it. In the case of the low-Reynolds-number $k - \epsilon$ models, the LSY improved prediction of the reattachment length and near-wall velocity, compared with the LS and CH. This is consistent with reports in the literature. The S-A model performs well, but not as well as the LSY.

- **2D ribbed-duct flow**. Compared with the $k-\epsilon$ and HCubic, the EASM improves predicted reattachment length and Reynolds stresses. However, neither the near-wall velocity distribution nor Nu by the EASM are better than those from the other two models. The $k-\epsilon$ and HCubic models again behave similarly.

As in the case of the step flow, the LSY has improved velocity and reattachment length predictions, and thus too Nu, by comparison with the LS and CH. Again, this confirms the results from other researchers.

The performance of the zonal models, $k-l/k-\epsilon$, $k-l$/EASM and $k-l$/HCubic, is similar to the LSY. However, the $k-l$/EASM has overpredicted reattachment length. The nonlinear $k-l$/EASM and $k-l$/HCubic models do not demonstrate improvement in Nu compared with the linear $k-l/k-\epsilon$. All zonal models improve their respective high-Reynolds-number form predictions.

For near-wall velocity and Nu predictions, most of the low-Reynolds-number models perform better than do the high-Reynolds-number models. However, the cubic model does not perform well for either near-wall velocities or heat transfer. This needs further exploration.

- **Square-duct flow**. The nonlinear EASM-1, EASM-2 and cubic models are capable of capturing secondary motion. However, predicted spanwise velocity distributions are sensitive to turbulence damping modelling in the corner regions.

- **3D channel flow**. For relatively coarse RANS grids, the $k-l$ based LES (ZLES) demonstrates that it performs better than the S-A based DES, and pure LES.

- **The CPU case**. For the flow field prediction, within URANS, the $k-l$/EASM performs better than the $k-l/k-\epsilon$, $k-l$/HCubic, S-A and the high-Reynolds-number models. Generally, the ZLES gives better predictions than URANS. Given the coarse grids used, the LES predictions have not shown any advantage compared with the ZLES. However, the LES gives the best unsteadiness magnitude predictions, followed by the ZLES and then URANS.

For heat transfer, none of the low-Reynolds-number models investigated performed well. However, the EASM and HCubic models, coupled with the wall functions, showed best agreement with measurements. This is surprising since the velocity profiles in the heat transfer region have the wrong trend. The LES and ZLES predictions like the low-Reynolds-number URANS show considerable error in the predicted heat-transfer levels. However, the ZLES and LES models display a more consistent predictive behaviour relative to the URANS. This is useful in a design context.

With regard to computing time, for the complex geometry generally all forms of the EASM and cubic were considerably more expensive than linear counterparts. However, the cubic models generally converged faster than the EASM models. This is perhaps surprising considering its more non-linear nature. For all non-linear models, various terms must be introduced gradually and with care. This increases user effort and time input. Although generally the LES and ZLES showed robust convergence and required little external user input, they took around five times more computing time.

- **Recommendation for future work on the CPU case**
  (a) It might be useful to apply the GGDH heat flux model (see Chaper 3) to improve heat transfer prediction;
  (b) If well-known stability problems can be overcome, the dynamic SGS model (see Chapter 3) could be usefully tested to improve LES predictions;
  (c) Non-linear LES models might also be explored;
  (d) Hybrid MILES-RANS modelling might be worth testing. This approach acknowledges the strong role that discretization errors can play in LES solutions. However, it is important not to ignore the impact of problem definition assumption on solution accuracy. This is an area of ongoing research.

Appendix A

The Tri-diagonal Matrix Algorithm

A set of equations that has a tri-diagonal form can be expressed as

$$-C_i\phi_{i-1} + A_i\phi_i - B_i\phi_{i+1} = D_i \tag{A.1}$$

where i=1, 2, $\cdots$, n denotes grid nodes, i=0 and $i = n$+1 indicate boundary nodes.

A.1 The standard TDMA

Eq. (A.1) can be rewritten as

$$\phi_1 = \frac{B_1}{A_1}\phi_2 + \frac{C_1}{A_1}\phi_0 + \frac{D_1}{A_1} \tag{A.2}$$

$$\phi_2 = \frac{B_2}{A_2}\phi_3 + \frac{C_2}{A_2}\phi_1 + \frac{D_2}{A_2} \tag{A.3}$$

$$\cdots\cdots\cdots\cdots$$

$$\phi_n = \frac{B_n}{A_n}\phi_{n+1} + \frac{C_n}{A_n}\phi_{n-1} + \frac{D_n}{A_n}$$

The forward elimination can be accomplished by removing ϕ_1 from Eq. (A.3) by substitution of Eq. (A.2) into Eq. (A.3), then removing ϕ_2 from the equation of ϕ_3, and so on unitil the equation for ϕ_n is obtained. The general form of ϕ_i after forward elimination is

$$\phi_i = E_i\phi_{i+1} + G_i \tag{A.4}$$

where

$$E_i = \frac{B_i}{A_i - C_i E_{i-1}}, \quad G_i = \frac{C_i G_{i-1} + D_i}{A_i - C_i E_{i-1}}$$

Generally, the value of ϕ is known at the boundary location (n+1). The values for ϕ can then be obtained in reverse order ($\phi_n, \phi_{n-1}, \cdots, \phi_1$) from Eq. (A.4). The procedure is termed back-substitution.

A.2 The cyclic tri-diagonal matrix algorithm (CTDMA)

If a boundary condition is periodic, then

for i=1, $\phi_{i-1} = \phi_n$

for i=n, $\phi_{i+1} = \phi_1$.

When i=1, Eq. (A.2) can be rewritten as

$$\phi_1 = \frac{B_1}{A_1}\phi_2 + \frac{C_1}{A_1}\phi_n + \frac{D_1}{A_1} \tag{A.5}$$

Substituting Eq. (A.5) into Eq. (A.2), then

$$\phi_2 = \frac{B_2}{A_2 - C_2\frac{B_1}{A_1}}\phi_3 + \frac{C_2\frac{C_1}{A_1}}{A_2 - C_2\frac{B_1}{A_1}}\phi_n + \frac{D_2 + C_2 D_1}{A_2 - C_2\frac{B_1}{A_1}} \tag{A.6}$$

Repeating the above procedure until $i = n$, the following general form can be obtained from

$$\phi_i = E_i\phi_{i+1} + F_i\phi_n + G_i \tag{A.7}$$

For i=2, 3, $\cdots$ n, $E_i = \frac{B_i}{A_i - C_i E_{i-1}}$, $F_i = \frac{C_i F_{i-1}}{A_i - C_i E_{i-1}}$, $G_i = \frac{D_i + C_i G_{i-1}}{A_i - C_i E_{i-1}}$.

For i=1, $E_1 = \frac{B_1}{A_1}$, $F_1 = \frac{C_1}{A_1}$ and $G_1 = \frac{D_1}{A_1}$. When $i = n$, then

$$\begin{aligned} A_n\phi_n &= B_n\phi_{n+1} + C_n\phi_{n-1} + D_n \\ &= B_n\phi_1 + C_n\phi_{n-1} + D_n \end{aligned} \tag{A.8}$$

After substituting Eq. (A.5) for ϕ_1 into Eq. (A.8), then successively for $\phi_2, \phi_3, \cdots \phi_{n-1}$ until ϕ_n is the only unknown left in the equation. The equation for ϕ_n can be obtained from

$$\phi_n = \frac{(q_{n-1} + C_n)G_{n-1} + r_{n-1}}{P_{n-1} - (q_{n-1} + C_n)(E_{n-1} + F_{n-1})} \tag{A.9}$$

where

$$P_i = P_{i-1} - q_{i-1}F_{i-1} \tag{A.10}$$

$$q_i = q_{i-1}E_{i-1} \tag{A.11}$$

$$r_i = r_{i-1} + q_{i-1}G_{i-1} \tag{A.12}$$

Eqs. (A.10-12) are for i=2, 3, $\cdots$ n-1. For i=1, $P_1 = A_n$, $q_1 = B_n$ and $r_1 = D_n$. Finally, by back substitution, the values of $\phi_{n-1}, \cdots \phi_1$ can be calculated.

References

Abe, K., Kondoh, T. and Nagano, Y., 1994, "A new turbulence model for predicting fluid flow and heat transfer in separating and reattaching flows - I. flow field calculations", *Int. J. Heat Mass Transfer*, Vol. 37, pp. 139-151.

Abid, R., Morrison, H. J. and Gatski, T. B., 1996, "Prediction of aerodynamic flows with a new explicit algebraic stress model", *AIAA, J.*, Vol. 34, No. 12, pp. 2632-2635.

Abid, R., Rumsey, C. and Gatski, T. B., 1995, "Prediction of nonequilibrium turbulent flows with explicit algebraic stress model", *AIAA J.*, Vol. 33, pp. 2026-2031.

Acharya, S., Dutta, S., Myrum, T. A. and Baker, R. S., 1994, "Turbulent flow past a surface-mounted two-dimensional rib", *ASME J. Fluids Engineering*, Vol. 116, pp. 238-246.

Acharya, S., Dutta, S., Myrum, T. A., 1998, "Heat transfer in turbulent flow past a surface-mounted two-dimensional rib", *ASME J. Heat Transfer*, Vol. 120, pp. 724-734.

Acharya, S., Dutta, S., Myrum, T. A., and Baker, R. S., 1993, "Periodically developed flow and heat transfer in a ribbed duct", *Int. J. Heat Mass Transfer* , Vol. 36, No. 8, pp. 2069-2082.

Amon, C. H., 1992, "Heat transfer enhancement by flow destabilization in electronic chip configuration", *ASME J. Electronic Packaging*, Vol. 114, pp. 35-40.

Apsley, D. D. and Leschziner, M. A., 1998, "Advanced turbulence modelling of separated flow in a diffuser", *Flow, Turbulence and Combustion*, Vol. 63, pp. 81-112.

Baelmans, M., 2002, "On the future of computational fluid dynamics for electronics cooling", *Thermal Challenges in Next Generation Electronic Systems*, Joshi, Y. K., Garimella, S. V. and Santa Fe, N. M (Eds.).

Bailey, C., 2003, "Modelling the effect of temperature on product reliability", *19th IEEE SEMI-THERM Symposium*, pp. 324-331.

Balaras, E., Benocci, C. and Piomelli, U., 1996, "Two-layer approximate boundary conditions for large-eddy simulation", *AIAA J.*, Vol. 34, pp. 1111-1119.

Baldwin, B.S. and Lomax, H., 1978, "Thin-layer approximation and algebraic model for separated turbulent flows", *AIAA paper*, No. 78-257.

Barakos, G. and Drikakis, D., 2000, "Investigation of nonlinear eddy-viscosity turbulence models in shock/boundary-layer interaction", *AIAA J.*, Vol. 38, No.3, pp. 461-469.

Bardina, J., Ferziger, J. H. and Reynolds, W. C., 1980, "Improved subgrid scale models for large eddy simulation", *AIAA paper*, No. 80-1357.

Batten, P., Goldberg, U. and Chakravarthy, S., 2000, "Sub-grid turbulence modelling for unsteady flow with acoustic resonance", *AIAA paper*, No. 00-0473.

Bosch, G. and Rodi, W., 1998, "Simulation of vortex shedding past a square cylinder with different turbulence models", *Int. J. Numer. Meth. Fluids*, Vol. 28, pp. 601-616.

Boussinesq, J., 1877, "Théorie de l'écoulement tourbillant", *Mém. Prés. par div. savant à l'Acad Science*, Paris, Vol. 23, pp. 46.

Brandt, A., 1972, "Multilevel adaptive technique for fast numerical solution to boundary value problems", *Proc. 3rd Int. Conf. on Numerical Method in Fluid Dynamics, Lecture Notes in Physics*, Vol. 18, pp. 82-29.

Brandt, A., 1977, "Multilevel adaptive solutions to boundary-value problems", *Mathematics of Computation*, Vol. 31, No. 138, pp. 333-390.

Bredberg, J. and Davidson, L., 1999, "Prediction of flow and heat transfer in a stationary two-dimensional rib roughened passage using low-Re turbulent models", *3rd European Conf. on Turbomachinery, IMech*, pp. 963-972.

Bredberg, J., Davidson, L. and Iacovides, H., 2000, "Comparison of near-wall behavior and its effect on heat transfer for $k-\omega$ and $k-\epsilon$ turbulence models in rib-roughened 2D channels", *Proc. 3rd Int. Symp. on Turbulence, Heat and Mass Transfer*, Nagano, Y., Hanjalić, K. and Tsuji, T. (Eds.), pp. 381-388.

Cabot, W. H., 1996, "Near-wall models in large-eddy simulations of flows behind a backward-facing step", *Annu. Res. Briefs*, pp. 199-210, Center Turbul. Res., Stanford

Uni., Calif..

Cabot, W. H. and Moin, P., 1999, "Approximate wall boundary conditions in the large-eddy simulation of high Reynolds number flows", *Flow, Turbulence and Combustion*, Vol. 63, pp. 269-291.

Cebeci, T. and Smith, A. M., 1974, "Analysis of turbulent boundary layers", *series in Applied Mathematics and mechanics*, Vol. XV.

Chapman, D. R., 1979, "Computational aerodynamics development and outlook", *AIAA J.*, Vol. 17, p. 1293.

Cheesewright, R., McGrath, G. and Petty, D. G., 1990, "LDA measurements of turbulent flow in a duct of square cross section at low Reynolds number", Aeronautical Engineering Department, University of London, Report No. ER 101.

Chen, H. C. and Patel, V. C., 1988, "Near-wall turbulence models for complex flows including separation", *AIAA J.*, Vol. 26, pp. 641-649.

Chen, W. L., Lien, F. S. and Leschziner, M. A., 1998a, "Non-linear eddy-viscosity modeling of transitional boundary layers pertinent to turbomachine aerodynamics", *Int. J. Heat Fluid Flow*, Vol. 19, pp. 297-306.

Chen, W. L., Lien, F. S. and Leschziner, M. A., 1998b, "Computational prediction of flow around highly loaded compressor cascade blades with non-linear eddy-viscosity models", *Int. J. Heat Fluid Flow*, Vol. 19, pp. 307-319.

Chien, K. Y., 1982, "Prediction of channel and boundary layer flows with a low-Reynolds-number turbulence model", *AIAA J.*, Vol. 20, pp. 33-38.

Chieng, C. C. and Launder, B. E., 1980, "On the calculation of turbulent heat-transport downstream from an abrupt pipe expansion", *Numerical Heat Transfer*, Vol. 3, pp. 189-207.

Chung, Y. M. and Tucker, P. G., 2004, "Numerical studies of heat transfer enhancements in laminar separated flows", *Int. J. Heat Fluid Flow*, Vol. 25, pp. 22-31.

Chung, Y. M., Tucker, P. G. and Roychowdhury, D.G., 2003, "Unsteady laminar flow and convective heat transfer in a sharp 180° bend", *Int. J. Heat Fluid Flow*, Vol. 24, pp. 67-76.

Craft, T. J., Launder B. E. and Suga, K., 1993, "Extending the applicability of eddy-viscosity models through the use of deformation invariants and nonlinear elements", *Proc. 5th Int. Symp. Refined Flow Modeling and Turbulence Measurements*, Paris.

Craft, T. J., Launder, B. E. and Suga, K., 1996, "Development and application of a cubic eddy-viscosity model of turbulence", *Int. J. Heat Fluid Flow*, Vol. 17, No. 2, pp. 108-115.

Daly, B. J. and Harlow, F. H., 1970, "Transport equation in turbulence", *Phys. Fluids*, Vol. 13, pp. 2643-2649.

Davidson, L., 2000, "LESFOIL: a European project on large eddy simulations around a high-lift airfoil at high Reynolds number", *European Congress on Computational methods in Applied Sciences and Engineering*, Barcelona, pp. 1-22.

Davidson, L., 2001, "An introduction to turbulence models", lecture notes, Chalmers University of Technology, Sweden.

Davidson, L. and Peng, S. H., 2001, "A hybrid LES-RANS model based on a one-equation SGS model and a two-equation $k - \omega$ model", *Proc. 2rd Int. Symp. on Turbulence and Shear Flow Phenomena*, Kasagi, N. *et al.* (Eds.), pp. 175-180.

Deardorff, J. W., 1970, "A numerical study of three-dimensional turbulent channel flow at large Reynolds numbers", *J. Fluid Mech.*, Vol. 41, pp. 453-465.

Dittus, F. W., Boelter, L. M. K., 1930, Publications on Engineering, Vol. 2, pp. 443, University of California, Berkeley.

Djilali, N. and Bouhadji, A., 2001, "Effect of periodic upstream oscillations on convective heat transfer in an unsteady separated flow", *CHT'01: Advances in Computational Heat Transfer II*, Davis, G. d. V. and Leonardi, E. (Eds.), Begell House Inc., pp. 575-582.

Durbin, P. A. and Pettersson-Reif, B. A., 2001, *Statistical theory and modelling for turbulent flows*, John Wiley & Sons, New York.

Durst, F. and Rastogi, A. K., 1980, "Turbulent flow over two-dimensional fences", *Turbulent Shear Flows 2*, Bradbury *et al.* (Eds.), Spring-Verlag, Berlin, pp. 218-231.

Durst, F., Founti, M. and Obi, S., 1988, "Experimental and computational investigation of the two-dimensional channel flow over two fences in tandem", *ASME J. Fluids Engineering*, Vol. 110, pp. 48-54.

Eveloy, V., Lohan, J. and Rodgers, P., 2000, "A benchmark study of computational fluid dynamics predictive accuracy for component-printed circuit board heat transfer", *IEEE Transactions on Component and Packaging Technologies*, Vol. 23, No. 3, pp. 568-577.

Ferziger, J. H., 1996, "Large Eddy Simulation", *Simulation and Modeling of Turbulent Flows*, Gatski, T. B., Hussaini, M. Y. and Lumley, J. H. (Eds.), Oxford University Press.

Fluent 5 User's Guide.

Garimella, S. V., Joshi, Y. K., Bar-Cohen, A., Mahajan, R., Toh, K. C., Carey, V. P., Baelmans, M., Lohan, J., Sammakia, B. and Andros, F., 2002, "Thermal challenges in next generation electronic systems - summary of panel presentations and discussions", *IEEE Transactions on Component and Packaging Technologies*, Vol. 25, No. 4, pp. 569-575.

Gatski, T. B. and Speziale, C. G., 1993, "On explicit algebraic stress models for complex turbulent flows", *J. Fluid Mech.*, Vol. 254, pp. 59-78.

Germano M., Piomelli U., Moin P. and Cabot W. H., 1991, "A dynamic subgrid-scale eddy viscosity model", *Phys. Fluids A*, Vol.3, p. 1760.

Ghaddar, N. K., Korczak, K. Z., Mikic, B. B. and Patera, A. T., 1986a, "Numerical investigation of incompressible flow in grooved channel. Part I: stability and self-sustained oscillations", *J. Fluid Mech.*, Vol. 163, pp. 99-127.

Ghaddar, N. K., Magen, M., Mikic, B. B. and Patera, A. T., 1986b, "Numerical investigation of incompressible flow in grooved channel. Part II: Resonance and oscillatory heat-transfer enhancement", *J. Fluid Mech.*, Vol. 168, pp. 541-567.

Gibson, M. M. and Launder, B. E., 1978, "Ground effects on pressure fluctuations in the atmospheric boundary layer", *J. Fluid Mech.*, Vol. 86, pp. 491-511.

Hamba, F., 2001, "An approach to hybrid RANS/LES calculation of channel flow", *Engineering Turbulence Modelling and Experiment - 5*, Rodi, W. and Fueyo, N. (Eds.), pp. 297-305.

Hanjalić, K., 1994, "Achievements and limitations in modeling and computation of buoyant turbulent flows and heat transfer in an enclosure", *Proc. Int. Heat Transfer Conf.*, Brighton, Vol. 1, pp. 1-18.

Heindel, T. J., Incropera, F., P. and Ramadhyani, S., 1995, "Laminar natural convection in a discretely heated cavity: II – comparisons of experimental and theoretical results", *ASME J. Heat Transfer*, Vol. 117, pp. 910-916.

Heindel, T. J., Ramadhyani, S. and Incropera, F., P., 1996, "Conjugate natural convection from an array of protruding heat sources", *Numerical Heat Transfer. Part A*, Vol. 29, pp. 1-18.

Heyerichs, K. and Pollard, A., 1996, "Heat transfer in separated and impinging turbulent flows", *Int. J. Heat Mass Transfer*, Vol. 39, No. 12, pp. 2385-2400.

Hirsch, C., 1988, *Numerical Computation of Internal and External flows*, John Wiley & Sons Publisher.

Hishida, M., Nagono, Y. and Tagawa, M., 1986, "Transport processes of heat and momentum in the wall region of turbulent pipe flow", *Proc. 8th Int. Heat transfer Conf.*, San Francisco, Vol. 3, pp. 925-930.

Iacovides, H. and Raisee, M., 1997, "Computation of flow and heat transfer in 2D rib roughened passages", *Proc. 2nd Int. Symp. on Turbulence, Heat and Mass Transfer*, Hanjalić, K. and Peeters, T. (Eds.), Delft University Press, pp. 21-30.

Iacovides, H. and Raisee, M., 1999, "Recent progress in the computation of flow and heat transfer in internal cooling passages of turbine blades", *Int. J. Heat Fluid Flow*, Vol. 20, pp. 320-328.

Iacovides, H. and Raisee, M., 2000, "Computation of flow and heat transfer in two-dimensional rib-roughened passages, using low-Reynolds-number turbulence models", *Int. J. Numer. Meth. Heat Fluid Flow*, Vol. 11, No. 2, pp. 138-155.

Iacovides, H. and Toumpanakis, P., 1993, "A turbulence modelling of flow in axisymmetric rotor-stator systems", *Proc. IAHR, 5th Int. Symp. on Refined Flow Modelling and Turbulence Measurements*, Paris.

Jayatillaka, C., 1969, "The influence of Prandtl number and surface roughness on the resistance of the laminar sublayer to momentum and heat transfer", *Progr. in Heat and Mass Transfer 1*, Vol. 193.

Johansson, S. H., Davidson, L. and Olsson, E., 1993, "Numerical simulation of vortex shedding past triangular cylinder at high Reynolds number using a $k-\epsilon$ turbulence model", *Int. J. Numer. Meth. Fluids*, Vol. 16, pp. 859-878.

Johnson, R. W. and Launder, B. E., 1982, "Discussion of 'on the calculation of turbulent heat transfer downstream from an abrupt pipe expansion", *Numerical Heat Transfer*, Vol. 5, pp. 493-496.

Jones, W. P. and Launder, B. E., 1972, "Some properties of sink flow turbulent boundary layers", *J. Fluid Mechanics*, Vol. 56, pp. 337-351.

Kader, B. A., 1981, "Temperature and concentration profiles in fully turbulent boundary layers", *Int. J. Heat Mass Transfer*, Vol. 24, No. 9, pp. 1541-1544.

Kim, J., Moin, P. and Moser, R., 1987, "Turbulence statistics in a fully developed flow at low Reynolds number", *J. Fluid Mech.*, Vol. 177, pp. 133-166.

Lam, C. K. G. and Bremhorst, K. A., 1981, "Modified form of the $k - \epsilon$ model for predicting wall turbulence", *ASME J. Fluids Engineering*, Vol. 103, pp. 456-460.

Larousse, A., Martinuzzi, R. and Tropea, C., 1991, "Flow around surface-mounted, three-dimensional obstacles", *Selected papers of the 8th Symp. on Turbulent Shear Flows*, Springer-Verlag, New York, pp. 127-139.

Laufer, J., 1954, "Investigation of turbulent flow in a two-dimensional channel", NACA Rep. 1053.

Launder, B. E., 1988, "On the computation of convective heat transfer in complex turbulent flows", *ASME J. Heat Transfer*, Vol. 110, No. 11, pp. 1112-1118.

Launder, B. E. and Spalding, D. B., 1974, "The numerical computation of turbulent flows", *Comput. Methods Appl. Mech. Engrg.*, Vol. 3, pp. 269-289.

Launder, B. E. and Sharma, B.I., 1974, "Application of the energy-dissipation model of turbulence to the calculation of flow near a spinning disc", *Letters in Heat and Mass Transfer*, Vol.1, pp. 131-138.

Leonard, A., 1974, "Energy cascade in large-eddy simulations of turbulent fluid flows", *Adv. in Geophys*, Vol. 18, pp. 237-248.

Leschziner, M. A., 2002, "Turbulence modelling strategies for unsteady flows - report on EPSRC visiting fellowship grant GR/R04263/01".

Lien, F.S. and Leschziner, M. A., 1994, "Assessment of turbulent transport models including non-linear RNG eddy-viscosity formulation and second-moment closure", *Computers and Fluids*, Vol. 23, No. 8, pp. 983-1004.

Lilly, D. K., 1992, "A proposed modification of the Germano subgrid-scale closure method", *Phys. Fluids*, Vol. 4, pp. 633-635.

Liou, T. M., Wu, Y. Y. and Chang, Y., 1993, "LDV measurements of periodic fully developed main and secondary flows in a channel with rib-disturbed walls", *J. Fluids Engineering*, Vol. 115, pp. 109-114.

Malan, P., 1999, "Industrial computational fluid dynamics", *Lecture Series*, von Karman Institute for Fluid Dynamics, May 31 - June 4.

Martinuzzi, R. J. and Tropea, C., 1993, "The flow around surface mounted, prismatic obstacles placed in a fully developed channel flow", *ASME J. Fluids Engineering*, Vol. 115, pp. 85-92.

Mathey, F., Fröhlich, J. and Rodi, W., 1999, "LES of heat transfer in turbulent flow over a wall-mounted matrix of cubes", *Proc. of Workshop on Direct and Large Eddy Simulation*, Isaac Newton Institute Cambridge, Kluwer Academic, pp. 51-62.

Maudgal, V. and Joshi, Y., 1995, "Numerical simulation of natural convection cooled electronic enclosures", *Proc. IEEE 45th Electron. Comp. Technol. Conf.*, Las Vegas, pp. 1166-1173.

Meinders, E. R. and Hanjalić, K., 1998, "Experimental evaluation of the local convective heat transfer from configurations of wall-mounted cubes in a channel flow", *Electronics Cooling*, Vol. 4, pp. 34-38.

Meinders, E. R., Hanjalić, K. and Martinuzzi, R. J., 1999, "Experimental study of the local convection heat transfer from a wall-mounted cube in turbulent channel flow", *ASME J. Heat Transfer*, Vol. 121, pp. 564-573.

Meinders, E. R. and Hanjalić, K., 1999, "Vortex structure and heat transfer in turbulent flow over a wall-mounted matrix of cubes", *Int. J. Heat Fluid Flow*, Vol. 20, pp. 255-267.

Moffat, R. J., 1988, "Describing the uncertainties in experimental results", *Experimental Thermal and Fluid Science*, Vol. 1, pp. 3-17.

Moin, P. and Kim, J., 1982, "Numerical investigation of turbulent channel flow", *J. Fluid Mech.*, Vol. 118, pp. 341-377.

Moin, P., Reynolds, W. C. and Ferziger, J. H., 1987, "Large eddy simulation of incompressible turbulent channel flow", *Report TF-12*, Dept. of Mechanical Engineering, Stanford University.

Mompean, G., Gavrilaski, S., Machiels, L. and Deville, M. O., 1996. "On predicting the turbulence-induced secondary flows using nonlinear $k-\epsilon$ models", *Phys. Fluids*, Vol. 8, No. 7, pp. 1856-1868.

Myers, B. A., 2003, "Cooling issues for automotive electronics", *Electronics Cooling*, Vol. 9, No. 3, pp. 24-39.

Ničeno, B., Gronkers, A. D. T. and Hanjalić, K., 2002, "Turbulent heat transfer from a multi-layered wall-mounted cube matrix: a large eddy simulation", *Int. J. Heat Fluid Flow*, Vol. 23, pp. 173-185.

Nigen, J. S. and Amon, C. H., 1993, "Forced convection cooling enhancement of electronic package configurations through self-sustained oscillatory flows", *ASME J. Electronic Packaging*, Vol. 117, pp. 356-365.

Nikitin, N. V., Nicoud, F., Wasistho, B., Squires, K. D. and Spalart, P. R., 2000, "An approach to wall modeling in large-eddy simulation", *Phys. Fluids, LETTERS*, Vol. 12, pp. 1629-1632.

Nisizima, S. and Yoshizawa, A., 1987, "Turbulent channel and Couette flows using an anisotropic $k-\epsilon$ model", *AIAA J.*, Vol. 25, pp. 414-420.

Nishimura, M., Tokuhiro, A., Kimura, N. and Kamide, H., 2000, "Numerical study on mixing quasi-planar jets with low Reynolds number turbulent stress and heat transfer equation models", *Nuclear Engineering and Design*, Vol. 202, pp. 77-95.

Ooi, A., Iaccarino, G., Durbin, P. A. and Behnia, M., 2002, "Reynolds averaged simulation of flow and heat transfer in ribbed ducts", *Int. J. Heat Fluid Flow*, Vol. 23, pp. 750-757.

Patankar, S. V., Liu, C. H. and Sparrow, E. M., 1977, "Fully developed flow and heat transfer in ducts having streamwise-periodic variations of cross-sectional area", *ASME J. Heat Transfer*, Vol. 99, pp. 180-186.

Patel, V. C., Rodi, W. and Scheuerer, G., 1985, "Turbulence models for near-wall and low Reynolds number flows: a review", *AIAA J.*, Vol. 23, pp. 1308-1319.

Peng, S. H., Davidson, L. and Holmberg, S., 1997, "A modified low-Reynolds-number

$k-\epsilon$ model for circulating flows", *J. Fluid Engineering*, Vol. 119. pp. 867-875.

Piomelli, U., 1988, "Model consistency in large eddy simulation of turbulent channel flows", *Phys. Fluids*, Vol. 31, pp. 1884-1891.

Piomelli, U., 1993, "High Reynolds number calculations using the dynamic subgrid-scale stress model", *Phys. Fluids A*, Vol. 5, pp. 1484-1490.

Piomelli, U., 1999, "Large-eddy simulation: achievements and challenges", *Progress in Aerospace Sciences*, Vol. 35, pp. 335-362.

Piomelli, U. and Balaras, E., 2002, "Wall-layer models for large-eddy simulations", *Annu. Rev. Fluid Mech.*, Vol. 34, pp. 349-374.

Piomelli, U., Balaras, E., Pasinato, H., Squires, K. D. and Spalart, P. R., 2003, "The inner-outer layer interface in large-eddy simulations with wall-layer models", *Int. J. Heat Fluid Flow*, Vol. 24, pp. 538-550.

Pope, S. B., 1975, "A more general effective viscosity hypothesis", *J. Fluid Mech.*, Vol. 72, pp. 331-340.

Prandtl L., 1925, "Bericht *über*die ausgebildete Turbulenz", *ZAMM*, Vol. 5, pp. 136-139.

Ratts, E., Amon, C. H., Mikic, B. B. and Patera, A. T., 1988, "Cooling enhancement of forced convection air cooled chip array through flow modulation induced by vortex-shedding cylinders in cross-flow", *Cooling Technology for Electronic Equipment*, Aung, W. (Ed.), Hemisphere Publishing Company, New York, pp. 183-194.

Rau, G., Cakan, M., Moeller, D. and Arts, T., 1998, "The effect of periodic ribs on the local aerodynamics and heat transfer performance of a straight cooling channel", *J. Turbomach.*, Vol. 120, pp. 368-375.

Rodi, W., Ferziger, H. J., Breuer, M., Pourquié, M., 1997, "Status of large eddy simulation: results of workshop", *ASME J. Fluids Engineering*, Vol. 119, pp. 248-262.

Rodi, W., 1976, "A New Algebraic Relation for Calculation the Reynolds Stresses", *Zeitschrift für Angewandte Mathematik und Mechanik*, Vol. 56, pp. T219-T221.

Rodi, W. and Spalding, D. B., 1970, "A two parameter model of turbulence and its application to free jet", *Wärme und Stoffübertragung*, Vol. 3, p. 85.

Rokni and Sunden , 1999, "Improved modeling of turbulent forced convective heat transfer in straight ducts", *ASME J. Heat Transfer*, Vol. 121, pp. 712-718.

Rotta, J., 1951, "Statische Theorie nichthomogener Turbulenz", *Zeitsch. für Physik*, Vol. 129, p. 547 and Vol. 131, p. 51.

Runchal A.K., 1987, "CONDIF. A modified central-difference scheme for convective flows", *Int. J. Num. Meths in Engineering*, Vol. 24, pp. 1593-1608.

Sagaut, P., 2000, *Large eddy simulation for incompressible flows, an introduction*, Springer-Verlag, Berlin.

Schmidt, S. and Thiele, F., 2002, "Comparison of numerical methods applied to the flow over wall-mounted cubes", *Int. J. Heat Fluid Flow*, Vol, 23, pp. 330-339.

Shih, T. H., Zhu, J. and Lumley, J. L., 1993, "A realizable Reynolds stress algebraic equation model", *NASA Tech. Memo.* 105993.

Shur, M., Spalart, P. R., Strelets, M. and Travin, A., 1999, "Dettached-eddy simulation of an aerofoil at high angle of attack", *Proc. 4th Int. Symp. on Engineering Turbulence Modelling and Measurements*, Ajaccio, Corsica, France, pp. 669-678.

Smagorinsky, J., 1963, "General circulation experiments with the primitive equations. I: The basis experiment", *Month. Weath. Rev.*, Vol. 91, pp. 99-165.

Spalart P. R. and Allmaras S. R., 1994, "A one-equation turbulence model for aerodynamic flow", *La Recherche Aerospatiale*, vol. 1, pp. 5-21.

Spalart, P. R., Jou, W-H, Strelets, M. and Allmaras, S. R. , 1997, "Comments on the feasibility of LES for wings, and on a hybrid RANS/LES approach", *First AFOSR Int. Conf. on DNS/LES in Advances in DNS/LES*, pp. 137-147.

Spalart, P. R., 2000, "Strategies for turbulence modelling and simulations", *Int. J. Heat Fluid Flow*, Vol. 21, pp. 252-263.

Spalding, D. B., 1967, "The calculation of the length scale of turbulence in some turbulent boundary layers remote from walls", Imperial College, Heat Transfer Sec. Rep., TWF/TN/31.

Spalding, D. B., 1969, "The prediction of two-dimensional steady turbulent flows", Imperial College, Heat Transfer Sec. Rep., EF/TN/A/16.

Spalding, D. B., 1994, "Calculation of turbulent heat transfer in cluttered spaces", unpublished paper presented at the *10th International Heat Transfer Conference*, Brighton, U.K. .

Speziale, C. G., 1987, "On non-linear *k-l* and *k-ϵ* models of turbulence", *J. Fluid Mech.*, Vol. 178, pp. 459-475.

Speziale, C. G., Abid, R. and Anderson, E. C., 1992, "Critical evaluation of two-equation models for near-wall turbulence", *AIAA J.*, Vol. 30, pp. 324-331.

Speziale, C. G. and Ngo, T., 1988, "Numerical solution of turbulent flow past a backward facing step using a nonlinear $k - \epsilon$ model", *Int. J. Engng. Sci.*, Vol. 26, No. 10, pp. 1099-1112.

Speziale, C. G., Sarkar, S. and Gatski, T. B., 1991, "Modelling the pressure-strain correlation of turbulence: an invariant dynamical system approach", *J. Fluid Mech.*, Vol. 227, pp. 245-272.

Suga, K. 1995, "Development and application of a non-linear eddy viscosity model sensitizes to stress and strain invariants", PhD thesis, Dept. of Mech. Eng. Faculty of Technology, University of Manchester.

Temmerman, L., Leschziner, M. A. and Hanjalić, K., 2002, "A-priori studies of a near-wall RANS model within a hybrid LES/RANS scheme", *Engineering Turbulence Modelling and Experiment - 5*, Rodi, W. and Fueyo, N. (Eds.), pp. 317-326.

Temmerman, L., Leschziner, M. A. and Hanjalić, K., 2003, "A combined RANS-LES strategy with arbitary interface location for near-wall flows", *Proc. 3rd Int. Symp. on Turbulence and Shear Flow Phenomena*, Kasagi, N. *et al.* (Eds.), Sendai, Japan, pp. 929-934.

Tennekes, H. and Lumley, J. L., 1972, *A first course in turbulence*, The MIT Press, Cambridge, Massachusetts.

Travin, A., Shur, M., Strelets M. and Spalart, P. R., 1999, "Detached-eddy simulations past a circular cylinder", *Flow, Turbulence and Combustion*, Vol. 63, pp. 293-313.

Tropea, C. D. and Gackstatter, R., 1985, "The flow over two-dimensional surface-mounted obstacles at low Reynolds numbers", *ASME J. Fluids Engin.*, Vol. 107, pp. 489-494.

Tucker, P. G., 1990, "Numerical and experimental work on rotaing cavities", *Technical Report 90/TFMRC/TN91*, Thermo-fluid Mechanics Research Centre, School of

Engineering and Applied Sciences, University of Sussex.

Tucker, P. G., 1997, "CFD applied to electronic systems: a review", *IEEE Transactions on Component, Packaging and Manufacturing Technology*, Vol. 20, No. 4, pp. 518-529.

Tucker, P. G., 1998, "Assessment of geometric multilevel converfence robustness and a wall distance method for flows with multiple internal boundaries", *Applied Methematical Modelling*, Vol. 22, pp. 293-311.

Tucker, P. G.. and Pan, Z., 2000, "URANS Computation for a Complex Internal isothermal Flow", *Comput. Methods Appl. Mech. Engrg.*, Vol. 190, pp. 1-15.

Tucker, P. G., 2000, "Prediction of turbulent oscillatory flows in complex system", *Int. J. Numer. Meth. in Fluids*, Vol. 33, pp. 869-895.

Tucker, P. G., 2001, *Computation of Unsteady Internal Flows*, Kluwer Academic Publisher, Dordrecht.

Tucker, P. G., Liu, Y., Chung, Y. M. and Jouvray, A., 2003a, "Computation of an unsteady complex geometry flow using novel non-linear turbulence models", *Int. J. Numer. Meth. Fluids*, Vol. 43, pp. 979-1001.

Tucker, P. G. and Davidson, L., 2003b, "Zonal *k-l* based large eddy simulations", *41st AIAA Aerospace Sciences Meeting and Exhibits*, 6-9 January, Reno, Nevada.

Tucker, P. G., 2003c, "Differential equation-based wall distance computation for DES and RANS", *J. Comput. Phys.*, Vol. 190, pp. 229-248.

Tucker, P. G., Davidson, L. and Liu, Y., 2003d, "Hybrid $k - l$ based large eddy simulation modelling", *Proc. 4th Int. Symp. on Turbulence, Heat and Mass Transfer*, Hanjalić, K., Nagano, Y. and Tummers, M. J. (Eds.), Antalya, Turkey, pp. 681-688.

Tucker, P. G., 2004, "Novel MILES computations for jet flows and noise", accepted by *Int. J. Heat Fluid Flow.*

van Driest E. R., 1956, "On turbulent flow near a wall", *J. Aeronautical Sciences*, Vol. 23, p. 1007.

Versteeg, H. K. and Malalasekera, W., 1995, *An Introduction to Computational Fluid Dynamics*, Pearson Education Limited.

Viswanath, R, Wakharkar, V., Watwe, A. and Lebonheur, V., 2000, "Thermal performance challenges from silicon to system", *Intel Technology Journal*, 3rd quarter.

Wietrzak, A. and Poulikakos, D., 1990, "Turbulent forced convective cooling of microelectronic devices", *Int. J. Heat Fluid Flow*, Vol. 11, No. 2, pp. 105-113.

Wilcox, D. C., 1998, *Turbulence Modelling for CFD*, DCW Industries, Inc..

Wolfshtein, M., 1969, "The velocity and temperature distribution in one-dimensional flow with turbulence augmentation and pressure gradient", *Int. J. Heat Mass Transfer*, Vol. 12, pp. 301-318.

Yap, C. R., 1987, "Turbulent Heat and Momentum Transfer in Recirculation and Impinging Flows", PhD thesis, Dept. of Mech. Eng., Faculty of Technology, Univ. of Manchester.

Yoshizawa, A., 1984, "Statistical analysis of the deviation of the Reynolds stress from its eddy viscosity representation", *Phys. Fluids*, Vol. 27, pp. 1377-1387.

Yoshizawa, A., 1993, "Bridging between eddy-viscosity-type and second-order models using a two-scale DIA", *Proc. 9th Int. Symp. on Turbulent Shear Flow*, Kyoto, Vol. 3, pp. 23.1.1-6.

Zhong, B., Tucker, P. G. and Liu, Y., 2003, "On a hybrid LES/RANS approach and its application to flow over a matrix of surface mounted cubes", *Proc. 4th Int. Symp. on Turbulence, Heat and Mass Transfer*, Hanjalić, K., Nagano, Y. and Tummers, M. J. (Eds.), Antalya, Turkey, pp. 705-712.